NONLINEAR OPTICAL STUDIES OF GRAPHENE BASED HYBRID MATERIALS, BIO-REDUCED SILVER NANOPARTICLES AND ORGANIC MOLECULES TOWARDS OPTICAL LIMITING APPLICATION

A Thesis Submitted for the Degree of

DOCTOR OF PHILOSOPHY

By

B. M. KRISHNA MARISERLA

School of Physics

University of Hyderabad

Hyderabad - 500 046

India

November 2012

To

my sweet mom

&

my thesis supervisor

The first, my mother Mrs. M. Subhadhra for raising me, guiding me, and continuing to be my sounding board for every important decision I make. Thank you, mom for listening and for always being there through everything. Your love and care are what have made possible the many opportunities I have had, thank you.

The second, my thesis supervisor Prof. D. Narayana Rao, influenced my life and his great support throughout the course of duration. He inspired me to think, dream, and stand tall on a daily basis.

DECLARATION

I here by declare that the matter embodied in the thesis entitled "**Nonlinear optical studies of Graphene based hybrid materials, Bio-reduced silver nanoparticles and Organic molecules towards optical limiting application**" is the result of investigation carried out by me in the School of Physics, University of Hyderabad, India, under direct supervision of Prof. D. Narayana Rao.

Place: Hyderabad

Date: (B. M. Krishna Mariserla)

CERTIFICATE

This is to certify that the work described in this thesis entitled "**Nonlinear optical studies of Graphene based hybrid materials, Bio-reduced silver nanoparticles and Organic molecules towards optical limiting application**" has been carried out by **B. M. Krishna Mariserla**, under my direct supervision and this has not been submitted for any degree or diploma at this or any other University.

Place: Hyderabad

Date: **(Prof. D. Narayana Rao)**

Dean
School of Physics

ACKNOWLEDGEMENTS

It is really hard to thank properly all the people who helped in various stages of my Ph. D research life. I thank my family first, always whispering positive words and offering warm care during many difficulties.

I am grateful to my advisor, Prof. D. Narayana Rao, for all his help and guidance throughout the years, and for sharing the elegant way of doing science. And I think that now, I finally understand that "why" is as important as "how" one does an experiment.

I thank Prof. S. P. Tewari, Dean, School of Physics, former Deans Prof. Vipin Srivastava and Prof. C. Bansal, and faculty for their co-operation in providing facilities in the School. I would like to thank Dr. Suneel Singh, Dr. V. S. Ashoka, Dr. V. Nirmal Kumar, Dr. P. Anantha Lakshmi, and Prof. S. Dutta Gupta, for their valuable suggestions at Doctoral committee meetings.

I thank my labmates (Dr. R. Sai Santosh Kumar, Dr. N. Venkatram, Dr. B. M. Manoj, K. Shadak Ali, Dr. K. Deepak, V. Praveen, H. Shekar, V. Sriramulu, G. Sriram, Kuladeep, and Dr. Satyavati) who contributed to my positive feelings in the darkness of a Laser Lab, where things were harder than the hardest thoughts.

I would like to thank Dr. R. Venkatesan, School of Chemistry, Pondicherry University and his student N. Venkatramaiah for providing samples. I would also like to thank Dr. L. Giribabu, IICT, Hyderabad, for his valuable discussions and phthalocyanine sample.

Best friends are a rare find. Two of them are Paladugu Sathyanarayana and M. Suman Kalyan with whom I spent a good time in the campus. My sincere thanks to D. Bharat, who is the best among all the friends I had, for his constant support from my graduation days. Many thanks to Dr. N. Sreedhar, Dr. Jagadeesh, Dr. Phani Pavan, Dr. D. K. Srinivas, Dr. Chitu and Dr. Sathish.

At this juncture, I should extend my sincere thanks and deep appreciation to my friends G. Srinivasa Rao, Ch. Anjaneyulu, K. Ramesh, Yashaswini, Thotreithem Hongray, Regina Jose, V. V. G. Krishna, S. Siva N Chari,

S. Saipriya, P. Suresh, B. Yugandhar, T. Arun Kumar, M. Ramudu, M. Anil Kumar, Ch. Ravi Kumar, Shankar, B. Aalu, P. J. Monisha, K. Vasu, M. Durga Rao, A. Rambabu and Parthasarathy for their constant encouragement and support throughout the duration of this period.

I would like to thank technical assistants Deepti, Laxmi Narayana and Prasad for their cooperation in using micro-Raman spectrometer, FESEM and TEM instruments.

The encouragement and support provided by the Non-teaching staff, Abraham, in particular and others in general, in the school are highly appreciable.

Financial assistance in the form of BBL fellowship, CAS-RFMS and Senior Research Fellowship from University of Hyderabad, University Grants Commission (UGC) and Council of Scientific and Industrial Research (CSIR), respectively, are gratefully acknowledged.

Thanks are also due to all those whose names are missing in this list and have helped me in various stages of my work.

The unconditional love of my father, sister and brother and their prayers made me what I am today and I owe everything to them. I would like to thank all my family members and relatives for their support and guidance throughout my life.

B. M. Krishna Mariserla

Table of Contents

List of abbreviations

DFWM	: Degenerate four wave mixing
ESA	: Excited state absorption
FOM	: Figure of merit
fs	: Femtosecond
FTIR	: Fourier transform infrared spectroscopy
FESEM	: Field emission scanning electron microscope
ISC	: Inter system crossing
LT	: Linear transmittance
NLO	: Nonlinear optical
NLA	: Nonlinear absorption
NLR	: Nonlinear refraction
ns	: Nanosecond
OL	: Optical limiting
ps	: Picosecond
RSA	: Reverse saturable absorption
SA	: Saturable absorption
SEM	: Scanning electron microscope
TPA	: Two photon absorption
3PA	: Three photon absorption
XRD	: X-ray diffraction

List of publications

1. **M. Bala Murali Krishna**, N. Venkatramaiah, R. Venkatesan and D. Narayana Rao, "*Synthesis, Structural, Spectroscopic and nonlinear optical measurements of graphene and its organic composites*", Journal of Materials Chemistry, 22, 3059 (2012), Impact Factor (I.F) = 5.1. Citations: 1.

2. **M. Bala Murali Krishna**, V. Praveen Kumar, N. Venkatramaiah, R. Venkatesan and D. Narayana Rao. "*Nonlinear optical properties of covalently linked graphene-metal porphyrin composite materials*", Appl. Phys. Lett, 98, 081106 (2011) (appeared in Virtual Journal of Nanoscale Science & Technology, Volume 23, Issue 9, 2011). I.F = 3.84. Citations: 8.

3. **M. Bala Murali Krishna**, L. Giribabu and D. Narayana Rao. "*Nanosecond, Picosecond, and Femtosecond nonlinear optical properties of a water soluble zinc octacarboxy phthalocyanine*, Journal of porphyrins and phthalocyanines, 16, 1015 (2012). I. F =1.3. Citations: 1.

4. R. Sathyavathi (post.doc), **M. Bala Murali Krishna** and D. Narayana Rao, "*Biosynthesis of silver Nanoparticles using Moringa Oleifera leaf extract and its application to optical limiting*", J. Nanosci. Nanotechnol. 11, 2031-2035 (2011). I.F= 1.5. Citations: 7.

5. Prabhakar,Ch.(Chem. student), Bhanuprakash, K.(Chem.Prof), Rao, V.J.(Chem. Prof), **Bala murali krishna, M**.(Phy. student), Rao, D.N.(Phy. Prof) "*Third Order Nonlinear Optical Properties of Squaraine Dyes Having Absorption below 500 nm: A Combined Experimental and Theoretical Investigation of Closed Shell Oxyallyl Derivatives*", J. Phys. Chem. C, 114 (13), pp 6077–6089, 2010. I.F= 4.8. Citations: 9.

6. R.Sathyavathi (post.doc), **M. Bala Murali Krishna**, S.VenugopalRao, R.Saritha, and D.NarayanaRao. "*Biosynthesis of Silver Nanoparticles Using Coriandrum Sativum Leaf Extract and Their Application in Nonlinear Optics*", Advanced Science Letters, 3, 138–143,2010. I. F: 1.253. Citations: 43.

7. K. Shadak Alee, **M. Bala Murali Krishna**, B. Ashok and D. Narayana Rao., "*Experimental verification of enhanced electromagnetic field intensities at the band edge of 3D polystyrene photonic crystals using Z-Scan technique*", photonics and nanostructures: fundamentals and applications, 10,236-242, 2012. I. F: 2.75.

8. Prakash C. Srivastava, Shrinkhal Dwivedi, Vikas Singh, Tripurari Pujan, Arun K. Bhuj, Ray J. Butcher, **M. Bala Murali Krishna** and D. Narayan Rao, "*Supramolecular assemblies of organotellurium (IV) dithiocarbamates and third order nonlinear optical susceptibility ($\chi^{(3)}$) of $C_4H_7(CH_3)Te[S_2CN(C_2H_5)_2]_2$*", Inorganica chemical acta, 388, 175, 2012. I. F: 1.899.

9. Prakash C. Srivastava, Vikas Singh, Shrinkhal Dwivedi, Tripurari Pujan, Arun K. Bhuj, Ray J. Butcher, **M. Bala Murali Krishna** and D. Narayana Rao, "*Synthesis, crystal structure, supramolecular associations and third-order nonlinear optical (NLO) properties of some organotellurium (IV) derivatives*", Polyhedron, 42, 36, 2012. I.F: 2.

10. Kiran, P.P., Rao, S.V., Ferrari, M., **Krishna, B.M.**, Sekhar, H., Alee, S., Rao, D. N. "*Enhanced optical limiting performance through nonlinear scattering in nanoparticles of CdS, co-doped Ag-Cu, and BSO*", Nonlinear Optics Quantum Optics 40, (1-4), pp. 223-234, 2010.

11. Rao, S.V., Kiran, P.P., Giribabu, L., Ferrari, M., Kurumurthy, G., **Krishna, B.M.**, Sekhar, H., Rao, D.N. "*Anomalous nonlinear absorption behavior in an unsymmetrical phthalocyanine studied near 800 nm using femtosecond and picosecond pulses*", Nonlinear Optics Quantum Optics 40, (1-4), pp. 183-191, 2010.

12. **M. Bala Murali Krishna**, N. Venkatramaiah, R. Venkatesan and D. Narayana Rao. "*Optical transmission control in graphene oxide and its organic composites with ultra-short pulses*", (Under Review in Mat. Chem. Phys).

13. **M. Bala murali Krishna** and D. Narayana Rao."*Influence of solvent contribution on material nonlinearities with ultrafast laser excitation*". (Manuscript is ready to submit).

14. **M. Bala Murali Krishna**, N. Venkatramaiah, R. Venkatesan and D. Narayana Rao., "*Synthesis, spectroscopic and optical study of graphene*

oxide-semiconductor (ZnO, TiO_2) nanoparticle composites: application towards broad band optical limiter", (Manuscript is ready to submit).

15. **M. Bala Murali Krishna**, N. Venkatramaiah, R. Venkatesan and D. Narayana Rao., "*Nonlinear optical measurements of GO-metal (Au, Ag) nanoparticles composites*", (Manuscript under preparation)

Conferences:

1. **M. Bala Murali Krishna**, "*Novel Graphene hybrid materials for NLO and Optical limiting Studies*", OSA Student Conference, Hyderabad University, India, Jan 8th 2012. {Oral presentation}

2. **M. Bala Murali Krishna**, N. Venkatramaiah, R. Venkatesan and D. Narayana Rao. "*Nonlinear optical properties of graphene-(OH, Sn) porphyrin composites in picosecond regime*" International conference on light (OPTICS 11), NIT, Calicut, Kerala, India, may 23-25, 2011.{Oral presentation} (AIP Conf. Proc. 1391, 680-682 (2011); doi: 10.1063/1.3643647)

3. K. Shadak Alee, **M. Bala Murali Krishna**, B. Ashok, D. Narayana Rao, "*Optical limiting studies of 3D polystyrene photonic crystals with the central band gap at 536 nm at normal incidence in reflection geometry*", International conference on light (OPTICS 11), NIT, Calicut, Kerala, India, may 23-25, 2011. {Oral presentation} (AIP Conf. Proc. 1391, 260-262 (2011); doi: 10.1063/1.3646850).

4. **M. Bala Murali Krishna**, V. Praveen Kumar, N. Venkatramaiah, R. Venkatesan and D. Narayana Rao, "*NLO studies of Graphene and its composites*", International Conference on Fiber Optics and Photonics (PHOTONICS-2010), Indian Institute of Technology Guwahati, Guwahati, India, Dec 11-15, 2010. [Poster presentation]

5. **M. Bala Murali Krishna**, V. Praveen Kumar, N. Venkatramaiah, R. Venkatesan and D. Narayana Rao, "*Enhanced optical nonlinearities of covalently linked Graphene-Zinc porphyrin composite materials*", DAE-BRNS National Laser Symposium (NLS-19), RRCAT, Indore, India, Dec 1-4, 2010. [Poster Presentation]

6. **M. Balamurali Krishna**, R. Sathyavathi, D. Narayana Rao. "*Nonlinear optical properties of Au/Ag Bimetallic nanoparticles*" India Singapore Joint Physics Symposium 2010 (ISJPS 2010), University of Hyderabad, Hyderabad, India, February 19th-21st, 2010. [Poster Presentation].

7. **M. Bala murali Krishna**, N. Venkatramaiah, R. Venkatesan and D. Narayana Rao, "*Optical nonlinearities of graphene-(sn, OH) porphyrin*

composites in nanosecond region", Workshop on "Physics at small scales", school of physics, university of Hyderabad, Hyderabad, India, March 18th-19th, 2011. [Poster Presentation]

8. **M. Balamurali Krishna**, R. Sathyavathi, S. Venugopal Rao, R. Saritha, D. Narayana Rao. "*Nonlinear optical properties of silver nanoparticles synthesized using coriander leaves*", International Conference on Advanced Nanoscience and Nanotechnology (ICANN-2009), IIT Guwahati, Guwahati, India, Dec. 9th- Dec. 12th 2009. [Poster Presentation]

9. **B. M. Krishna Mariserla**, D. Narayana Rao, R. Sai Santosh Kumar, L. Giribabu, S. Venugopal Rao. "*Nanosecond, Picosecond, and Femtosecond Nonlinear Optical Properties of a Zinc Phthalocyanine studied using Z-scan and DFWM techniques*", International Conference on Optics & Photonics(ICOP-2009), CSIO, Chandigarh, India, Oct. 30th-Nov. 1st 2009. [Oral Presentation].

10. D. Narayana Rao, **B.M. Krishana**, H. Sekhar, K. Shadak Alee, P. Prem Kiran, S. Venugopal Rao "*Optical Limiting studies in BSO nanocrystals dispersed in solution and a polymer matrix*" , International Conference on Optics & Photonics(ICOP-2009), CSIO, Chandigarh, India, Oct. 30th-Nov. 1st 2009. [Poster Presentation].

11. Kiran, P.P., Rao, S.V., Ferrari, M., **Krishna, B.M.,** Sekhar, H., Alee, S., Rao, D. N. "*Enhanced optical limiting performance through nonlinear scattering in Nanoparticles of CdS, co-doped Ag-Cu, and BSO*" , 5th International Symposium on Materials and Devices for Nonlinear Optics (ISOPL5). Porquerolles (France), June 26th - July 1st 2009. [Poster Presentation].

12. Rao, S.V., Kiran, P.P., Giribabu, L., Ferrari, M., Kurumurthy, G., **Krishna, B.M.,** Sekhar, H., Rao, D.N. "*Anomalous nonlinear absorption behavior in an unsymmetrical phthalocyanine studied near 800 nm using femtosecond and picosecond pulses*", , 5th International Symposium on Materials and Devices for Nonlinear Optics (ISOPL5). Porquerolles (France), June 26th - July 1st 2009. [Poster Presentation].

.

CHAPTER I

INTRODUCTION

Abstract

This chapter describes the fundamental concepts of nonlinear optics, related to third order nonlinear optical processes which include mainly two-photon absorption and nonlinear refraction. Other mechanisms like excited state absorption and free carrier absorption that lead to nonlinear absorption behavior are also discussed. These basic mechanisms are responsible for optical limiting in various classes of materials which we have studied. Motivation of the thesis and importance in choosing the materials for optical limiting is explained.

1.1 Introduction and motivation

Following the prominent utilization of high power laser sources over wide range of wavelengths and pulse durations as short as few femtoseconds to attoseconds, it was recognized that intense laser beams can easily damage delicate optical instruments and the human eye. Nowadays, lasers have become common in daily life so much so that they are being incorporated into toys. Thus, protection from lasers is not only a scientific subject but also a potential public safety issue. In this context, optical limiters have received significant attention for protection of these optical elements and have led to a comprehensive and extensive research. The characteristic optical limiting effect can be explicated as when the incident laser irradiance upon a sample is weak, the relationship between input þuence and output þuence (þuence = optical energy density) is linear with increasing incident laser irradiance, corresponding to a linear optical effect (i.e. obeying Beerôs law). Here, transmittance of the sample remains almost constant. However, when the incident laser irradiance increases beyond a threshold value, the output þuence will stay in a particular level which is unaffected by further increasing of the input þuence, and the nonlinear optical (NLO) effect comes into play to reduce the þuence of the transmitted light to a safe level. The minimum criteria identified for a material to act as an effective optical limiter are (i) Low limiting threshold and large dynamic range, (ii) High optical damage threshold, (iii) Broadband response, (iv) Fast response time and (v) High linear transmittance, optical clarity, and robustness. So, much research interest towards passive optical limiters (typically nonlinear optical materials) over active or dynamic devices is due to its inherent properties of sensing, processing and actuating [1]. Various organic materials, metal and semiconductor nanoparticles are being studied to achieve efficient optical limiting [2]. Several approaches have been developed towards achieving better optical limiting based on, e.g., electro-optical [3], magneto-optical [4], and all-optical [5] mechanisms. All-optical limiters rely on materials that exhibit one or more of the nonlinear optical mechanisms: two-photon absorption (TPA), reverse saturable absorption

(RSA), free carrier absorption, thermal defocusing and nonlinear scattering, photo-refraction, nonlinear refraction and induced scattering [1]. Enhancement in optical limiting has also been achieved by combing two or more of these mechanisms like self-defocusing in conjunction with TPA [6] and TPA of one molecule with excited state absorption (ESA) in another molecule [7].

1.2 Nonlinear optics and its origin

Nonlinear optics deals with interaction of applied electromagnetic fields with matter to generate the polarized electric field, altered in frequency, phase, or other physical properties. In other words, optical nonlinearities occur as a consequence of change of the optical properties such as absorption, refraction and scattering, etc. of a material system by the presence of light. Nonlinear phenomena in optics; electro-optical effects (Pockels and Kerr effects); the Zeeman effect, in which spectral lines are split by a magnetic field; the magneto-optical effect, which is magnetic field induced double refraction (Cotton-Mouton and Faraday effects). Nonlinear optics originates from the pioneering work of Maria Göppert-Mayer, who in her Ph.D. thesis (1931) described the concept of two-photon absorption. Since the inception of laser in 1960 nonlinear optics grown rapidly and rise its significance. Observation of the second harmonic generation (SHG) by Franken in 1961 was the first experimental evidence of optical nonlinearities. He observed that light of 347.1 nm could be generated when a Quartz crystal was irradiated with light of 694.2 nm, obtained from a ruby laser.

1.2.1 Interaction of light with a linear media

In order to interpret the refraction, reflection, dispersion, scattering and birefringence of light propagation in a medium, we should consider an important physical quantity, the electric polarization induced in a medium. The charge distribution induced in the molecule by the field is approximated by that of an induced dipole. The applied field polarizes the molecules in the medium, displacing them from their equilibrium positions and induces a dipole moment $\mu_{ind} = -er$, e is the electronic charge and r is the field induced displacement. The polarization resulting from this induced dipole is given

by $P = -Ner$, where N is the electron density in the medium. In the conventional optics, the electric polarization vector $\overline{P}$ is linearly proportional to the electric field strength $\overline{E}$,

i.e., $\overline{P} = \chi^{(1)} \cdot \overline{E}$ (1.1)

The proportionality constant is related to the dielectric constant by $\varepsilon = 1 + 4\pi\chi^{(1)}$. $\chi^{(1)}$ is susceptibility, a second rank tensor, because it relates all of the components of the polarization vector to all of the components of the electric field vector. Based on this linear assumption, Maxwellôs equations lead to a set of linear differential equations in which only the terms proportional to the first power of the field $\overline{E}$ are involved. As a result, there is no coupling between different light beams when they pass through a medium and only single photon absorption takes place in an absorbing medium.

The attenuation of an optical beam propagating in an absorbing medium can be described as

$$\frac{dI}{dz} = -\alpha I \,, \tag{1.2}$$

where I is the beam intensity, z is the variable distance along the beam propagation direction, and Ŭ is a absorption coefficient for a given medium. The physical meaning of Eq. (1.2) is that the decrease of beam intensity in a unit propagation length is linearly proportional to the intensity itself. From the Eq. (1.2), we can obtain a well known Beer-Lambert law expression

$$I(z) = I(0).e^{-\alpha z} \tag{1.3}$$

This implies that for a given propagation length z = ℓ, the transmitted intensity I(ℓ) is linearly proportional to the initial intensity of I = I(0).

1.2.2 Interaction of light with a nonlinear media

When a medium is subject to an intense electric field such that due to an intense laser pulse, the polarization response of the material is not adequately described by equation (1.1). Assuming that the polarization of the medium is still weak compared to the binding forces between the electrons and nuclei, polarization can be expressed in a power series of the field strength $\overline{E}$

$$\overline{P} = \chi^{(1)} \cdot \overline{E} + \chi^{(2)} : \overline{\mathrm{EE}} + \chi^{(3)} \vdots \overline{E}\overline{E}\overline{E} \ldots \tag{1.4}$$

The term that is quadratic in the field strength $\overline{E}$ describes the first nonlinear effect. The coefficient $\chi^{(2)}$ relating the polarization to the square of the field strength $\overline{E}$ is called the second-order nonlinear susceptibility of the medium. Its magnitude describes the strength of second-order process.

The term $\chi^{(3)}$ describes the third order processes. For most materials, the higher-order effects are extremely difficult to observe. For this reason, we limit our discussion to third-order effects.

Substituting Eq. (1.4) into Maxwellôs equations leads to a set of nonlinear differential equations that involve high order power terms of optical electric field strength. These terms are responsible for various observed coherent optical frequency mixing effects [8].

The manifestation of the optical behavior can be clearly seen by considering a sinusoidal field equation

$$E(z,t) = E_0 \cos(\omega t - kz), \text{ with } k^2 = \varepsilon\omega^2 / c^2 \tag{1.5}$$

where, E_0 defining the amplitude of the field, k is the propagation vector, characterizing the phase of the optical wave with respect to a reference point, kz describes the relative phase of the wave. Substituting Eq. (1.5) in Eq. (1.4) we have:

$$\begin{aligned} P &= \chi^{(1)} E_0 \cos(\omega t - kz) + \chi^{(2)} E_0^2 \cos^2(\omega t - kz) + \chi^{(3)} E_0^3 \cos 3(\omega t - kz) \ldots \\ \Rightarrow P &= \chi^{(1)} E_0 \cos(\omega t - kz) + \left(\frac{1}{2}\right)\chi^{(2)} E_0^2 [1 + \cos(2\omega t - 2kz)] \\ &\quad + \chi^{(3)} E_0^3 \left[\left(\frac{3}{4}\right)\cos(\omega t - kz) + \left(\frac{1}{4}\right)\cos(3\omega t - 3kz)\right] \ldots \end{aligned} \tag{1.6}$$

The above equation clearly shows the presence of new frequency components due to the nonlinear polarization.

Beer-Lambert law (Eq. 1.2 and 1.3) fails, when an intense laser beam propagates in an absorptive optical medium. In a one photon absorptive medium, if the intensity of the incident beam is high enough, the attenuation coefficient Ŭ is no

longer a constant and may become a variable that depends on the incident intensity. Therefore, the attenuation formula like Eq. (1.3) cannot hold. In this case either a saturable absorption or a reverse saturable absorption effect may take place. Suppose, if there is RSA due to a two-photon absorption process involved in the medium, the attenuation of an intense incident beam can be described as

$$\frac{dI}{dz} = -\alpha I - \beta I^2 \qquad (1.7)$$

where ϐ is the two-photon absorption coefficient. If we consider the multi-photon absorption processes, then the above equation becomes

$$\frac{dI}{dz} = -\alpha I - \beta I^2 - \gamma I^3 - \cdots\cdots\cdots \qquad (1.8)$$

Here ɔ is the three-photon absorption coefficient and so on.

1.3 Nonlinear absorption

Nonlinear absorption refers to the change of transmittance of a material as a function of intensity or fluence. The high intensities can induce profound changes in the optical properties of a material leading to a nonlinear response of the real and imaginary parts of polarization. The imaginary part of the nonlinear polarization is associated, for instance, with multiphoton transitions and will exhibit a *n*-photon resonance when two level of an atomic or molecular system can be connected by *n* optical quanta.

1.3.1 Two-photon and multi-photon absorption

Two photon Absorption:

Two photon Absorption (TPA) involves a transition from ground state (1) of a material to a higherï lying state (2) by the simultaneous absorption of two photons via an intermediate virtual state, as schematically shown in figure 1.1

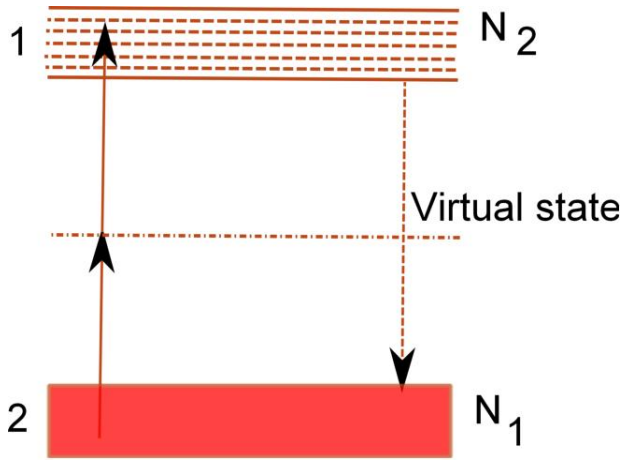

Figure 1.1 Schematic energy level diagram for two-photon absorption (TPA).

In this case, the attenuation of the incident light is described by

$$\frac{dI}{dz} = -\beta I^2 \tag{1.9}$$

where β is the two-photon absorption coefficient.

Multiphoton absorption:

At sufficiently high intensities, the probability of a material absorbing more than one photon before relaxing to the ground state can be greatly enhanced. As early as 1931 Göppert-Mayer derived the two-photon transition probability in a system using the second order quantum perturbation theory [9]. With the availability of high intensities with fs pulses, in addition to numerous investigations on the phenomenon of the simultaneous absorption of two photons, multiphoton (>2) absorption has also been widely studied. Multiphoton absorption processes are highly promising for a number of processes including optical limiting [10], 3D microfabrication [11], optical data storage [12], and biomedical applications [13]. Three-photon or multi-photon absorption involves a transition from the ground state to a higher-lying state by the simultaneous absorption of three or more number photons via multiple numbers of virtual states. Energy level diagrams of 1-photon to n-photon absorption are shown in the figure 1.2.

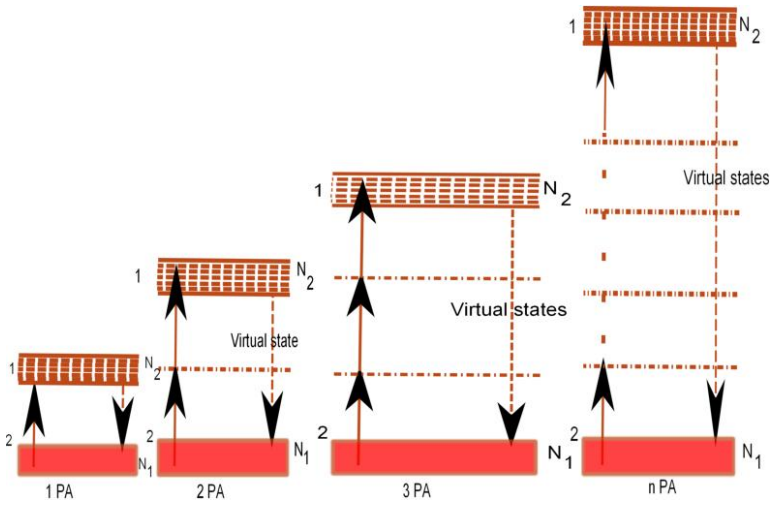

Figure 1.2 Schematic energy level diagrams for 1-photon to n-photon absorption.

In this case, the attenuation of the incident light is described by

$$\frac{dI}{dz} = -\alpha_n I^n \tag{1.10}$$

Where α_n is the n-photon absorption coefficient.

$$\frac{dI(z)}{dz} = -\alpha_n I^n(z) \tag{1.11}$$

$$\int_{I_{in}}^{I_{out}} \frac{1}{I^n(z)} dI(z) = -\alpha_n \int_0^L dz \tag{1.12}$$

$$\left[\frac{I^{-n+1}}{-n+1}\right]_{I_{in}}^{I_{out}} = -\alpha_n L \tag{1.13}$$

$$\frac{1}{n-1}\left[\frac{1}{I_{in}^{n-1}} - \frac{1}{I_{out}^{n-1}}\right] = \alpha_n L \tag{1.14}$$

where transmittance $T = \frac{I_{out}}{I_{in}}$

$$\frac{1}{(n-1)I_{in}^{n-1}}\left[1 - \frac{1}{T^{n-1}}\right] = \alpha_n L \tag{1.15}$$

$$T^{n-1} = \frac{1}{1+(n-1)\alpha_n L I_{in}^{n-1}} \tag{1.16}$$

$$T = \frac{1}{\left[1+(n-1)\alpha_n L I_{in}^{n-1}\right]^{1/n-1}} \tag{1.17}$$

$$\frac{I_{in}}{\omega_0^2} = \frac{I_{00}}{\omega_z^2}$$

$$I_{in} = \frac{I_{00}}{\left[1+\frac{z^2}{z_0^2}\right]} \tag{1.18}$$

where $\omega_z^2 = \omega_0^2\left[1+\frac{z^2}{z_0^2}\right]$

$$T = \frac{1}{\left[1+(n-1)\alpha_n L\left(\frac{I_{00}}{\left(1+\left(z/z_0\right)^2\right)}\right)^{n-1}\right]^{1/n-1}} \tag{1.19}$$

$$T_{OA(nPA)} = \frac{1}{\left[1+(n-1)\alpha_n L\left(\frac{I_{00}}{\left(1+\left(z/z_0\right)^2\right)}\right)^{n-1}\right]^{1/n-1}} \tag{1.20}$$

where I_{00} is the peak intensity (at Z = 0), I_{in} is intensity at sample position (if Z- is the distance from focal point, $I_{in}(I_Z)$ is the intensity at the point), $Z_0 = \pi\omega_0^2/\lambda$ is Rayleigh range, ω_0 is the beam waist at the focal point (Z = 0), dz is a small slice of the sample, I_{in} is input intensity and I_{out} is output intensity of the sample.

1.3.2 Excited state absorption (ESA)

At high incident light intensities, the excited state absorption (ESA) can become important due to significant population of the excited sates. The excited electron can rapidly make a transition to the higher excited states before it decays back to the ground state. There could also be a number of higher-lying states which can coupled with these intermediate states, for which the energy differences are in near-resonance with the incident photon energy. In such a case, before the electron completely relaxes to the ground state, it may experience an absorption that promotes it to a higher-lying state. The ESA mechanism for nonlinear absorption, usually understood by five-level model that refers to five distinct electronic states [8, 14] is shown in figure 1.3.

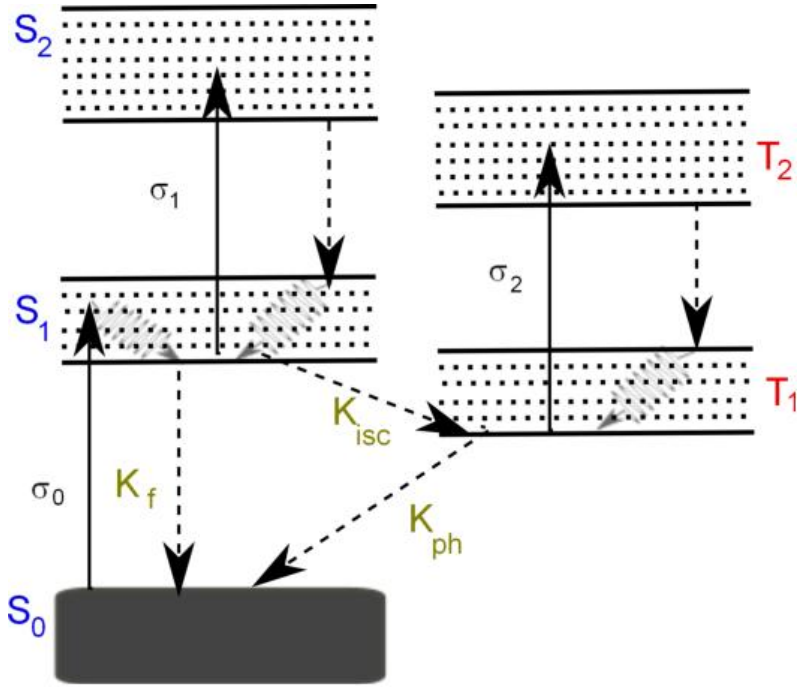

Figure 1.3 Schematic energy level diagram for the excited state absorption (ESA).

Absorption of an incident photon promotes an electron to the first excited singlet state, S_1, from which one of the following can happen: (i) the electron can relax back to ground state by radiative or nonradiative transition, with rate constant k_f, (ii) it can undergo spin flip transition to a triplet state T_1(intersystem crossing) with rate constant, k_{isc}, or (iii) the material can absorb another photon, promoting the electron to higher-lying singlet state, S_2, from which it can relax back to the

first excited singlet state. Electron in the lowest triplet state has two options: (a) it can relax back to the ground state by another spin flip transition, leading to phosphorescence, with rate constant k_{ph}, or (b) the material can absorb another photon, promoting the electron to a higher-lying triplet state T_2, from which it can relax back to T_1.

1.3.3 Saturable absorption (SA) and reverse saturable absorption (RSA)

If the absorption cross-section of the excited state is smaller than that of the ground state, the transmission of the system will be increased when the system is strongly excited. This process is called saturable absorption (SA) which is similar but more complex than that of saturation of absorption occurring in simple two-level systems. On the other hand, if the absorption cross-section of the excited state is larger than that of the ground state, the system will be less transmissive when excited; since this phenomenon is opposite to that of saturable absorption, it is called reverse saturable absorption (RSA). Free carrier absorption (FCA) has similar characteristics as RSA. Among these three nonlinear processes RSA and FCA contribute to optical limiting and hence are discussed further below.

Materials showing RSA show enhanced nonlinear absorption as the input optical intensity /fluence is increased [15]. Such a nonlinear optical response is exhibited when materials have weak ground state absorption over some spectral range and strong excited state absorption in the same wavelength range. Reverse saturable absorbers are of special interest since they display large nonlinear attenuation while maintaining high linear transmittance, making the limiting process more reliable and useful in fast (highly convergent) optical systems and materials with prompt singlet excited-state absorption and long-lived triplet-state absorption may be effectively used for optical limiting of a wider range of pulse widths (sub-picosecond to microsecond duration).

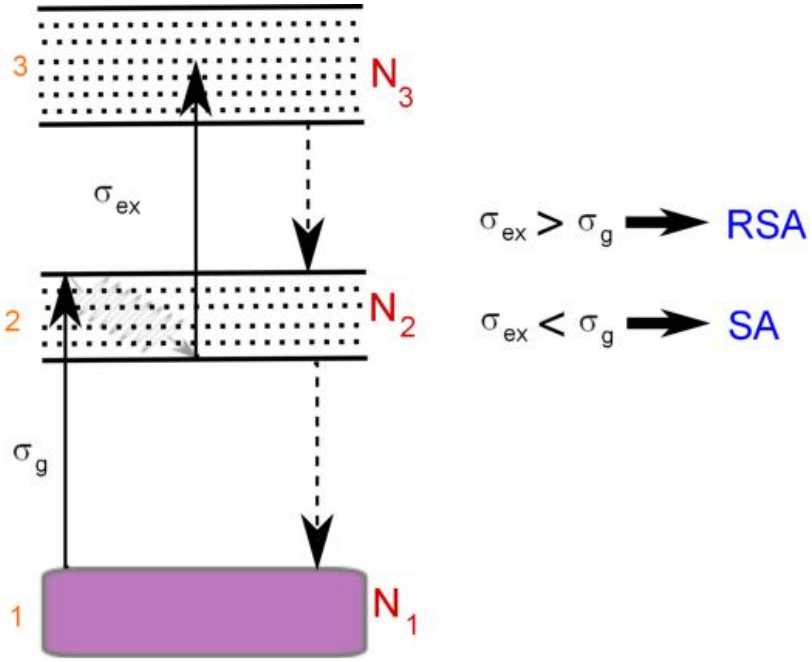

Figure 1.4 Schematic energy level diagram for reverse saturable absorption (RSA).

A simple model of sequential one-photon absorption in a two-step process [8, 14] can be used to explain RSA as shown schematically in figure 1.4. In the figure, 1, 2 and 3 are the ground, first and higher-lying excited states respectively, N_1, N_2 and N_3 are their respective populations. $\mathring{u}_g$ and $\mathring{u}_{ex}$ are the absorption cross-sections for the ground and excited states respectively. If the material has resonant linear absorption for the incident laser, excitation of a definite population to state 2 occurs, followed by further transition from state 2 to 3 via further photon absorption. Probability of the latter transition depends on N_2, $\mathring{u}_{ex}$ and the incident intensity, I, N_2 is determined by N_1, $\mathring{u}_g$ and I. With increase in the intensity, N_2 increases continuously and hence the sequential one-photon absorption from state 2 to 3 becomes significant provided $\mathring{u}_{ex} \gg \mathring{u}_g$. Under steady state conditions,

$$\frac{dI}{dz} = -\sigma_g (N_1 - N_2) I - \sigma_{ex} N_2 I \qquad (1.21)$$

In the simplest situation, it can be assumed that $N_1 \gg N_2$, N_3 å 0 and N_1 å N where N is the total population of the absorbing species. If N_2 å $b\mathring{u}_g N$, where b is a proportionality constant, the attenuation of the light inside the medium,

$$\frac{dI}{dz} = -\sigma_g NI - b\sigma_g \sigma_{ex} NI^2 \tag{1.22}$$

$$\frac{dI}{dz} = -\alpha_0 I - \beta' I^2 \tag{1.23}$$

The linear and nonlinear absorption coefficient α_0 and ß' are defined as

Ŭ$_0$ = ů$_g$ N, ß' = bů$_g$ ů$_{ex}$ N

The solution of Eq. (1.23) gives the intensity of the light at a distance, z inside the medium,

$$I(z) = \frac{I_0 e^{-\alpha_0 z}}{1 + \left(1 - e^{-\alpha_0 z}\right)\frac{\beta'}{\alpha_0} I_0} \tag{1.24}$$

where I_0 is the input intensity incident on the medium. If the linear absorption is small, then

$e^{-\alpha_0 z} \approx 1 - \alpha_0 z$,

Transmittivity $T(I_0) = \frac{I}{I_0} = \frac{T_0}{1 + \beta' z I_0}$ (1.25)

here $T_0 = e^{-\alpha_0 z}$ is the linear transmittivity of the material for low input intensity. $T(I_0)$ is the intensity dependent transmittivity of the same material at high input intensity. This simplest quantitative description of RSA explains how the transmittivity decreases with increasing input intensity.

1.3.4 Free carrier absorption (FCA)

Absorption of photons with energy greater than the band gap will promote electrons to the conduction band, where they become free carriers. With sufficiently high intensities, there is a high probability for them to absorb more photons although they are still in the conduction band. This can lead to nonlinear absorption. Once free carriers are generated in semiconductors, they may experience phonon-assisted absorption to higher lying states in the conduction band.

1.4 Nonlinear refraction

Change in the refractive index or spatial distribution of the refractive index of a medium due to the presence of optical wave called nonlinear refractive

index (NRI). Nonlinear refraction has led to a variety of fascinating applications. It is also central to many fundamental investigations.

$$n_t = n_0 + \Delta n = n_0 + n_2 I \tag{1.26}$$

where n_t is the total refractive index, n_0 is the linear refractive index, n_2 is the nonlinear refractive index and I is intensity of the light. Different physical phenomena can lead to this nonlinear refractive index.

Electronic Polarization: Distortion of the electron cloud about an atom or molecule by the optical field results in the nonlinearity. Highly polarizable atom or molecule shows significant electron nonlinearity.

Optical Kerr Effect: This effect comes due to the third order nonlinear polarization. The change in the NRI is proportional to the square of the time average of the optical electrical field or linearly proportional to the optical intensity.

$$\Delta n = n_2 I \tag{1.27}$$

Nonlocal effects: In this case, NRI again depends on the time averaged electric field or intensity, but is due to a gradient in the field or long range order that can be due to a focused beam or interference of two coherent light beams.

Saturation: The change in the NRI accompanies absorption of optical energy by the medium. For small intensities, NRI will be approximately proportional to the intensity, but at higher intensities, it will depend on the higher orders of intensity.

Changes in the physical properties of a medium: An intense optical wave can induce changes in certain physical properties of the medium, like temperature and concentration. In this case, NRI will be depending on intensity, the time integrated intensity (fluence) as well as pulse width of the excitation. For thermal linearity,

$$\Delta n_{th} = \frac{dn}{dt}\frac{F_0 \alpha}{2\rho_0 C_p} \tag{1.28}$$

where $\frac{dn}{dt}$ is the thermo-optic coefficient, F_0 is the light fluence, C_p is specific heat of the medium, ρ_0 is the density of the medium and α is the absorption coefficient of the medium.

Cascading effects: NRI can be due to a combination of second order effects, or sequential effects of linear and second order phenomena (change in the optical phase of the electromagnetic wave in second harmonic generation (SHG) or frequency mixing process). Slightly away from the phase matching, there will be a flow of power between the pump wave and the newly generated frequency wave (i.e. SHG), as the generated wave propagates periodically in and out of phase with the driving nonlinear polarization. This will impress phase retardation on the pump wave, which is dependent on intensity of the generated wave. In this case the effective NRI can be either positive or negative depending on the sign of the phase mismatch. This effects are absent in our studies due to inversion symmetry of liquid samples.

Self-Focusing (or Self-Defocusing): This occurs when a light beam of non uniform intensity falls on a nonlinear medium. Since the nonlinear index follow the shape of the beam (for local effects without saturation), an index gradient is induced in the medium. For a positive nonlinearity, induces greater index, and hence, larger phase retardation on-axis than the wings results to focus the beam, negative nonlinearity induces the defocusing of the beam.

The NRI has generated significant scientific and technological interest. It has been utilized in or considered for a variety of the applications such as nonlinear spectroscopy, correcting (or finding) optical distortions, optical switching, optical logic gates, optical data processing, optical communications, optical limiting, passive laser mode-locking, waveguide switches and modulators.

1.5 Third order nonlinear optical process

The third term in Eq. (1.6) describes two terms (a) a frequency response at the frequency of the optical field at 3ω that leads to third harmonic generation (THG), and (b) the a nonlinear contribution to the polarization at the frequency of the incident field: this term hence leads to a nonlinear contribution to the refractive index experienced by a wave at frequency ω. The refractive index in the presence of this type of nonlinearity can be represented as in Eq. 1.26.

i.e. $n = n_0 + n_2 I$

where n_0 is the usual refractive index, and $n_2 = \frac{12\pi^2}{n_0^2 c}\chi^{(3)}$ (1.29)

is an optical constant that characterizes the strength of the optical nonlinearity. Some of the processes that can occur as a result of the intensity-dependent refractive index of our interest are self-focusing, and self-phase modulation.

1.6 Techniques for measuring $\chi^{(3)}$ nonlinearity

The magnitude and response of third-order nonlinear susceptibility are important parameters in characterizing and determining the applicability of any material as a nonlinear optical device. There are several techniques [16-19] for measuring these parameters that include

- ✓ Z-scan: For measurement of sign and magnitude of third-order nonlinearity
- ✓ Degenerate Four Wave Mixing (DFWM): For measurement of both magnitude and response time of the third-order nonlinearity.
- ✓ Third Harmonic Generation: For measurement of magnitude of third-order nonlinearity only.
- ✓ Time-resolved Optical Kerr Effect and Transient Absorption techniques: For the study of photo-physical processes determining the nonlinearity.
- ✓ Time Correlated Single Photon Counting (TCSPS) technique to measure the radiative (fluorescence) lifetimes.

Among which Z-scan and DFWM are widely used techniques for measuring both absorptive and non-absorptive nonlinearities. We employed these techniques in the studies presented in this work and the details of each technique are presented in chapter 2.

1.7 Optical limiting: concepts and materials

Advances in the field of lasers have led to revolutionary changes in many fields of science and technology. Power flux densities from 10^{12} to 10^{19} Wcm^{-2} can easily be obtained from the ultra-short light pulses from the nanosecond, picosecond and femtosecond laser sources. High-power lasers find use not only in academic research, but also in several industrial and military applications.

Semiconductor and solid-state lasers are portable, compact and efficient, and hence of special interest in the realm of laser weaponry. With the advent of such high power laser sources operating over wide ranges of wavelengths and pulse durations, the necessity for protection of sensors, optical components and human eyes from laser inflicted damages has increased enormously over the last decade. In this context, optical limiters which can display decreasing transmittance at high intensities (power per unit area) and fluence (energy per unit area) have received significant attention. In an ideal optical limiter, the transmittance change abruptly at some critical input intensity or threshold and therefore exhibits an inverse dependence on the intensity; the output is thus clamped at a certain value (figure 1.5). If this value is below the minimum that can damage the particular equipment, the optical limiter becomes an efficient safety device. The limiting threshold ($I_{1/2}$) of the material is defined as the input intensity/fluence at which the transmittance reduces to half of the linear transmittance [20]. Clamping threshold of the material is defined as the input intensity/fluence at which the transmittance starts clamping. An optical limiter can clamp the output intensity /fluence over a wide range of input intensity/fluence, but may breakdown after certain value, most probably due to the material damage, and exhibit increased transmittance again. The threshold up to which the material can provide effective limiting is called the damage threshold and the ratio of damage threshold to the limiting threshold is called the dynamic range of the optical limiter [20]. Desirable attributes of an effective optical limiter are (i) low limiting threshold and high optical damage threshold and stability, leading to a large dynamic range, (ii) sensitive broadband response to long and short pulses, (iii) fast response time and (iv) high linear transmittance, optical clarity and robustness (i.e. resistance to damage/degradation with time due to humidity, temperature etc.) [21].

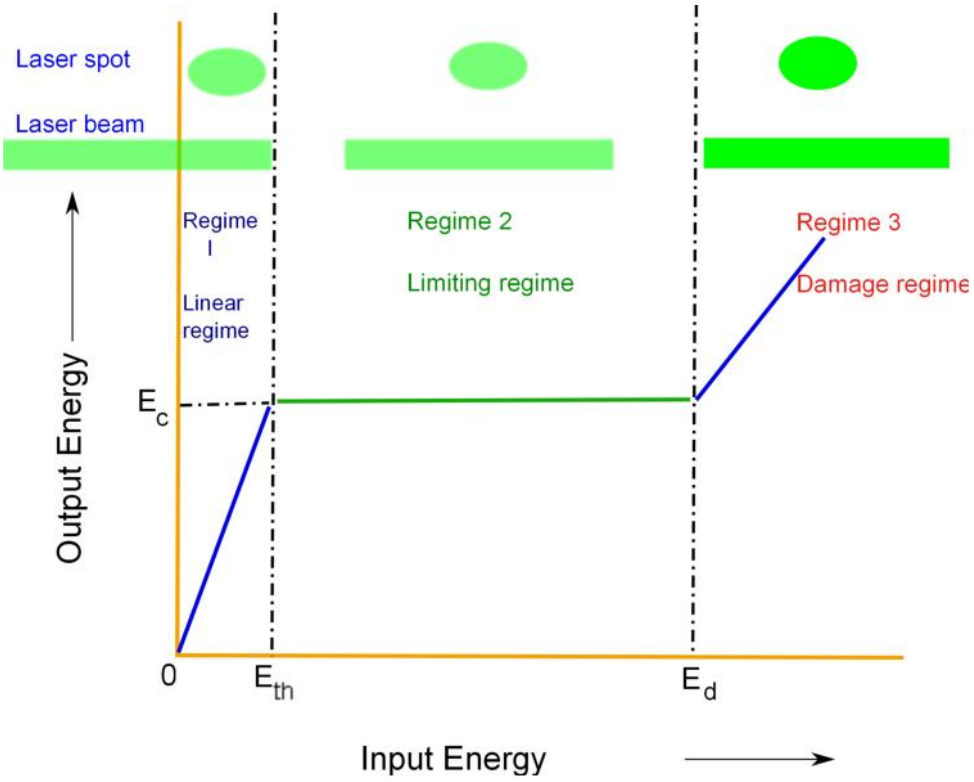

Figure 1.5 Schematic representation of the behavior of an ideal optical limiter.

1.7.1 Process leading to optical limiting

Optical limiting can be achieved by various nonlinear optical mechanisms. The most common ones are mostly by nonlinear refraction effecting self- focusing, self-defocusing, induced aberration, induced scattering, induced refraction, etc., and nonlinear absorption mediated by excited state absorption (ESA), reverse saturable absorption (RSA), free-carrier absorption (FCA), two-photon absorption (TPA) and multi photon absorption (MPA) [1, 22]. Figure 1.6 shows a classification of the various mechanisms that can lead to optical limiting broadly based on energy spreading and energy absorbing modes.

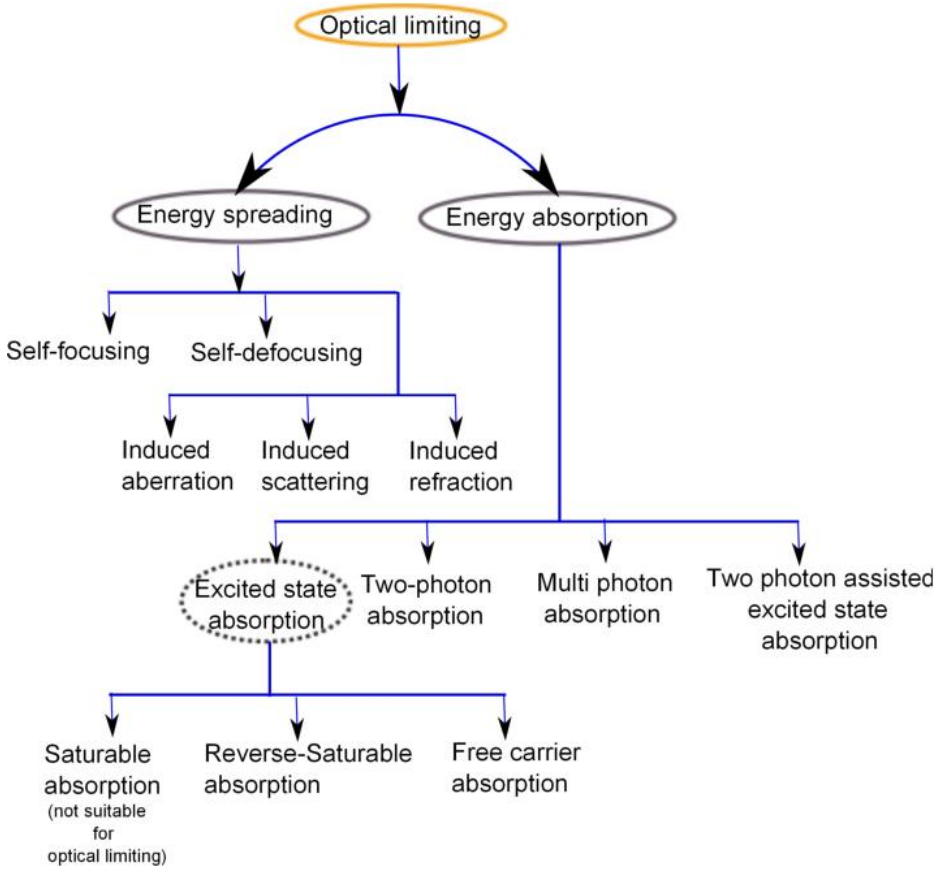

Figure 1.6 Schematic representation of the various mechanisms responsible for optical limiting.

1.7.2 Energy-absorption type optical limiters

Nonlinear absorption is another mechanism employed for optical limiting. In this case no aperture or pinhole is necessary, and the optical limiting relies on the fact that the transmittance of nonlinear absorbing media decreases when the input laser intensity increases. At sufficiently high intensities, the probability of a material absorbing more than one photon or an excited molecule (or electron in the case of, say, semiconductors) being elevated to a higher-lying excited state before relaxing to ground state can be greatly enhanced. The optical limiting devices based on this mechanism can be called the energy-absorption type of optical limiters and other processes leading to optical limiting are listed below.

1.7.3 Energy-spreading type optical limiters

The key requirement for energy-spreading type materials is to place an aperture or pinhole in front of a detector or the target where the laser light is directed. The limiting of the detected laser beam is based on the change in the spatial energy distribution of the transmitted beam. With the increase of input laser intensity/fluence, a larger fraction of the incident laser energy is spread out to a wider solid-angle range; as a result the fraction passing through the aperture will decrease accordingly. In these cases, the observed limiting behavior depends not only on the input laser intensity and the nonlinear medium, but also on the pinhole size and the geometric configuration of the optical system for a given device. For most of this type of materials, thermally induced refractive index changes play a key role. Typical effects operating in energy-spreading type of optical limiting materials are schematically shown in figure 1.7. In all these cases the size of the aperture is chosen in such a way that when the input fluence is very low, the laser beam transmitted through the medium can totally pass through the aperture without any part of the beam getting blocked. In the case self-focusing (figure 1.7(a)) and self-defocusing (figure 1.7(b)), when the input fluencies are high, the detected energy is significantly reduced due to the energy spreading in the aperture plane. Figure 1.7(c) represents the mechanism based on induced aberration. It is well known that induced refractive index change is a function of the local intensity distribution of the laser beam inside the nonlinear medium. An irregular spatial distribution of local light intensity can lead to random refractive index changes at high intensity levels, causing severe aberration influences on the wave front of the transmitted laser beam. By keeping a small pinhole in the focal plane of a focusing lens, the portion of the laser energy passing to the detector can be decreased as the induced aberration becomes larger [1, 14]. Figure 1.7(d) and 1.7(e) show optical limiting based on laser-induced intensity dependent scattering and refraction. In the case of induced scattering, the limited medium is a system of linearly absorbing particles randomly distributed in a transparent host changes of the particles due to light absorption in the system is negligible, whereas for strong input intensity, the absorption-induced heating of the center and medium becomes highly

inhomogeneous resulting in considerable part of the energy spreading out into a wider spatial range and only a small fraction passing through the aperture [23]. In the case of induced refraction, the medium is composed of two microscopic components that have the same static refractive index but are in different phase (e.g. liquid and solid mixture). If one component is transparent and the other absorbs the incident laser beam, the selective heating, makes the whole system inhomogeneous at the boundary between the two components [8]. Although, all energy-spreading type of optical limiting are featured using an aperture, in some experimental cases no aperture is used; in the later case, the limited sensitive area of the detector plays the role of aperture.

Although all these mechanisms lead to slow temporal response, the opto-thermal effect-induced refractive index change is considered to be important for optical limiting. Even though impurities or external particles cause only small residual linear absorption in transparent and non-resonantly absorptive medium, this small absorption is strong enough to create remarkable thermally induced refractive index changes at higher input laser intensity. The induced refractive index change will be significant for a resonant and linearly absorbing medium even at low input intensity.

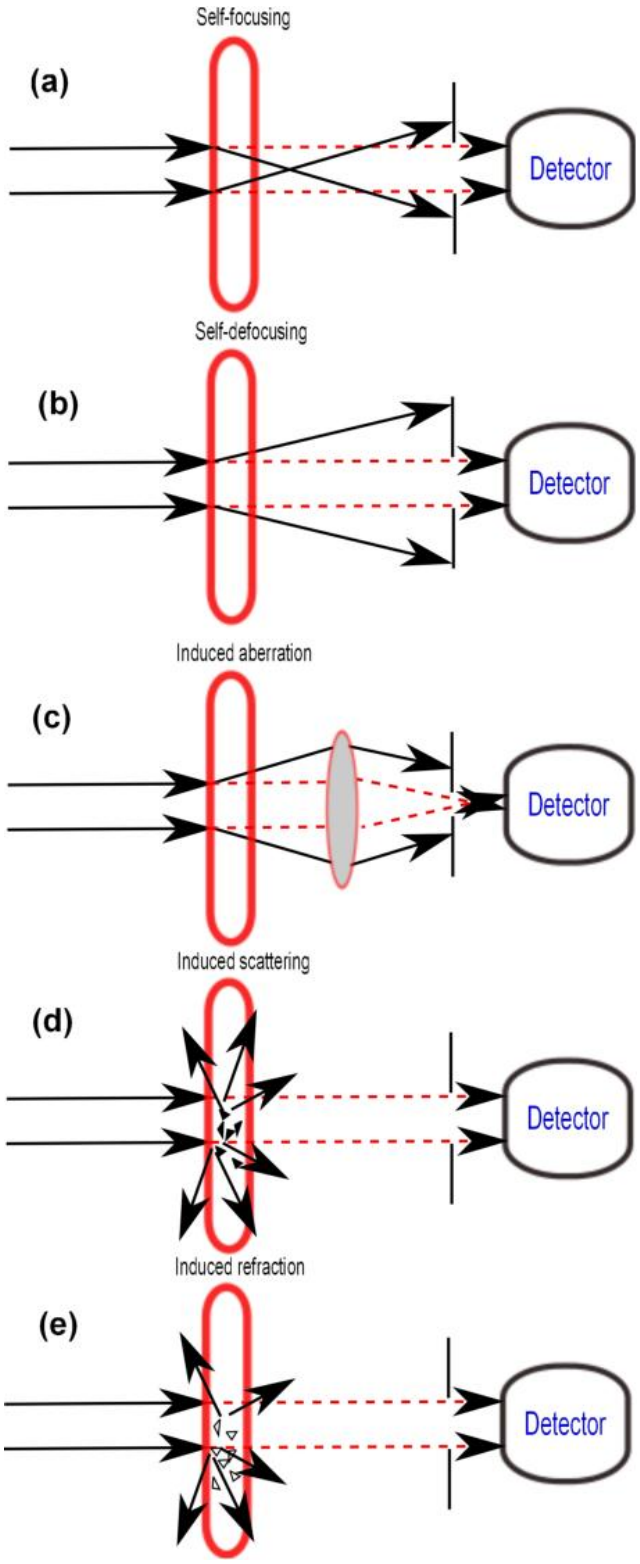

Figure 1.7 schematic illustrations of energy-spreading type optical limiter

1.8 Materials for optical limiting

A wide variety of materials have been studied for optical limiting applications based on different processes. Nonlinear materials with higher sensitivity and negligible linear absorption are prime targets for development and incorporation into optical systems. Particular attention is focused on optical limiters for pulsed lasers in the visible and near infrared range, in view of their importance for eye protection [24]. Colloidal suspensions provide optical limiting in the UV to near IR range, using scattering mechanisms [25]. Several dye molecules are useful in the visible band because of nonlinear absorption and refraction. The most extensively studied systems are phthalocyanimines [26], porphyrins [27], fullerenes and their derivatives [28] in which long-lived triplet excited state can be produced conveniently. Liquid crystals are another class of materials studied in the visible to mid IR region; they cause optical limiting via refraction and TPA [29]. Other materials where optical limiting was investigated and have shown efficient optical limiting properties are: bacteriorhodopsin [30], Photorefractive materials [31], photonic band gap materials [32], nonlinear absorbers doped in xerogels and sol-gel films [33], glasses [34], filters [35], organic/inorganic clusters [36] and layered systems [37].

Over the last few years, semiconductor nanoparticles and carbon nanotubes [38], as well as metal nanoparticles [39] have emerged as promising candidates for optical limiting in the nanosecond, picosecond and femtosecond regime. Semiconductor quantum dots [40], metal nanoparticles [41], carbon nanostructures [42], fullerene functionalized polymers [43] and organometallics [44] have been reported to show optical limiting of femtosecond laser pulses. Optical limiting properties of Graphene based hybrid materials such as GO-Cu porphyrin, GO-Zn porphyrin, GO-Sn porphyrin, GO-VO porphyrin, GO-H_2 porphyrin, GO-ZnO nanoaprticles, GO-TiO_2 nanoparticles and GO-metal nanoparticles, Bio-synthesized silver nanoparticles, Zinc Octa Carboxy phthalocyanine and few porphyrin molecules with the nanosecond, picoseocnd and femtosecond pulse excitations are presented in this thesis.

1.9 Aim of the thesis

This thesis is an attempt to study the several nonlinear optical mechanisms (Two photon absorption, Three photon absorption, Excited state absorption and Nonlinear scattering) shown by different materials for optical limiting application. As the optical limiting relies on the material absorption of excited electrons/molecules and its nonlinearity, there is an importance in understanding the behavior of excited states and evolution of parameters like nonlinear absorption cross sections, relaxation lifetimes of excited states. We have characterized different types of the material like bio-synthesized silver nanoparticles, chemically synthesized graphene based materials, organic molecules such as porphyrins, phthalocyanines and laser assisted graphene oxide-metal nanoparticle hybrid materials for optical limiting applications. Due to strong excited state absorption, porphyrins and phthalocyanines are largely used for NLO applications. Strong nonlinear optical absorption of the materials provide low limiting threshold values, but this type of materials has low damage threshold values that limits their applications for optical limiting studies. It can be overcome by introducing the nonlinear scattering so that these materials can be used efficiently even at high input intensities or fluences. Our efforts have been to combine the different materials in which one has to show strong nonlinear optical absorption and other show nonlinear scattering mechanism. In this regard we have chosen graphene oxide, which shows good nonlinear scattering and two photon absorption has been used to conjugate with porphyrin molecules that is known for the strong excited state absorption. In this way, damage threshold of the optical limiting material can be increased. Energy transfer from porphyrins to graphene oxide will lead to stronger excited state absorption, which will enhance the nonlinear optical absorption resulting in low limiting threshold values.

1.10 Organization of the thesis

Chapter 2 is ordained for the discussion on the experimental details of various experiments carried out during the period of the thesis work.

All the work described in this dissertation involves the interaction of short laser pulses with transparent materials, several different nonlinear phenomena were studied and many different experimental techniques were used.

Chapter 3 this chapter contains the synthesis of silver nanoparticles through bio-reduction method. In this method we have used coriander and moringa oleifera leaf extracts as reducing and stabilizing agent. These nanoparticles were used for linear and nonlinear optical measurements. Compared to chemically synthesized silver nanoparticles, bio-reduced silver nanoparticles have shown good nonlinear absorption beaviour, leads to good optical limiting behavior. Among the two leaf extracts, moringa oleifera reduced silver nanoparticles have shown better optical limiting behavior.

Chapter 4 This chapter contains the synthesis of zinc octacarboxy phthalocyanine (ZnOCPc) and third order nonlinear optical characterization of ZnOCPc using Z-scan and degenerate four wave mixing (DFWM) techniques. Nonlinear absorption and refraction behavior in the nanosecond (ns), picoseconds (ps) and femtosecond (fs) domains are well studied in detail. Three-photon absorption was a prevalent mechanism with femtosecond laser excitation whereas strong reverse saturable absorption due to dominant two-photon absorption (TPA) was observed with picosecond and nanosecond excitations. We have evaluated the sign and magnitude of the third-order nonlinearity in fs, ps, and ns regimes. We recorded large off-resonant second order hyperpolarizability (ↄ) with ultrafast nonlinear optical response in the femtosecond domain using DFWM technique. We have also shown optical limiting and figure of merit (FOM) of ZnOCPc for optical switching. And few porphyrin molecules were studied for third order optical nonlinearities.

Chapter 5 This chapter contains three sub-chapters; 1) Graphene oxide-(Cu, Zn, Sn, VO, H_2) porphyrins, 2) Graphene oxide-Semiconductor (ZnO, TiO_2) nanoparticles and 3) Graphene oxide-metal (Ag, Au) nanoparticles

The nonlinear optical (NLO) and optical limiting (OL) properties of covalently linked graphene oxide-porphyrin composite materials were investigated using Z-scan technique in nanosecond and femtosecond regime. We observed enhanced NLO and OL properties of graphene oxide-porphyrin composites in comparison to the individual graphene oxide and porphyrins. The improved OL property of composites is attributed to energy transfer between porphyrin and graphene oxide, which improved excited state absorption and nonlinear scattering. Nonlinear optical susceptibilities $\chi^{(3)}$ of graphene oxide and graphene oxide-porphyrin composites are in the order of 10^{-12} esu, which were measured using degenerate four wave mixing technique in nanosecond regime. High values of excited state absorption and two-photon absorption were observed for the composites. Both graphene oxide-copper porphyrin and graphene oxide-zinc porphyrin composites exhibit enhanced optical limiting behavior which arises from ESA, TPA, and nonlinear scattering in nanosecond region.

Graphene oxide-semiconductor nanoaprticles were synthesized and characterized for nonlinear optical studies. To observe broad optical limiting behavior, we carried out studies at 532 nm and 1064 nm laser wavelengths in nanosecond pulse regime. We observed good limiting behavior at both these wavelengths. Compared to pure graphene oxide and semiconductor nanoparticles, graphene oxide with semiconductor nanoparticles have shown better nonlinear absorption and limiting behavior.

Graphene oxide-metal (Ag, Au) nanoparticles were synthesized via chemical method and laser irradiation. Through in-situ process attachment of nanoparticles to graphene oxide in the presence Polyvinyl alcohol (PVA) using laser irradiation. Once nanoparticles were formed, they get attached to graphene oxide via physical adsorption/chemical modification. Better optical limiting behavior was observed for these composites in both 532 nm and 1064 nm wavelength laser excitations.

Chapter 6 This chapter contains solvent effects on third order nonlinearities in ultra short pulse regimes like picosecond and femtosecond time scales. We have carried out Z-scan studies on solvents in picosecond and femtosecond regions. We have studied common solvents such as CS_2, acetone, DMF, chloroform, CCl_4, THF, ethanol and toluene. All of the solvents show third order nonlinearities. The nonlinear absorption in these solvents is a RSA behavior which is predominantly from three photon absorption mechanism in femtosecond regime. Nonlinear refractive index of these solvents are positive in both pico and femtosecond regime. Main aim of this work is to know the contribution of solvents on third order nonlinearities and should be excluded from sample nonlinearities.

Chapter 7 Conclusions of the results in this present work. A future direction in achieving better optical limiter materials is presented.

1.11 References

1. L.W. Tutt and T.F. Boggess, Prog. Quant. Electr. **17**, 299 (1993); R.C. Hollins, Current Opinion in Solid State & Mat. Sci. **4**, 189 (1999)
2. R.C. Hollins, Current Opinion in Solid State & Mat. Sci. **4**, 189 (1999); M. Bala Murali Krishna, V. Praveen Kumar, N. Venkatramaiah, R. Venkatesan, and D. Narayana Rao, Appl. Phys. Lett., **98**, 081106 (2011); N. Venkatram, M. A. Akundi and D. Narayana Rao, Optic. Exp. **13**, 867 (2005); X. Zhang, X. Zhao, Z. Liu, S. Shi, W. Zhou, J. Tian, Y. Xu and Y. Chen, J. Opt, **13**, 075202 (2011); N. Venkatram, P. Lakshminarayana, M. K. Kumar, B. M. Goh, K. P. Loh, Q. Xu and Wei Ji, Nanotechnology, **21**, 415203 (2010); X. Zhang, X. Zhao, Z. Liu, Y. Liu, Y. Chen and J. Tian, Opt. Exp., **17**, 23959 (2009); Z. Liu, Y. Xu, X. Zhang, X. Zhang, Y. Chen and J. Tian, J. Phys. Chem. B, **113**, 9681 (2009); Y. Xu, Z. Liu, X. Zhang, Y. Wang, J. Tian, Y. Huang, Y. Ma, X. Zhang and Y. Chen, Adv. Mater. **21**, 1275 (2009).
3. J. Guo, T.Y. Chang, I. McMichael, J. Ma, and J.H. Hong, Opt. Lett. **24**, 981 (1999).
4. R. Frey and C. Flytzanis, Opt. Lett. **25**, 838 (2000)

5. Y.-P. Sun and J.E. Riggs, Int. Rev. Phys. Chem. **18**, 43 (1999); Y-P. Sun, J.E. Riggs, K.B. Henbest, and R.B. Martin, J. Nonlinear Opt. Physics & Materials. **9**, 481 (2000)
6. E. W. Van Stryland, H. Vanherzeele, M. A. Woodall, M. J. Soileau, A. L. Smirl, S. Guha, and T. F. Boggess, Opt. Engg. **24**, 613 (1985)
7. M. P. Joshi, J. Swiatkiewicz, F. Xu, P.N. Prasad, B. A. Reinhardt, and R. Kannan, Opt. Lett. **23**, 1742 (1998)
8. Gung S. He and Song H. Liu, *Physics of Nonlinear Optics*, World Scientific,Singapore (1999)
9. M. Göppert-Meyer, Ann. Phys. **9**, 273 (1931).
10. G. S. He, L-S. Tan, Q. Zheng, and P. N. Prasad, Chem. Rev., **108**, 1245 (2008); N. Venkatram L. Giribabu , S. Venugopal Rao and D. N. Rao, Appl. Phys. B, **91**, 149 (2008); P. P. Kiran, D. R. Reddy, B. G. Maiya, A. K. Dharmadhikari, G. R. Kumar, and D. N. Rao, Appl. Opt., **41** , 7631 (2002); G. S. He, G. C. Xu, P. N. Prasad, B.A. Reinhardt; J.C. Bhatt, R. McKellar, and A.G. Dillard, Opt. Lett. **20,** 435 (1995**)**, 20, 435.
11. S. Maruo, O. Nakamura, and S. Kawata, Opt. Lett., **22**, 132 (1997); B.H. Cumpston, S.P. Ananthavel, S. Barlow, D.L. Dyer, J.E. Ehrlich, L.L Erskine, A.A. Heikal, S. M. Kuebler, I.-Y. S. Lee, D. McCord-Maughon, J. Qin, H. Röckel, M. Rumi, X.-L. Wu, S.R. Marder, and J. W. Perry, Nature, **398**, 51(1999); S. Kawata, H.-B. Sun, T. Tanaka and K. Takada, Nature, **412**, 697 (2001); W. H. Zhou, S. M. Kuebler, K.L. Braun, T.Y. Yu, J.K. Cammack, C.K. Ober, J.W. Perry, and S.R. Marder, Science, **296**, 1106 (2002).
12. D. A. Parthenopoulos and P.M. Rentzepis, Science, **245**, 843 (1989); J. H. Strickler, and W. W. Webb, Opt. Lett., **16**, 1780 (1991); A.S. Dvornikov, and P.M. Rentzepis, Opt. Commun. **119**, 341 (1995); K.D. Belfield and K. J. Schafer, Chem. Mater., **14**, 3656 (2002).
13. M. F. Yanik, H. Cinar, H. N. Cinar, A. Gibby, A. D. Chisholm, Y. Jin, and A. Ben-Yakar, IEEE Journ. Quantum Electron., **12**, 1283 (2006); P.N. Prasad, *Introduction to Biophotonics*, Chapter-12, Wiley-Interscience, New Jersey (2003); A. Karotki, M. Khurana, J. R. Lepock and B. C. Wilson,

Photochem. and Photobio., **82**, 443 (2006); I. G. Meerovich, V. M. Derkacheva, G. A. Meerovich, N. A. Oborotova, Z. S. Smirnova, A. P. Polozkova, I. Y. Kubasova, E. A. Lukyanets, and A. Y. Baryshnikov, Proc. of SPIE, **6427**, 64270X (2007).

14. R. L. Sutherland, *Handbook of Nonlinear Optics*, Second Edition, and Revised and expanded, New York, NY: Marcel Dekker (2003).
15. Kim S., McLaughlin D. and Potasek M., Phys. Rev. A, **61**, 025801 (2000); Lepkowicz R., Koyakov A., Hagan D. J. and Strylabd E. W. V., J. Opt. Soc. Am. B, **19**, 94 (2002).
16. Y. R. Shen, *The principles of Nonlinear Optics*, Wiley, New York (2002); A. Yariv, *Quantum Electronics*, John Wiley & Sons, New York, USA, 1988; P. N. Butcher and D. Cotter, *The Elements of Nonlinear Optics*, Cambridge University Press, Cambridge, 1990;
17. R. L. Sutherland, *Handbook of Nonlinear Optics*, Second Edition, Revised and expanded, New York, NY: Marcel Dekker (2003).
18. R. W. Boyd, Nonlinear Optics, 2nd Ed. Academic Press, New York (2003)
19. M. D. Levenson, *Introduction to Nonlinear Laser Spectroscop*y, New York: Academic (1982); R. A. Fischer, *Optical Phase Conjugatio*n, New York: Academic, USA (1983); H. J. Eichler, P. Gunter, and D. W. Pohl, *Laser-Induced Dynamic Gratings*, Springer-Verlag, Berlin, Heidelberg, Germany (1986); D.M. Pepper, Ed. *Opt. Engg.* **21,** 2 (1982); M. Sheik-Bahae, A. A. Said, T. H. Wei, D. J. Hagan, and E. W. Van Stryland, *IEEE J. Quant. Electron.* **QE-26**, 760 (1990).
20. Hagan D. J., Van Stryland E. W., Wu Y. Y., Wei T. H., Sheik-Bahae M., Said A., Mansour K., Young J. and Soileau M. J., *Materials for Optical Switches, Isolators, and Limiters*; Proceedings of SPIE, SPIE: Bellingham, WA, 1105, 103 (1989).
21. Van Stryland E. W., Soileau M. J., Ross S. and Hagan D., J. Nonlinear Optics, **21**, 29 (1999).
22. Kukaswadia, A. K. Feng, Z. C. And Tang, S. H. J., Appl. Phys., **75**, 3340 (1994).

23. Khoo, I. C., Michael, R. R., Finn and G. M., Appl. Phys. Lett. **52**, 2108 (1988); Tian, J.-G., Zhang, C., Zhang, G. and Li, J., App. Opt., **32**, 6628 (1993).
24. Wood, G. L., Mott, A. G. and Sharp, E. J., Proc. SPIE, **2**, 1692 (1992); Hollins, R. C., Nonlinear Optics, 27, 1 (2001).
25. Lawson, C. M., Euliss, G. W. and Michael, R. R., Appl. Phys. Lett., **58**, 2195 (1991); Micheal, R. R. and Lawson, C. M., Opt. Lett., **17**, 1055 (1992); Durand, O. Grolier-Mazza, V. and Frey, R., Opt. Lett., **23**, 1471 (1998); Fougeanet, F. and Riehl, D., Nonlin. Opt., **21**, 435 (1999); (e) Hernandez, F. E., Shensky, W., Cohanoschi, I., Hagan, D. J. and Stryland, E. W. V., Appl. Opt., **41**, 1103 (2002).
26. Messier, J., Kajzar, F. And Prasad, P., Organic molecules for Nonlinear Optics and Phtotonics, Series E, applied Science, Kluwer Academic Publishers: New York, 194 (1991); Shirk, J. S., Pong, R. G. S., Bartoli, F. J., Snow, A. W., Appl. Phys. Lett., **63**, 1880 (1993).
27. Kiran, P. P., Srinivas, N. K. M. N., Reddy, D. R., Maiya, B. G., Sandhu, A. S., Dharmadhikari, A., Kumar, G .R. and Rao, D. N., Opt. Commun., **202**, 347 (2002).
28. Taheri, B., Liu, H., Jassemnejad, B., Appling, D., Powell, R. C. and Song, J. J. Appl. Phys. Lett., **68**, 1317 (1996); Sun, Y-P., Riggs, J. E. and Liu, B. Chem. Mater., **9**, 1268 (1997); Ma, B., Riggs, J. E. and Sun, Y.-P., J. Phys. Chem. B, **102**, 5999 (1998).
29. Khoo, I. C., Wood, M. V., Lee, M. and Guenther, B. D. Opt. Lett., 21, 1625 (1996); Ono, H. and Kawatsuki, N. Opt. Commun., **139**, 60 (1997).
30. Rao, D. N., Yelleswarapu, C. S., Kothapalli, S. R. and Rao, D. V. G. L. N., Optics Express, **11**, 2848 (2003).
31. Rao, D. N. and Kiran, P. P. Nonlinear Optics, **27**, 347 (2001).
32. Scalora, M., Dowling, J. P., Bowden, C. M. and Blemer, M. J. Phys. Rev. Lett., **73**, 1368 (1994).
33. Bentivegna, F., Canve, M., Georges, P., Brun, A., Chaput, F., Malier, L. and Boilot, J. C. Appl. Phys. Lett., **62**, 1721 (1993); Schell, J. Brinkmann,

D., Ohlmann, D., Honerlage, B., Levy, R., Joucia, M., Rehspringer, J. L., Serughetti, J. and Bovier, C. J. Chem. Phys., **108**, 8599 (1998).

34. Bindra, K. S., Oak, S. M. and Rustagi, K. C. Opt. Commun., **124**, 452 (1996).
35. Fischer, G. L., Boyd, R. W., Moore, T. R. and Sipe, J. E. Opt. Lett., **21**, 1643 (1996).
36. Shi, S., Ji, W., Tang, S. H., Lang, J. P. and Xin, X. Q., J. Am. Chem. Soc., **116**, 3615 (1994); Low, M. K. M., Hou, H., Zheng, H., Wong, W., Jin, G., Xin, X. and Ji, W. Chem. Commun., 505 (1998).
37. Herbert, C. J., Cpinski, W. S. and Malcuit, M. S. Opt. Lett., **17**, 1037 (1992); Kahn, L. M., Phys. Rev. B, 53, 1429 (1996).
38. Sun, X., Yu, R. Q., Xu, G. Q., Hor, T. S. A. and Ji, W., Appl. Phys. Lett., **73**, 3632 (1998); Sun, Y.-P., Riggs, J. E., Henbest, K. B. and Martin, R. B. J. Nonlinear Opt. Phy. & Mater., **9**, 481 (2000); Venkatram, N., Rao, D. N. and Akundi, M. A., Opt. Express, **13**, 867 (2005); Venkatram, N., Kumar, R. S. S. and Rao, D. N., J. App.Phys., **100**, 074309 (2006).
39. Qu, S., Zhao, C., Jiang, X., Fang, G., Gao, Y., Zeng, H., Song, Y., Qiu, J., Zhu, C. and Hirao, K., Chem. Phys. Lett., **368**, 352 (2003); Shen, H., Cheng, B. L., Lu, G. W., Guan, D. Y., Chen, Z. H.; Yang, G. Z. J. Phys. D: Appl. Phys., **39**, 233 (2006); Martin, R. B.; Meziani, M. J.; Pathak, P.; Riggs, J. E.; Cook, D. E.; Perera, S.; Sun, Y.-P. Opt. Mater., **29**, 788 (2007).
40. He, J.; Mi, J.; Li, H.; Ji, W. J. Phys. Chem. B, **109**, 41, 19184 (2005); Gong, H.-M.; Wang, X.-H.; Du, Y.-M.; Wang, Q.-Q. J. Chem. Phys., **125**, 024707 (2006).
41. (a) Kyoung, M.; Lee, M. Opt. Comm., **171**, 145 (1999); (b) Elim, H. I.; Yang, J.; Lee, J.-Y. Appl. Phys. Lett., **88**, 083107 (2006); (c) Liu, T.-M.; Tai, S.-P.; Yu, C.-H.; Wen, Y.-C.; Chu, S.-W. Appl. Phys. Lett., **89**, 043122 (2006).
42. Neto, N. M. B., Mendonca, C. R., Misoguti, L. and Zilio, S. C. Appl. Phys. B, **78**, 1 (2004).

43. (a) Kamanina N., Putilin, S.; Staselôko, D. Synth. Metals, **127**, 129 (2002), (b) Tong, R.; Wu, H.; Li, B., Zhu, R.; You, G.; Qian, S.; Lin, Y.; Cai, R. Physica B, **366**, 192 (2005).
44. Vestberg R., Westlund R., Eriksson A., Lopes C., Carlsson M., Eliasson B., Glimsdal E., Lindgren M., Malmström E., Macromolecules, **39**, 2238 (2006).

Chapter - II

EXPERIMENTAL TECHNIQUES

Abstract

Experimental techniques for measuring third order optical nonlinearities namely, four-wave mixing and Z-scan that form the basis of the studies are presented in this thesis and explained in detail. Description is presented on several structural and spectroscopic characterization techniques that are used in this dissertation.

2.1 Degenerate four wave mixing (DFWM)

A four wave mixing (FWM) experiment [1] can be considered as an interaction of three optical electric fields in a medium leading to the generation of fourth field, via third order polarization. The presence of a third-order optical nonlinear susceptibility $\chi^{(3)}$ leads to the creation of various components of material polarization, giving rise to new optical fields. If the phase-matching condition is fulfilled (i.e. the phase relation between the waves emitted by different parts of the nonlinear medium leads to constructive build up of the resulting wave), new beams of light are created. If the fields are of identical frequencies, the process is called degenerate four wave mixing (DFWM) and the output beam will have the same frequency. The time resolution of the FWM measurements depends on two parameters. The first is related to the time duration of the laser pulses and the second is related to the coherence time of the laser pulses. DFWM provides information about the magnitude and response of the third-order nonlinearity. In this process, three coherent beams incident on a nonlinear medium and generate a fourth beam due to the third order nonlinearity. The strength of this fourth beam is dependent on a coupling constant that is proportional to effective $\chi^{(3)}$ and hence measurements on observed signal will yield information about the $\chi^{(3)}$ tensor components of the medium. DFWM can be employed in backward (or generally called the Phase Conjugate), forward or boxcar configurations, with the choice on the experimental conditions and the requirements. Using different polarizations of the three beams it is possible to measure all the independent $\chi^{(3)}$ tensor components of a material

Box-car geometry:

The basic principle of the method is as follows: Two synchronized pulses (called the k_1 and k_2 pulse) propagating in two slightly different directions ($\boldsymbol{k_1}$, $\boldsymbol{k_2}$) interfere in the sample to form a grating by spatially modulating its optical properties. Depending on the experimental conditions, the absorption (amplitude grating), or the refractive index (phase grating) can be modulated. After the laser pulse interaction, the amplitude of the modulation decreases: the dynamics of the

modulation (i.e. the grating) will depend on the population lifetime (for amplitude grating) and/or the dynamics of the changes in the refractive index (for phase grating). A third beam, k_3, propagating in direction $\boldsymbol{k_3}$, is sent into the sample and is diffracted by the grating in directions $\boldsymbol{k_4}$, which satisfies the conservation of momentum: $\boldsymbol{k_4} = \boldsymbol{k_3}-\boldsymbol{k_2}+\boldsymbol{k_1}$.

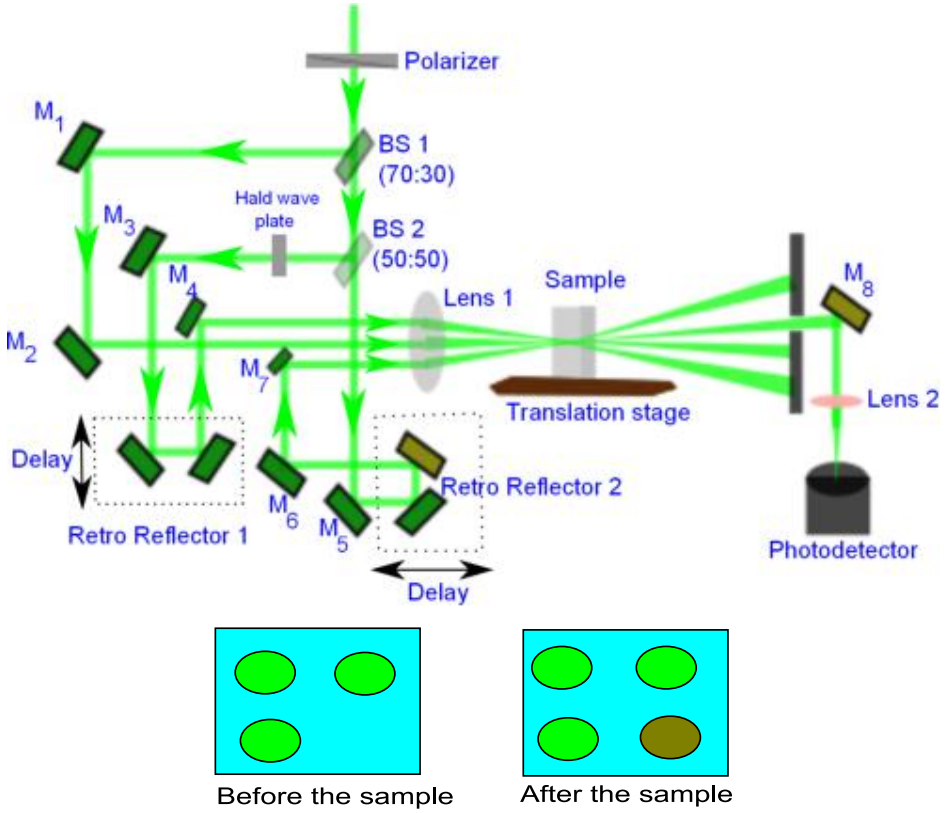

Figure 2.1 Experimental schematic for femtosecond and nanosecond degenerate four wave mixing set-up in box-car configuration. Beams 1-3 are coincident on the sample. The resultant fourth beam is the DFWM signal that occurs because of the interaction $k_4 = k_3-k_2+k_1$. The lower panel of the figure shows formation of the fourth beam at the vacant corner of the box formed by the interacting three waves.

The experimental schematic of the DFWM set-up used in our studies is as shown in the figure 2.1. Since all the pumps are in same plane, the three beams form three corners of the square and the signal is seen at the fourth corner of the square. The delays of beams 2 and 3 could be varied using the stepper motor. Observing and optimizing the diffracted signals, in both horizontal and vertical directions, ensured the zero delay of different beams. The signal(s) obtained are spatially filtered before being fed to the fast photo detector to lock-in amplifier

and to analog to digital converter (ADC) which finally gets recorded in the computer. In the set-up, a lens of focal length 400 mm (φ = 50 mm) is used to focus the three beams into the sample. For the relative measurements of $\chi^{(3)}$ of the sample under study we used pure CCl_4 or DMF as solvents in case of samples in solution. Other details related to the specific experiments carried out in the thesis work are explained in the subsequent chapters appropriately. The time-resolved DFWM profiles were obtained by delaying beam 3 with respect to the other two beams with a time resolution of ~33 fs. Since we used 110 fs input pulses we used solvent taken in a 1 mm cuvette as a standard sample for relative studies. CCl_4 and DMF are known to show only the electronic response (~few fs) and thus the time-resolved signal obtained can be treated as an autocorrelation trace of the input fundamental pulses.

2.2 Z-scan

The Z-scan technique is a single beam technique, which allows the determination of the real and imaginary parts of the third order susceptibility [2]. This technique is a simple, sensitive, single beam method that uses the principle of spatial beam distortion to measure both the sign and the magnitude of refractive nonlinearities of optical materials. The experiment uses a Gaussian beam from a laser in tight focus geometry to measure the transmittance of a nonlinear medium through a finite aperture in the far field as a function of the sample position Z, from the focal plane. In addition to this, the sample transmittance without an aperture is also measured to extract complementary information about the absorptive nonlinearities of the sample.

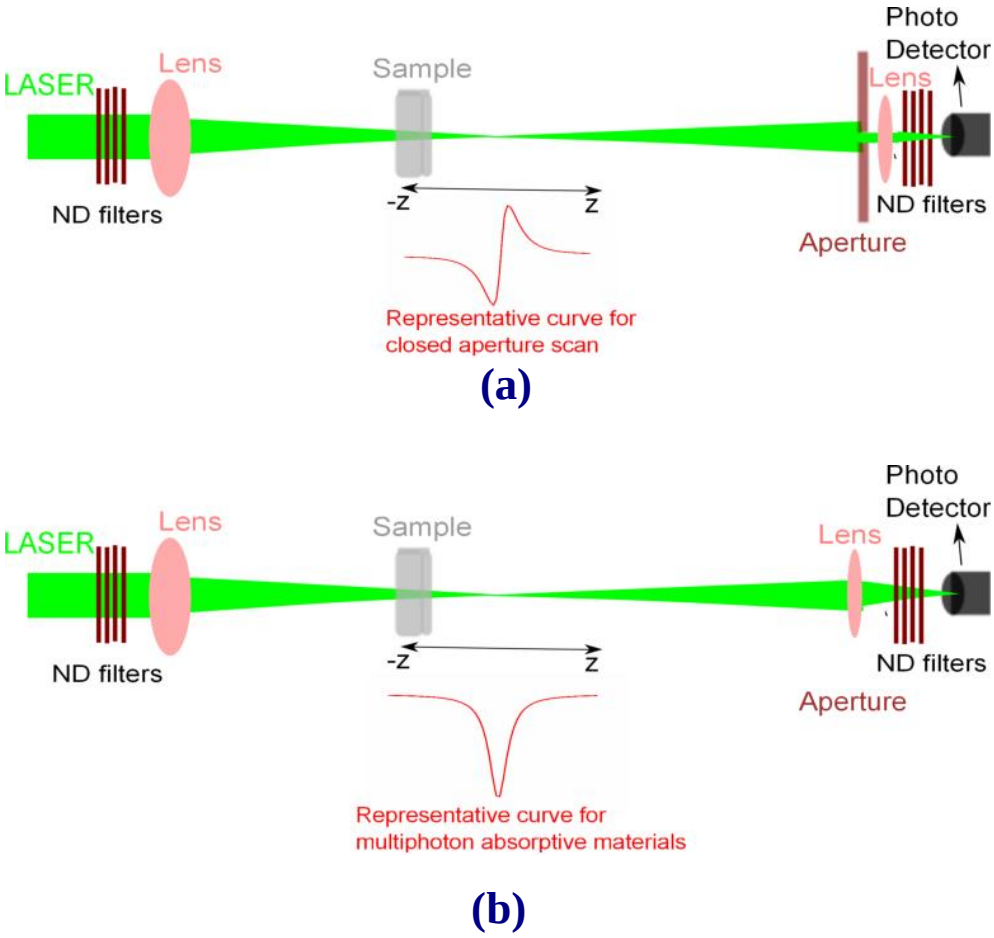

Figure.2.2 Schematic of a Z-scan setup. (a) closed aperture; (b) open aperture.

Closed-aperture Z-scan for sign and refractive nonlinearity:

Consider, for instance, a material with a negative nonlinear refraction and of thickness smaller than the diffraction length ($\pi\omega_0^2/\lambda$) of the focused beam being positioned at various positions along the Z-axis as shown in figure 2.2 (a). This situation can be regarded as treating the sample as a thin lens of variable focal length due to the change in the refractive index at each position ($n = n_0 + n_2 I$). When the sample is far from the focus and closer to the lens, the irradiance is low and the transmittance characteristics are linear. Hence the transmittance through the aperture is fairly constant in this region. As the sample is moved closer to the focus, the laser irradiance increases, which inducing a negative

lensing effect. A negative lens before the focus tends to collimate the beam. This causes the beam narrowing leading to an increase in the measured transmittance at the aperture (assuming a negative nonlinearity). A negative lens after the focus tends to diverge the beam resulting in the decrease of transmittance. As the sample is moved far away from the focus, the transmittance becomes linear in Z as the irradiance becomes low again. Thus the curve for Z versus transmittance has a peak followed by a valley for a negative refractive nonlinearity. The curve for a positive refractive nonlinearity will give rise to the opposite effect, i.e. a valley followed by a peak.

Open-aperture Z-scan for absorptive nonlinearity:

In the above discussion a purely refractive nonlinearity was considered assuming that absorptive nonlinearities are absent. The presence of multi-photon (two or more) absorption suppresses the peak and enhances the valley, while saturation of absorption produces the opposite effect. The sensitivity of the experiment to refractive nonlinearities is entirely due to the aperture. The removal of the aperture will make the Z-scan sensitive to absorptive nonlinearities alone. The schematic of an open aperture Z-scan is as shown in figure 2.2 (b).

Nonlinear scattering measurement from Z-scan

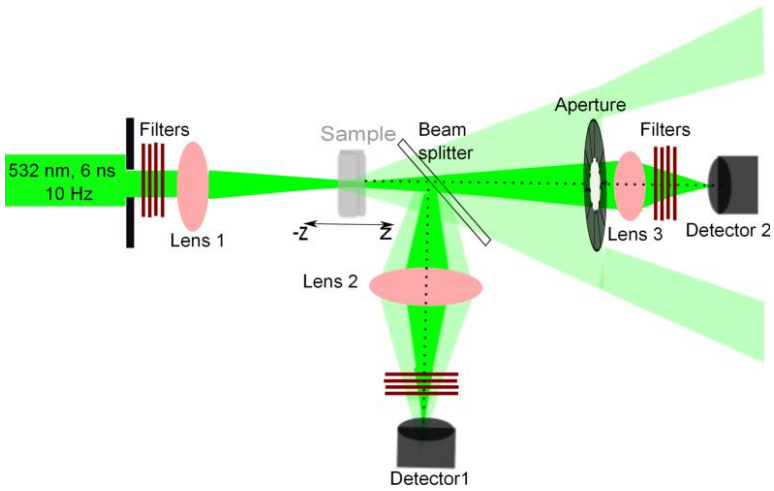

Figure 2.3 Schematic of nonlinear scattering measurement.

In the Z-scan setup itself we are able to measure nonlinear scattering; by introducing the beam splitter and detector in one arm of the Z-scan setup as shown in the figure 2.3 to measure the nonlinear transmittance (N. T) which is arises from the effect of nonlinear absorption. Detector 2 was used to measure the N. T which is arises from the effect of nonlinear absorption and nonlinear scattering. The pure nonlinear scattering effect can be measured by subtracting signal of detector 1 from detector 2.

Thus by doing the Z-scan with and without aperture both the refractive and absorptive nonlinearities of the sample can be studied. Spatially filtered input beam is focused using a lens. In the case of fs pulse excitation we used an achromatic doublet of focal length 120 mm. Usage of achromatic doublet for focusing the fs and ps pulses is essential to overcome the chromatic aberration at the focus owing to the large bandwidth of the input spectrum when compared to ns or ps pulses. The sample is scanned across the focus using a stepper motor controlled by computer. The transmitted light is then collected using another lens (large area) of f ~ 100 mm and fast photodiode (FND100). Different neutral density filters are used for attenuation to ensure that the photodiode does not get saturated. The photodiode output is fed to a lock-in amplifier or a boxcar averager/gated integrator and is finally recorded. The averaged signal is then sent to an interfaced ADC card and then to a computer.

2.3 Optical characterization

Optical properties of organic molecules, bio-reduced silver nanoparticles and graphene based materials were studied using a JASCO V-670 UV-VIS-NIR double beam spectrophotometer. The absorption was recorded in the wavelength range 190 to 2700. Wavelength accuracy in UV/VIS region was ±0.3 nm and ±1.5 nm in NIR region at room temperature.

2.4 Steady-state and time resolved fluorescence emission

Steady-state fluorescence emission studies were carried with Spex Fluoro Log-3 spectrofluorometer (Jobin-Yvon Inc.) equipped with a Hamamatsu R928

photo- multiplier tube and double excitation and emission monochromators with a wavelength resolution of ± 1 nm. The phosphorescence emission was collected with IR sensitive photo multiplier by cooling with liquid nitrogen. Time resolved fluorescence methods give the kinetic information on the various processes involved in the deactivation of the excited state. With the advent of lasers as excitation light sources, it is possible to have the time resolution of the order of ps and ns for the excited processes under investigation. The typical fluorescence intensity decay is a plot of fluorescence intensity as a function of time. For a simple system having a single fluorophore the fluorescence intensity decay, I(t), is a single exponential and is given as

$$I(t) = I_o e^{-t/Ű}$$

where I_0 is the initial intensity and Ű is the fluorescence lifetime. The fluorescence lifetime, Űrepresents the average time spent by the fluorophore in the excited state before coming to ground state. Time resolved fluorescence decay measurements were carried out using the time-correlated single-photon counting with Nano LED (459 nm; FWHM < 1.3 ns) with repetition rate of 10 kHz used to excite the samples. Pico-second (ps) lifetime measurements were carried out with Nano LED (469 nm; FWHM < 200 ps) with repetition rate of 1 kHz. The excitation source was mounted directly on the sample chamber at 90° to the collection optics of a double grating emission monochromator (2.1 nm/mm dispersion; 1200 grooves/mm) and collected by a TBX-4-X single-photon-counting detector. Light scattering sample was used to obtain an instrument response function as a reference for the de-convolution of the fluorescence lifetime profiles. The photons collected at the detector are correlated by a time-to-amplitude converter to the excitation pulse. Signals were collected using an IBH Hub photon counting module and data analysis was performed using the commercially available DAS6 software (HORIBA JobinYvon IBH). The goodness of fit was assessed by minimizing the reduced $ɢ^2$ with an error of 5-10 % and visual inspection of the weighted residuals.

2.5 Micro-Raman spectrometer

Raman spectroscopy is a light scattering technique, and can be thought of in its simplest form as a process where a photon of light interacts with a molecule in the sample to produce scattered radiation of different frequencies. If frequency of scattered photon is less than the incident photon, then it is known as Stokes scattering. If frequency of scattered photon is greater than the incident photon then it is called anti-Stokes scattering. Raman spectroscopy is extremely information rich, for example it is useful for chemical identification, characterization of molecular structures, effects of bonding, environment and stress on a sample.

In Raman experiments, the sample is irradiated with monochromatic light and the scattered light is traditionally observed at right angles to the incident radiation. However, in modern confocal Raman microscopes, the scattered signals are recollected by a microscope objective in 180° geometry. Selection of appropriate light source for micro-Raman spectroscopy is of great importance because the Raman signals are usually much weaker than the excitation intensity. For strong scattering material only one Raman scattered photon can be explored for every 10^7 incident photon. Further a coherent light source (laser) is preferred due to its high power, monochromatic and collimated beam nature. The most commonly used laser sources in Raman applications are He-Ne, Ar^+ ion and diode lasers delivering at 632.8, 514.5 and 785 nm respectively.

In the present work Raman scattering measurements were performed with a LabRAM HR800 micro-Raman spectrometer manufactured by HORIBA Jobin Yvon. It includes a variety of optical components arranged as illustrated in Figure 2.5. A collimated laser beam is sequentially passed through several optical components including the spatial filter, optical density filters, an edge filter which serves as a dichroic mirror, and the microscope objective lens which focuses the beam on the core sample. An automated x-y motorized stage allows moving the sample to acquire Raman spectra at each position. The scattered radiation emanating from the sample is collected through the same objective lens and is passed through the edge filter for elimination of the excitation line. A controllable

slit and a confocal hole are used before the Raman radiation reaches the spectrograph. The spectrograph utilizes two gratings with 600 and 1800 lines/mm. The spectrograph focuses the scattered wavelength spectrum on a CCD camera. All these optical components are controlled through a graphical user interface on a computer attached to the system.

2.6 Field emission-scanning electron microscopy (FESEM)

A high energy (typically 10-30 keV) electron beam, emitted from a tungsten tip is focused to a spot size of 1 nm to 5 nm by the condenser magnetic lenses. The focused beam passes through a pair of scanning coils, which raster the beam across the surface. The secondary electrons emitted from the sample are detected by a scintillator-photomultiplier device and the resulting signal is rendered into a two-dimensional intensity distribution that can be viewed and saved as a digital image. The most common imaging mode monitors low energy (<50 eV) secondary electrons which originates within a few nanometers from the surface.

2.7 Transmission electron microscopy (TEM)

In the present work we have used Transmission electron microscope (model: Tecnai 20 G2 STwin, FEI electron microscope operated at 20 kV using Gatan CCD camera) to investigate nanoparticle nucleation and growth and to determine crystal structure of Ag nanoparticles.

2.8 References

1. R. L. Sutherland, *Handbook of Nonlinear Optics*, Second Edition, and Revised and expanded, New York, NY: Marcel Dekker (2003).
2. M. Sheik-Bahae, A.A. Said, T.H. Wei, D.J. Hagan, and E.W. Van Stryland, IEEE J. Quant. Electron. **QE-26**, 760 (1990).

Chapter -III

BIO-SYNTHESIZED SILVER NANOPARTICLES USING CORIANDER AND MORINGA OLEIFERA LEAF EXTRACTS AND THEIR APPLICATIONS IN NONLINEAR OPTICS

Abstract

The development of biologically inspired experimental processes for the synthesis of nanoparticles is evolving into an important branch of nanotechnology. The work presented in this chapter contains the biosynthesis of silver nanoparticles using coriander and moringa oleifera leaf extracts as a reducing and a stabilizing agent, and its application in nonlinear optics. The aqueous silver ions when exposed to coriander or moringa oleifera leaf extract are reduced resulting in the formation of silver nanoparticles demonstrating the biosynthesis. These silver nanoparticles are characterized using UV-Visible, X-ray diffraction, Fourier transform infra-red spectroscopy and Transmission electron microscopy techniques. The third order nonlinear optical susceptibility, nonlinear refractive index and nonlinear optical absorption studies are measured using Z-scan technique with a 6 ns, 532 nm pulsed laser. These silver nanoparticles suspended in solution exhibited very strong reverse saturable absorption with low optical limiting threshold.

3.1 Introduction

Owing to its unique properties, colloidal silver nanoparticles are widely used in photonics [1, 2], microelectronics [3, 4], catalysis [5], sensing devices [6, 7], surface-enhanced Raman spectroscopy [8, 9] and pharmaceuticals [10, 11]. These diverse applications have generated a great deal of interest in developing versatile methods to synthesize silver nanoparticles with well-defined and controlled properties. Their performance depends critically on their size, shape and composition. The reactants and starting materials used in many chemical methods are toxic and potentially hazardous. Synthesis based on naturally occurring biomaterials provides advancement over chemical and physical methods as a cost effective and environment friendly method. Further, there is no need to use high pressure, energy, temperature and toxic chemicals. Thus increasing environmental concerns over chemical synthesis routes have resulted in attempts to develop bio-mimetic approaches. Bio-mimetics is a technique in which biological systems such as yeast, fungi, bacteria and plants are used for the synthesis of biocompatible metal and semiconductor nanostructures. One of them is the synthesis using plant parts, where eliminating the elaborate process of maintaining the microbial culture, and often found to be kinetically favorable than other bioprocesses. Recently, several groups have achieved success in the synthesis of silver, gold and palladium nanoparticles using extracts obtained from unicellular organisms like bacteria [12-15], fungi [16-17], and plant extracts [18-20]. The spectacular success in this field has opened up the prospect of developing green methods of metal nanoparticles synthesis with tailor-made structural properties. In this work, for the first time we present a simple and bio inspired method for the preparation of silver (Ag) nanoparticles using the leaf broth of moringa oleifera and coriander as a both reducing and stabilizing agent. No other chemical reducing agents are used in this synthesis process. The reaction is carried out in an aqueous solution in a process that is benign to the environment. Moringa oleifera and coriander are multipurpose tropical trees with most of their parts being useful for medicinal and commercial applications in addition to its nutritional value [21-22]. The moringa leaves are known as ‘drumstick’ leaves in the southern part of India. They are rich source of vitamins

A and C. They also have polyphenols, calcium, iron, folic acid and beta-carotene. Coriander leaf extracts are chosen for the present study, since coriander possesses minerals and vitamin contents including calcium, phosphorus, iron, carotene, thiamine, riboflavin, and niacin. They also contain sodium and oxalic acid.

Silver nanoparticles have an advantage over other metal nanoparticles (e.g. gold and copper) because the surface plasmon resonance energy of Ag is located far from the inter-band transition energy. The silver nanoparticles contained compounds are investigated for the nonlinear optical effects solely based on the surface plasmon contribution. *In situ* growth of metal nanoparticles in polymer films and their nonlinear optical properties have been reported by our group earlier [23]. The advantage of this method is the use of the aqueous medium for the fabrication process, employment of the polymer itself as the reducing agent, mild thermal annealing for generating the metal, and generation of the nanoparticles inside the polymer matrix which serves as the stabilizer as well. Here we have made an effort to show that the Ag nanoparticles synthesized through the bio-route show similar or better optical limiting results proving that the bio molecules that form as the capping molecules do not hinder the nonlinear activity of the Ag nanoparticles. Due to the local field enhancement with surface plasmon resonance, larger third-order optical nonlinearity of composite films has been observed in the presence of metal nanoparticles [24-25]. These materials with large optical nonlinearities have been considered to be good candidates for all optical and electronic devices [26]. The surface plasmon resonance (SPR), which plays an important role in enhancing the optical nonlinearities, can be altered by changing the size, shape, and volume of the particle. From the practical point of view, these metal composites can be optimized to meet the requirements of the optical device operation. Our endeavor is to develop eco-friendly methods for synthesis of Ag nanoparticles and study their nonlinear optical, optical limiting characteristics. We also attempt to compare the results obtained using this technique with those reported previously where the synthesis is through chemical routes [23, 27].

3.2 Bio-synthesized silver nanoparticles using moringa oleifera leaf extract

3.2.1 Experimental

3.2.1.1 Materials

Silver nitrate ($AgNO_3$, 99.99 %) is purchased from Sigma Aldrich chemicals. The moringa oleifera leaves ('drumstick' leaves) from moringaceae family are collected from home premises.

3.2.1.2 Biosynthesis of silver nanoparticles using moringa oleifera leaf extract

A 20 g of home-grown fresh leaves were washed thoroughly with double distilled water (DDW). Leaves were cut finely and boiled for 5 min in 100 ml of DD water and filtered. The extract was stored at 4°C for further experiments. This filtrate was used as reducing and stabilizing agent for silver nanoparticles. Silver nanoparticles were prepared by reducing 1mM $AgNO_3$ aqueous solution with freshly prepared leaf broth. The experiment was repeated in triplicate to confirm the reproducibility. Reduction of silver ions present in the aqueous solution of silver complex during the reaction with the ingredients present in the moringa oleifera leaf extract was monitored through the UV-Vis spectrum. The morphology of silver nanoparticles and its polydispersity in the solution may be easily followed by the UV-Vis spectrum. It is due to the strong absorption of electromagnetic waves in the UV-Vis region by the metal nanoparticles' surface Plasmon mode. As we mix the moringa oleifera leaf extract in the aqueous solution of the silver ion complex, after some time the solution start to change from pale colour to yellowish brown indicating the formation of Ag nanoparticles.

3.2.2 UV-Visible absorbance spectroscopy

The bio reduction of pure Ag^+ ions was monitored by measuring the UV-Vis spectra of the reaction medium at different time intervals. UV-Vis spectral analysis was carried out with a JASCO UV-Visible absorption spectrophotometer with a resolution of 1 nm between 300 and 800 nm. A small aliquot of 300 µl of

the sample was diluted 10 times with Millipore water to avoid errors due to high optical density of the solution. Figure 1 shows the absorption spectra of silver nanoparticles formed in the reaction media at different times as 10, 20, 30, and 40 minutes. The strong surface plasmon resonance band centered at around 460 nm clearly increases in intensity with time. Because of the polydispersity of the nanoparticles, we observe a broad peak around 460 nm and a second peak at around 360 nm.

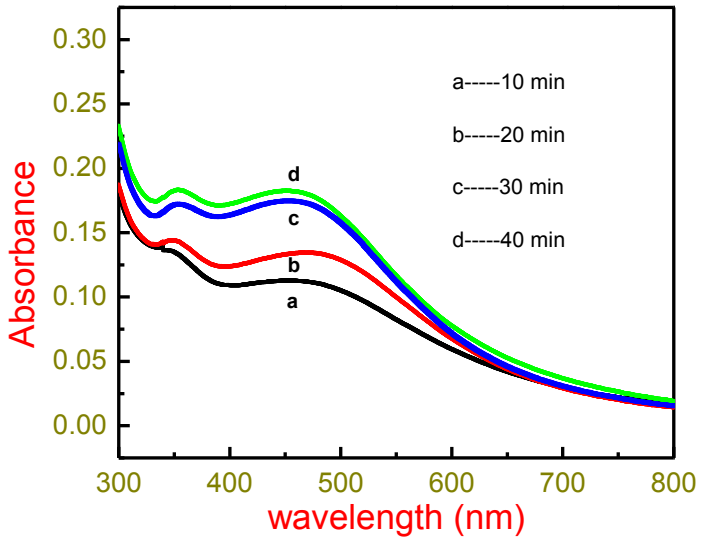

Figure 1. UV–Visible absorption spectra recorded at different reaction times of the aqueous solution of 10^{-3} M $AgNO_3$ with the Moringa oleifera leaf extract.

3.2.3 X-ray diffraction studies

A thin film of the Ag nanoparticles was prepared by dipping a glass plate in the solution to carry out the X-ray studies. The diffraction pattern was recorded by Co–Kα_1 radiation with a wavelength of 1.78 Å, scanning in the region from 20° to 90° for 2θ at 0.02°/min with a time constant of 2s. The crystalline nature of Ag nanoparticles was confirmed from the X-ray diffraction (XRD) analysis. Figure 2 shows the XRD pattern of Ag nanoparticles. The diffraction peaks at 44.98, 52.06, 77.15, 93.69 and 99.31 correspond to the (111), (200), (220), (311) and (222) facets of the FCC crystal structure respectively. The broadening of the Bragg peaks indicates the formation of nanoparticles. The unassigned peaks,

marked with # in the figure 2 could be due to the crystallization of bio-organic phase that occurs on the surface of the Ag nanoparticles. The XRD pattern thus clearly shows that the silver nanoparticles formed by the reduction of Ag^+ ions by Moringa oleifera leaf broth are crystalline in nature.

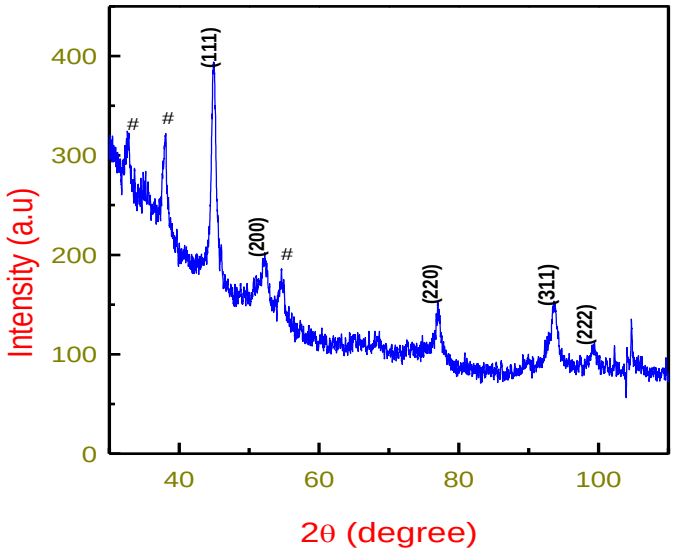

Figure 2. XRD pattern of as synthesized silver nanoparticles.

3.2.4 Fourier transform infrared spectroscopy (FTIR) studies

FTIR measurements were carried out to identify the possible biomolecules responsible for capping and efficient stabilization of the metal nanoparticles synthesized using the extract of moringa oleifera leaf. Ag nanoparticles solution was first centrifuged at 10,000 rpm for 30 min. The pellet was then washed three times with 20 ml of de-ionized water to get rid of all the free proteins/enzymes that are not capping the silver nanoparticles prior to the FTIR measurements. The sample was dried and grinded with KBr pellets for analysis on a JASCO FT/IR-5300 model operated in the diffuse reflectance mode at a resolution of 4 cm^{-1}. A typical FTIR spectrum of the obtained Ag nanoparticles is shown in figure 3(b), where the spectrum of moringa oleifera leaf broth (figure 3(a)), before the reaction is also displayed for a comparison.

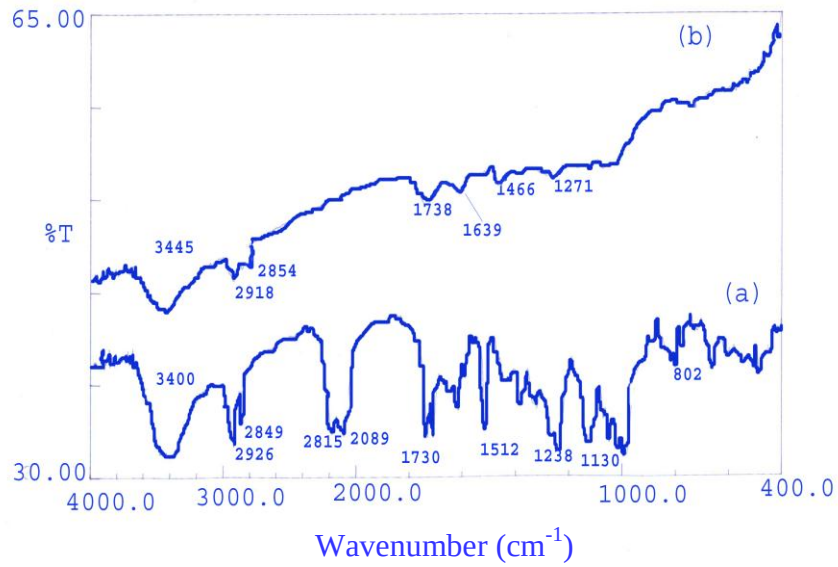

Figure 3. (a) FT-IR spectrum of fresh moringa oleifera leaf extract and (b) Ag nanoparticles prepared from the moringa oleifera extract.

The spectrum of leaf extract shows several absorption peaks at 3440, 2926, 2854, 2815, 1730, 1512, 1238, 1130 and 800 cm^{-1}. The intense broad line at 3440 cm^{-1} is characteristic of the hydroxyl functional group in alcohols and phenolic compounds. The peaks at 3440, 2918, 2854, 1738, 1639 and 1271 cm^{-1} appear in pure leaf broth spectrum as well as in the Ag nanoparticles' spectrum. The bands at 2918 and 2854 cm^{-1} could be due to alkane C-H stretch which is associated with the lipid molecules in the leaf broth. The IR bands at 1738 cm^{-1} is the stretch vibration of -C=O, 1639 cm^{-1} and is due to the amide II bond from proteins, and at 1466 and 1271 cm^{-1} bonds are –C-O- , -C- C- stretches respectively, which are due to lipids and sugars. The bands at 2815, 2809, 1512, 1130 and 802 cm^{-1} are attributed to the vibrations of C-H, C≡C, nitro compound, amine (C-N) and phenyl (C-H) stretches respectively. These bands disappear completely in the spectrum of Ag nanoparticles. Reduction of Ag^1 to Ag^0 is mainly responsible for the disappearance of these bands due to bio reduction. These observations are also indicative of the binding of protein with Ag nanoparticles through free carboxylate group. From FT-IR results it can be inferred that some of the bio-organics from broth of moringa oleifera formed a strong coating/capping on the nanoparticles.

3.2.5 Transmission electron microscopy (TEM)

The size and shape of Ag nanoparticles were visualized with the help of the 200 kV ultra high resolution transmission electron microscope (JEOL-2010). TEM grids were prepared by placing a drop of the particle solution on a carbon-coated copper grid and drying under a lamp.

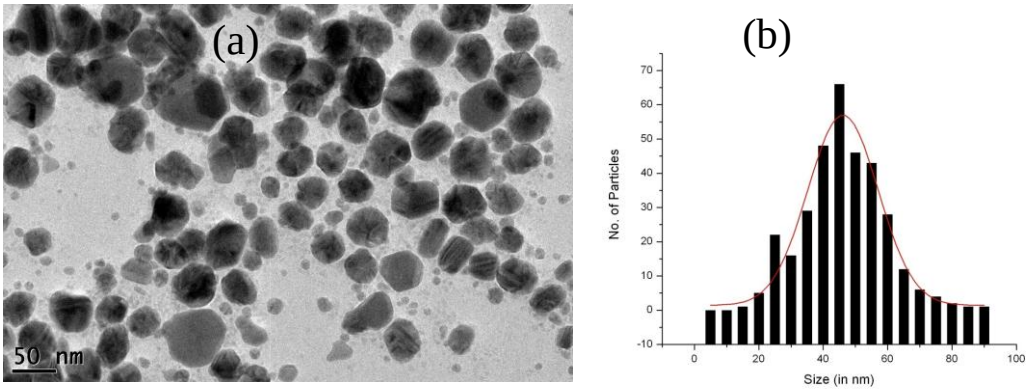

Figure 4. (a) A typical bright field TEM image of bio reduced silver nanoparticles (b) Histogram of the Ag nanoparticles

Figure 4(a) shows the typical bright-field TEM micrograph of the synthesized Ag nanoparticles. It can be seen that most of the Ag nanoparticles are spherical in shape. A few agglomerated silver nanoparticles can also be observed in some places, thereby indicating possible sedimentation with a time. Figure 4(b) shows the histogram taken from a large number of micrographs. It is evident that the particle size varies from 5 nm to 80 nm and the average size estimated is around 46 nm.

3.2.6 Nonlinear optical studies

The nonlinear optical properties were measured by the standard Z-scan technique [28], using a frequency doubled, Q-switched Nd: YAG (Spectra Physics, INDI-40) laser, delivering 6 ns laser pluses at 532 nm at a repetition rate of 10 Hz. Nonlinear absorption of the Ag nanoparticles in solution was studied by carrying out the open aperture Z-scan measurements. The experimental set up used is described in detail in the chapter 2. Briefly, in a typical Z-scan

experimental setup, a laser beam with a transverse Gaussian profile is focused using a lens. The sample in a 1 mm thick cell is then translated along the propagation direction of the focused beam. At the focal point, the sample experiences maximum intensity, which will gradually decrease in either direction from the focus. An f/40 configuration is used for our present studies. The thickness of the sample is chosen such that it is smaller than the Rayleigh range of the focused beam, which is nearly 3 mm. Apertures are introduced in the path for beam shaping and calibrated neutral density filters are used to vary the laser intensity. The data is then recorded by scanning the cell across the focus and collecting the data through a boxcar averager (model SRS 250), the output of which is given to a personal computer with an analog-to-digital (ADC) card. The nonlinear absorption coefficient (α_2) is obtained by fitting the nonlinear transmission expression for an open aperture Z scan curve [28, 30]

$$T_{OA(2PA)} = 1 - \frac{\alpha_2 I_0 L_{eff}}{2^{3/2}(1 + z^2 / z_0^2)} \qquad (1)$$

where z is the sample position, $z_0 = \pi\omega_0^2/\lambda$ is the Rayleigh range, ω_0 is the beam waist at the focal point (Z = 0), λ is the laser excitation wavelength, I_0 is the intensity on the sample at focus, α_2 is the effective nonlinear absorption coefficient incorporating both the excited state absorption and two-photon absorption, and effective optical path length in the sample of length L is given as $L_{eff} = \frac{1 - e^{-\alpha_0 L}}{\alpha_0}$, α_0 is linear absorption coefficient.

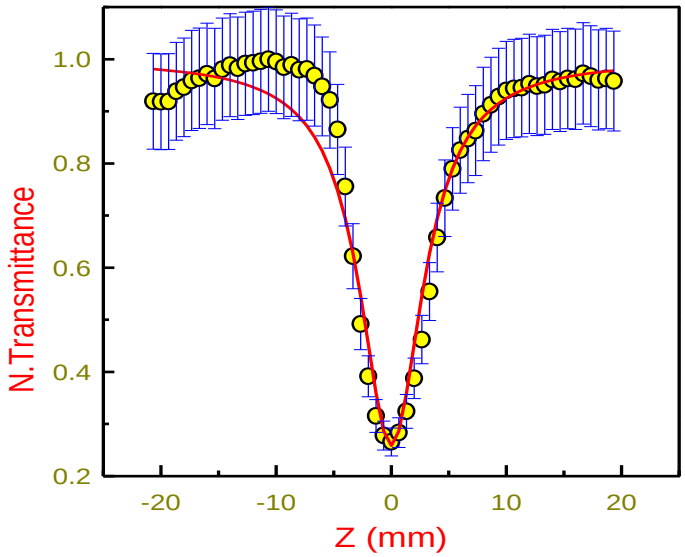

Figure 5. Open aperture Z-scan of bio-reduced silver nanoparticles (50 minutes reaction time) at 532 nm using 6 ns pulses.

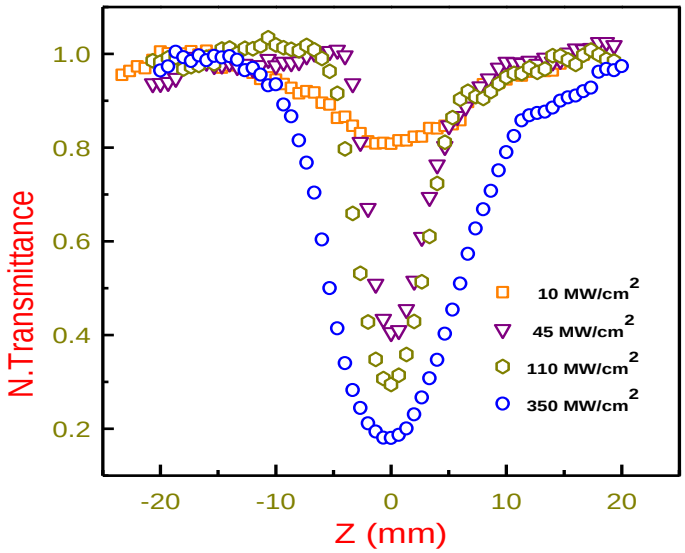

Figure 6. Intensity dependent open aperture Z-scan curves for silver nanoparticles

Figure. 5 illustrates the open aperture data of silver nanoparticles. Open circles are the experimental data and the solid curve is theoretical fit using equation (1).

We observe a reverse saturable absorption (RSA) behavior in the Ag nanoparticles which is attributed to the excitations from surface plasmon resonance (SPR) band to the free carrier band of nanoparticles and also the direct two-photon absorption (TPA) from ground state. From the fit we estimated α_2 to be ~ 2.72×10^2 cm/GW for the intensity 110 MW/cm^2. Intensity dependent Z-scan curves are shown in the figure 6. Nonlinear absorption coefficient remains unchanged with intensity dependent nonlinear transmission Z-scan curves.

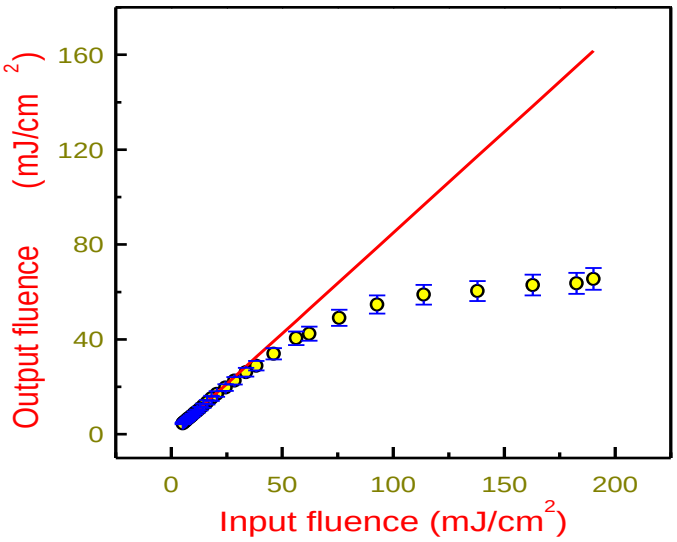

Figure 7. Optical limiting curve of silver nanoparticles (50 minutes reaction time) at 532 nm using 6 ns pulses, open circles represents experimental data and solid line represents linear transmittance (L.T).

Figure 7 shows the optical limiting data of silver nanoparticles. The values presented include an error of ±12% arising from the errors in estimation of the beam waist at focus, and the neutral density filter calibration to estimate the input power. We observe the limiting threshold as ~100 mJ/cm^2 and did not observe any nonlinear scattering suggesting that the limiting resulted from TPA and excited state absorption from surface Plasmon band.

3.2.7 Conclusions

We presented a simple, fast and economical biosynthesis of Ag nanoparticles using moringa oleifera leaf extracts and demonstrated that this method produces a reasonably sharp distribution of Ag nanoparticles. We have also shown that the particles synthesized by this method can be applied for nonlinear optical absorption and optical limiting phenomena with performance comparable to particles prepared through other routes.

3.3 Bio-synthesized silver nanoparticles using coriander leaf extract

3.3.1 Experimental

Preparation of leaf extract:

A 20 g of home-grown fresh coriander leaves were washed thoroughly with double distilled water and added to 100 ml of boiled and steriled DDW for 5 minutes and filtered. The extract is stored at 4°C for further experiments. The filtrate is used as a reducing and stabilizing agent for 1 mM of $AgNO_3$ (99.99 %, Sigma-Aldrich)

In a typical synthesis of silver (Ag) nanoparticles the leaf extract (1.5 ml) was added to 30 ml of 1×10^{-3} M $AgNO_3$ (99.99 %) aqueous solution and kept at 33°C. The experiment was done in triplicate to check for the reproducibility. After 10 minutes, the color of the solution changes from colorless to yellow indicating the formation of Ag nanoparticles. The bio-reduced Ag nanoparticles solution was collected and monitored by periodic sampling of aliquots (5 ml) of aqueous component and measuring UV-Visible spectra of the solution. The nanoparticles solution was diluted 10 times with Millipore TM water to avoid errors due to high optical density of the solution.

3.3.2 UV-Visible absorption spectroscopy

UV–Visible absorption spectroscopy analysis is carried out on a JASCO UV-Vis absorption spectrophotometer with a resolution of 1 nm between 300 and 800 nm possessing a scanning speed of 300 nm/min. Equivalent amounts of the

suspension (0.5 ml) were diluted in a constant volume of de-ionized water (5 ml) and subsequently analyzed at room temperature. The progress of the reaction between metal ions and the leaf extracts was monitored by UV–Visible spectra of Ag nanoparticles in aqueous solution with different reaction times and is shown in figure 8.

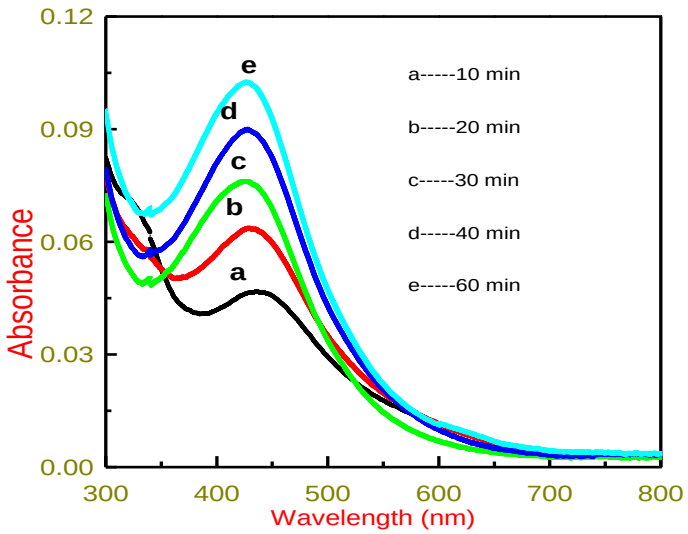

Figure 8. UV–Visible spectra recorded at various reaction times of the aqueous solution of 1×10^{-3} M $AgNO_3$ with the coriander leaf extract.

It is observed that the peak blue shifted in the absorption spectrum from 440 nm to 427 nm with increasing reaction time from 10 min to 30 min and the peak centered at 427 nm for 30, 40 and 60 minute samples. The reduction of silver ions and the formation of stable nanoparticles occur rapidly within an hour of the reaction, making it one of the fastest bio-reducing methods to produce silver nanostructures reported till date [17, 18, 30]

3.3.3 X-ray diffraction studies

A thin film of the silver nanoparticles was made by dipping a glass plate in the solution to carry out the X-ray studies. The diffraction pattern was recorded by Co–$K_{\alpha 1}$ radiation with a wavelength of 1.78 Å. The scanning is done in the

region of 20° to 80° for 2θ at 0.02°/min and the time constant is 2 s. The crystalline nature of Ag nanoparticles was confirmed from the X-ray diffraction analysis.

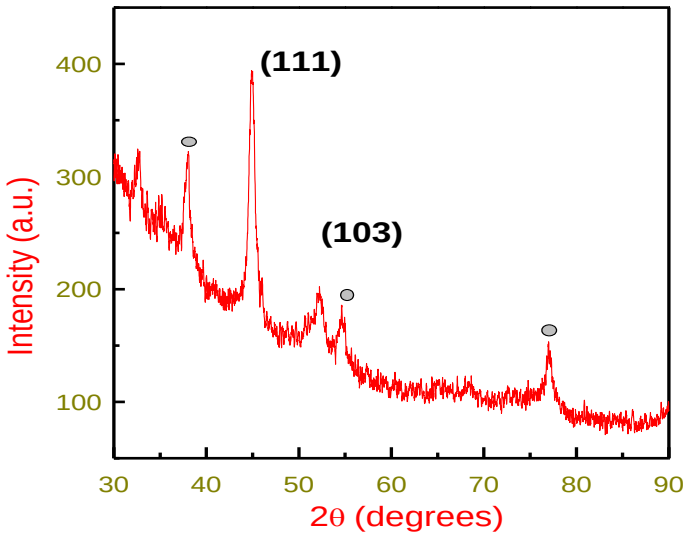

Figure 9. XRD pattern of as synthesised silver nanoparticles.

Figure 9 shows the XRD pattern with the diffraction peaks at 44.50 and 53.97 corresponding to the (111) and (103) facets of the face centered cubic crystal structure. The broadening of the Bragg peaks indicates the formation of nanoparticles. In addition to the Bragg peaks representing fcc silver nanocrystals, additional, and yet unassigned, peaks are also observed suggesting that the crystallization of bio-organic phase occurs on the surface of the silver nanoparticles.

3.3.4 Fourier transform infrared spectroscopy (FTIR) studies

For FTIR measurements, the silver nanoparticles solution was centrifuged at 10,000 rpm for 30 min. The residue was washed three times with 20 ml of de-ionized water to get rid of the free proteins/enzymes that are not capping the gold nanoparticles. The samples were dried and grinded with KBr pellets and analyzed on a JASCO FT/IR-5300 model in the diffuse reflectance mode operating at a resolution of 4 cm^{-1}.

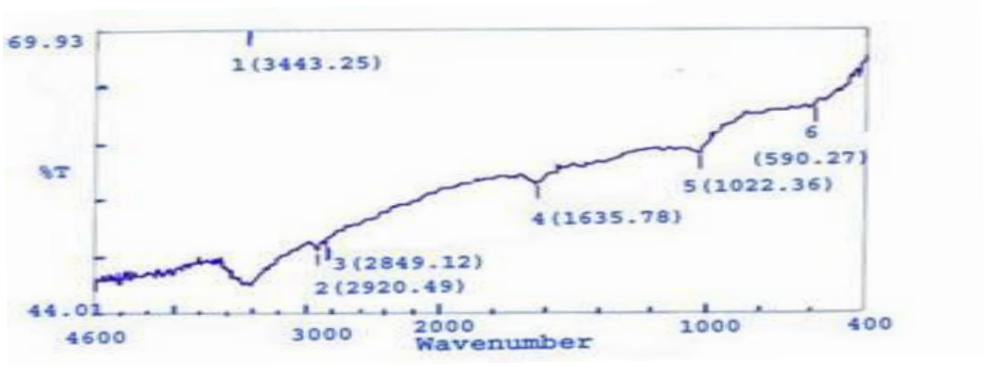

Figure 10. FT-IR spectrum recorded by making KBr disc with as synthesized silver nanoparticles prepared from the coriander extract.

Figure 10 shows the FTIR spectra of aqueous silver nanoparticles prepared from the coriander leaf extract. The peaks near 3430 cm^{-1} and near 2920 cm^{-1} are assigned to O–H stretching and aldehydic C–H stretching, respectively. The weaker band at 1635 cm^{-1} corresponds to amide I, arising due to carbonyl stretch in proteins. The peak at 1038 cm^{-1} corresponds to C–N stretching vibration of the amine. IR spectroscopic study has confirmed that the carbonyl group from amino acid residues and proteins have the stronger ability to bind to the metal indicating that the proteins could possibly form a layer covering the metal nanoparticles (i.e. capping of silver nanoparticles) and prevent the agglomeration and stabilization. This suggests that the biological molecules could possibly perform dual functions of formation and stabilization of silver nanoparticles in an aqueous medium.

3.3.5 Transmission electron microscopy (TEM)

TEM technique was employed to visualize the size and shape of silver nanoparticles. The 200 kV ultra high resolution transmission electron microscope (JEOL-2010) having high resolution optical microscope (Leica) was used. TEM grids were prepared by placing a drop of the particle solution on a carbon-coated copper grid and drying at room temperature.

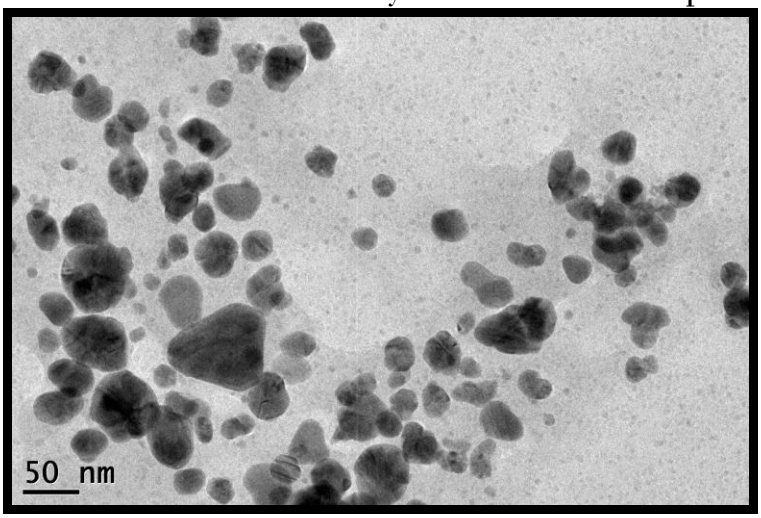

Figure 11. TEM image of bio reduced silver nano particles

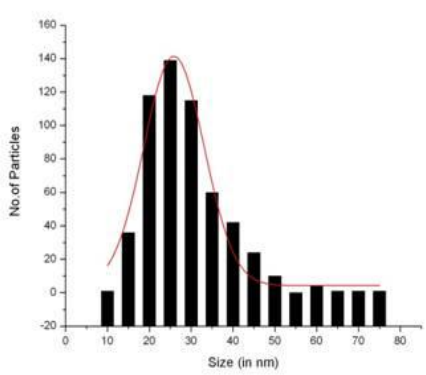

(a)

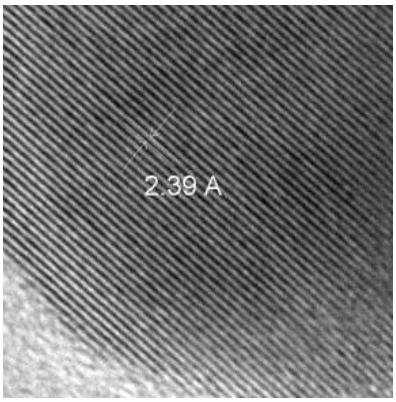

(b)

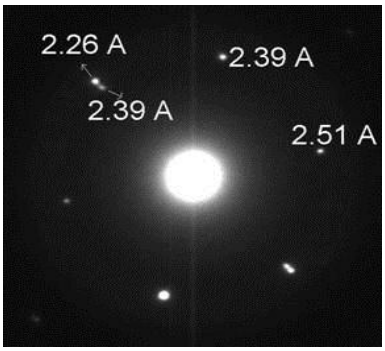

(c)

Figure 12. (a) Histogram of the Ag nanoparticles (b) lattice spacing and (c) crystalline planes

Figure 11 shows the typical bright-field TEM image of the synthesized silver nanoparticles. It is observed that most of the silver nanoparticles are spherical in

shape with sizes in the range of 10 to 80 nm indicating poly-dispersity. A few agglomerated silver nanoparticles are also observed in some places, thereby indicating possible sedimentation at a later time. The particle size distribution histogram determined from the TEM microscopy is shown in figure 12. It is evident that there is variation in particle sizes and the average size estimated is 25.8 nm.

3.3.6 Nonlinear optical studies

The nonlinear optical properties of silver nanoparticles are measured by Z-scan technique, with a frequency–doubled, Q-switched Nd: YAG (Spectra Physics, INDI 40) laser, delivering 6 ns laser pluses at 532 nm at a repetition rate of 10 Hz. Nonlinear absorption and refraction of the Ag nanoparticles in solution are studied by carrying out the open and closed aperture Z-scan measurements. The general set up used in these experiments has been described in chapter 2 and a brief explanation is also given in this chapter (section 3. 1. 6).

For obtaining the nonlinear coefficients (β_{eff} and nonlinear refractive index n_2) from Z-scan data we used equation (2) to fit the open aperture data and equation (3) for the closed aperture data.

$$T_{OA(2PA)} = 1 - \left(\frac{\beta_{eff} I_{00} L_{eff}}{2\sqrt{2}\left(1+\frac{Z}{Z_0}\right)^2}\right) \qquad (2)$$

where z is the sample position, $z_0 = \pi\omega_0^2/\lambda$ is the Rayleigh range; ω_0 is the beam waist at the focal point (Z = 0), λ is the laser wavelength; effective path lengths in the sample of length L is given as $L_{eff} = \frac{1-e^{-\alpha L}}{\alpha}$

$$T_{CA} = \frac{4\Delta\Phi_0 (z/z_0)}{[1+(z/z_0)^2][9+(z/z_0)^2]} \qquad (3)$$

where $\Delta\varphi_0$ is the phase change of laser beam due to the nonlinear refraction. $\Delta\varphi_0$ value is estimated from the theoretical fits to experimental data. Third order nonlinear refractive index n_2 is calculated from

$$n_2(cm^2W^{-1}) = \frac{|\Delta\Phi_0|\lambda}{2\pi I_{00} L_{eff}} \quad (4)$$

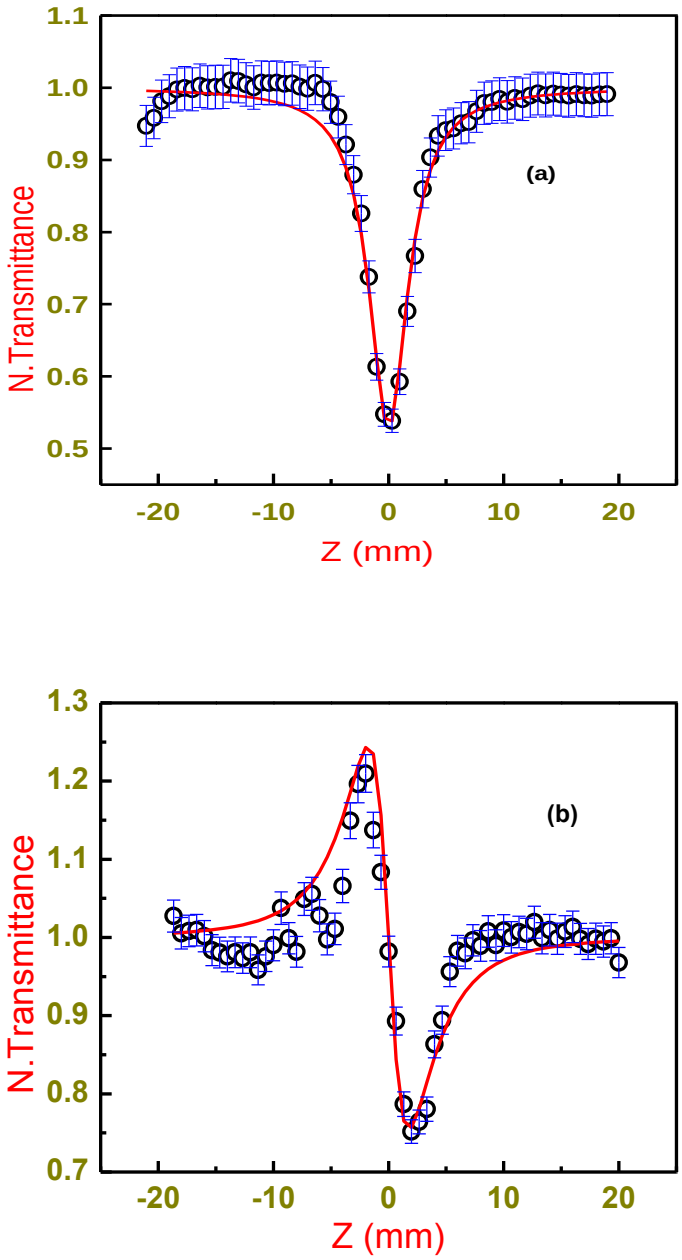

Figure 13. (a) Open and (b) closed aperture Z-scan curves of bio-reduced silver nanoparticles (60 minutes reaction time) at 532 nm using 6 ns pulses. The solid lines are the theoretical fits based on Eqs. (2) and (3), respectively.

Figure 13 (a) illustrates the open aperture data while figure 13 (b) shows the closed aperture data. Open circles are the experimental data and the solid curves are theoretical fits using equations (2) and (3).

RSA observed in Ag nanoparticles can be attributed to either the excitations from SPR band to the free carrier band of nanoparticles or the two-photon absorption. We have recorded open aperture Z-scan curves of Ag nanoparticles for different intensities ranging from 100 MW/cm^2 to 600 MW/cm^2.

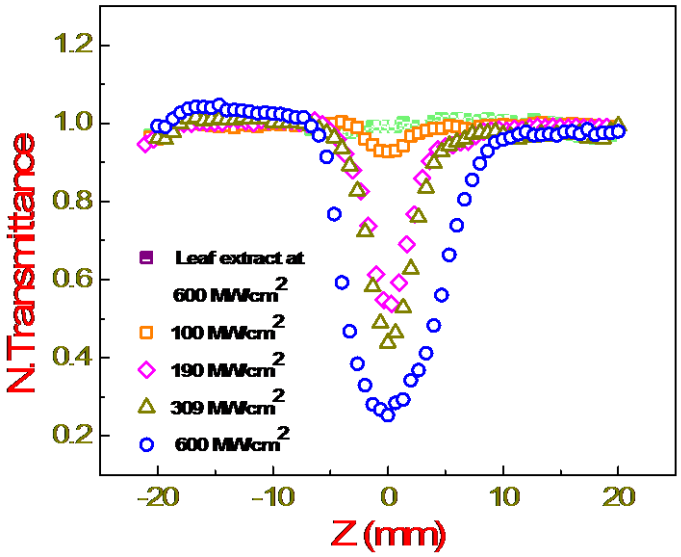

Figure 14. Intensity dependent open aperture Z-scan curves of silver nanoparticles

The nonlinear coefficient (β_{eff}) is a fairly constant for all the intensities. We observed that β_{eff} is ~ 72.5 cm/GW, where β_{eff} is the effective nonlinear absorption coefficient incorporating both the excited state absorption and two-photon absorption. From β_{eff} values we estimated the imaginary part of $\chi^{(3)}$, which is 1.38×10^{-11} esu. By recording the closed aperture Z scan curves, we estimated the nonlinear refractive index (n_2) to be -6.0×10^{-13} cm^2/W and 2.7×10^{-11} esu, respectively. The magnitude of $|\chi^{(3)}|$ is calculated to be ~1.38×10^{-11} esu.

The values presented above include an error of ±12 % arising from the errors in estimation of beam waist at focus, fitting errors, neutral density filter calibration errors, etc.

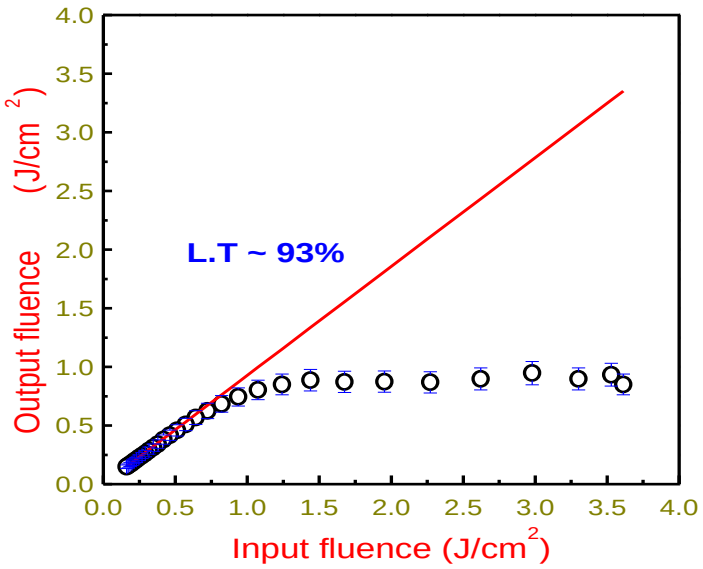

Figure 15. Optical limiting curve of silver nanoparticles (60 minutes reaction time) at 532 nm using 6 ns pulses.

Figure 15 shows the optical limiting curve of silver nanoparticles at 532 nm. The energy transmittance decreased with increasing input energy. The limiting threshold is ~1.80 J/cm^2. We did not observe any scattering from the nanoparticles suggesting that the limiting resulted from pure RSA. The higher values reported in the current study are compared with the earlier studies could be due to the longer lifetimes of the surface plasmon in the present case.

We made an attempt to compare current NLO results with chemically prepared silver nanoparticles in Table 1. These nanoparticles have shown comparable NLO coefficient values with chemical prepared silver nanoparticles.

Material	**λ(nm),τ_p(ns) and Rep.rate**	**TPA coefficient β (cm/GW)**	**Limting threshold**	**References**
In situ synthesis, Free standing films with Higly Mono disperse silver nanoparticles and optical limiting	532, 6 ns, 10 Hz	-----	0.83 J/cm^2	Chem. Mater (2005) 17, 9
Silver colloidal solution by in situ synthesis technique	532, 13 ns, 10 Hz	10.03	------	Current Appl. Phys (2008) 8, 13.
PDA/Ag composite vesicles	532, 16 ns	6.1	------	Nanotechnology (2008), 195703
Ag nanoparticles precipitated in glass	532, 10 ns, 1 Hz	10.3	------	Opt. Materials (2006) 28, 259
Silver nanoparticles in different liquids	532, 8 ns, 1 Hz	3	------	Optics and spectroscopy (2005) 99, 668.
silver nanoparticles synthesized by coriander leaves extract	532, 6 ns, 10 Hz	70.5	1.4 J/cm^2	Current Studies
silver nanoparticles synthesized by moringa oleifera leaves extract	532, 6 ns, 10 Hz	272	100 mJ/cm^2	Current studies

Table 1. NLO parameters comparison of chemical and bio synthesized silver nanoparticles

3.3.7 Conclusions

In conclusion we introduced a simple, fast, and economical biological procedure to synthesize Ag nanoparticles using coriander leaf extract. We characterized these nanoparticles using TEM, XRD, UV-Visible and FTIR spectroscopic techniques. We measured the nonlinear refraction and absorption coefficients using Z-scan technique with the ns laser pulses. The values of n_2, β_{eff}, and $|\chi^{(3)}|$ for silver nanoparticles obtained through these measurements are -6×10^{-13} cm^2/W, 72.5 cm/GW, and 1.38×10^{-11} esu, respectively. The limiting threshold of the sample is ~1.80 J/cm^2. The optical nonlinearity of these silver nanoparticles is comparable or superior to those synthesized through other procedures.

3.4 References

1. J. C. Lin and C. Y. Wang, Mater. Chem. Phys., **45**, 136 (1996).

2. R. Gould, J. R. Lenhard, A. A. Muenter, S. A. Godleski, S. Farid, J. Am. Chem. Soc., **122**, 11934 (2000).

3. G. Schimd, Chem. Rev., **92**, 1709 (1992).

4. W. A. Deheer, Rev. Mod. Phys., **65**, 611 (1993).

5. N. R. Jana, T. K. Sau, T. Pal, J. Phys. Chem. B., **103**, 115 (1999).

6. F. Frederix, J. M. Friedt, K. H. Choi, W. Laureyen, A. Campitelli, D. Mondelaers, G. Maes, G. Borghs, Anal. Chem., **75**, 6894 (2003).

7. J. Wang, Analytica Chimica Acta, **500**, 247(2003).

8. G. N. R. Tripathi, J. Am. Chem. Soc., **125**, 1178 (2003).

9. Z. Tian and B. Ren, Annu. Rev. Phys. Chem., **55**, 197 (2004).

10. I. Sondi and B. Salopek- Sondi, J. Colloids & Interface Sci., **275**, 177 (2004).

11. C. Aymonier, U. Schlotterbeck, L. Antonietti, P. Zacharias, R. Thomann, J. C. Tiller and S. Mecking, Chem. Comm., **24**, 3018 (2002).

12. A. Ahmad, S. Senapati, M. I. Khan, R. Kumar and M. Sastry, Langmuir, **19**, 3550 (2003).

13. B. Nair and T. Pradeep Crystal Growth and Design, **2**, 293 (2002).

14. T. Klaus, R. Joerger, E. Olsson and C. G. Granqvist, Proc. Trends Biotechnol., **19**, 15 (2001).

15. P. Mukherjee, A. Ahmad, D. Mandal, S. Senapati, S. R. Sainkar, M. I. Khan R. Ramani, R. Parischa, P.V. Ajaykumar, M. Alam, M. Sastry and R. Kumar, Angew. Chem. Int. Ed., **40**, 3585 (2001).

16. A. Ahmad, P. Mukherjee, S. Senapati, D. Mandal, M. I. Khan, R. Kumar and M. Sastry, Colloids Surf. B: Biointerfaces., **28**, 313 (2003).

17. S. Shiv Shankar, A. Ahmad, R. Pasricha and M. Sastry, Mater. Chem., **13**, 1822 (2003).

18. N. A. Begum, S. Mondal, Saswati Basu, R. A. Laskar and D. Mandal, Colloids and Surfaces B: Bio interfaces., **71**, 113 (2009).

19. D. Philip, Spectrochimica Acta Part A., **73**, 374 (2009).

20. K. Badri Narayanan and N. Sakthivel Mat. Lett., **62**, 4588 (2008).

21. J. P. Sutherland, G. K. Folkard, M. A. Mtawali, and W. D. Grant, 20th WEDC Conference Colombo, Sri Lanka, August 297 (1994).

22. A. Ndabigengesere , K. S. Narasiah, and B.G. Talbot ,Water Research., **29**(2),703 (1995).

23. S. Porel, S. Singh, S. S. Harsha, D. Narayana Rao, and T. P. Radhakrishnan, Chem. Mater., **17**(1), 9 (2005).

24. Q. Q. Wang, S. F. Wang, W. T. Hang and Q. H. Gong, J. Phys. D: Appl. Phys., **38**, 389 (2005).

25. R. F. Haglund, L. Yang, R. F. Magruder, J. E. Wittig, K. Becker, and R. A. Zuhr, Opt. Lett., **18**, 373 (1993).

26. N. N. Lepeshkin, W. Kim, V. P. Safonov, J. G. Zhu, R. L. Armstrong, C. W. White, R. A. Zuhr and V. M. Shalaev, J. Nonlinear Opt. Phys. Mater., **8**, 191 (1999).

27. X. Chen, G. Zou, Y. Deng and Zhang. Nanotechnology, **19**, 195703 (2008).

28. M. Sheik-Bahae, A. A. Said, T. Wei, D. J. Hagan and E. W. Van Stryland, IEEE J. Quantum Electron., **26**,760 (1990).

29. X. Gu, Q. Huang, S. Q. Tan , M. Wang, W. Ji, Appl. Phys B, **95**,375 (2009).

30. S. P. Chandran, M. Chaudhary, R. Pasricha, A. Ahmad, M. Sastry, Biotechnol. Prog., **22**, 577 (2006).

Chapter - IV

NONLINEAR OPTICAL PROPERTIES OF ORGANIC MOLECULES

- **ZnOCPc Phthalocyanine**
- **Metal and metal free Porphyrins**

Abstract

Synthesis and measurements of third order nonlinear optical (NLO) coefficients of water soluble zinc octacarboxy phthalocyanine (ZnOCPc) are presented in this chapter using different laser pulse durations. Nonlinear absorption and refraction behavior in the nanosecond (ns), picosecond (ps) and femtosecond (fs) time domains were studied in detail. Sign and magnitude of the third order nonlinearity in fs, ps, and ns regimes were evaluted. Observed off-resonant second order hyperpolarizability (γ) with ultrafast nonlinear optical response in the femtosecond domain using degenerate four wave mixing (DFWM) technique. Optical limiting characteristics and figure of merit (FOM) of ZnOCPc for optical switching were examined. Several porphyrins (Cu, Zn, VO, Sn and metal free porphyrin) were synthesized with metal and metal free substitutes in the core of porphyrin ring and examined for NLO studies.

4.1 Zinc-octa-carboxy phthalocyanine (ZnOCPc)

4.1.1 Introduction

Phthalocyanines (Pcs) family known for over a century [1, 2] is most appealing because of their potential application in photodetectors [3], optical storage [4], optical computing [5], harmonic generation [6, 7], light-emitting diodes [8, 9], solar cells [10], gas sensors [11], electro chromic displays [12, 13], optical switches [14], nonlinear optics [15], photoinactivators of viruses such as HIV [16] and bacteria [17], photodynamic therapy [18, 19], optical limiting [20, 21], lubricating greases [22], plastics [23] and printing inks [24]. The major interest to study the linear and nonlinear optical properties of phthalocyanines is because of their high and ultrafast nonlinear response, the flexibility of synthesis and modification of the properties through different metal derivatives. Nonlinearities in organic molecules usually arise from highly delocalized π-electron system. Phthalocyanines with their extensive two-dimensional π-electron system fulfil this requirement and they have been studied extensively as NLO materials. The enhancement of nonlinearities in phthalocyanines can be done from following process like π-π overlapping, aggregation effect, peripheral substitution with electron-rich moieties, enlargement of the π-electron conjugation [15]. They exhibit other additional advantages, namely, exceptional stability, versatility, intense absorption in the red region of visible spectrum. Phthalocyanines are versatile because they offer enormous structural flexibility with capacity of hosting ~ 70 different elements in its central cavity. One drawback of these molecules is that most of them are insoluble in common solvents. This may result in a limit to their applications. A variety of substituents can be attached to the phthalocyanine core, at the peripheral and non-peripheral positions leading to chemical variations and the electronic structure. This allows the fine tuning of the nonlinear response and has established to improve solubility. ZnOCPc was soluble in most of the common solvents. This chapter contains, optical characteristics of ZnOCPc which is, isomerically pure and

soluble in common solvents like water, DMF and ethanol. Water soluble Pcs shows diverse applications in biology like photosensitizes for photodynamic therapy, preparation of uniform thin films of phthalocyanines in polymer host for optical limiter applications. Solubility is greatly enhanced due to carboxyl groups substituted at eight peripherals. Intermolecular interactions of phthalocyanines influence the central atom and peripheral substituents result in changes of spectroscopic properties. Third order nonlinear optical properties of water soluble ZnOCPc were studied at 800 nm and 532 nm, which are non-resonant and far away from the linear absorption spectrum as shown in figure 1. The linear optical absorption spectrum of metal phthalocyanines (MPc's) show an absorption band in soret region at (300-350 nm) and the Q bands at (600-700 nm) due to π-π* transitions. The present studies on nonlinear absorption properties of water soluble Pcs is to look at their application towards an optical limiter, which finds use in protecting optical instruments and human eye from intense laser pulses.

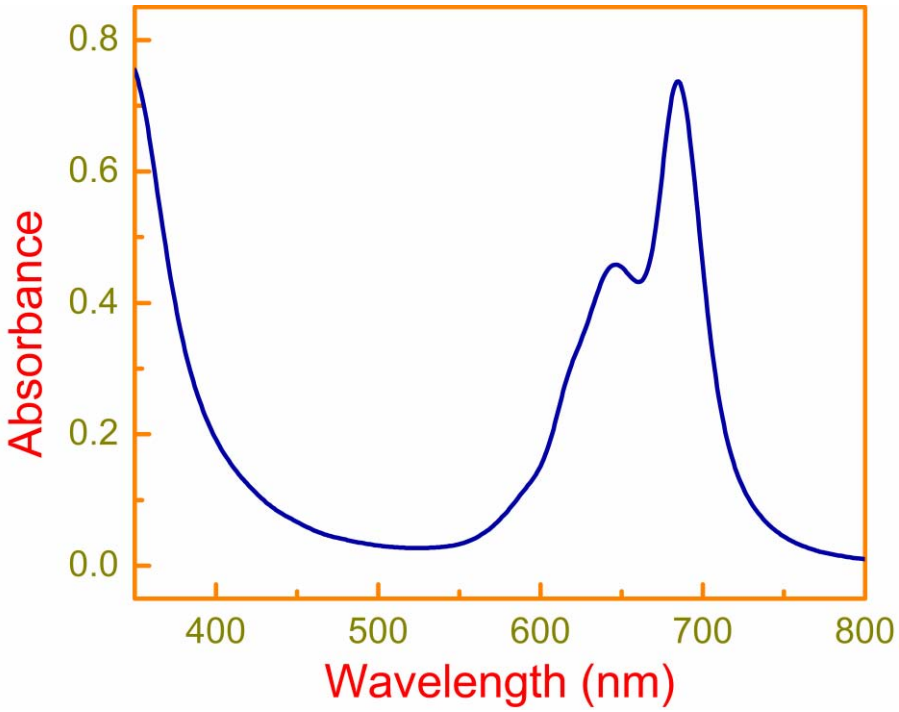

Figure 1. UV-Visible absorption spectra for water soluble ZnOCPc (Concentration: $5x10^{-6}$ M).

4.1.2 Experimental

Measurements were made using 800 nm femtosecond (fs), 532 nm picosecond (ps) and nanosecond (ns) pulses through Z-scan and degenerative four wave mixing (DFWM) techniques. ZnOCPc was dissolved in water at a concentration of 3×10^{-4} M (0.3 mg/ml) for the experiments. Z-scan technique [25] which is a single beam method for measuring both nonlinear absorption and nonlinear refraction was used. The DFWM setup was used in box-car geometry [26] to measure the magnitude of third order nonlinearity. The sample under consideration is used as solution filled in a 1 mm glass cuvette. Care was taken to reduce the contribution of the cuvette towards the overall DFWM signal by choosing suitable focusing conditions and laser intensities. While performing the nonlinear transmission experiments in the sample, the input powers for the three input pulses were chosen such that the effect of nonlinear absorption does not contribute and hence the obtained DFWM signal contains purely instantaneous nonlinear response of the sample in the ground state. The obtained $\chi^{(3)}$ data is, hence, purely real in nature without any contribution of imaginary components due to multi-photon absorption. Also, the choice of low input powers allow us to neglect the contribution of higher order nonlinearities.

4.1.3 Synthesis

4.1.3.1 Synthesis of 4-(1,1,2-tricarbethoxyethyl)-phthalonitrile (1): We followed the procedure for synthesis of (1) as reported by Kasim et. al [27].

4.1.3.2 Synthesis of 2(3),9(10),17(18),23(24)-(1,1,2-(tricarbethoxyethyl))-phthalocyanine (2):

Phthalonitrile (1) (0.3 g, 0.81 mmol) was dissolved in 5 ml of pentanol. To this catalytic amount of DBU was added and the resulting reaction mixture was heated at 140 ^{0}C under nitrogen atmosphere for 24 h. The solvent pentanol was removed under reduced pressure. The solid material was subjected to silica gel column chromatography and eluted with $CHCl_3$. Elemental analysis of $C_{76}H_{82}N_8O_{24}$ (calculated mass % in parentheses) gives the values as: C, 61.25 (61.20); H, 5.52 (5.54); N and 7.50 (7.51). UV-Vis absorption data in $CHCl_3$

shows peaks at [λ_{max} (log ε)]: 698 nm (4.80), 660 nm (4.29), 344 nm (2.5). ^{1}H NMR ($CDCl_3$) is summarized as δ ppm 9.22 (s, aromatic H), 8.20 – 7.20 (br, aromatic H), 4.75 – 3.60 (m, CH_2), 3.35 (s, CH_2), 2.70 – 1.25 (m, CH_2), 1.10 – 0.95 (t, CH_3), and -2.35 (br, -NH).

4.1.3.3 Synthesis of 2(3),9(10),17(18),23(24)-(1,1,2-(tricarbethoxyethyl))-phthalocyanato zinc(II) (3): Phthalocyanine (3) (0.2 g, 0.13 mmol) was dissolved in 20 ml of DMF. To this $Zn(CH_3COO)_2$ (0.2 g, 1.1 mmol) was added and the reaction mixture was refluxed until Q-bands of phthalocyanine have changed. The solvent was removed under reduced pressure. Pc was recrystallized from $CHCl_3$/hexane. Elemental analysis of $C_{76}H_{80}N_8O_{24}Zn$ (calculated mass % in parentheses) gives values as C, 58.65 (58.71); H, 5.20 (5.19); N, and 7.20 (7.21). UV-Vis absorption data in $CHCl_3$ shows peaks at [λ_{max} (log ε)]: 675 nm (4.80), and 348 nm (2.5).

4.1.3.4 Synthesis of 2(3),9(10),17(18),23(24)-(1,2-(dicarboxyethyl))-phthalocyanato zinc(II) (ZnOCPc): Sodium wires (0.20 g, 8.5 mmol) were added to 25 ml anhydrous ethanol kept in 50 ml flask and the contents were stirred under nitrogen atmosphere. After sodium gets completely dissolved compound (3) (0.135 g, 0.13 mmol) was added under nitrogen atmosphere. The resulting blue solution was stirred at room temperature under nitrogen atmosphere for 10 days. The solvent was removed under vacuum and the residue was dissolved in water and filtered to remove undissolved particles. The filtrate was acidified with 0.1 M HCl solution resulting in a green colour product, which gets precipitated. The precipitate was filtered, washed with water and dried in vacuum. Elemental analysis of $C_{48}H_{32}N_8O_{16}Zn$ (calculated mass % in parentheses) shows C, 55.30 (55.32); H, 3.11 (3.09); N, and 10.71 (10.75). UV-Vis absorption data in ethanol shows peaks at [λ_{max} (log ε)]: 672 nm (4.95), 641 nm (4.65), and 341 nm (4.98). Scheme for the synthesis of ZnOCPc is shown in figure 2.

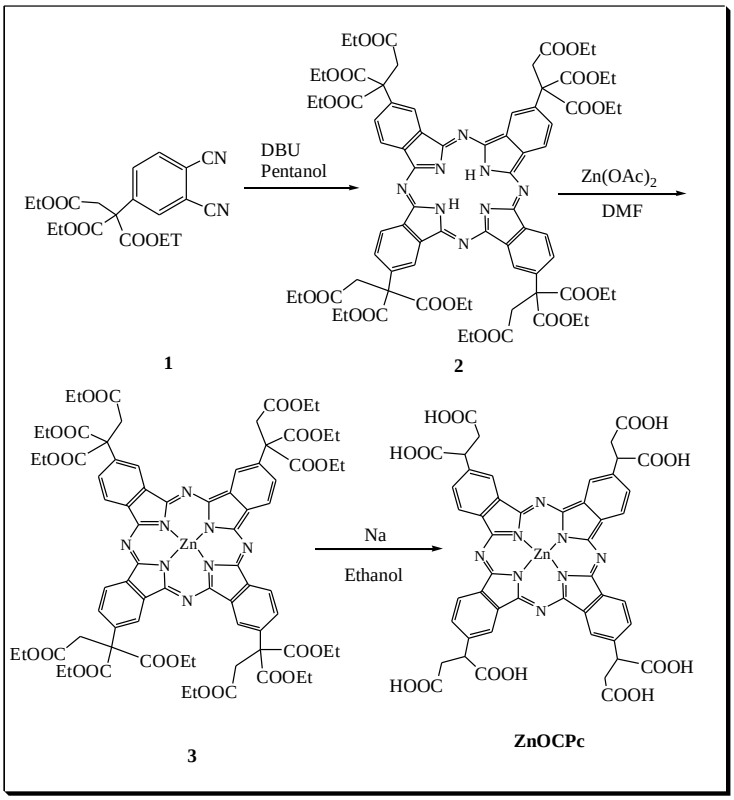

Figure 2. Synthesis scheme for water soluble ZnOCPc.

4.1.4 Results and discussions

4.1.4.1 Theoretical considerations

Open aperture Z-scan curves were fitted using 5-level rate equations model for ZnOCPc in the ns region [28]. The rate equations for five level model are

$$\frac{\partial N_0}{\partial t} = -\frac{\sigma_0 I N_0}{\hbar\omega} - \frac{\beta I^2}{2\hbar\omega} + \frac{N_1}{\tau_{s_1}} + \frac{N_3}{\tau_{t_1}} \tag{1}$$

$$\frac{\partial N_1}{\partial t} = \frac{\sigma_0 I N_0}{\hbar\omega} - \frac{\sigma_1 I N_1}{\hbar\omega} - \frac{N_1}{\tau_{s_1}} - \frac{N_1}{\tau_{isc}} + \frac{N_2}{\tau_{s_n}} \tag{2}$$

$$\frac{\partial N_2}{\partial t} = \frac{\sigma_1 I N_1}{\hbar\omega} + \frac{\beta I^2}{2\hbar\omega} - \frac{N_2}{\tau_{s_n}} \tag{3}$$

$$\frac{\partial N_3}{\partial t} = -\frac{\sigma_2 I N_3}{\hbar\omega} - \frac{N_3}{\tau_{t_1}} + \frac{N_1}{\tau_{isc}} + \frac{N_4}{\tau_{t_n}} \tag{4}$$

$$\frac{\partial N_4}{\partial t} = \frac{\sigma_2 I N_3}{\hbar\omega} - \frac{N_4}{\tau_{t_n}} \tag{5}$$

where N_j is the population per cc of the singlet (j = 0, 1, 2) and triplet states (j = 3, 4), ħ is the reduced Planck constant, ω is the optical frequency, τ_i is the lifetime for the singlet states and τ_{Ti} is the lifetime for the triplet states with i taking the values of 0 and 1 for singlet states and 1 and n for the triplet states and $1/\tau_{isc}$ is the intersystem crossing rate. I represent the input intensity.

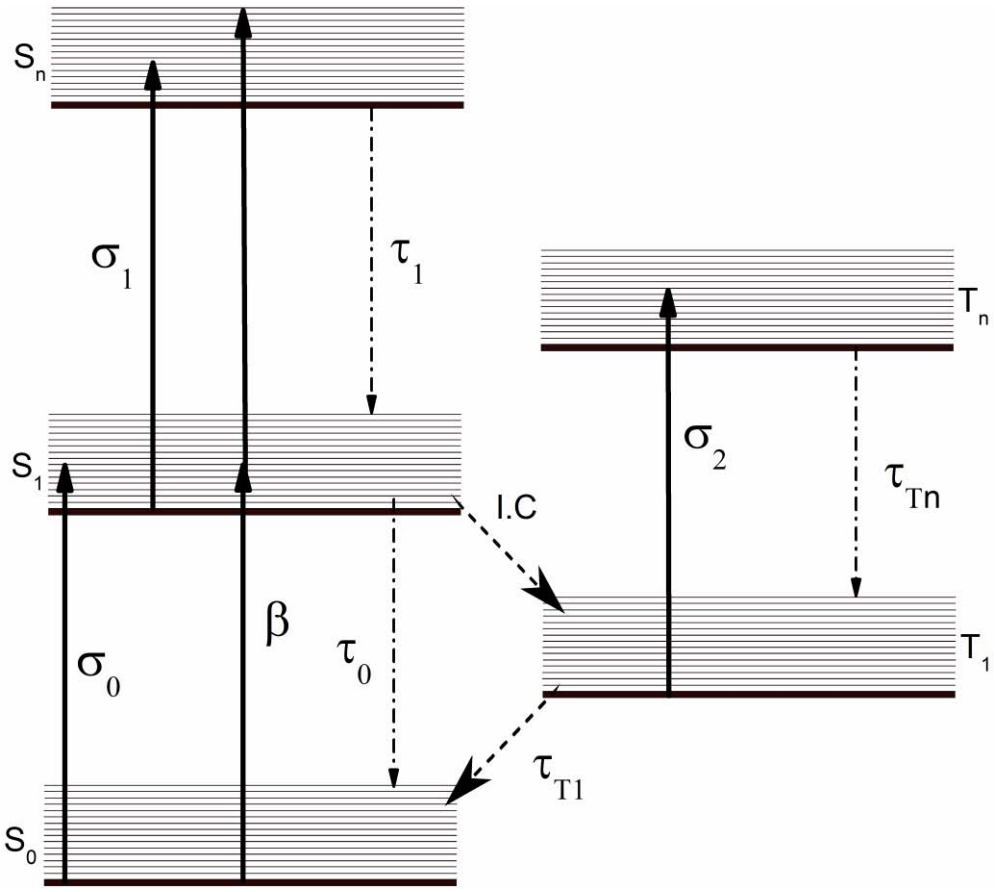

Figure 3. Five level energy level model for organic molecules.

Intensity transmitted through the sample is given by Beer's law

$$\frac{\partial I}{\partial z} = -(\sigma_0 N_0 + \sigma_1 N_1 + \sigma_2 N_3 + \beta I) I \tag{6}$$

where σ_0, σ_1, σ_2 are the ground state, excited singlet state and excited triplet state absorption cross sections, respectively.

For ultra-short pulses like ps and fs, the intersystem crossing rate ($1/\tau_{isc}$) from singlet to triplet state plays a very small role during the excitation pulse duration. Thus the generalized five level model effectively becomes three level model for these pulse durations by neglecting N_3/τ_{t1} and N_1/τ_{isc} terms in equations (1) and (2) and using $\frac{\partial N_3}{\partial t} = 0, \frac{\partial N_4}{\partial t} = 0$.

4.1.4.2 Z-scan studies with 800 nm, 110 fs pulses

Figure 3(a) shows representative open aperture scan for ZnOCPc recorded at 800 nm using ~ 110 fs pulses with a peak irradiance of 390 GW/cm^2. The femtosecond open aperture Z-scan curve shows dominant three photon absorption (3PA) process. So 3PA term was included instead of two photon absorpton (TPA) in Beer's law for fitting process. Then the Eq. 6 becomes

$$\frac{\partial I}{\partial z} = -(\sigma_0 N_0 + \sigma_1 N_1 + \sigma_2 N_3 + \alpha_3 I^2) I \qquad (7)$$

where α_3 is three photon absorption coefficient. Open circles represent the experimental data while the solid line represents theoretical fit with dominant three-photon absorption. Strong reverse saturable absorption (RSA) kind of behavior was observed in the intensity range of 250-390 GW/cm^2. Observed experimental data was fitted with the modified equations for three levels and we found the best fit was obtained with parameters listed in table 1. It is evident that 3PA is the dominant mechanism for the observed RSA kind of behavior. The three photon absorption coefficient estimated from the theoretical fitting is 38×10^{-23} cm^3/W^2. Evaluated the three photon absorption cross section (σ_3) as 1.3×10^{-79} cm^6. s^2/ Photon^2 using the relation

$\sigma_3 = \frac{(\hbar\omega)^2 \alpha_3}{N}$ where ω is the frequency of laser pulse, N is the molecular concentration and α_3 is three photon absorption coefficient. Interestingly, within these range of intensities, the samples remained stable even after long exposure to the laser irradiation. However, beyond the intensities of 390 GW/cm^2, we started noticing the sample degradation. Figure 3(b) illustrates the typical closed aperture Z-scan curve obtained for ZnOCPc with a peak intensity of 280

GW/cm^2. These curves represent normalized data obtained after division of closed aperture data with the open aperture data to eliminate the contribution of nonlinear absorption. It is apparent that ZnOCPc shows positive nonlinearity as indicated by the valley-peak structure. The closed aperture data was

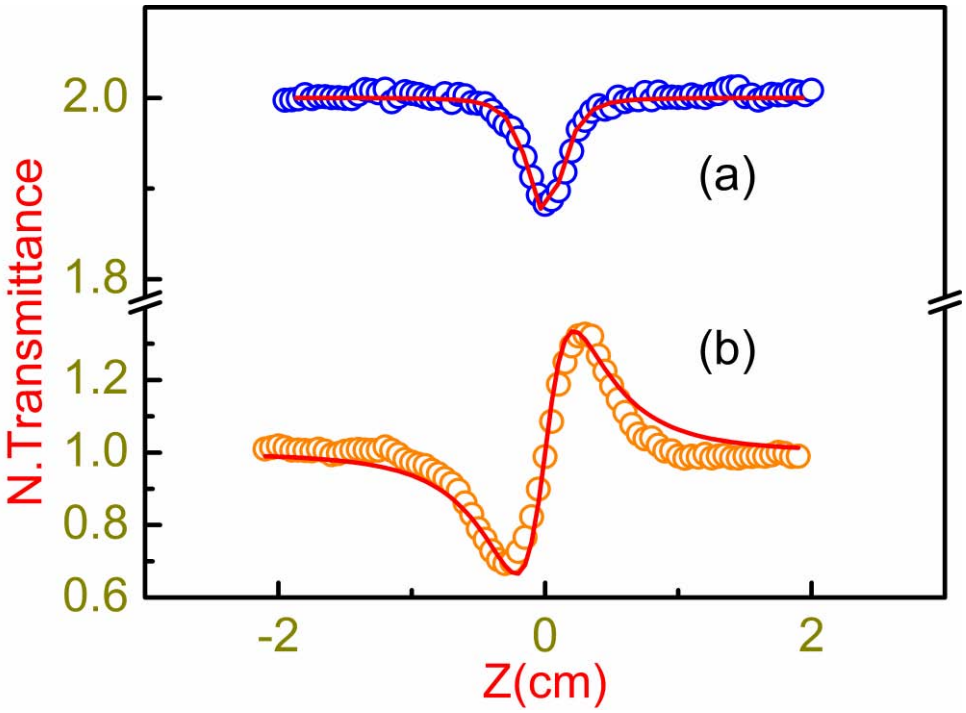

Figure 3. Open aperture and closed aperture Z-scan curves of water soluble ZnOCPc (a) for the input intensity 390 GW/cm^2 and (b) for the input intensity 280 GW/cm^2 with 800 nm, 110 fs laser pulses. Symbols represent the experimental data and solid line represents theoretical fittings.

fitted with the standard equation derived by Sheik Bahae et al [25]. The magnitude of the nonlinear refractive index n_2 evaluated was 7.5x10^{-16} cm^2/W for ZnOCPc. Estimated value of Re[$\chi^{(3)}$] from n_2 was 2.86x10^{-14} esu. The nonlinear refraction cross section [29] defined as $\delta_r = \frac{\hbar\omega k n_2}{N}$ where k is the wave number. Units of δ_r are same like TPA units, cm^4. s/photon, and 1 RGM = 10^{-50} cm^4. s/ photon. δ_r for ZnOCPc is 8.06 RGM. Optical limiting curve for ZnOCPc is shown in figure 6 (a). The sample exhibits limiting threshold (L_{th}) of 2 mJ/cm^2. The mechanism for optical limiting is predominantly three photon absorption.

4.1.4.3 Z-scan studies with 532 nm, 30 ps pulses

Figure 4 (a) shows the representative open aperture scan data of ZnOCPc obtained with 532 nm, 30 ps pluses. RSA behavior was observed for input intensity 50 GW/ cm^2. The two photon absorption coefficient estimated from theoretical fitting is 5.05 cm/GW, which is low compared with ns result due to the absence of nonlinear scattering and thermal nonlinearity observed for this sample in ps regime. Evaluated two photon absorption cross section (σ_{TPA}) is 1.04×10^{-47} cm^4. s/photon, using the relation $\sigma_{TPA} = \frac{\hbar\omega\beta}{N}$, where ω is the frequency of laser pulse, N is the molecular concentration and β is the two photon absorption coefficient.

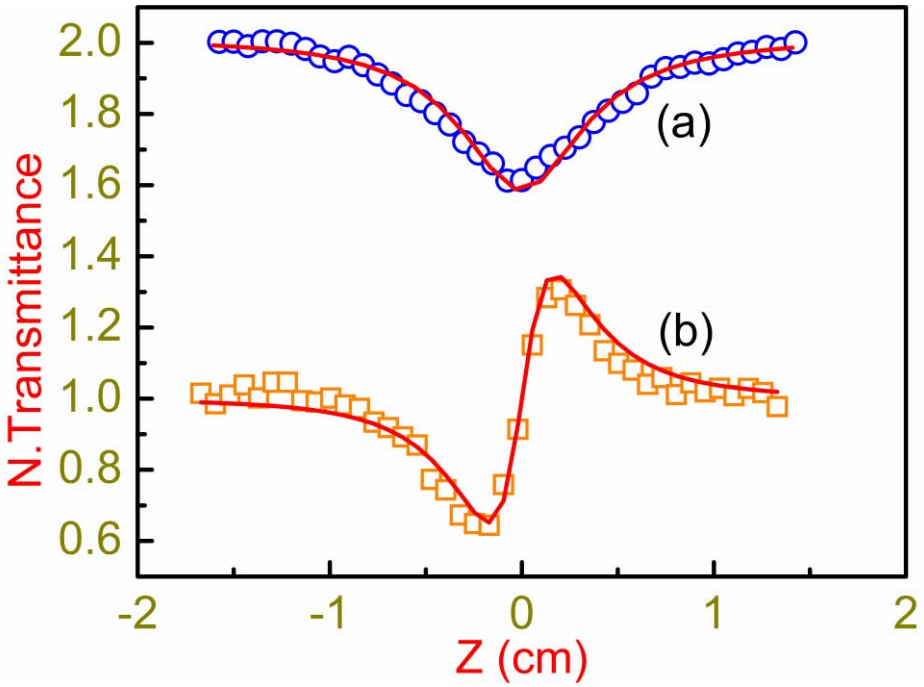

Figure 4. (a) Open aperture Z-scan curve for the input intensity 50 GW/cm^2 and (b) Closed aperture Z-scan curve for the input intensity 1.5 GW/cm^2 with 532 nm , 30 ps laser pulses.

Two-photon as well as strong excited state absorption (ESA) processes play key role in the RSA behavior. In this regime no nonlinear scattering was observed and β is from pure two-photon absorption. Figure 4(b) illustrates the typical closed aperture Z-scan curve obtained for ZnOCPc with a peak intensity of 1.5 GW/cm^2. The magnitude of the nonlinear refractive index n_2 evaluated is

$7.11x10^{-14}$ cm^2/W for ZnOCPc. Estimated value of $Re[\chi^{(3)}]$ from n_2 is $2.72x10^{-12}$ esu and $Im[\chi^{(3)}]$ is $8.21x10^{-13}$ esu. The nonlinear refraction cross section is $1.74x\ 10^3$ RGM. Optical limiting curve is shown in figure 6 (b) and sample shows a limiting threshold of 189 mJ/cm^2. The optical limiting arises predominantly from two photon absorption. Estimated magnitude of second order molecular hyperpolarizability (γ) for ZnOCPc from $\chi^{(3)}$ is 6.3×10^{-30} esu.

4.1.4.4 Z-scan studies with 532 nm, 6 ns pulses

Figure 5 (a) shows representative open aperture Z-scan curves for ZnOCPc with 532 nm, 6 ns pulses. The effective nonlinear absorption coefficient estimated from the theoretical fitting was 516 cm/GW, which includes both two-photon absorption as well as nonlinear scattering. Evaluated effective two photon absorption cross section (σ_{TPA}) is $1.07x10^{-45}$ cm^4. s/photon. RSA behavior was observed in these molecules for input intensities in the range of 20-790 MW/cm^2. These molecules exhibited a strong nonlinear absorption behavior in the nanosecond regime. It is well established that nonlinear absorption in such materials due to ns pulses has contributions from both excited singlet and/or triplet states apart from two-photon absorption depending on the excitation wavelength. The data obtained with ns pulses was fitted using rate equations from Eqs. (1)-(6).

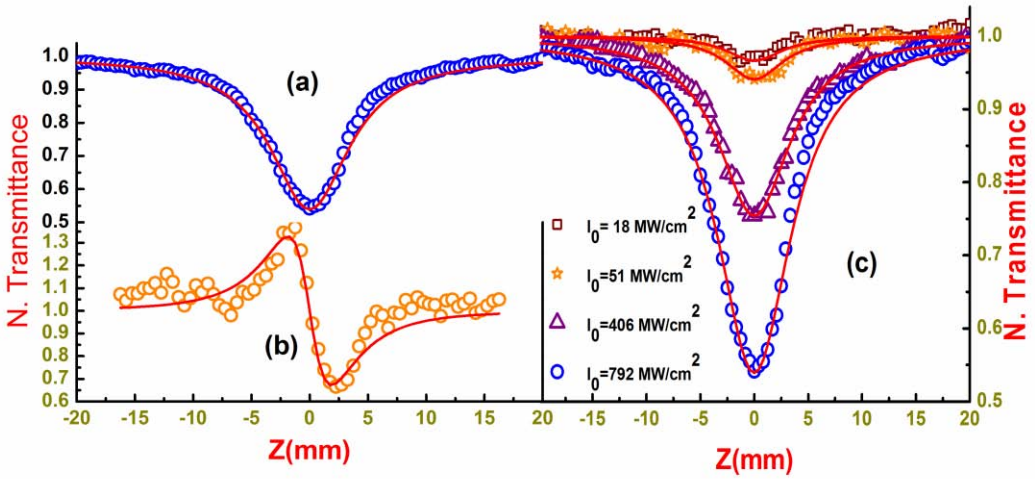

Figure 5. (a) Open aperture Z-scan curve for the input intensity 790 MW/cm^2 and (b) Closed aperture Z-scan curve for input intensity 15 MW/cm^2 and (c) Intensity dependent open aperture Z-scan curves with 532 nm, 6ns laser pulses.

The best fit produced an effective nonlinear absorption coefficient (β) of 516 cm/GW for ZnOCPc measured with a peak intensity of 790 MW/cm^2. Figure 5 (b) shows the typical closed aperture Z-scan curve obtained for ZnOCPc with a peak intensity of 15 MW/cm^2. The calculated nonlinear refractive index, n_2, is -9.05x10^{-12} cm^2/W, which is high compared to picosecond nonlinear refractive index due to contribution from thermal nonlinearity. The real and imaginary parts of third order nonlinearity for ZnOCPc were evaluated. Estimated Re[$\chi^{(3)}$] and Im[$\chi^{(3)}$] are 3.47x10^{-10} esu and 8.39x10^{-11} esu, respectively, for the ZnOCPc. Magnitude of second order molecular hyperpolarizability for ZnOCPc from $\chi^{(3)}$ is 7.9×10^{-28} esu. The nonlinear refraction cross section is 2.2x10^5 RGM. Optical limiting curve shown in figure 6 (c) and sample has limiting threshold value of 820 mJ/cm^2.

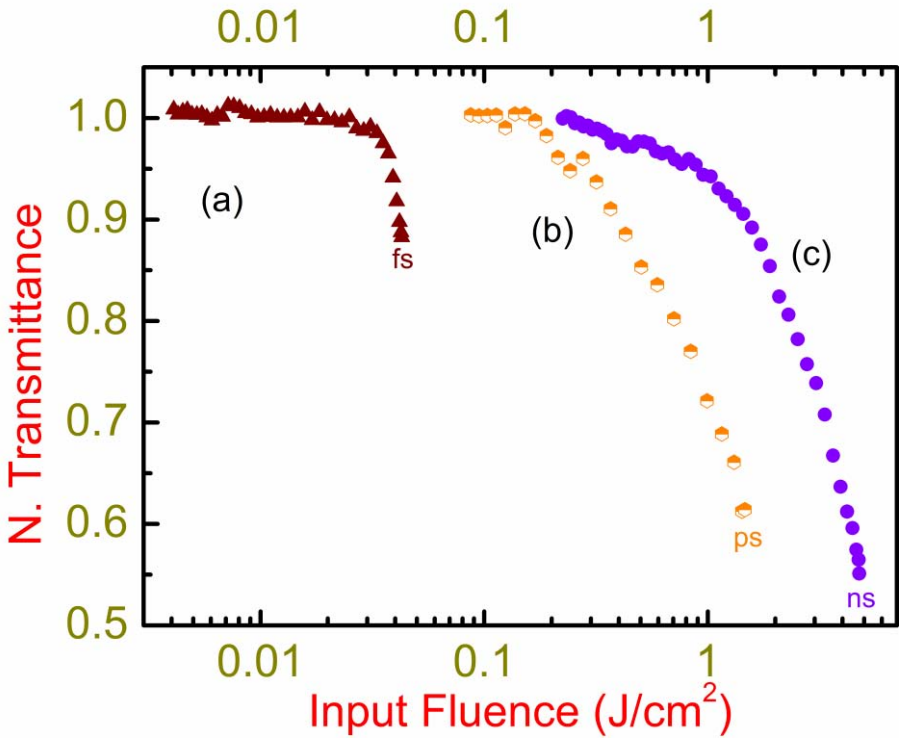

Figure 6. Optical limiting curves of ZnOCPc in water (concentration: $3x10^{-4}$ M) (a) at wavelength 800 nm with pulse duration 110 fs in femtosecond region (b) at wavelength 532 nm with pulse duration 30 ps in picosecond region and (c) at wavelength 532 nm with pulse duration 6 ns in nanosecond region.

Both TPA and ESA are found to contribute to the reverse saturable absorption and the optical limiting. ZnOCPc showing good limiting behavior in the ns, ps and fs pulse regimes and at two different wavelengths suggest that this material can act as a broad band optical limiter. Higher linear transmittance of 84 % at 532 nm and 87 % at 800 nm, low limiting threshold values and high damage threshold values of 800 MW/cm^2, 300 GW/cm^2 and 0.43 TW/cm^2 in ns, ps and fs regimes respectively, fulfil the requirements of an effective optical limiter. It also shows the significant dynamic range (ratio of damage threshold to limiting threshold) 5.9, 8.1, and 21.7 in ns, ps and fs regimes respectively. One can observe that the two-photon absorption and the three-photon absorption dominate at 532 nm and 800 nm wavelength laser excitations, respectively. Ground state and excited state parameters of different pulse regimes are shown in Table 1. Optical nonlinear

absorption in the phthalocyanines is a complex phenomena that depends on the duration of the excitation pulse as the electronic relaxation (internal conversion) from the excited singlet state, S_1, S_1 to T_1 inter-system crossing (ISC) rate, excited state absorption from S_1 to S_n states and from T_1 to T_n states depend on the time scales of observation and hence, their contributions with different pulse durations.

Technique/ Laser source	**σ_0 (10^{-19} cm^2)**	**σ_1(10^{-19} cm^2)**	**σ_1/σ_0**	**τ_{s1}**	**τ_{sn}**	**σ_{TPA} (GM)**	**δ_r (RGM)**	**n_2 (10^{-14}) cm^2/W**
Z-Scan 532 nm, 6 ns	**1.3**	**6.1**	**4.7**	**7 µs**	**3 ps**	**$1.07x10^5$**	**$2.21x10^5$**	**-905**
Z-Scan 532 nm, 30 ps	**1.3**	**2**	**1.54**	**10 ns**	**4 ps**	**$1.04x10^3$**	**$1.74x10^3$**	**+7.11**
Z-Scan 800 nm, 110 fs	**0.65**	**0.77**	**1.18**	**15 ps**	**40 fs**	**---**	**8.06**	**+0.074**
DFWM 800nm, 110 fs	**---**	**---**	**---**	**---**	**---**	**--**	**8.5**	**0.078**

Table 1. Excited state and ground state parameters σ_0, σ_1, σ_1/σ_0, τ_{s1}, τ_{sn}, two-photon absorption cross section (σ_{TPA}), nonlinear refraction cross section (δ_r) and n_2 for water soluble ZnOCPc at 532 nm in ns, ps regime and at 800 nm in fs regime.

Five level electronic structure model was used for the ns pulse excitations to take into account the S_1 to T_1 ISC rate and hence the excited state absorption of T_1 to T_n. Therefore at higher fluencies and longer pulse durations, larger excited state absorption resulting from both the S_1 and T_1 states (σ_1) compared to the ground state absorption (σ_0) lead to strong nonlinear absorption behavior. However at shorter pulse durations like ps and fs pulses, ISC contribution can be neglected

and the system can be treated as a three level system having S_0, S_1 and S_n levels. Increase in the peak powers with shorter pulse durations results in the domination of two photon absorption and three photon absorptions in the ps and fs pulse durations respectively. Thermalization due to fast vibrational relaxations and the triplet states contribute to the optical nonlinearities in the ns time regime. Measurements carried out at fs time scales and low pulse repetition rate effectively eliminates the thermal contributions and the long lived triplet state contributions. Thus, the measured third-order nonlinearities of the ZnOCPc in the femtosecond scale are 4 orders smaller than those in the nanosecond and 2 orders smaller than those in the picosecond.

4.1.4.5 Third order nonlinear optical measurements by DFWM technique

The DFWM signal was measured as a function of the laser intensity. A typical result for ZnOCPc is shown in the inset of figure 7. The cubic fit of the DFWM signal indicates the third order nature of the process. We ascertained that the origin of DFWM does not have contribution from any two-photon absorption through intensity dependent measurements. The temporal response for molecule ZnOCPc is shown in figure 7. The nonlinear responses are very fast and are of the order of 110 fs or faster. $\chi^{(3)}$ value was measured to be 3.015×10^{-14} esu. Nonlinear refractive index estimated from $\chi^{(3)}$ is 7.87×10^{-16} cm^2/ W and nonlinear refraction cross section is 8.5 RGM. The magnitude of second order hyperpolarizability γ obtained from the $\chi^{(3)}$ is 6.7×10^{-32} esu. Comparative study of β, $\chi^{(3)}$ and γ for ZnOCPc with recently reported literature is made in Table 2. Compared to other reported values in the table, ZnOCPc shows higher values of nonlinearity, which could be due to COOH peripheral substitution on eight sides resulting in large delocalization of electrons from core to peripherals. The magnitude of third-order nonlinear optical susceptibility $\chi^{(3)}$ in metallophthalocyanines varies by several orders depending on the central metal atom, crystal structure, and peripheral as well as axial substitutions [44-51]. Compared to pure zinc phthalocyanine [52], ZnOCPc shows an enhancement of the TPA coefficient values due to octa-substitution of COOH at peripheral position.

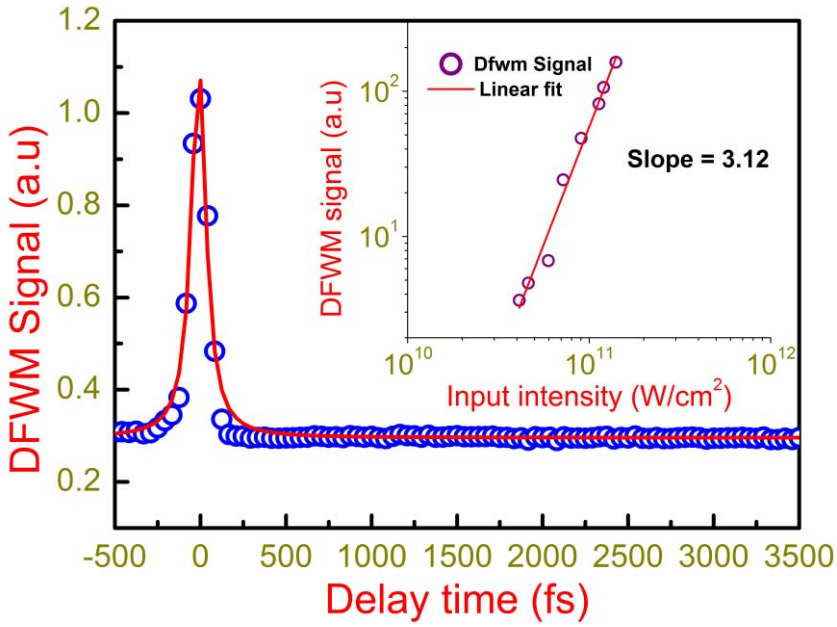

Figure 7. Temporal profile of DFWM signal of ZnOCPc in water (concentration: $3x10^{-4}$ M) as a function of beam 3 delay time and inset showing the logarithmic plot of the DFWM signal versus the total incident irradiance, at zero delay. The solid line is a best linear fit to the data, giving power dependency of $I^{3\pm0.12}$ in the femtosecond regime.

Sample	Laser details	β, cm/GW	$\chi^{(3)}$, esu	γ, esu	References
$Eu(Nc)_2$ to FePc	532 nm, ns	—	$(0.35 \text{ to } 1.86) \times 10^{-13}$	$(13 \text{ to } 55) \times 10^{-32}$	[30]
Octaalkyl Pcs and metal derivatives	532, 6 ns, 10 Hz	1.5–96	Im $(0.05 \text{ to } 3.6) \times 10^{-11}$	Im $(0.34 \text{ to } 36) \times 10^{-33}$	[31]
Gallium Pcc	532, 6 ns, 10 Hz	—	Im $(0.73 \text{ to } 1.3) \times 10^{-11}$	$(0.84 \text{ to } 1.76) \times 10^{-32}$	[32]
Zn Pc nanoparticles	532, 6 ns, 10 Hz	0.4–2	—	—	[33]
Gallium Pc dimer	532, 6 ns, 10 Hz	32–35	—	—	[34]
Gallium Pc & naphthalocyanines	532, ns	—	Im $(0.73 \text{ to } 3.9) \times 10^{-11}$	$(0.69 \text{ to } 3.84 \times 10^{-32})$	[35]
Zn Pc in polymer	532, 5 ns, 10 Hz	29–43	—	—	[36]
Alkyl Pcs	532, 6 ns, 10 Hz	420	—	—	[37]
Co Pc	532, 30 ps, 1 Hz	0.32	2.52×10^{-12}	—	[38]
Nickel Pc- HPAEK	532, 4.5 ns, 1 Hz	15.1	9.8×10^{-12}	—	[39]
Octakis-POSS substituted Cu Pc	532, 4 ns, 10 Hz	70	—	—	[40]
Double-decker Lu Pc	532, 4 ns, 10 Hz	77.6	—	—	[41]
Zn Pc	532, 4 ns, 10 Hz	14	—	—	[42]
Silicon Pcs	532, 6 ns, 10 Hz	1.1–2.3	—	—	[43]
Zinc-Octa-Corboxy Pc	532 nm, 6 ns, 10 Hz	**516**	**3.57×10^{-10}**	**7.9×10^{-28}**	Current work
			Im 8.39×10^{-11}	Im 1.86×10^{-28}	
			Re 3.47×10^{-10}	Re 7.7×10^{-28}	
	532 nm, 30 ps, 10 Hz	**5.05**	**2.84×10^{-12}**	**6.3×10^{-30}**	Current work
			Im 8.21×10^{-13}	Im 1.82×10^{-30}	
			Re 2.72×10^{-12}	Re 6.04×0^{-30}	
	800 nm, 110 fs, 1 kHz	—	**3×10^{-14}**	**0.67×10^{-31}**	Current work

Table 2. Comparison of β, $\chi^{(3)}$ and γ for ZnOCPc with various phthalocyanines studied recently

Earlier reports on γ values of other water soluble naphthalocyanines [53, 54] measured with a 0.3 ps laser exciting resonantly into the Q-band yielded a value of the order of 2.1-7.5 $x10^{-29}$ esu. In the current studies the nonlinear susceptibility was measured in the DFWM geometry at nonresonant wavelength, and at power levels where do not observe nonlinear absorption.

4.1.4.6 Figures of merit (FOM) for photonic switching applications

All optical switches require materials with low linear and nonlinear losses, large Kerr nonlinearity and ultrafast response. A convenient way to quantify the losses is to consider the appropriate merit factors formulated by Stegeman [55] for photonic switching applications. The figure of merit (FOM) factors are defined as

$$W = \left[\frac{n_2 I}{\alpha\lambda}\right] \text{ and } T = \left[\frac{\beta\lambda}{n_2}\right]$$

where I is the incident light intensity, λ is excitation wavelength, α is the linear absorption coefficient and β is the TPA coefficient. Materials which shows W > 1 and T < 1 are good candidates for photonic switching applications.

We have estimated the FOM for optical switching at 532 nm in both ns and ps pulse durations. The estimated values for W, T are 3.22, 0.06 in ns region and 2.60, 0.07 in ps region respectively. These are well within the acceptable values [55] for a photonic switching device. The combination of instantaneous nonlinear response and excellent figures of merit propels ZnOCPc as an ideal candidate for photonic switching applications.

4.1.5. Conclusions

- ✓ Obtained large third order nonlinearities in both nanosecond and picosecond regions.
- ✓ Experiments with different pulse durations reveals that the materials shows positive nonlinearity in the femto to pico second regime, while the sign is negative for the nonlinear susceptibility in ns pulse duration studies.

- ✓ Picosecond nonlinear optical coefficients are low compared to nanosecond nonlinear coefficients due to absence of thermal nonlinearity.
- ✓ Large nonlinear refraction cross section $2.21x10^{5}$ RGM, $1.74x10^{3}$ RGM and two photon absorption cross section $1.07x10^{5}$ GM, $1.0^{4}x10^{3}$ GM were observed for ZnOCPc with nanosecond and picosecond pulses respectively.
- ✓ High second order hyperpolarizability values were observed for ZnOCPc are 7.9×10^{-28}, 6.3×10^{-30} and 0.67×10^{-31} esu in ns, ps and fs regimes respectively.
- ✓ Observed good figure of merit and optical limiting properties for water soluble ZnOCPc.

4.2 Metal and metal free porphyrins

4.2.1 Introduction

Prophyrins are among most attractive macrocyclic systems for NLO applications. Porphyrins are an ubiquitous in numerous biological process that are performed or catalyzed by prophyrin containing important biological representatives such as hemes, chlorophylls and vitamin B_{12}. Porphyrins are involved in various processes such as oxygen binding, electron transfer, catalysis, light harvesting and photodynamic therapy. They uesd as optical bio sensors [56], light harvesters in solar cells [57], photosensitizers [58], mass transducers [59], ChemFET [60] and optoelectronic nose [61]. The basic structrue of the porphyrin molecule consists of four pyrrolic subunits linked by four methine bridges [62]. Among various classes of NLO materials, porphyrins appear to have unique propeties make them superior to other compounds as optical materials. Their ground state absorption is mostly confined to a few narrow regions (Soret and Q bands) allowing the high transmission in the spectral window other than these regions. Their optical properties can be modulated by changing the metal centre, its oxidation state, the type of axial ligands, or the substituents at the periphery of porphyrin molecule without altering its chemical stability. Variety of porphyrin molecules have been studied extensively for both second order and third order NLO properties. Large first order hyperpolarizability (β) and second order hyperpolarizabilty (γ) for variety of porphyrins were observed through different techniques (EFISH, HRS, Z-SCAN, DFWM, OKE, THG) in recent years [63]. Functonalizaton of porphyrins with Polymer, C_{60}, CNTs, Graphene oxide enhances NLO response as observed in recent reports [64-68]. This chapter contains synthesis of porphyrins and different metal substitution at porphyrin central ring leading to change in optical properties.

4.2.2. Synthesis

4.2.2.1 ***Synthesis of 5-(p-hydroxyphenyl)-10,15,20-tritolylporphyrin [H_2MHTP]***

This compound was synthesized from the corresponding 5-(p-methoxyphenyl)-10,15,20-tritolylporphyrin [H_2MMTP] by Adler's method [69]. 4-methoxy benzaldehyde (4 g, 33 mmol), 4-methylbenzaldehyde (7.7 mL, 66 mmol) and pyrrole (6.8 mL, 99 mmol) was added to 250 mL of propionic acid and brought to reflux for 2 h and allowed to cool overnight. The dark purple colour product was filtered and washed thoroughly with methanol until the filtrate became clear and the crude product was purified through column chromatography. The compound H_2MHTP was obtained by hydrolysis of methoxy group using the known procedure as described earlier [70].

4.2.2.2 ***Synthesis of Zn(II)MHTP and Cu(II)MHTP***

This complex was obtained by refluxing H_2MHTP (0.5 mg, 0.07 mmol) in 50 ml of dimethylformamide with saturated solution of M(II) acetate (M = Zn, Cu) in methanol for 1 h. The completion of the reaction was checked by thin layer chromatography and optical absorption spectrum. The reaction mixture was concentrated and purified through silica gel column using chloroform as eluant. Yield 0.45 g (90 %); IR (KBr): 3019, 2915, 1023 cm^{-1}.

4.2.2.3 ***Synthesis of Sn(IV)MHTP(OH)$_2$***

$SnCl_2.2H_2O$ (0.20 mg, 0.07 mmol) and H_2TPP (0.5 mg, 0.07 mmol) and sodium acetate (100 mmol) were refluxed in 100 mL of glacial acetic acid for 6 h. An additional amount of 10 mmol of $SnCl_2.2H_2O$ was added to the reaction mixture and refluxed for additional 6 h. The reaction mixture was cooled to room temperature and the reaction mixture was concentrated to dryness under vacuum at 30 ^oC. The residue was dissolved in small volume of chloroform and purified over silica gel column using 2 % chloroform in benzene. The eluant was filtered and dried. The residue was dissolved in 1:1 mixture of chloroform and acetone. This mixture was treated with few ml of concentrated HCl and it was stirred for 1 h. The final solution was washed with water and dried under vacuum, the complex was further recrystallised from a 1:1 mixture of chloroform and petroleum ether. Yield: 60 %. A similar methodology was adopted for the synthesis of VO(II)MHTP by taking $VO(acac)_2$ and H_2MHTP as the starting

materials. We termed Zn(II)MHTP, Cu(II)MHTP, VOMHTP, Sn(IV)MHTP$(OH)_2$ as Zn porphyrin, Cu porphyrin VO porphyrin and Sn porphyrin, respectively throughout the thesis.

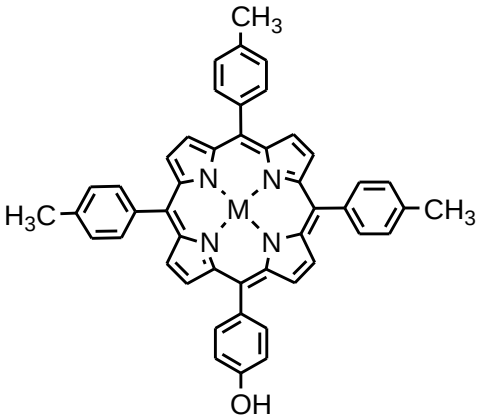

where M= 2H, Zn, Cu,Vo, Sn(IV)OH_2

molecular weights:

M=2H, M.Wt: 672
M=Zn, M.Wt: 736
M=Cu, M.Wt: 733
M=Vo, M.Wt: 736
M=Sn(IV)OH2 M.Wt: 824

Figure 8. Chemical structure of porphyrins

4.2.3 Structural and spectroscopic characterization

4.*2.3.1* Field emission-scanning electron microscopy (FE-SEM) studies

The scanning electron micrographs for Cu and Zn porphyrins are shown in the figure 9. Surface of of the porphyrins are smooth and these are macro molecules type extended π conjugated systemes.

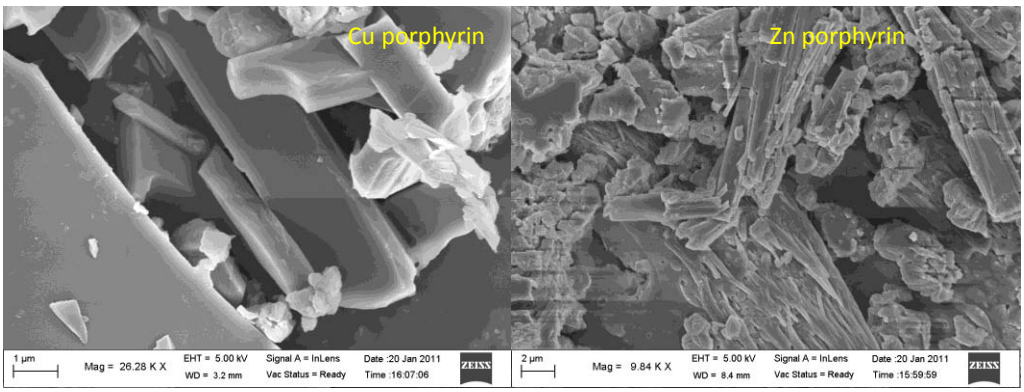

Figure 9. FE-SEM images of Cu and Zn porphyrin molecules

4.2.3.2 Optical absorption studies

The optical absorption spectra of porphyrins is shown in the figure 10. Different metal substitutes in the core of the porphyrin ring show changes in the optical absorption spectra. One can see red shift in the absorption spectra with different metal

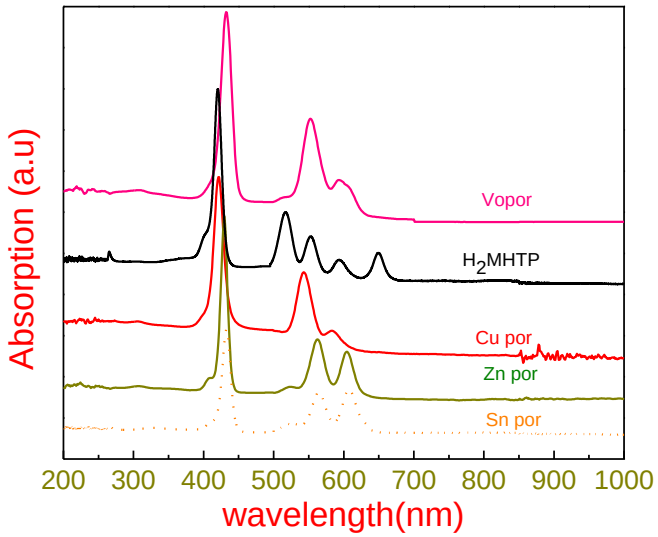

Figure 10. UV-visible absorption spectra of copper porphyrin, zinc porphyrin composite, tin porphyrin composite, VO porphyrin and H_2MHTP in DMF. The absorbance in the region 500 nm to 890 nm amplified by 10 times for clear visibility.

substitutions. This red shift can be observed from metal free porphyrin H_2MHTP→VO porphyrin→Cu porphyrin→Zn porphyrin to Sn porphyrin. The difference in optical absorption from metal to metal free porhyrins can be observed as a reduction of peaks in Q-band region. Linear transmittances of H_2MHTP, VO porphyrin, Cu porphyrin, Zn porphyrin and Sn porphyrin were 82 (0.81), 79 (1.05), 97 (0.13), 87 (0.61) and 84 % (0.77) respectively at 532 nm and 92 (0.37), 92 (0.37), 91 (0.40), 93 (0.32) and 92 % (0.37) respectively at 800 nm wavelength (with the corresponding optical densities given in brackets). The absorbance in the region 500 nm to 900 nm (figure 10) is magnified by a factor of 10 for the sake of clarity.

4.2.3.3 Time-correlated single photon counting (TCSPC) studies

The fluoroscence life time decay profiles were presented in figure 11. The fluoroscence life time of porphyrins show single exponential decay with life times shown in the table 3.

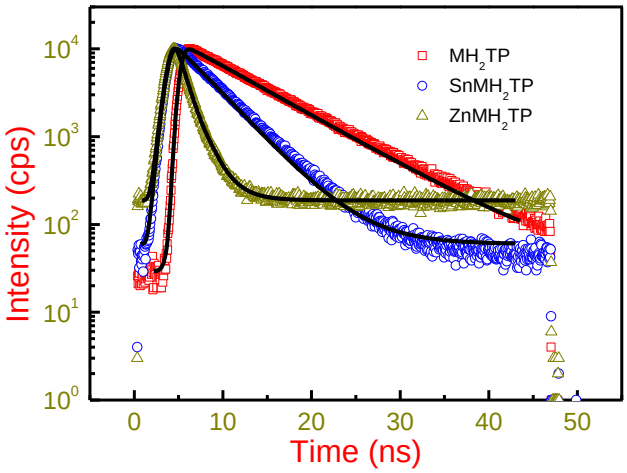

Figure 11. The fluorescence lifetime decay of various porphyrin molecules. Symbol represents experimental data and solid line represents theoretical fit.

The steady state emission of these poprhyrins are discussed in the chapter 5.

porphyrin	absorption		Steady state emission		Lifetime (ns)
	Soret Band (nm)	Q-band (nm)	λ_{ex} (nm)	λ_{em} (nm)	
H_2MHTP	420	517,553, 594,650	420	650, 718	9.2
Zn porphyrin	429	563, 605	420	472, 592, 652	1.4
Cu porphyrin	421	544,583	420	594, 649	----
Sn porphyrin	433	564, 609	420	483, 599,654	4.1
VO porphyrin	432	553, 594	420	593, 647	----

Table 3. Optical absorption and Emission maxima, Lifetime of singlet state of pure porphyrin molecules.

4.2.4 NLO studies

A frequency doubled Nd :YAG laser pulses with 6 ns pulse duration and a repetition rate of 10 Hz at a 532 nm wavelength was used for Z-scan experiment. Porphyrins are taken as solutions in DMF for the experimental studies. Open aperture Z-scan studies were carried out by focusing the input beam on to the sample using a lens of 120 mm focal length forming 27 μm spot size at the focus. The peak intensity, I_{00}, estimated at the focus in Z-scan experiment was 300 MW/cm^2. Figure 12 shows typical open aperture Z-scan curves for Cu porphrin, Zn porphyrin, metal free poprhyrin, Sn porphyrin and VO poprhyrin molecules. Curves show RSA type behavior of nonlinear optical absorption. To understand the experimental observations, we followed the rate equation model as mentioned in the section 3.1. Effective excited state absorption was measured by combaining singlet excited state and triplet state absorption. It is well established that nonlinear absorption in such materials due to ns pulses has contributions from both excited singlet and/or triplet states apart from two-photon absorption depending on the excitation wavelength. From the theoretical fittings, β value for porphyrins was observed in the range of 130 to 370 cm/GW. Zn porphyrin has

shown highest TPA coefficent as well as excited state absorption crossection over the other poprhyrin molecules. Figure of merit (FOM) tells the best material for optical limiting, the calculated FOM values for porphyrins lies from 17 to 26 and reasonbly good for optical limiting applications. Optical nonlinear parameters of individual porphyrin molecules are tabulated in Table 4.

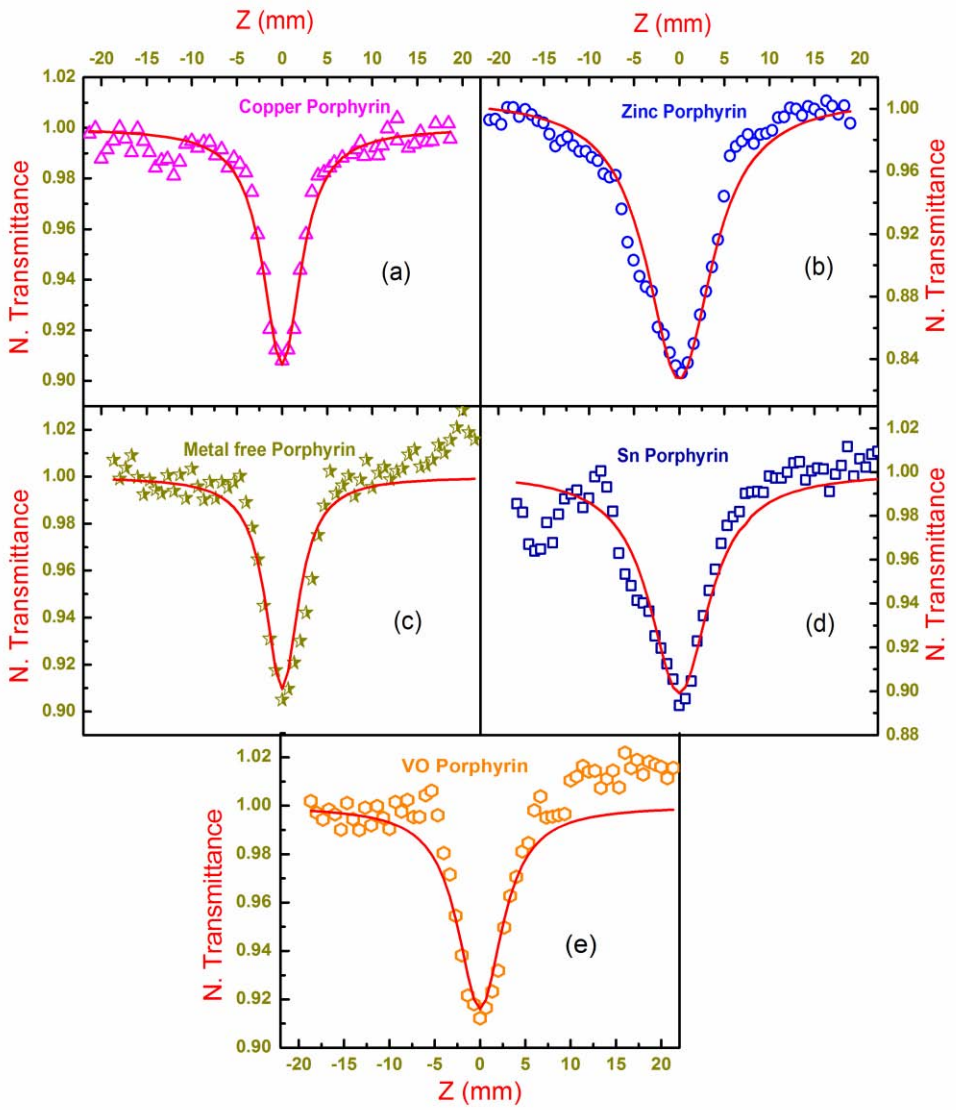

Figure 12. Open aperture Z-scan curves for (a) Cu porphyrin, (b) Zn porphyrin, (c) metal free poprhyrin, (d) Sn porphyrin and (e) VO porphyrin molecules of concentration 5×10^{-5} M.

Sample	β (cm/GW)	$\sigma_1(cm^2) \times 10^{-19}$	FOM ($\sigma_{1/} \sigma_0$)
Cu porphyrin	132	79	19.75
Zn porphyrin	366	113	25.68
Metal free porphyrin	159	98	20.9
Sn porphyrin	168	102	22.7
VO porphyrin	142	84	17.5

Table 4. Excited state and ground state parameters of Cu porphyrin, Zn porphyrin, metal free poprhyrin, Sn porphyrin and VO porphyrin molecules at a concentration of 5×10^{-5} M.

Based on their good nonlinear optical coefficents, they were further used to functionlize with graphene oxide to achive enhanced optical nonlinear absorption coefficents as well as optical limiting behavior. This is dicussed in the chapter 5.

4.3 Conclusions

- ✓ Various porphyrin molecules were studied for NLO properties
- ✓ Shift in the absorption spectra with different metal substitutions was observed.
- ✓ Porphyrin molecules at a concentration of 5×10^{-5} M have shown good optical nonlinear absorption coefficients
- ✓ Resonably good FOM vales was observed for porphyrin molecules

4.4 References

1. Braun A and Tcherniac J, Ber. Dtsch. Chem. Ges., **40**, 2709 (1907).

2. Barnett CE, Ind. Eng. Chem., **41** (2), 272 (1949).

3. Morimune T, Kajii H, and Ohmori Y, IEEE Photon. Tech. Lett., **18** 2662 (2006).

4. Gu D, Chen Q, Tang X, Gan F, Shen S, Liu K and Xu H, Opt. Commun., **121,** 125 (1995).

5. Hiramotoa M, Kumaokaa H and Yokoyama M, Synth. Met., **91,** 77 (1997).

6. Wojdyla M, Bala W, Derkowska B, lukasiak Z, Czaplicki R, Sofiani Z, Seignon SD and Sahraoui B, Nonlinear Optics and Quantum Optics, **35**, 103(2006).

7. Rojo G, Hierro A, Diaz-Garcia MA, Agullo-Lopez F, del Rey B, Sastre A, and Torres T, Appl. Phys. Lett., **70**, 1802 (1997).

8. Blochwitz J, Pfeiffer M, Fritz T, and Leo K, Appl. Phys. Lett., **73,** 729 (1998).

9. Kao PC, Chu SY, Liu SJ, You ZX, and Chuang CA. J. Electrochem. Soc., **153**, H122 (2006).

10. Reddy PY, Giribabu L, Lyness Ch, Snaith HJ, Vijayakumar Ch, Chandransekharam M, Lakshmikantam M, Yum J-H, Kalyanasundaram K, Gratzel M and Nazeeruddin M Angew. Chem. Int. Ed., **46,** 373 (2007).

11. Xie D, Pan W, Jiang DY, Li RY, Mater. Lett., **57**, 2395 (2003).

12. Liu Y, Shigehara K, Hara M, Yamada A, J. Am. Chem. Soc., **113**, 440 (1991).

13. Gaffo L, Goncalves D, Dhanabalan A, Moreira CW, Oliveria NO Jr, Synth. Met., **124,** 351 (2001).

14. Henari FZ, J. Opt. A: Pure Appl. Opt., **3**, 188 (2001).

15. Torre G, Vazquez P, Agullo-lopez F and Torres T, Chem. Rev., **104,** 3723 (2004).

16. Ben-Hur E, Oetjen J, Horowitz B, Photochem. Photobiol., **65,** 456 (1997).

17. Minnock A, Vernon DI, Schofield J, Griffiths J, Parish JH, Brown SB, J. Photochem. Photobol. B, **32,** 159 (1996).

18. Lopez T, Ortiz E, Alvarez M, Navarrete J, Odriozola JA, Ortega FM, Mozo EAP, Escobar P, Espinoza KA and Rivero IA, Nanomedicine, **6,** 777 (2010).

19. Angelica MG, Alarcon E, Munoz M, Scaiano JC, Edwards AM and Lissi E, Photochem. Photobiol. Sci., **10**, 507 (2011).

20. Dini D, Barthel M, Schneider T, Ottmar M, Verma S, Hanack M, Solid State Ionics, **165**, 289 (2003).

21. Qu S, Gao Y, Zhao C, Wang Y, Fu S, Song Y, Wang D, Qiu J, Zhu C, Chem. Phys. Lett., **367**, 767 (2003).

22. Fitzsimmons VG, Merker RL, Singleterry CR, Ind. Eng. Chem., **44** (3), 556 (1952).

23. Wormald G, Spengeman WF, Ind. Eng. Chem., **44,** (5), 1104 (1952).

24. Dahlen MA, Ind. Eng. Chem., **31,** (7), 839 (1939).

25. Sheik-Bahae M, Said AA, Wei T, Hagan DJ, and Van Stryland EW, IEEEJ. Quantum Electron., **26,** 760 (1990).

26. Prabhakar Ch, Bhanuprakash K, Rao VJ, Bala murali krishna M, Rao DN, J. Phys. Chem. C, **114,** 6077 (2010).

27. Kasim Sener M, Gul A and Kocak MB, J. Porphyrins and Phthalocyanines, **7**, 617 (2003).

28. Rao SV, Narayana Rao D, Akkara JA, DeCristofano BS and Rao DVGLN, Chem. Phys. Lett., **297,** 491 (1998).

29. Balu M, Padilha LA, Hagan DJ, Stryland EV, Yao S, Belfield K, Zheng S, Barlow S and Marder S, J. Opt. Soc. Am. B., **25**, 159 (2008).

30. Unnikrishnan KP, Thomas J, Nampoori VPN, Vallabhan CPG, Chem. Phys., **279,** 209 (2000).

31. Auger A, Blau WJ, Burnham PM, Chambrier I, Cook MJ, Isare B, Nekelson F and O'Flaherty SM, J. Mater. Chem., **13,** 1042 (2003).

32. Chen Y, O'Flaherty SM, Hanack M and Blau WJ, J. Mater. Chem., **13,** 2405 (2003).

33. Nitschke C, O'Flaherty SM, Kroll M, Doyle JJ, Blau WJ, Chem. Phys. Lett., **383**, 555 (2004).

34. Bertagnolli H, Blau WJ, Chen Y, Dini D, Feth MP, O'Flaherty SM, Hanack M and Krishnan V, J. Mater. Chem., **15**, 683 (2005).

35. Chen Y, Hanack M, Araki Y and Ito O, Chem. Soc. Rev., **34,** 517 (2005).

36. Ostuni R, Larciprete MC, Leahu G, Belardini A, Sibilia C, and Bertolotti M, J. Appl. Phys., **101,** 033116 (2007).

37. Kumar RSS, Rao SV, Giribabu L, Rao DN, Chem. Phys. Lett., **447**, 274 (2007).

38. Derkowska B, Wojdyła M, Bała W, Grote JG, Krupka O, Kajzar F, and Sahraoui B, J. Appl. Phys., **101,** 083112 (2007).

39. Wang D, Zhang S, Zhang Y, Wang H, Mu J, Wang G and Jiang Z, Dyes and Pigments, **79**, 217 (2008).

40. Ceyhan T, Yuksek M, Yaglıoglu HG, Salih B, Erbil MK, Elmalı A and Bekaroglu O, Dalton. Trans., 2407 (2008).

41. Saydam S, Yılmaz E, Bagcı F, Yaglıoglu HG, Elmalı A, Salih B, and Bekaroglu O, Eur. J. Inorg. Chem., 2096 (2009).

42. Ozdag MA, Ceyhan T, Unver H, Elmali A, Bekaroglu O, Opt. Commun., **283,** 330, (2010).

43. Ishii K and Sakai N, phys. Chem. Chem. Phys., **12**, 15354 (2010).

44. Nalwa HS, Adv. Mater., **5,** 341 (1993).

45. Ho ZZ, Ju CY, and Hetherrington III WM, J. Appl. Phys., **62**, 716 (1987).

46. Shirk JS, Lindle JR, Bartoli FJ, Hoffman CA, Kafafi ZH, and Snow AW, Appl. Phys. Lett., **55**, 1287 (1989).

47. Grund A, Kaltbeitzel A, Mathy A, Schwarz R, Bubeck C, Verme-hren P, and Hanack M, J. Phys. Chem., **96,** 7450 (1992).

48. Nalwa HS and Kakuta A, Thin Solid Films, **254,** 218 (1995).

49. Terasaki A, Hosoda M, Wada T, Yamada A, Sasabe H, Garito AF,and Kobayashi T, Nonlinear Opt., **3,** 161 (1992).

50. Wang NQ, Cai YM, Helfin JR, and Garito AF, Mol. Cryst. Liq. Cryst., **189,** 39 (1990).

51. Shirk JS, Pong RGS, Flom SR, Heckmann H, and Hanack M, J. Phys. Chem. A, **104,** 1438 (2000).

52. Santhi A, Namboodiri VV, Radhakrishnan P, and Nampoori VPN, J. App.Phy., **100,** 053109 (2006).

53. Fu G, Kasatani K, Arita E, Okamoto H, Takenaka S, ITE Lett., **4,** 628 (2003).

54. Fu G, Yoda T, Kasatani K, Okamoto H, Takenaka S, Synthetic Metals, 155, 68 (2005).

55. Gomez LA, de Araujo CB, Messias DN, Misoguti L, Zilio SC, Nalin M and Messaddeq Y, J. Appl. Phys., **100,** 116105 (2006).

56. Dmitry B. papkovsky, Sensors and Actuators B, **11,** 293 (1993).

57. Wayne M. Campbell, Anthony K. Burrell, David L. officer, Kenneth W. Jolley, Coordination chemistry reviews, **248,** 1363 (2004).

58. James R. Darwent, Peter Douglas, Anthony Harriman, George Porter and Marie-Claude Richoux, Coordination Chemistry Reviews, **44**, 83 (1982).

59. J. Brunink, C. Di Natale, F. Davide, F. Bungaro, A. D'Amico, R. Poalesse, T. Boschi, M. Faccio, G. ferri, Analytica Chemical Acta, **325,** 53 (1996).

60. C. Gui, L. Sun, T. Zhang, T. Li, Thin Solid Films, **284,** 863 (1996).

61. Corrado Di Natale, Danio Salimbeni, Roberto Poalesse, Antonella Macagnano, Arnaldo D'Amico, Sensors and Actuators B, **65,** 220 (2000).

62. Mario Calvete, Guo Ying, Michael Hanack, Synthetic Metals, **141,** 231 (2004).

63. Mathias O. Senge, Marijana Fazekas, Eleni G. A. Notaras, Werner J. Blau, Monika Zawadzka, Oliver B. Locos , Eimhin M. Ni Mhuircheartaiagh, Adv. Mater., **19,** 2737 (2007).

64. Thomas E. O. Screen, Katrina B. Lawton, G. Scott Wilson, Nicole Dolney, Radu Ispasoiu, Theodore Goodson III, Simon J. Martin, Donal D. C. Baradley and Harry L. Anderson, J. Mater. Chem., **11,** 312 (2001).

65. Zhi-Bo Liu, Jian-Guo Tian, Zhen Guo, Dong-Mei Ren, Feng Du, Jian-Yu Zheng, and Yong-Sheng Chen, Adv. Mater., **20**, 511 (2008).

66. Yanfei Xu, Zhibo Liu, Xiaoliang Zhang, Yan Wang, Jianguo Tian, Yi Huang, Yanfeng Ma, Xiaoyan Zhang, and Yongsheng Chen, Adv. Mater. **21**, 1275 (2009).

67. M. Bala Murali Krishna, V. Praveen Kumar, N. Venkatramaiah, R. Venkatesan, and D. Narayana Rao, App. Phys. Lett. 081106 (2011).

68. M. Bala Murali Krishna, N. Venkatramaiah, R. Venkatesan and D. Narayana Rao, J. Mater. Chem., **22**, 3059 (2012).

69. A. D. Adler, F. R. Longo, J. D. Finarelli, J. Goldmacher, J. Assour and L. Korsakoff, J. Org. Chem., **32,** 476 (1967).

70. N. Venkatramaiah and R. Venkatesan, Solid State Sci., **13**, 616 (2011).

Chapter -V

LINEAR, NONLINEAR OPTICAL AND SPECTROSCOPIC PROPERTIES OF GRAPHENE BASED HYBRID MATERIALS

Abstract

This chapter contains three sub-chapters; (1) Graphene oxide-(Cu, Zn, Sn, VO, H_2) porphyrin, (2) Graphene oxide-Semiconductor (ZnO, TiO_2) nanoparticles and (3) Graphene oxide-metal (Ag, Au) nanoparticles. First sub chapter describes the structure, spectroscopic, photo-physical and nonlinear optical studies of covalently functionalized novel graphene oxide – [Cu, Zn, Sn, H_2 (metal free), VO] porphyrin composites. The composites are characterized by field enhanced scanning electron microscopy (FE-SEM), micro-Raman, optical absorption, Fourier transform infrared (FT-IR), steady state and time resolved fluorescence spectroscopic techniques. Nonlinear optical absorption studies of graphene oxide-porphyrin composites are investigated using Z-scan technique at 532 nm with nanosecond (ns) and 800 nm with femtosecond (fs) laser pulses. Second sub chapter describes the novel materials of graphene oxide (GO) -ZnO/TiO_2 nanoparticles for photonics, and their synthesis, spectroscopic and optical characterizations. Transmission electron microscopy, X-ray diffraction, micro-Raman, Fourier transform infrared spectroscopy, and ultraviolet-visible absorption spectrum results demonstrated the GO-ZnO/TiO_2 nanoparticles are successfully conjugated. The functionalization of graphene oxide with ZnO/TiO_2 nanoparticles is expected to lead large improvement of optical property in the nonlinear regime. The functionalized graphene oxide-semiconductor nanoparticle composite exhibits reverse saturable absorption due to dominant two-photon absorption. The results show that graphene oxide composite is a promising candidate for practical and efficient photonic material for broadband optical limiting. Sub chapter (3) describes the nonlinear optical properties of graphene oxide-metal (Ag, Au) nanoparticles and

their synthesis via chemical and laser irradiation methods. We describe a process of attachment of Ag/Au nanoparticles to graphene oxide in the presence polyvinyl alcohol (PVA) by laser irradiation method. Simultaneous formation of nanoparticles and attachment to the GO through physical adsorption/chemical modification takes place in this process. Structural morphology studies are done by SEM and TEM. These studies confirm the attachment of metal nanoparticles to graphene oxide. Nonlinear optical absorption and optical limiting studies for graphene-metal nanoparticles are carried out by Z-scan technique. Better optical limiting behavior was observed for these composites in both 532 nm and 1064 nm wavelength laser excitations. Nonlinear optical results are compared among chemically prepared graphene oxide-metal nanoparticle composites and laser irradiated synthesis of graphene oxide-metal nanoparticles.

5.1 Graphene oxide-(Cu, Zn, Sn, VO, H_2) porphyrins

5.1.1 Introduction

Graphene, a single 2D carbon sheet having sp^2 carbon atoms forming a honeycomb lattice, initiated enormous scientific interest since its discovery [1]. Their extraordinary electric, thermal and mechanical properties take it ahead of other materials in terms of applications [2-4]. It was also predicted to be a plausible material for the construction of next-generation flexible solar-energy-conversion and optoelectronic devices that are low-cost, highly-efficient, thermally stable, environmentally friendly and lightweight [5]. Graphene has shown many unique properties like quantum hall effect, good optical transparency, high Young's modulus, high carrier mobility and excellent thermal conductivity. Various forms of graphite, nanotubes and fullerenes can be viewed as derivatives of graphene. Despite many potential applications that graphene promises to offer, processability of graphene is of critical importance in facilitating its integration with substrates and materials to ensure the stability and to preserve the integrity of the graphene materials. Hence, the attention is focussed on the functionalization of graphene to improve its solubility/processability in both water and organic solvents [6]. Anchoring of different types of nanoparticles like Pd, Ag, Pt on reduced graphene oxide with controllable size exhibit excellent performance in various oxidation reactions [7,8]. The covalent and non-covalent functionalization of graphene with different types of oligothiophenes exhibits high mobility and superior optical limiting effect, better than that of the benchmark optical limiting material C_{60} [9]. Different types of covalently linked porphyrin/phthalocyanines-graphene hybrids exhibit remarkable competitive entry into the realm of light harvesting and solar energy conversion materials. Recent studies of functionalized graphene hybrid materials exhibits good nonlinear optical (NLO) absorption behavior with their high values of coefficients in ns and fs time scale regimes [11-15]. These properties make graphene an ideal photonic and optoelectronic material. It has been shown that porphyrins have many potential applications in optoelectronics, nonlinear optics [16], and harvesters in solar cells, photodynamic therapy and

optical limiting. Porphyrins and graphene having large π-electron conjugation are ideal to fulfill the requirement of a perfect nonlinear material. Through the conjugation of graphene with porphyrins, we have succeeded in enhancing the NLO coefficients of few graphene-porphyrin composites [10]. Since, Porphyrins/metallo porphyrins have strong electronic transitions in the visible and near infrared, their energies can be shifted by chemically modifying the ring or by changing the coordinated metal or both. Metal substituted porphyrins have shown better third order NLO properties than metal free porphyrins [17-23]. Therefore, it is timely and important to prepare various types of novel metallo-porphyrins and modified porphyrins covalently linked to graphene for better optoelectronic and NLO materials. In this context, we explored our investigations on synthesis of novel covalently graphene oxide with different metallo-porphyrins. In this sub chapter, we explored the NLO properties of graphene oxide with various metal porphyrins and metal free porphyrin in the fs regime and compared it with the long duration ns pulse excitations. We have observed that metal free porphyrin with graphene oxide shows enhanced nonlinear absorption properties compared to graphene oxide with metal porphyrins in ns time scales. Unlike in nanosecond time scale results, we have observed saturable absorption (SA) behavior in the fs open aperture Z-scan experiment. Absorption spectrum revealed that this could be due to low density of states at this wavelength. Therefore these graphene oxide composites can find an application also as saturable absorbers in pulse shaping application.

5.1.2 Experimental details and results

5.1.2.1 Synthesis

5.1.2.1.1 Synthesis of 5-(p-hydroxyphenyl)-10,15,20-tritolylporphyrin [H_2MHTP]

The compound H_2MHTP was obtained by hydrolysis of methoxy group using the known procedure as described earlier [25]. Synthesis procedure for this compound is briefly explained in the chapter 4, section 4.2.2.1.

5.1.2.1.2 Synthesis of Zn(II)MHTP and Cu(II)MHTP

For these compounds synthesis procedure is briefly explained in chapter 4, section 4.2.2.2.

5.1.2.1.3 Synthesis of Sn(IV)MHTP(OH)$_2$ and VO(II)MHTP

For these compounds synthesis procedure is briefly explained in chapter 4, section 4.2.2.3.

5.1.2.1.4 Synthesis of graphene oxide (GO) from graphite

Graphene oxide was prepared using a modification of Hummers and Offeman's method [26-28]. Briefly in a typical reaction, 1g graphite, 1g $NaNO_3$, and 50 mL H_2SO_4 are stirred together in an ice bath. $KMnO_4$ (3 g) was slowly added while stirring, and the rate of addition was controlled to prevent the mixture temperature from exceeding 20 ^oC. The mixture was then transferred to a 35 ^oC water bath and stirred for about 1h, forming a thick paste. Subsequently, 50 mL de-ionized water was added gradually and the temperature was raised to 98 ^oC. The mixture was further treated with 150 mL de-ionized water and 10 mL 30 % H_2O_2 solution. The warm solution was then filtered and washed with de-ionized water until the pH was 7 and dried at 65 ^oC under vacuum.

5.1.2.1.5 Synthesis of GO-COOH

0.5 g of graphene oxide (GO) was loaded in a 100 mL round-bottomed flask and 50 mL de-ionized water was added and stirred for 1h and sonicated for 30 min. To the resulting solution 5 mL of 50% hydrazine hydrate was gradually added and refluxed at 100 ^oC for 4h. The resulted solution was filtered and washed thoroughly with anhydrous tetrahydrofuron (THF) and dried under vacuum for 24 h.

5.1.2.1.6 Synthesis of GO-COCl

GO-COOH (0.5 g) was suspended in $SOCl_2$ (30 mL) and 5 mL of DMF was added and refluxed at 70 ^oC for 24 h under nitrogen atmosphere. The resultant solution was filtered and washed with anhydrous THF and dried under vacuum yielding acylated graphene oxide (GO-COCl) (0.4953 g).

5.1.2.1.7 Synthesis of covalently attached porphyrin graphene oxide hybrids

A mixture of GO-COCl (30 mg) and H_2MHTP (60 mg) are taken in 100 mL round bottom flask and 3 mL of triethylamine and 15 mL of DMF was added and heated to 80 ^oC for 72 h under nitrogen atmosphere and an additional 6 h with intermittent sonication to give a homogeneous black dispersion. After the reaction, the solution was cooled to room temperature, and then poured into diethyl ether (300 mL) to precipitate the product. The precipitate was collected by centrifuging at 8000 rpm for 0.5 h. The supernatant which contained dissolved H_2MHTP was discarded and the precipitate was washed thoroughly. By adding another 100 mL of diethyl ether, the mixture was sonicated for 5 min and then centrifuged at 8000 rpm for 0.5 h to collect the H_2MHTP-GO, discarding the supernatant. Finally, the precipitate was washed with $CHCl_3$ five times following the above procedure. UV–Vis spectra and thin layer chromatography (TLC) were used to check the supernatant layer to ensure no H_2MHTP existed in the final washing. This methodology was implemented for metallo porphyrin-graphene oxide composites [metal = Zn, Cu, Sn(IV)]. We termed Zn(II)MHTP, Cu(II)MHTP, VOMHTP, Sn(IV)MHTP$(OH)_2$ as Zn porphyrin, Cu porphyrin VO porphyrin and Sn porphyrin, respectively throughout the article. The synthesis scheme of covalently linked GO-porphyrin composites is shown in figure 1.

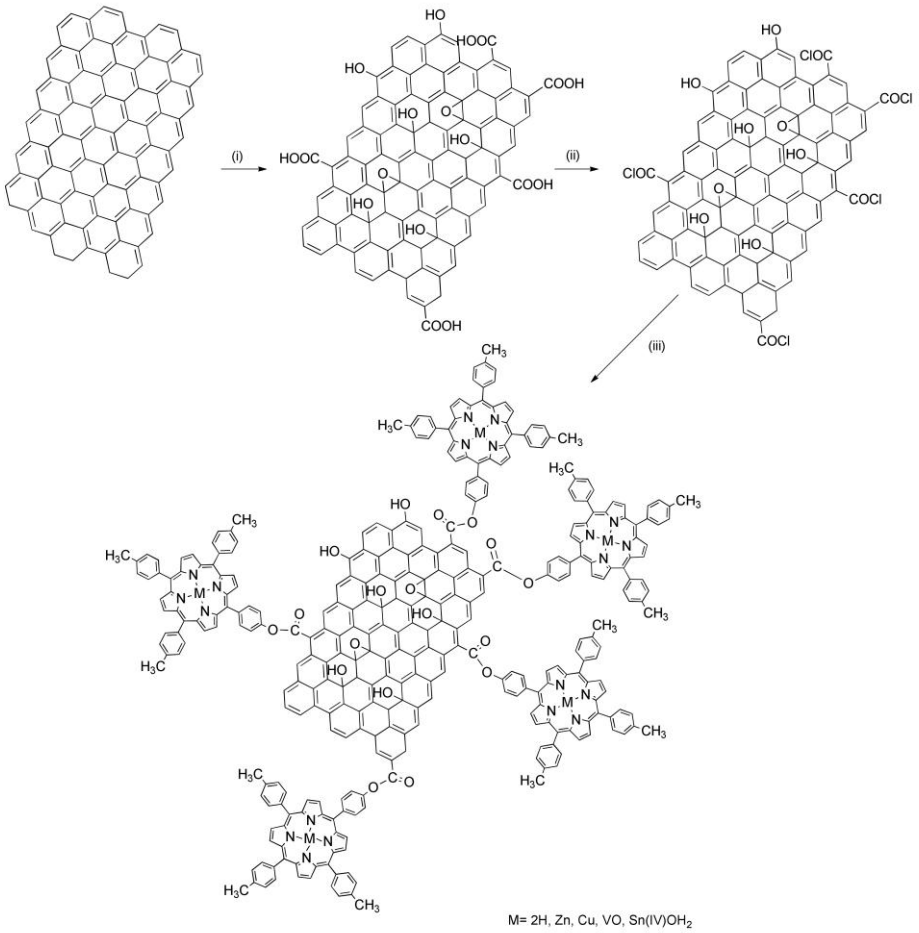

Figure 1. Synthesis scheme of novel graphene oxide-(H_2, Cu, Zn, VO, $Sn(OH)_2$) porphyrin composites
(i) $NaNO_3$, H_2SO_4/$KMnO_4$, 1h, $N_2H_4.2H_2O$,100 ^oC, 4h (ii) $SOCl_2$/DMF, 70 ^oC (iii) Et_3N/ DMF, 80 ^oC , 72h.

5.1.3 Structural and spectroscopic characterization

5.1.3.1 Field emission-scanning electron microscopy (FE-SEM) studies

The scanning electron micrographs for the GO-porphyrin hybrid materials demonstrate that a homogeneous system with the size of a micrometer order of magnitude was obtained. FE-SEM images of GO-porphyrin composites were recorded using Carl-Zeiss Ultra 55 model.

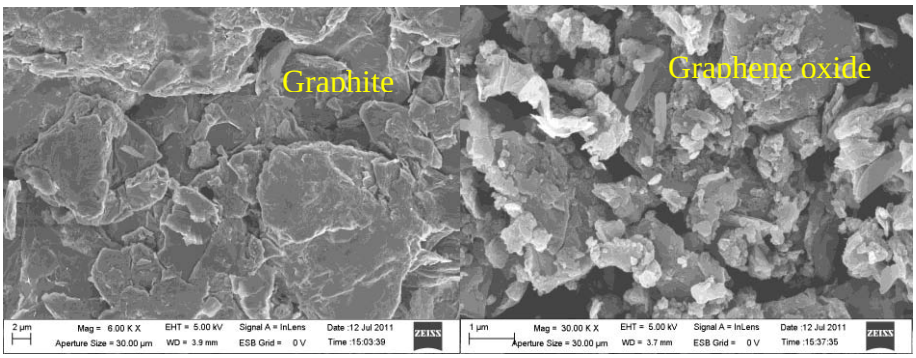

Figure 2. FE-SEM images of graphite and Graphene oxide

Pure graphite exhibits ordered flakes of 4-5 µm range. On functionalization, GO exhibit a three-dimensional network of randomly oriented sheet-like structures with wrinkled texture and hierarchical pores with the wide size distribution has shown in the figure 2.

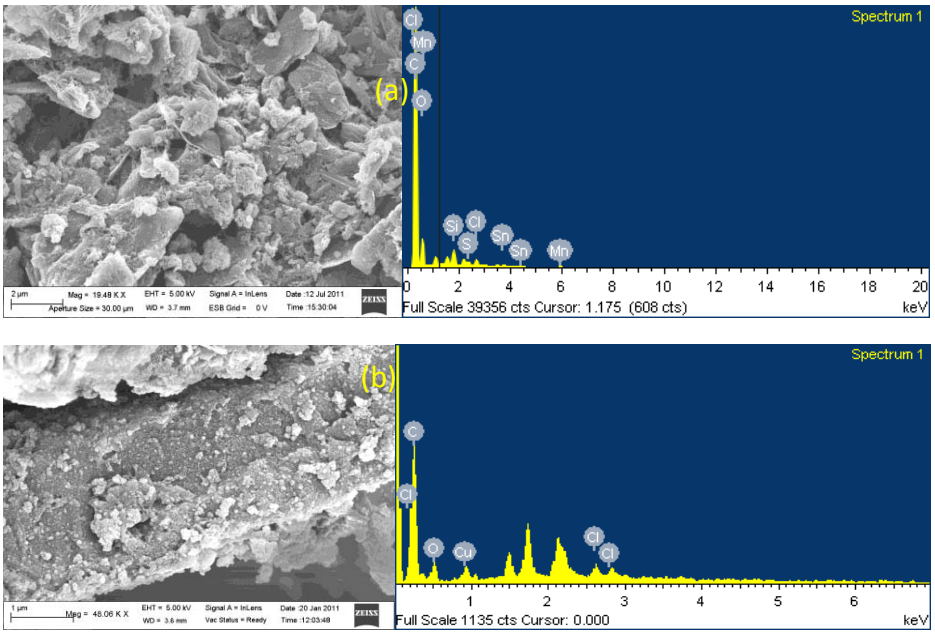

Figure 3. FE-SEM and EDS images for a) GO-H_2MHTP and b) GO- Zn Porphyrin composites.

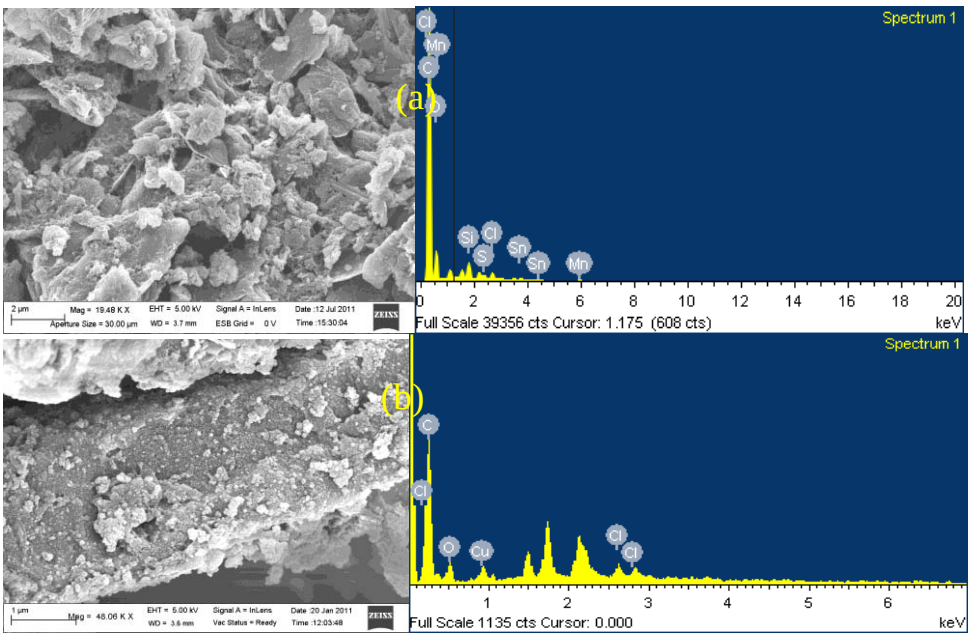

Figure 4. FE-SEM and EDS images of a) GO-Sn Porphyrin and b) GO- Cu Porphyrin composites

It is clearly seen from the top-view image of figure 3 that the composites have a uniform and dense surface, composed of plate-like particles with slightly scrolled edges ranging from several tens of nanometers to several hundreds of nanometers in lateral dimension. Similar structural images are observed for GO-Sn, Cu porphyrin composites as shown in figure 4. Some of GO flakes of composites fold together and show crinkly sheets. The surface is much rougher than that of GO which can be attributed to the covalent linkage of porphyrins to GO sheet.

5.1.3.2 Micro-Raman studies

Raman spectroscopy is a versatile and non-destructive characterization technique for obtaining information on the nature of binding of these poly-aromatic hydrocarbons. Raman spectra were recorded at room temperature using a micro-Raman spectrometer (LABRAM-HR) with laser excitation of 514.5 nm at room temperature. As can be seen in figure 5, the Raman spectrum of pure graphite exhibits a characteristic peak at 1591 cm^{-1} corresponds to G band of ordered sp^2-bonded carbon atoms.

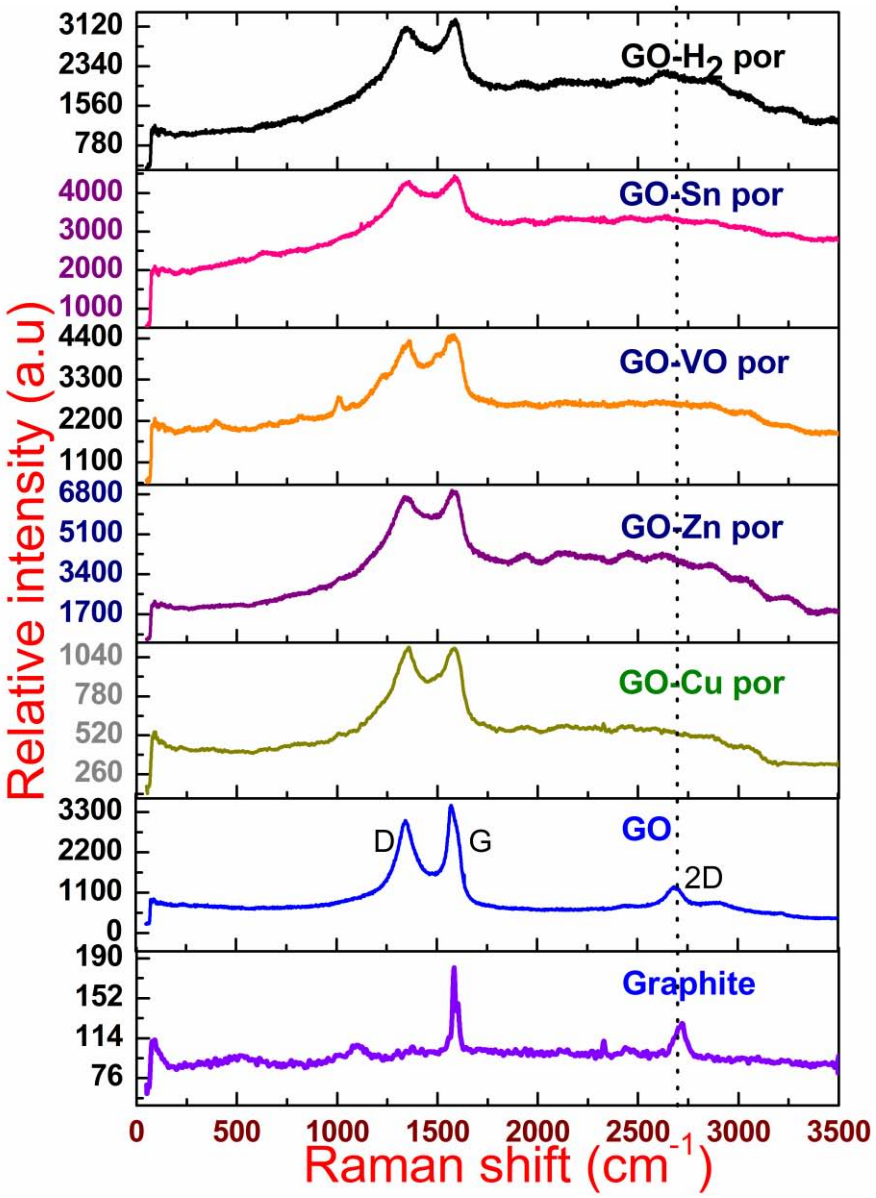

Figure 5. Micro-Raman spectra of graphite, GO, GO-H_2MHTP, GO-Zn porphyrin, GO-Cu porphyrin, GO-VO porphyrin and GO-Sn porphyrin composite.

As per the spectrum of GO (figure 5) exhibits D-band at 1345 cm^{-1} due to edges, other defects, and disordered carbon. The G-band appearing at 1575 cm^{-1} is broadened and blue shifted slightly while the intensity of the D band increases substantially. These phenomena could be attributed to the significant decrease in size of the in-plane sp^2 domains due to oxidation. It is well known that the increased intensity ratio of D/G accounts for a lower crystalline degree of graphite materials [29]. The functionalized GO with various porphyrins results in small changes of the D and G peaks. When the Raman spectrum of GO–

porphyrins was compared with that of GO, subtle rather than drastic changes are observed. The G band shifted upward from 1575 to 1583 cm^{-1}, which might be caused by the increasing number of layers in their solid states. As porphyrins are covalently linked to GO can absorb on both sides of the graphene sheets. The weak π–π stacking interaction with porphyrins can occur between two monolayer sheets in the same way as anchoring of phenyl rings on one GO sheet [30]. The intensity ratio of D/G bands increased from 0.932 for GO to 0.982 for GO-Cu porphyrin, 0.956 for GO-Zn porphyrin and 0.978 for GO-Sn porphyrin. However, the ratio of D/G band intensity has decreased for GO-H_2MHTP hybrids (0.89). This indicates that some of the oxygenated groups lead to the re-established conjugated graphene network.

5.1.3.3 Linear optical absorption studies

The optical absorption measurements were carried out by UV-Visible spectrometer (Model: JASCO V-670). Figure 6 shows optical absorption spectra of pure porphyrins and figure 7 for composite materials, H_2MHTP and graphene oxide molecules. Graphene oxide shows absorption peak at 268 nm which agrees with literature value [31]. Copper porphyrin peak at 421 nm is enhanced in graphene oxide-copper porphyrin composite while zinc porphyrin peak at 429 nm gets suppressed in graphene oxide-zinc porphyrin composite material. H_2MHTP absorption peak at 420 nm gets completely vanished in graphene oxide-H_2MHTP composite.

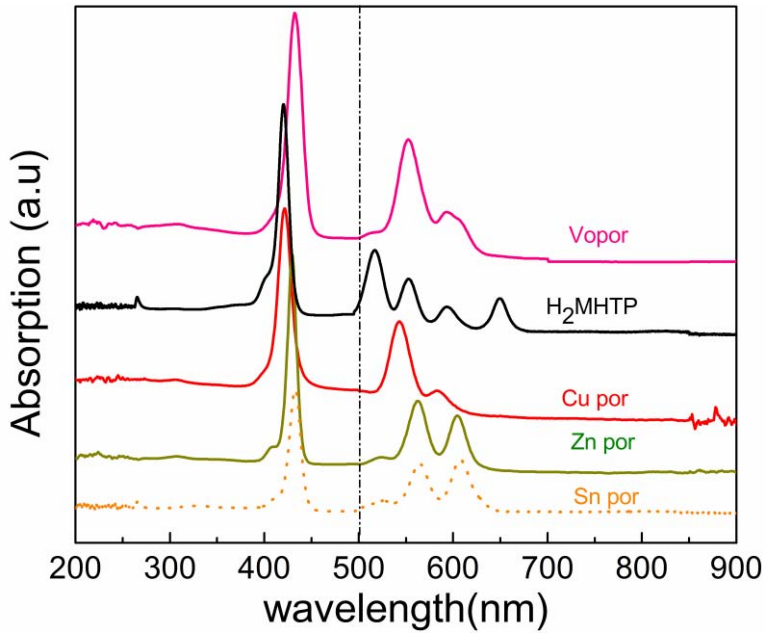

Figure 6. UV-Visible absorption spectra of VO porphyrin, copper porphyrin, zinc porphyrin, Sn porphyrin, H_2MHTP, in DMF. The absorbance in the region 500 nm to 890 nm is multiplied by 10 times to have more clarity near the excitation wavelengths.

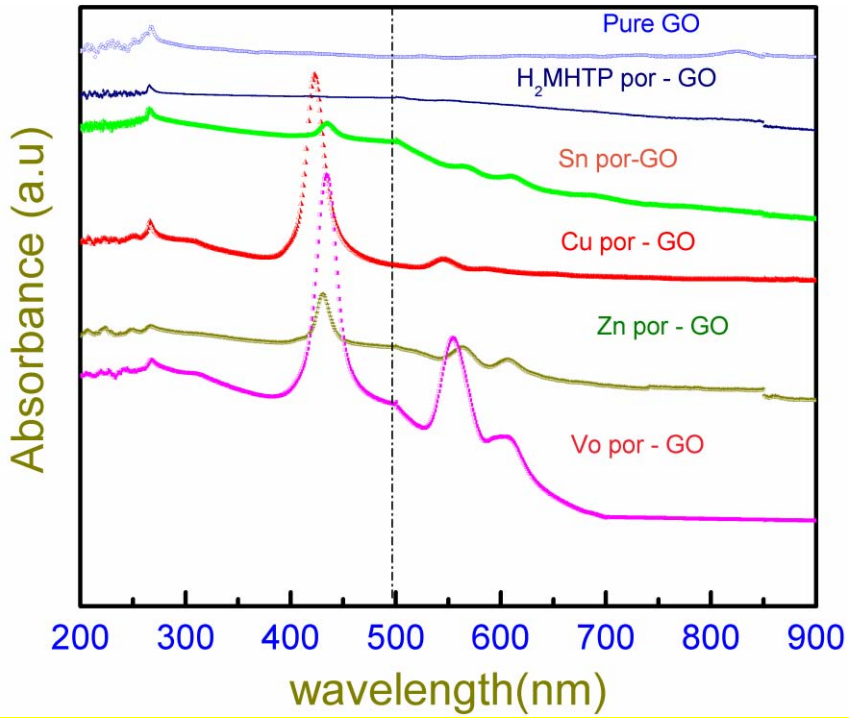

Figure 7. UV-visible absorption spectra of pure graphene oxide (GO), GO-copper porphyrin composite, GO-zinc porphyrin composite, GO-tin porphyrin composite, GO-H_2MHTP composite and GO-VO porphyrin composite in DMF. The absorbance in the region 500 nm to 890 nm is multiplied by 10 times to have more clarity near the excitation wavelengths.

Similarly, Sn porphyrin has absorption peak at 432 nm which is suppressed in graphene oxide-Sn porphyrin composite. These observations indicate the formation of composites and also the tunability of optical properties through different substitutes in porphyrin molecules. Porphyrins exhibit several peaks near the wavelength of 532 nm, whereas they almost disappear in the composites. The absorbance in the region 500 nm to 900 nm (figure 6 and figure 7) is amplified by 10 times for clear visibility. 0.2 mg/mL of graphene oxide-porphyrin composites were taken for Z-scan experiments.

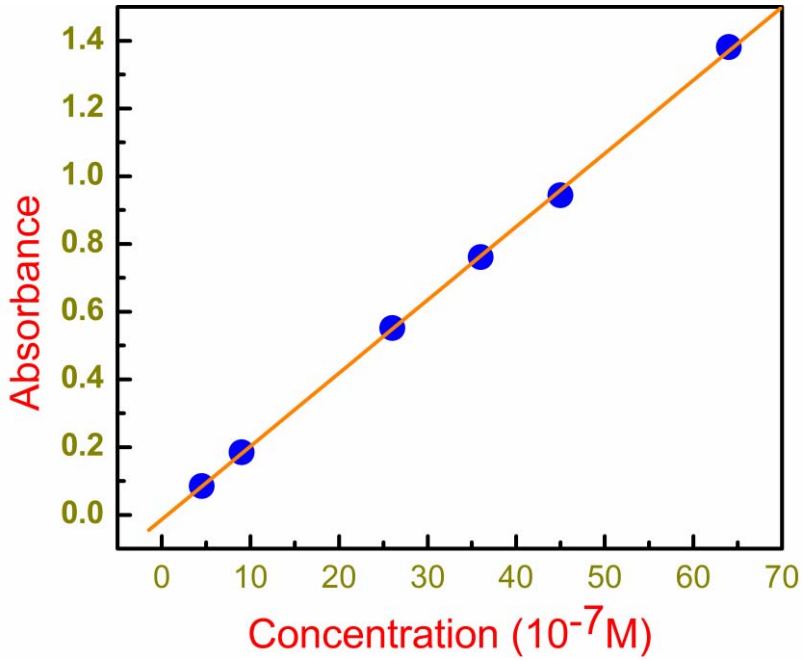

Figure 8. Variation of copper porphyrin absorbance with concentration at 421 nm peak wave length, the straight line is a linear fit to the experimental data.

To find out the concentration of graphene and porphyrin in the composite materials, we recorded absorption spectra for porphyrins and graphene separately at various concentrations and draw the absorbance versus concentration calibration curves. Matching the absorbance value with that of graphene-porphyrin composite, we estimated the porphyrin and graphene contents in the composite as 0.037 mg/ml ($5x10^{-5}$M) and 0.163 mg/ml respectively. Figure 8 shows the variation of copper porphyrin absorbance with concentration at 421 nm peak wave length. The straight line is a linear fit to the experimental data. Linear transmittances of graphene oxide, copper porphyrin, zinc porphyrin, Sn

porphyrin, H_2MHTP, VO porphyrin and graphene oxide-copper porphyrin, graphene oxide-zinc porphyrin, graphene oxide-Sn porphyrin, graphene oxide-H_2MHTP, graphene oxide-VO porphyrin composites were 85 (0.71), 97 (0.13), 87 (0.61), 84 (0.77), 82 (0.61), 79 (1.05) 75 (1.26), 80 (0.99), 68 (1.65), 60 (2.22) and 60.8 %(2.16 cm^{-1}) respectively at 532 nm and 77 (1.12), 91 (0.40), 93 (0.32), 92 (0.37), 92 (0.37), 92 (0.37), 77 (1.16), 82 (0.88), 76 (1.19), 67 (1.76) and 74 %(1.3 cm^{-1}) respectively at 800 nm wavelength (with the corresponding optical densities given in the bracket).

5.1.3.4 Fourier Transform Infrared Spectroscopy (FT-IR)

The FT-IR spectra were recorded in KBr method in the range 500–4000 cm^{-1} using Nicolet 6700 FT-IR spectrometer.

Figure 9 (a) shows the typical FTIR spectrum obtained for graphene-porphyrin composites. The most characteristic features are the broad, intense band at 3430 cm^{-1} (O-H stretching vibrations) and the bands at 1725 cm^{-1} (C=O stretching vibrations from carbonyl and carboxylic groups), 1639 cm^{-1} (skeletal vibrations from unoxidized graphitic domains), 1380 cm^{-1} (C-OH stretching vibrations), and 1027cm^{-1} (C-O stretching vibrations). The appearance of the peaks at around 2900 cm^{-1} is ascribed to the aromatic stretching vibrations of C-H bonds of GO. After covalent functionalization with porphyrins, new peak appears at ~1582 cm^{-1} corresponding to the C=C vibrations of porphyrins and the peak of the C–O stretching vibration shifts to 1108 cm^{-1}, and gets broadened. The peak present at ~1707 cm^{-1} is assigned to the bending vibration of C=N of porphyrin ring. The disappearance of the peak at 1380 cm^{-1} clearly indicates that in porphyrin-GO composites the porphyrin molecules are covalently bonded to the graphene oxide via carboxylic acid linkage. However, the appearance of sharp intense peaks at 1390 cm^{-1} and 793 cm^{-1} for Sn porphyrin-GO composites are due to the axial Sn-OH stretching and bending vibrations.

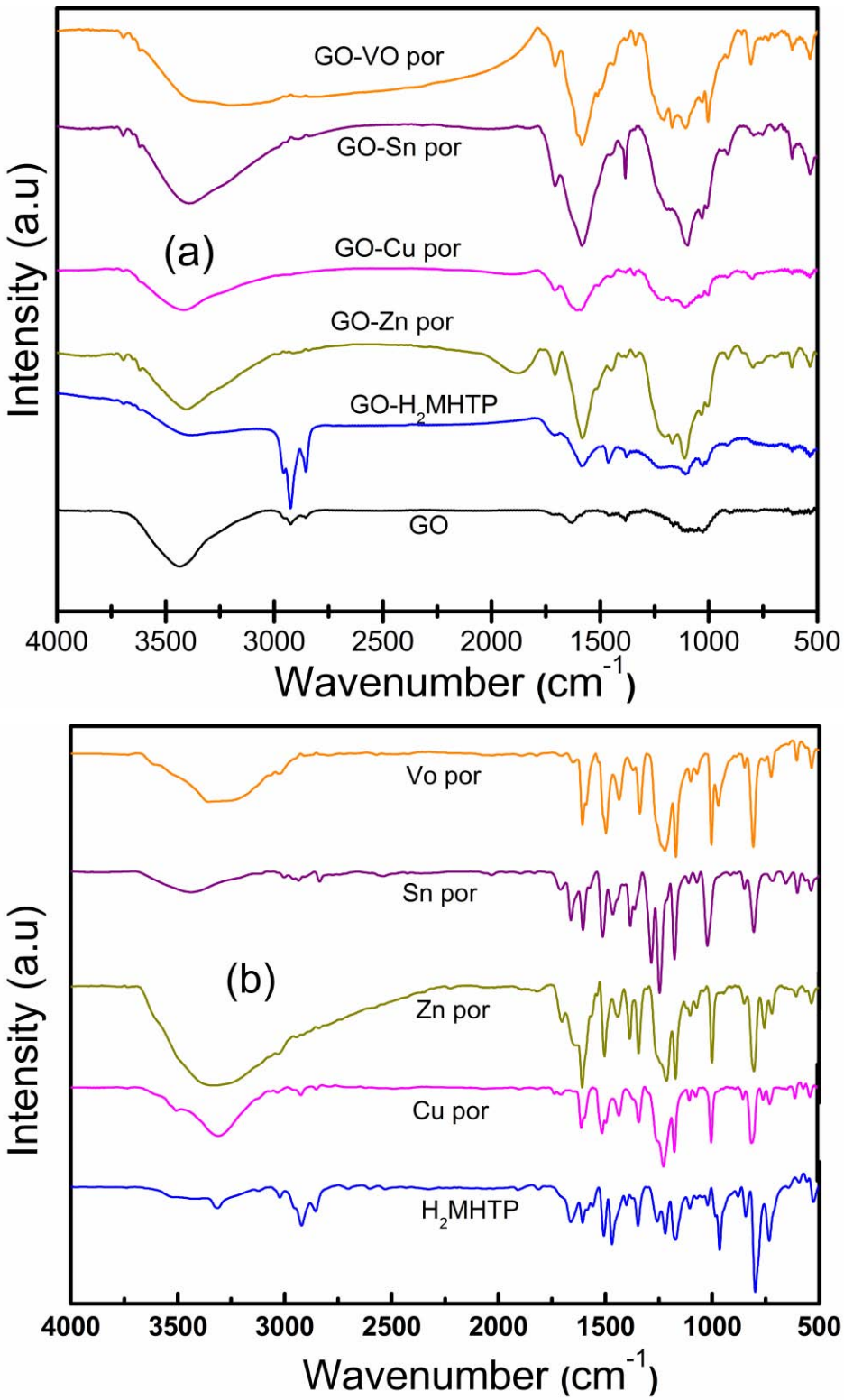

Figure 9. FT-IR Spectra of a) grpahene oxide, graphene oxide-H_2MHTP, graphene oxide-Zn porphyrin, graphene oxide-Cu porphyrin, graphene oxide-Sn porphyrin, graphene oxide-VO porphyrin composite and b) H_2MHTP, Cu porphyrin, Zn porphyrin, Sn porphyrin, VO porphyrin molecules.

VO porphyrin-GO composites shows more broadened –OH stretching vibration than the other composites. Figure 9 (b) shows the typical FTIR spectra obtained for pure porphyrins.

5.1.3.5 Steady state fluorescence studies

The electronic interaction between various porphyrins units and GO is studied through steady state and time resolved fluorescence techniques. Steady state fluorescence emission is performed with a Spex FluoroLog-3 spectrofluorometer (Jobin Yvon) equipped with a Hamamatsu R928 photomultiplier tube and a resolution of ±1 nm. On excitation at λ_{ex} = 420 nm (figure 10), GO-H_2MHTP exhibits emission peaks at 650 and 718 nm which arise due to $S_1 \rightarrow S_0$ transition. The emission intensity of H_2MHTP is decreased by 21 % as compared with the control sample (which is prepared with the pure porphyrin so that the control sample has the same absorbance value as that of the composite, that is 0.18) indicates that H_2MHTP-GO undergoes fluorescence quenching. The effective emission quenching of porphyrin in GO–H_2MHTP composites is indicative of electronic interactions between the singlet excited state of the porphyrin ($^1H_2MHTP^*$) and GO.

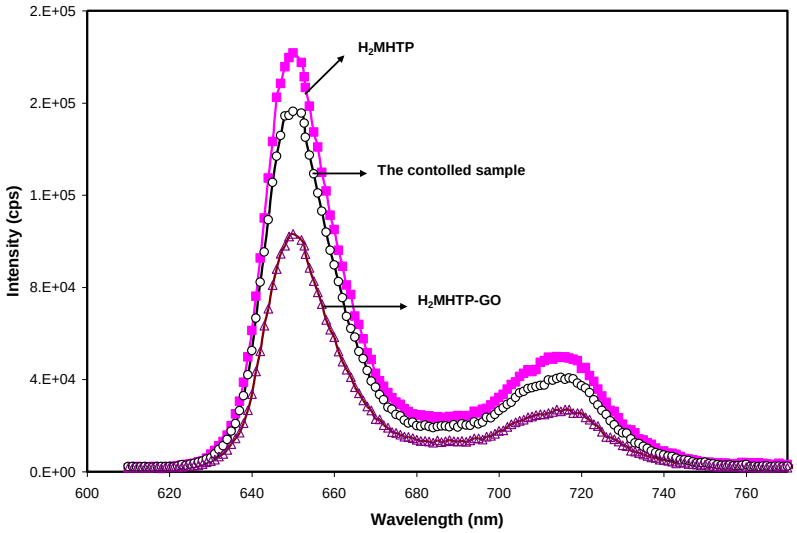

Figure 10. Steady state emission spectra of H_2MHTP, the control sample, and H_2MHTP-GO in chloroform, with the normalization of the absorbance of the soret band excitation wavelength (420 nm) to the same value (0.18).

Therefore, covalently linked H_2MHTP with GO can act as an energy absorbing and electron transporting antenna, while GO acts as an electron acceptor unit, in this hybrid system where the porphyrin moiety resides near the surface of the GO framework.

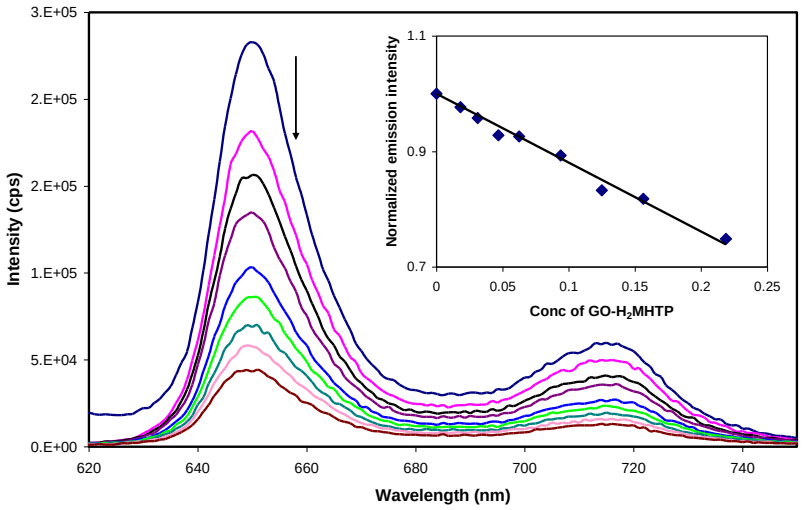

Figure 11. Fluorescence quenching behavior of GO-H_2MHTP. Inset shows emission normalized intensity with respect to concentration of graphene oxide-H_2MHTP composite.

It is also interesting to note that with increase in the concentration of GO–H_2MHTP (wt/ml), the fluorescence emission intensity decreases gradually without any change in the spectral pattern indicating that the composites undergo self-quenching as shown in figure 11. About 27% quenching is observed for H_2MHTP-GO (0.2 mg/ml) with a highest quenching constant of 3.57×10^9 S^{-1}. However, Zn porphyrin-GO exhibits better quenching of 21 % (for 2 mg/ml) among other metalloporphyrin-GO composites with quenching constant of 3.16×10^9 S^{-1}.

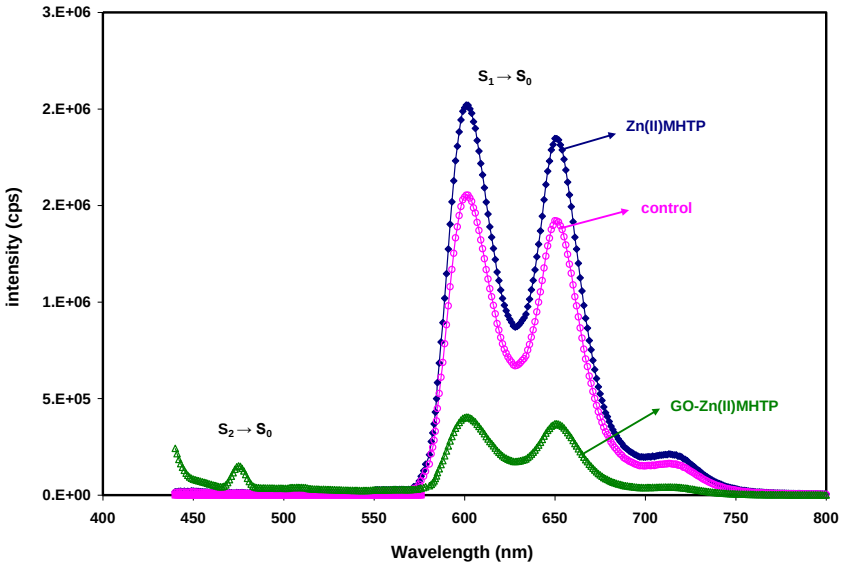

Figure 12. Steady state emission spectra of Zn porphyrin, the control sample, and Zn porphyrin-GO in chloroform, with the normalization of the absorbance of the Soret band excitation wavelength (420 nm) to the same value (0.18)

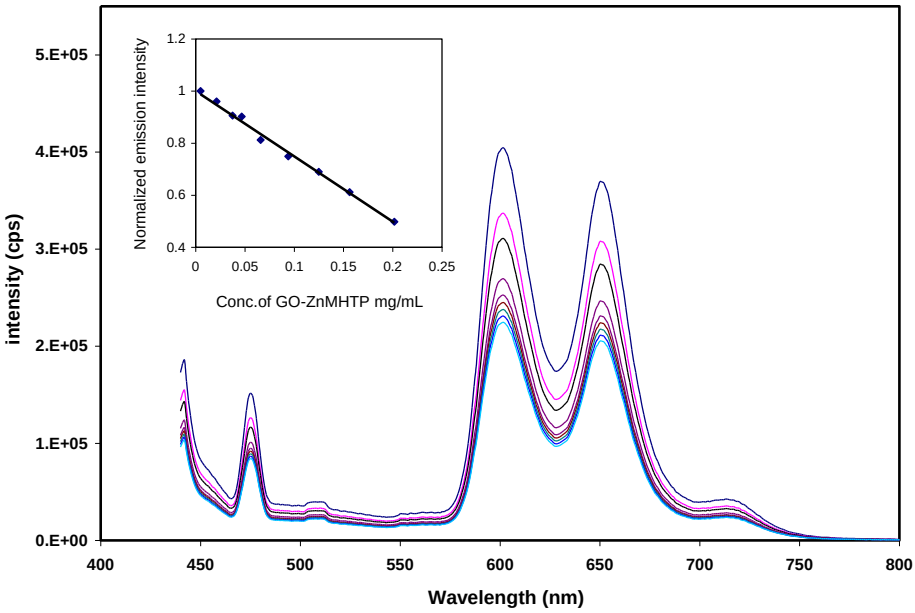

Figure 13. Fluorescence quenching behavior of GO-Zn porphyrin. Inset shows emission normalized intensity with respect to concentration of graphene-Zn porphyrin porphyrin composite.

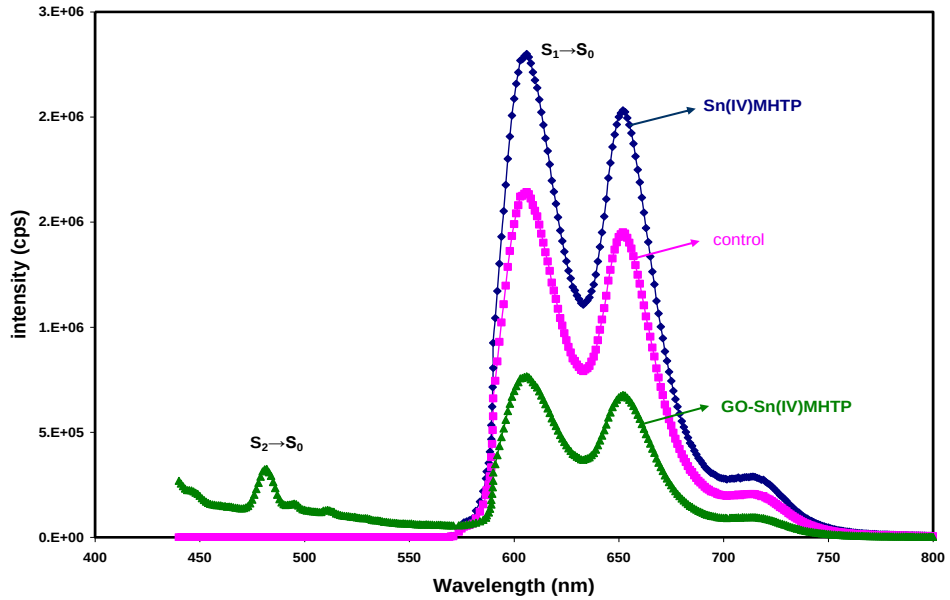

Figure 14. Steady state emission spectra of Sn porphyrin, the control sample, and Sn porphyrin-GO in chloroform, with the normalization of the absorbance of the Soret band excitation wavelength (420 nm) to the same value (0.18)

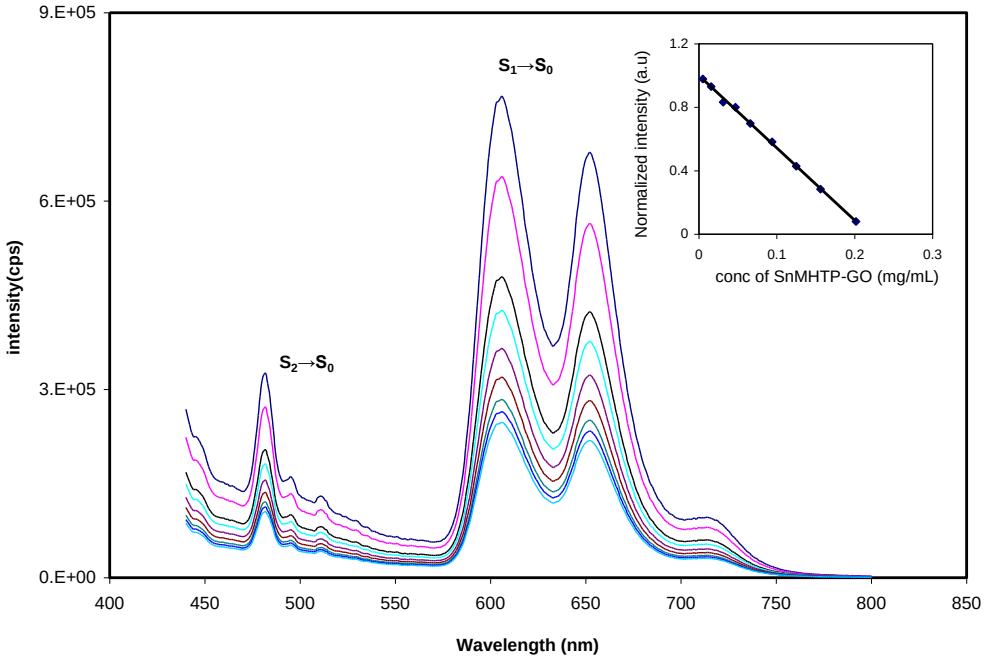

Figure 15. Fluorescence quenching behavior of GO-Sn porphyrin. Inset shows emission normalized intensity with respect to concentration of graphene-Sn porphyrin porphyrin composite.

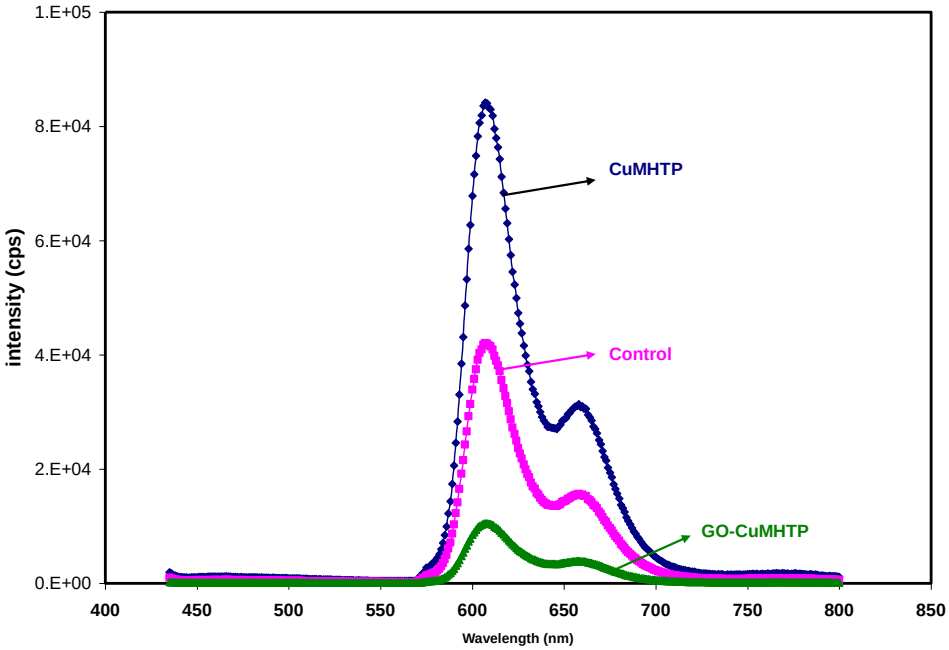

Figure 16. Steady state emission spectra of Cu porphyrin, the control sample, and Cu porphyrin-GO in chloroform, with the normalization of the absorbance of the Soret band excitation wavelength (420 nm) to the same value (0.18).

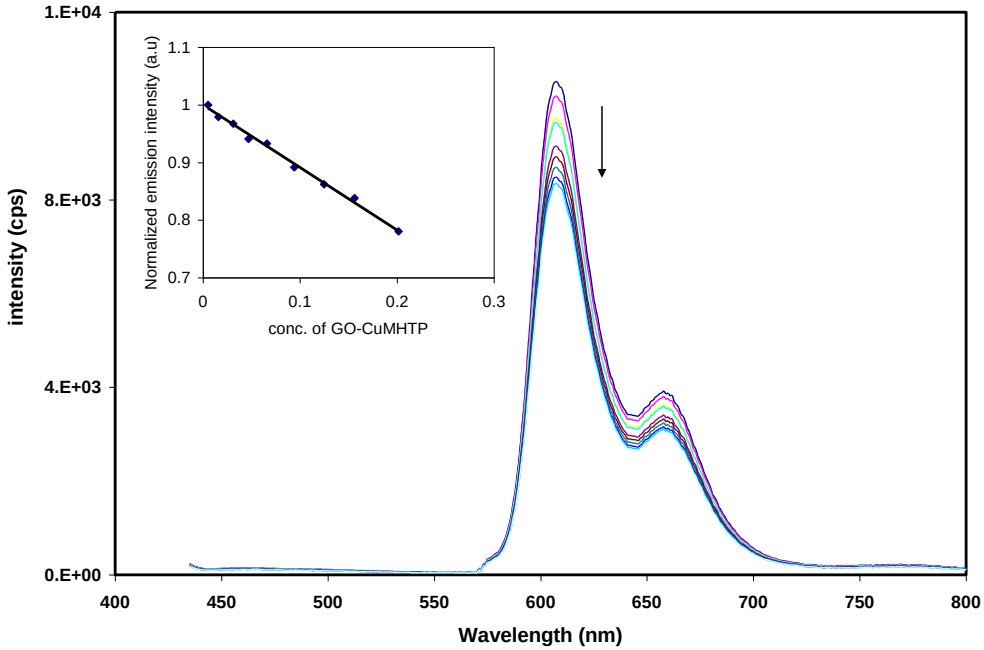

Figure 17. Fluorescence quenching behavior of GO-Cu porphyrin. Inset shows emission normalized intensity with respect to concentration of graphene-Cu porphyrin porphyrin composite.

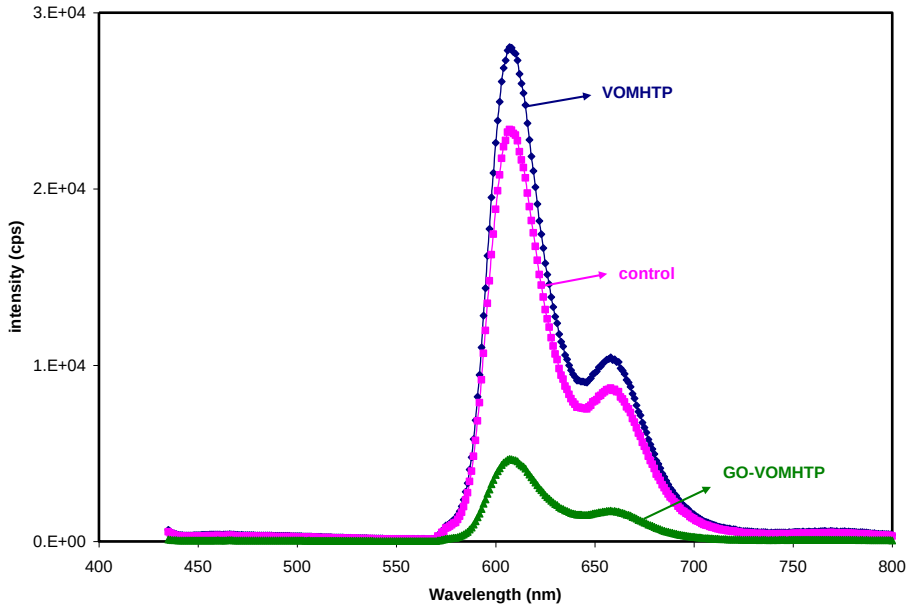

Figure 18. Steady state emission spectra of VO porphyrin, the control sample, and VOporphyrin-GO in chloroform, with the normalization of the absorbance of the Soret band excitation wavelength (420 nm) to the same value (0.18).

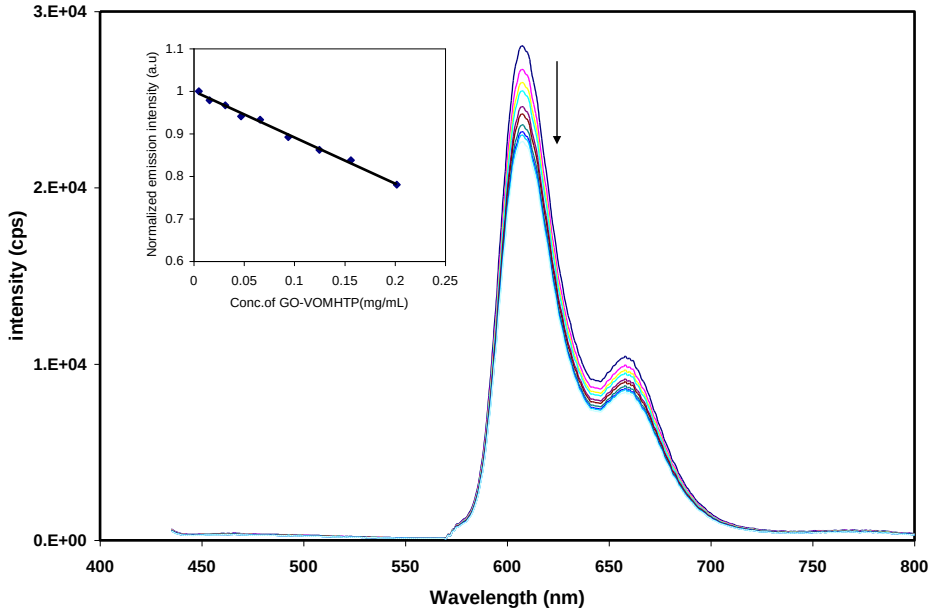

Figure 19. Fluorescence quenching behavior of GO-VO porphyrin. Inset shows emission normalized intensity with respect to concentration of graphene-VO porphyrin composite.

Similar results are observed in other GO-porphyrins composites shown in the figures 12 to 19 and the pertinent data is summarized in the Table 1.

Samples	absorption		Steady state emission		Life time(ns)	k^s_q/s^{-1}
	Soret Band (nm)	Q-band (nm)	λ_{ex}nm)	λ_{em}(nm)		
GO-H_2MHTP	425	516, 551, 592, 648	420	650, 718	6.4	$3.57x10^9$
GO-Zn porphyrin	431	564, 606	420	472, 592, 652	1.41	$3.16\ x10^9$
GO-Cu porphyrin	423	545	420	594, 649	----	$1.08\ x10^9$
GO-Sn porphyrin	435	568, 612	420	483, 599,654	4.06	$2.57\ x10^9$
GO-VO porphyrin	434	554, 606	420	593, 647	----	$1.05\ x10^9$

Table 1. Optical absorption and Emission maxima, Lifetime of singlet state, quenching rate constant of graphene oxide-H_2MHTP, graphene oxide-Zn porphyrin, graphene oxide-Cu porphyrin, graphene oxide-Sn porphyrin and graphene oxide-VO porphyrin composite.

porphyrin	absorption		Steady state emission		Life time(ns)
	Soret Band (nm)	Q-band (nm)	λ_{ex}nm)	λ_{em}(nm)	
H_2MHTP	420	517,553, 594,650	420	650, 718	9.2
Znporphyrin	429	563, 605	420	472, 592, 652	1.4
Cuporphyrin	421	544,583	420	594, 649	----
Snporphyrin	433	564, 609	420	483, 599,654	4.1
VOporphyrin	432	553, 594	420	593, 647	----

Table 2. Optical absorption and Emission maxima and Lifetime of singlet state of H_2MHTP, Zn porphyrin, Cu porphyrin, Sn porphyrin and VO porphyrin molecule.

All the metalloporphyrins (M = Zn, Sn(IV),VO and Cu) exhibit $S_1 \rightarrow S_0$ emission at ~595 and ~653 nm as shown in figure 20. The intensity of the $S_1 \rightarrow S_0$ emission is found to vary with metal centre. GO-Cu porphyrin and GO-VO porphyrins exhibit weak emission. In contrast to GO-H_2MHTP, GO-Zn porphyrin and GO-Sn porphyrins exhibit an $S_2 \rightarrow S_0$ emission peaks at 472 nm and 483 nm. In porphyrin-GO hybrids, after photo excitation, donor–acceptor interaction between the two moieties of H_2MHTP (Zn porphyrin) and GO have an inter-molecular charge transfer from the photo excited singlet H_2MHTP to the graphene oxide moiety, and this results in the observed fluorescence quenching and energy release. Hence, they can be used as sources for the solar energy harvesting in solar cells.

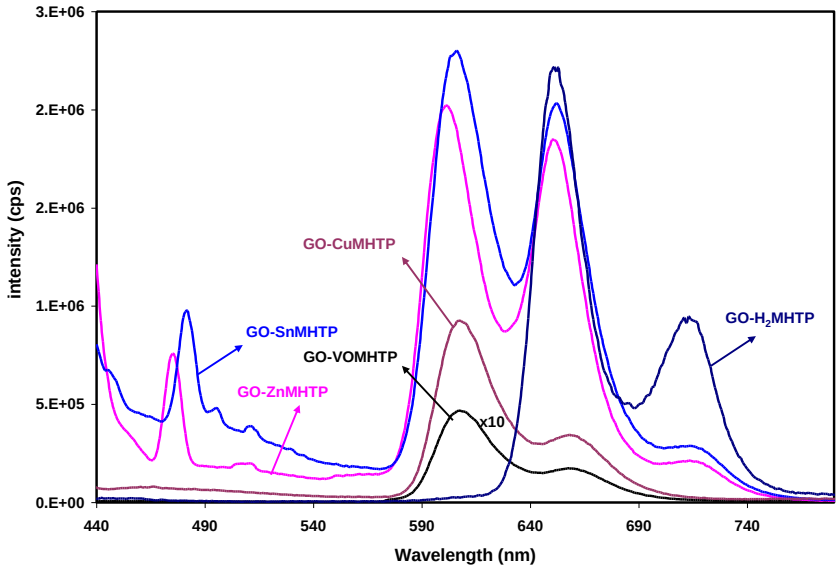

Figure 20. Fluorescence spectra of graphene oxide-H_2MHTP, graphene oxide-Zn porphyrin, graphene oxide-Sn porphyrin, graphene oxide-Cu porphyrin and graphene oxide-VO porphyrin composite. (Spectra for graphene oxide-VO porphyrin is amplified by 10 times)

5.1.3.6 Time-correlated single photon counting (TCSPC) studies

To understand further, the energy transfer between GO-porphyrins, the fluorescence lifetime studies were carried out with TCSPC using 460 nm LED with FWHM of 1.3 ns. The fluorescence lifetime decay profiles are presented in figure 21.

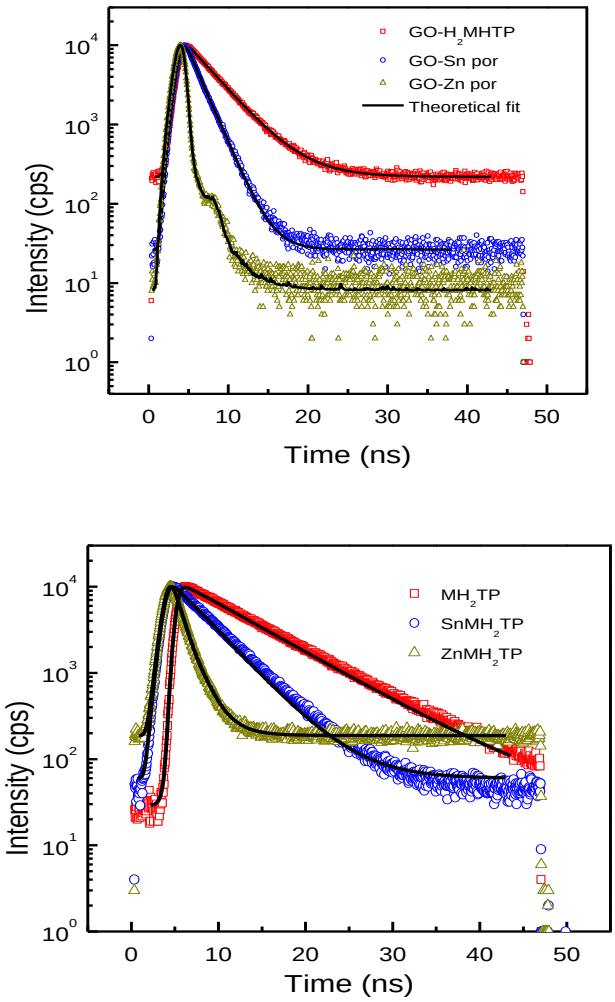

Figure 21. The fluorescence lifetime decay of various GO-porphyrin composites and pure porphyrins.

The fluorescence lifetime of GO-H_2MHTP shows single exponential decay with a lifetime of 6.4 ns. However, H_2MHTP exhibits lifetime of 9.1 ns in chloroform solution. The significant decrease in the lifetime indicates that charge-separation and/or electron transfer scenario in the GO–H_2MHTP via ($^1H_2MHTP^*$). This further supports the fluorescence quenching behavior of GO–H_2MHTP shown in figure 10. The $S_1 \rightarrow S_0$ fluorescence lifetime of metallo porphyrins are also estimated and the data is presented in the Table. 2.

5.1.3 NLO Measurements

The ns laser source was a frequency doubled Nd: YAG laser (INDI-40, Spectra physics) with 6 ns pulse duration and a repetition rate of 10 Hz at 532 nm wavelength. The fs laser is a spectra physics Ti-sapphire regenerative amplifier with 100 fs pulse duration and it is operated at 1 KHz repetition rate and 800 nm wavelength. Graphene oxide, porphyrins and their composites are taken as solutions in DMF for the experimental studies.

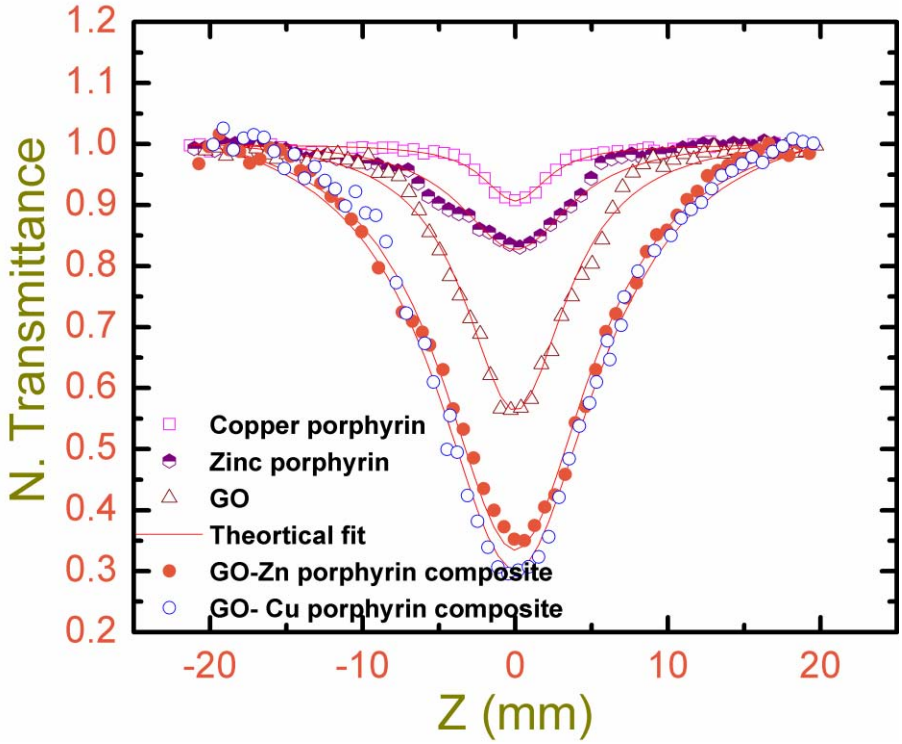

Figure 22. Open aperture Z-scan curves of copper porphyrin, zinc porphyrin, GO, GO-zinc porphyrin and GO-copper porphyrin composites in DMF with input intensity 300 MW/cm^2 at 532 nm in nanosecond regime. Red lines represent theoretical fittings.

Open aperture Z-scan studies were carried out by focusing the input beam on to the sample using a lens of 120 mm focal length forming a 27 μm and 40 μm spot sizes at the focus in ns and fs regimes respectively. The transmitted light is collected with a photodiode. The peak intensities estimated at the focus in Z-scan experiments are 300 MW/cm^2 in ns experiments and 300 GW/cm^2 in fs experiments.

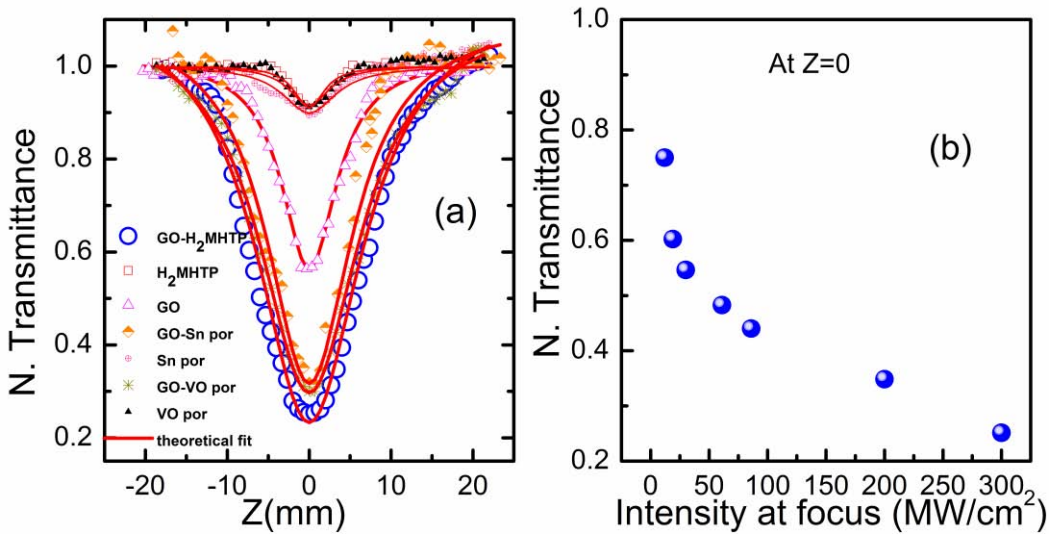

Figure 23. (a) Open aperture Z-scan curves of H_2MHTP, graphene oxide-H_2MHTP composite, Sn porphyrin, graphene oxide-Sn porphyrin composite, VO porphyrin, graphene oxide-VO porphyrin composite and pure graphene oxide in DMF with peak intensity (I_{00}) 0.3 GW/cm^2 at 532 nm in ns regime. Dashed line represents theoretical fit. (b) Intensity dependent normalized transmittance at focus for graphene oxide-H_2MHTP composite material.

Figure 22 shows open aperture nanosecond Z-scan results of pure GO, copper and zinc porphyrin and GO-copper and zinc porphyrin composites in DMF with concentration of 0.2 mg/ml at an input intensity of 300 MW/cm^2. Figure 23 (a) shows typical open aperture Z-scan curves for pure graphene oxide, H_2MHTP, Sn porphyrin, VO porphyrin, graphene oxide-H_2MHTP, graphene oxide-Sn porphyrin and graphene oxide-VO porphyrin composites. Curves for pure porphyrins, graphene oxide and composites show RSA behavior in ns regime and composites show strong SA behavior in fs time scales. In order to determine the linear and nonlinear absorption parameters and excited state lifetime, we have assumed a three level model for the graphene because of its absortipon behavior as shown in figure 7. As normally done for the porphyrin molecules, we have taken a five level model with $\frac{1}{\tau_{isc}}$, intersystem crossing rate to include the contribution of triplet states T_1 and T_n. For the composite molecules, we have reduced it to a simplified model of three level system, where σ_{eff}^{ex} is taken as the effective excited state absorption cross-section includes the $S_1 \rightarrow S_n$, $T_1 \rightarrow T_n$ of the

porphyrin molecules and $S_1 \rightarrow S_n$ of graphene molecules and β_{eff} as the effective TPA coefficient for both graphene and porphyrin molecules. This is quite reasonable as the absorption levels S_1 (T_1) and S_n (T_n) of porphyrins closely match in energy of graphene molecules. As there is a strong TPA in the composites and the energy levels of the S_n states of porphyrin materials match with the graphene S_n states, there will be an energy transfer from the excited states of porphyrins to graphene and then graphene's S_n states relax to the ground state nonradiatively. The composite molecule comes to the ground state through sub-nanosecond relaxation times.

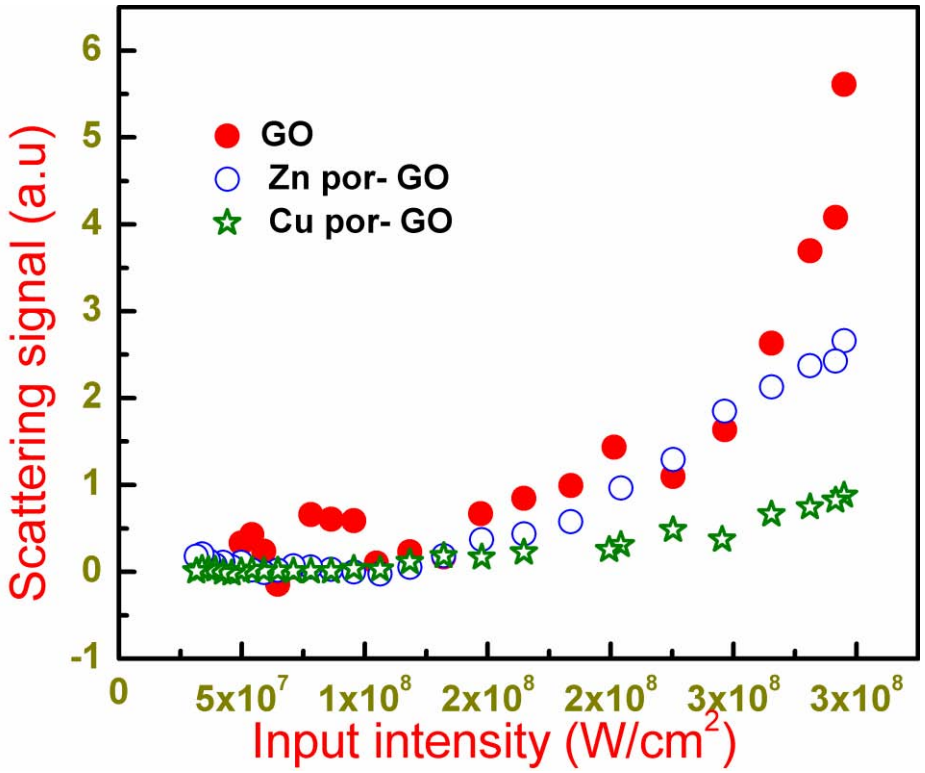

Figure 24. Scattering signal with input intensity of GO and GO-(Zn,Cu) porphyrin composites

Because of the strong excited state absorption and cumulative TPA of porphyrin as well as the graphene, and immediate energy transfer to the graphene, the role of triplet state lifetimes does not appear to influence the fittings of the nanosecond data, though it does influence the excited state absorption cross-section σ_{eff}^{ex}. Optical nonlinear susceptibilities of graphene, graphene-zinc porphyrin and graphene-copper porphyrin measured through the DFWM in the

boxcar geometry are found to be $4.2x10^{-12}$ esu, $7.1x10^{-12}$ esu and $8.5x10^{-12}$ esu respectively, estimated with reference to CS_2 value of $6.8x10^{-13}$ esu. We also observed nonlinear scattering from the grapheme oxide and its composite materials as shown in the figure 24, while the pure porphyrin samples do not show any nonlinear scattering. The experimental procedure to determine the nonlinear scattering is discussed in detail in the chapter 2. The same model is used to fit the open aperture Z-scan curves with fs pulses, for porphyrins the intersystem crossing rate from singlet to triplet state is a faster process compared to excitation pulse width and the generalized five level models for porphyrins effectively becomes a three level. From the absorption spectra it is very clear that due to the absorption band at 268 nm, the incident 532 nm laser beam can undergo a TPA. Also because of the weak linear absorption at the excitation wavelengths, the incident laser beam can undergo one-photon absorption. Because of the very broad absorption spectrum exhibited by the graphene oxide molecule, the levels at 268 nm show fast relaxations. Porphyrins are known to show strong ESA and TPA. A good energy transfer from the excited states of porphyrins to the GO band, leads to enhancement of the TPA of the porphyrins and at the same time the GO excited states relax fast to the ground state through the continuous band structure. Because of the good overlap and energy transfer between the porphyrin and the GO energy levels, we assume a model with three levels: the ground state, first excited state of porphyrin together with the absorbing levels of GO at 532 nm and higher excited states of Porphyrin and GO as the third (shown in the figure 24), for the graphene oxide-porphyrin composites to simplify the analysis of the otherwise complex scenario. GO is a non-stoichiometric compound, so it has no constant molecular weight.

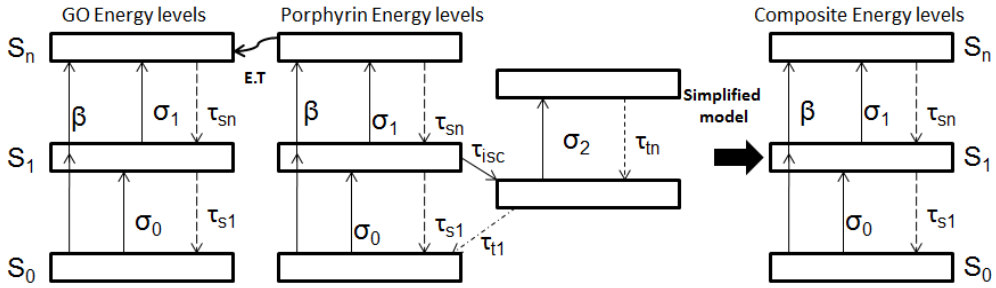

Figure 24. Schematic energy-level diagram of graphene oxide-porphyrin composite and its simplified model.

It is impossible to estimate the σ_0 from the formula $\sigma_0 = \alpha/N$ where $N = N_A \times C$. N_A is Avogadro's number and C is concentration of compound. As one can't determine the concentration, there is no easy way to estimate the σ_0 from any formulae. Therefore, we have tried to estimate σ_0 from theoretical modelling. The generalized rate equations for graphene oxide, porphyrins and composites are

$$\frac{\partial N_1}{\partial t} = -\frac{\sigma_0 I N_1}{\hbar\omega} - \frac{\beta I^2}{2\hbar\omega} + \frac{N_2}{\tau_{s_1}} \tag{1}$$

$$\frac{\partial N_2}{\partial t} = \frac{\sigma_0 I N_1}{\hbar\omega} - \frac{\sigma_1 I N_2}{\hbar\omega} - \frac{N_2}{\tau_{s_1}} + \frac{N_3}{\tau_{s_n}} \tag{2}$$

$$\frac{\partial N_3}{\partial t} = \frac{\sigma_1 I N_2}{\hbar\omega} + \frac{\beta I^2}{2\hbar\omega} - \frac{N_3}{\tau_{s_n}} \tag{3}$$

where N_j is the population per cubic centimetre of state S_j, while j = 1,2,3. h is the Planck constant, ω is the laser frequency and τ_{s_i} is the lifetime for state S_i, while i = 1,n. Where

$I = I_{00} \left(\frac{\omega_0^2}{\omega^2(z)}\right) \exp\left(-\frac{t^2}{\tau_p^2}\right) \exp\left(-\frac{2r^2}{\omega^2(z)}\right)$ and $\omega(z) = \omega_0 \left(1 + (z/z_0)^2\right)^{1/2}$,

z varies from -2 to +2 cm. I_{00} is the peak intensity at focus of Gaussian beam. $z_0 = \frac{\pi\omega_0^2}{\lambda}$, $\omega_0 = \frac{4\lambda f}{\pi d}$, τ_p is the input pulse width, z_0 is Rayleigh range, λ is wavelength, ω_0 is beam waist, f is focal length of the lens and d is diameter

of laser beam before the lens. For graphene oxide and porphyrins, intensity transmitted through the sample is given by Beer's law

$$\frac{\partial I}{\partial z} = -(\sigma_0 N_1 + \sigma_1 N_2 + \beta I) I \qquad (4)$$

where σ_0, σ_1 and β are ground state absorption cross section, excited state absorption cross section and two-photon absorption coefficient respectively.

For the composite molecules σ_1 is taken as the effective excited state absorption cross section which includes $S_1 \rightarrow S_n$ and $T_1 \rightarrow T_n$ of porphyrin molecules and $S_1 \rightarrow S_n$ of graphene oxide molecules and β is taken as the effective TPA coefficient for both graphene oxide and porphyrin molecules. Figure 23 (a) also shows theoretical fits, which matches quite well with experimental data. From the fit, we derive σ_0, σ_1, and β. τ_{s1} and τ_{sn} for pure graphene and porphyrins are taken from reported literature [32-35]. These parameters are compared for different molecules and the composites in Table 3. One can observe that β_{por} for porphyrin is much smaller than β_{gr} and β_{comp} in ns regime. Figure 23 (b) shows the intensity dependent NLO transmission of graphene oxide-H_2MHTP composite at focus, corresponding intensity dependent open aperture Z-scan curve is shown in figure 25. Intensity dependent NLO transmission curves for GO-Cu, VO, Sn, Zn porphyrin composites have shown in the figures 26 to 29.

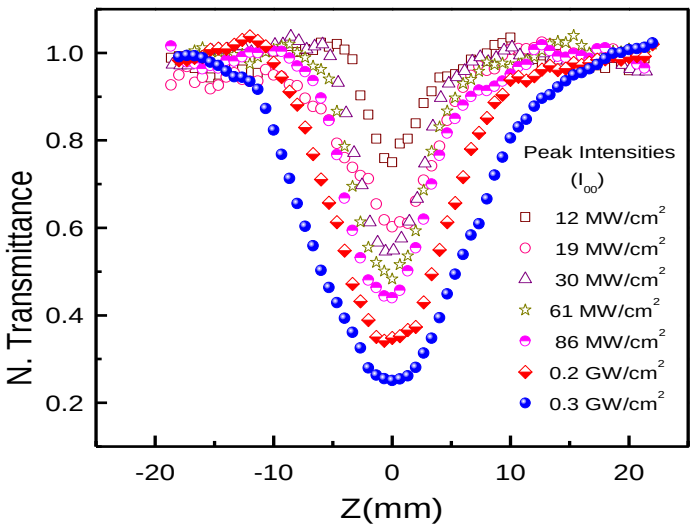

Figure 25. Intensity dependent open aperture Z-scan curves for GO-H_2MHTP composite material.

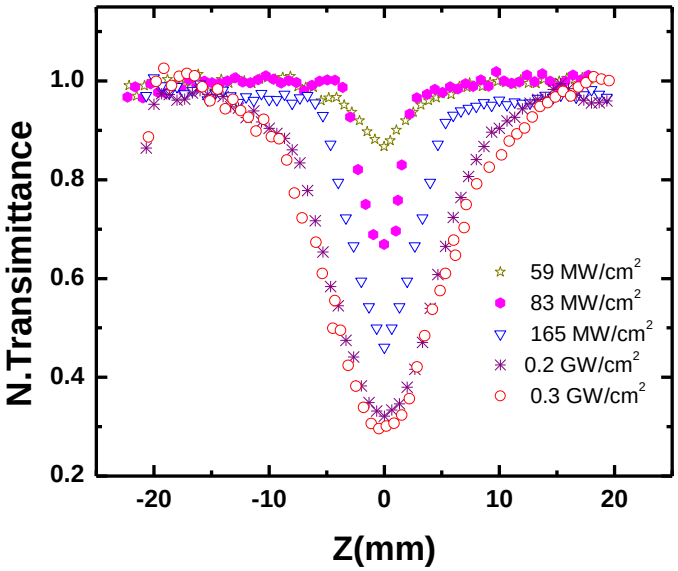

Figure 26. Intensity dependent open aperture Z-scan curves for GO-Cu porphyrin composite material.

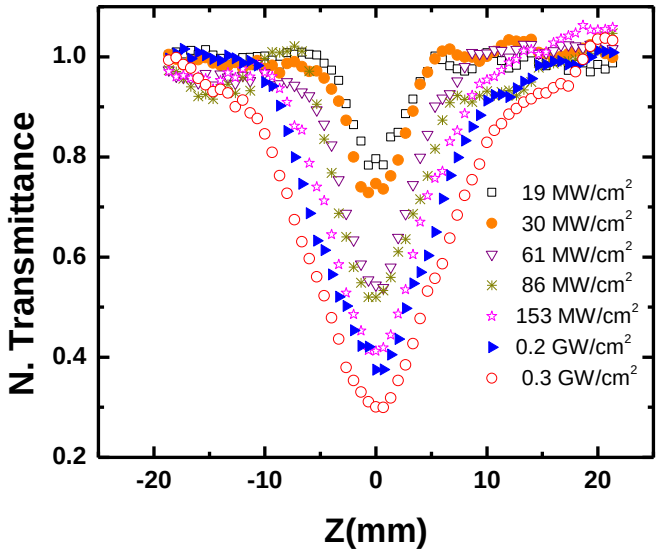

Figure 27. Intensity dependent open aperture Z-scan curves for GO-VO porphyrin composite material.

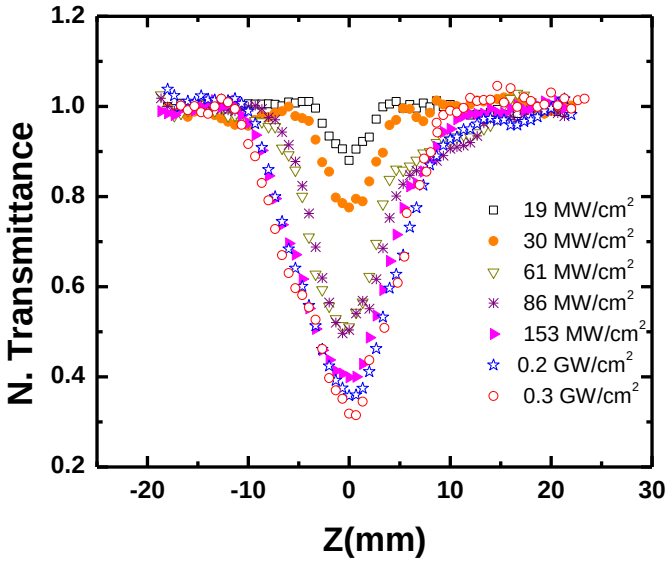

Figure 28. Intensity dependent open aperture Z-scan curves for GO-Sn porphyrin composite material.

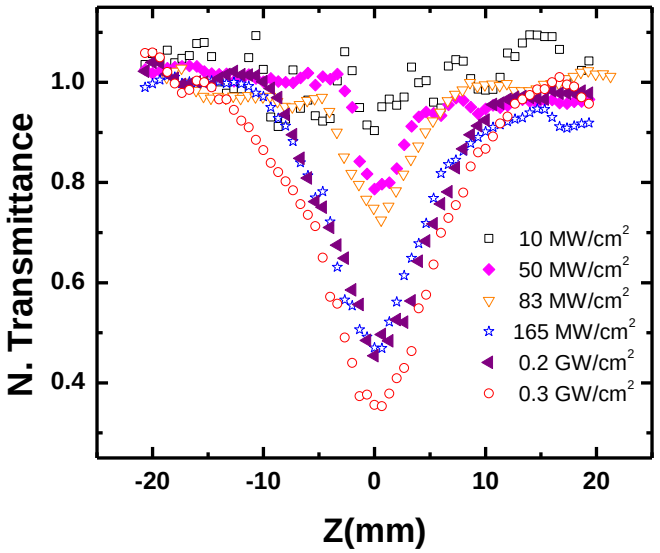

Figure 29. Intensity dependent open aperture Z-scan curves for GO-Zn porphyrin composite material.

It confirms that the obtained nonlinear coefficient values remain constant in the intensity range from 12 MW/cm^2 to 300 MW/cm^2. The optical limiting curves are plotted and shown in figure 11 for Cu porphyrin, pure graphene oxide and graphene oxide-porphyrin composite materials in nanosecond time scales.

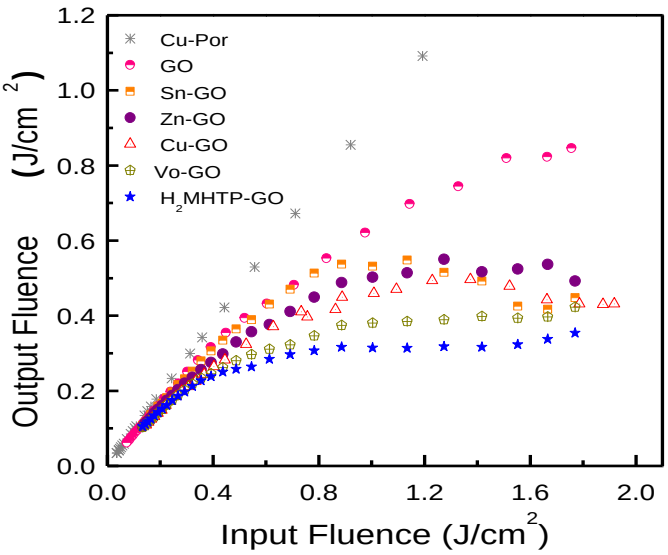

Figure 30. Optical Limiting behavior of graphene oxide-Porphyrin composites at 532 nm wavelength, ns regime.

Compared to individual porphyrin and graphene oxide, composite molecules show better limiting behavior. We estimated the figure of merit for pure porphyrins, and composite materials and they are shown in Table 3. Capability of a material for optical limiting can be described by FOM (= σ_{ex}/σ_0), where σ_{ex} and σ_0 are excited state and ground state absorption cross sections. We estimated the limiting thresholds of copper porphyrin, Zinc porphyrin, VO porphyrin, Sn porphyrin, H_2MHTP, graphene oxide, graphene oxide-VO porphyrin, graphene oxide-Sn porphyrin and graphene oxide-H_2MHTP, graphene oxide-zinc porphyrin, graphene oxide- copper porphyrin as 1.7, 1.3, 0.8, 0.9, 1.1, 0.8, 0.32, 0.45 and 0.25, 0.2, 0.1 J/cm^2, respectively. While the current studies involve larger number of metal porphyrins, their composites with GO, and a compassion with metal free porphyrin with GO.

Samples	**β (cm/GW)**	**σ_1 (cm^2) X 10^{-19}**	**FOM (σ_1/σ_0)**	**τ_1 (ns)**	**τ_2 (ps)**
VO porphyrin	142	84	17.5	1.3	2.2
Zn porphyrin	366	113	25.7	0.8	5
Copper porphyrin	132	79	19.8	0.9	0.8
Snporphyrin	168	102	22.7	4.1	2.3
H_2MHTP	159	98	20.9	9.2	2.8
GO	900	30	5.7	0.009	0.009
GO- VO porphyrin	3760	262	30.1	1.2	0.55
GO- Snporphyrin	3650	248	29.2	4.06	0.6
GO- H_2MHTP	4920	412	46.8	6.4	0.65
GO-Copper porphyrin	4720	380	45.8	0.5	7
GO-Zinc porphyrin	3570	214	43.7	0.68	9

Table 3. Excited state and ground state parameters β, σ_1, σ_1/σ_0, τ_1 and τ_2 of graphene oxide, VO porphyrin, Sn porphyrin,Zn porphyrin, Copper porphyrin, H_2MHTP, graphene oxide-VO porphyrin, graphene oxide-Zn porphyrin, graphene oxide-copper porphyrin, graphene oxide-Sn porphyrin and graphene oxide-H_2MHTP composite in ns regime.

Composites exhibit enhanced optical limiting behavior which arises from ESA, TPA and nonlinear scattering. It is important to notice that behavior of the curves is quite different at ns (532 nm) and fs (800 nm) time scales. In ns time scales excitation at 532 nm has a very strong TPA in graphene oxide and it dominates both in pure graphene oxide and the composites. From our experimental observations metal free porphyrin with graphene oxide show enhanced nonlinear absorption behavior compared to metal porphyrins with graphene oxide. Previous NLA results on metal porphyrins show high nonlinearities due to metal substituents in the core of porphyrin molecules, whereas in our results graphene oxide plays superior role than metal substitutes. Graphene oxide completely

dominates as a good electron acceptor. GO-H_2MHTP show highest β, ESA than GO-metal porphyrins.

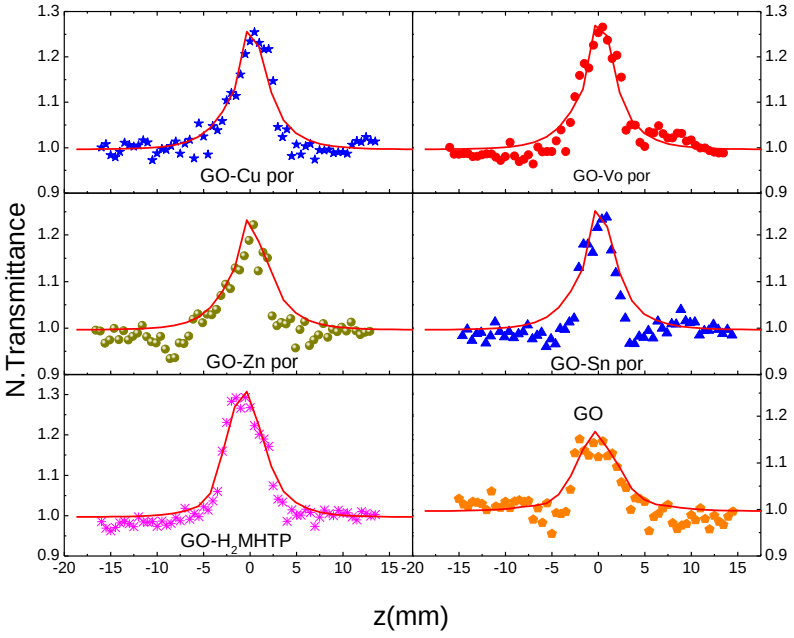

Figure 31. Open aperture Z-Scan Curves for Pure graphene oxide and graphene oxide-porphyrin composites at 800 nm wavelength, fs regime.

However at fs time scales, we have introduced saturation for ground state absorption to fit the SA behavior open aperture Z-scan curves. Excitation at 800 nm has a very poor TPA cross section for graphene oxide. We recorded the pure solvent contribution and the nonlinear absorption when porphyrins, graphene oxide and the composites are dissolved in DMF solution in order to estimate the effect of the solvent, while with graphene oxide and the composites the curves exhibit shallower depths in the RSA curves shown in figure 32. This is explained as due to the opposite nature of nonlinear absorption properties of graphene oxide and its composites in comparison to the DMF solvent. DMF has strong TPA/3PA at higher intensities while graphene oxide and the composites show SA behavior at fs time scales with an excitation wavelength of 800 nm. When the transmission curves are divided by the pure solvent curve to eliminate the effect of solvent, we observe SA behavior for both graphene oxide and composites as shown in figure 31. In our experiment we observe RSA curve for graphene oxide and graphene

oxide composites at 800 nm while the earlier report [32] shows SA behavior at 790 nm, 80 fs laser excitation.

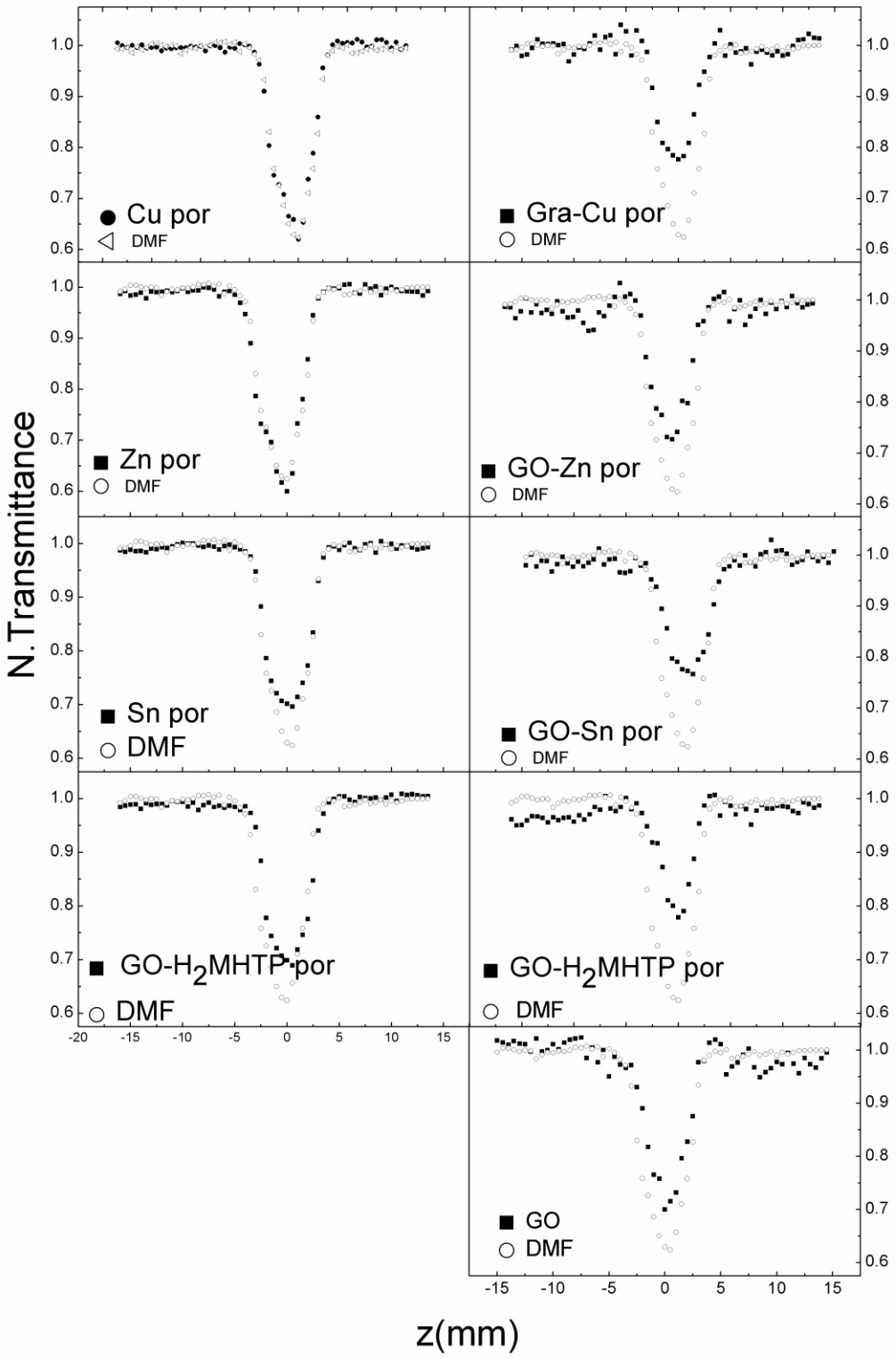

Figure 32. Open aperture Z-scan curves of pure porphyrins, GO and GO-porphyrin composites at 800 nm, fs regime before removing the solvent contribution.

However both results are in good agreement when we eliminate the solvent contribution. TPA coefficient (β) for graphene oxide composites is of order 10^{-11} cm/W with highest value of $1.37X10^{-11}$ cm/W for graphene oxide-Cu porphyrin composite compared to other composites. FS results suggest that graphene oxide composites act as good saturable absorbers, which can replace traditional saturable absorbers for different applications like pulse shaping and shutter in fs systems.

5.1.4 Conclusions

We have studied structural, spectroscopic and NLO properties of porphyrins (Cu, Zn, Sn, H_2MHTP, and VO) and their covalently linked composites with graphene oxide. Conjugation of porphyrins and graphene oxide is confirmed by optical absorption, FT-IR and FE-SEM studies. Fluorescence quenching in composites suggests the strong electronic interaction between porphyrin and graphene oxide excited states. This interaction is made through the energy transfer from porphyrin excited states to graphene oxide excited states resulting in reduction of singlet state lifetimes of graphene oxide composites. We have done comprehensive study of graphene oxide with different metal porphyrins and metal free porphyrin for NLA measurements and figure it out that graphene oxide with metal free porphyrin shows giant nonlinear absorption properties due to strong electron acceptor capability of graphene oxide molecule. In comparison with the metal porphyrins with graphene oxide composites, graphene oxide with metal free porphyrin shows high β, ESA. We also observed that fluorescence quenching is more for graphene oxide-metal free porphyrin. In ns time scales composites show good NLA coefficients compared to other regime. These high NLA coefficients are attributed due to Strong TPA, ESA and nonlinear scattering. The composite molecules of graphene oxide and porphyrin have higher FOM values leading to better optical limiting applications. FS results show SA behavior in all graphene oxide composites indicating that these materials can be used as good saturable absorbers in fs regime.

5.2 Graphene oxide-semiconductor (ZnO, TiO_2) nanoparticles

5.2.1 Introduction

After experimental breakthrough of graphene in 2004 [1] as a one atom thick sheet of sp^2-bonded carbon atoms in a hexagonal 2D lattice with high specific surface area (2630 m^2/g) available for sensing and metallic conductivity [5,36] at room temperature. Graphene has rapidly come out as a high promising nanomaterial with unique properties to open up a new research area for materials science, optoelectronics and photonics, with an aim for a wide range of technological applications [37–45]. Possible way to utilize the unique properties of graphene would be its incorporation in a composite. In this regard, graphene-containing composite materials have attracted a lot of attention [36, 46–51]. These properties make the 2-D graphene as an ideal platform to load metal or semiconductor nanoparticles, organic and biological molecules for optoelectronic, cellular imaging and drug delivery applications [52–55]. Moreover, the discovery of the ability of accepting electrons of graphene is to quench the electron donors, result in enhancement of the NLO properties. The covalent and noncovalent interactions of GO with different organic chromophores such as porphyrin/phthalocyanine hybrid materials exhibit excellent nonlinear absorption and optical limiting properties [10]. Recently, semiconductor nanoparticles have shown excellent optical properties that are dependent on the size and shape. In this sub-chapter we are presenting synthesis, spectroscopic and optical study of graphene oxide-(ZnO/TiO_2) nanoparticles towards optical limiting application. Quantum confinement induces the absorption shift towards higher energies in semiconductor nanocrystals have been proposed as light-emitting diodes [56] and single-electron transistors [57]. They have potential applications in optical limiting, optical computing, real time holography, optical correlators, and phase conjugators because of their high optical nonlinearity. Some physical, chemical and structural properties of the (ZnO, TiO_2)/graphene oxide composite are studied using micro-Raman, SEM, TEM FTIR, Powder XRD and optical absorption measurement techniques. Furthermore, we have studied the nonlinear optical absorption and optical limiting properties.

5.2.2 Experimental procedure

Graphene oxide (GO) is synthesized by the oxidative treatment of purified natural graphite using a modified Hummers method. Composites of graphene with nano particles (NPs) of ZnO and TiO_2 are prepared in situ as follows. For the 1:1 (by weight) GO–ZnO composite, Zn (II)acetate (0.020 g) is dissolved in methanol (35 ml), stirred for 15 min while the temperature is maintained at 55–60 ^oC. GO (0.007 g) is added and the mixture is stirred for another 20 min. To this mixture, KOH solution (0.060 g KOH in 20 ml methanol) is added drop wise under continued stirring. After stirring for 2 h, a gray mixture is obtained which is centrifuged at 13000 rpm for 15 min. The product is washed 3–5 times with water and ethanol and dried at 50 ºC. The 1:1 composite (by weight) of TiO_2 NPs with GO is prepared by adding titanium isopropoxide (0.027 ml) to 2-propanol (8 ml) under stirring. After 15 min, GO (0.007 g) is added to the solution which is again stirred for 15 min. A mixture of acetic acid and water (2+2 ml) is added to the solution to initiate hydrolysis. The stirring is continued for 6 h followed by aging for 5 h. The product is maintained at 80 ^oC for drying. The final product is obtained after annealing in a N_2 atmosphere at 410 ^oC for 1–2 h and then in air at 150 ^oC for 1 h.

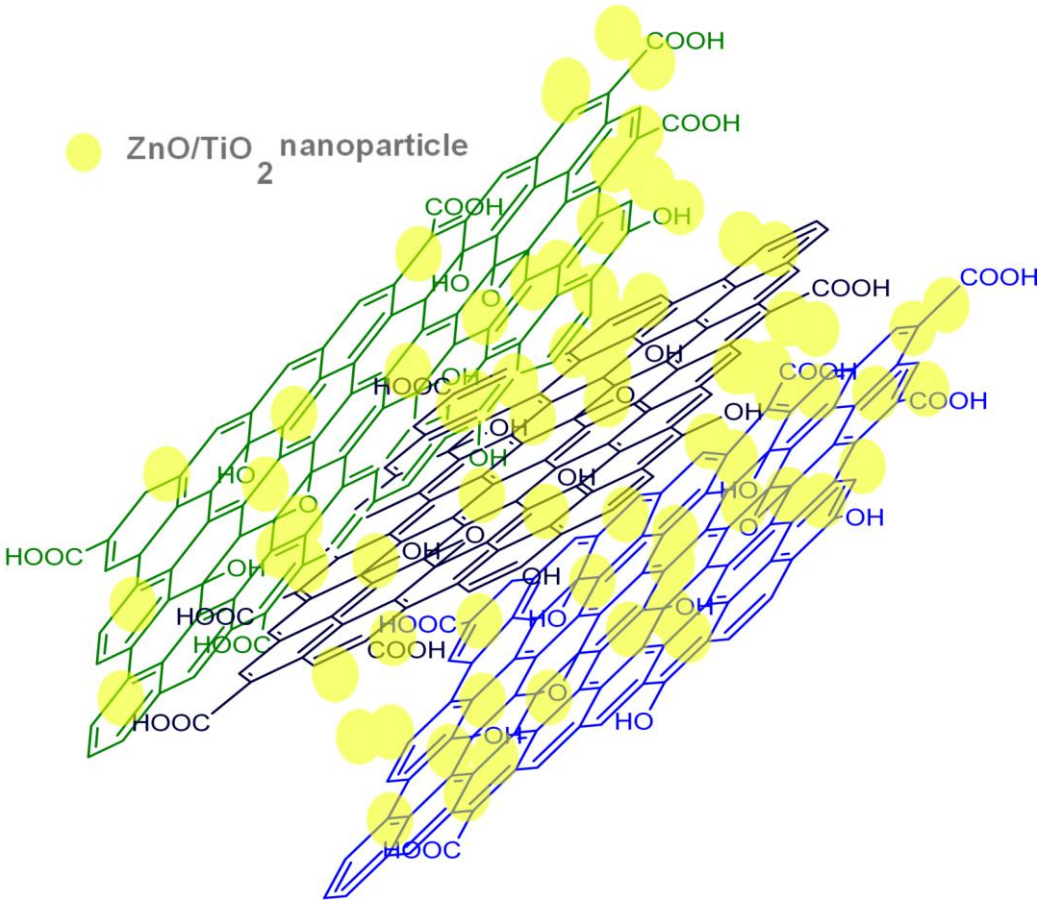

Figure 33. Schematic illustration of GO-ZnO/TiO_2 semiconductor nanoparticles composite materials.

5.2.3 Structural and spectroscopic characterization

5.2.3.1 Transmission electron microscopy (TEM)

The TEM images of GO, GO-ZnO and GO-TiO_2 are compared in figure 34. Graphene oxide sheet (figure 34 (a)) exhibits a smooth surface with lateral dimensions of about ~2 μm while the edges tend to fold and roll implying the crystallinity and the multilayer nature of the sheet. The TEM image of GO-ZnO designate that the particles typically have equiaxial morphology and are agglomerated.

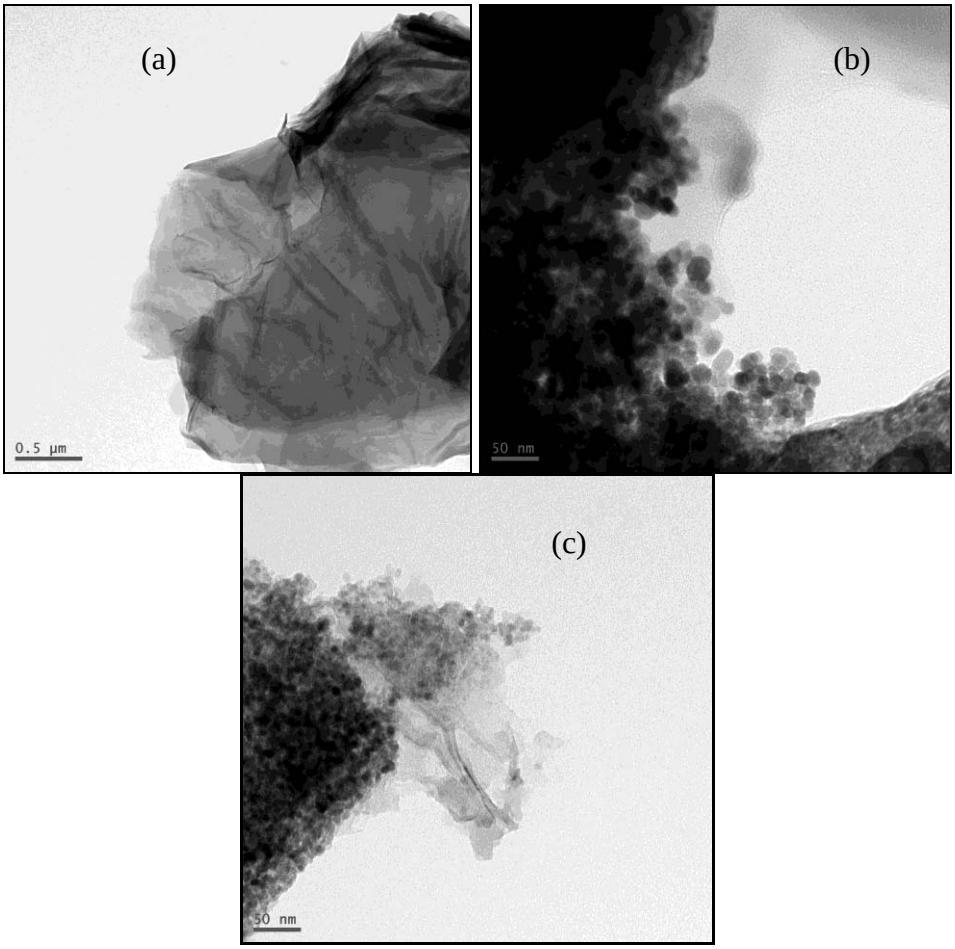

Figure 34. TEM image of (a) GO, (b) GO-ZnO and (c) GO-TiO_2.

The particle size distributions are resolute from TEM images shows that ZnO nanoparticles are anchored on the GO surface with a mean diameter of 15-20 nm with a narrow size distribution. It also should be noted that the particle size of the composite nanoparticle grown on GO is much smaller than metal nanoparticle prepared by the same method, mostly due to the confining effect of disordered in graphene nanosheets. Comparing the three images, the graphene layer can be clearly distinguished from the background and the ZnO and TiO_2 nanocrystals are directly grown on GO appeared to exhibit strong interactions with the underlying GO sheets. The prepared GO has hydrophilic functional groups (e.g., –OH, –COOH) in the outer layers of graphite that favours the nucleation and growth of nanomaterials on the GO surface.

5.2.3.2 Field emission-scanning electron microscopy studies

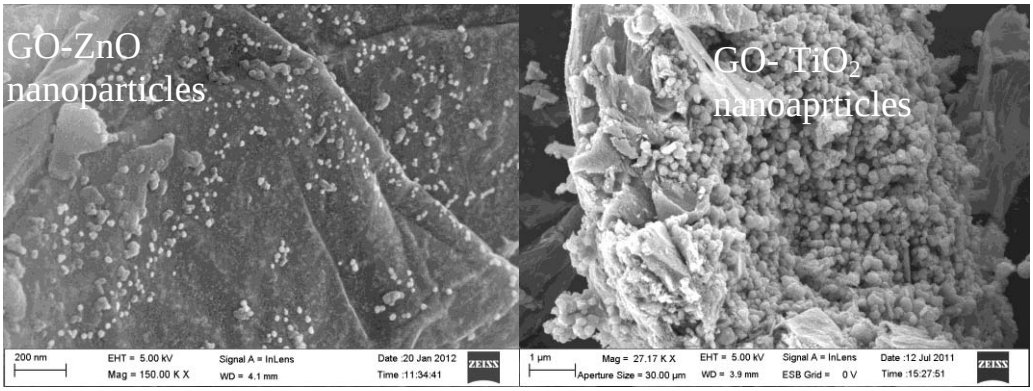

Figure 35 SEM images of GO-ZnO and GO-TiO_2 nanoparticles.

FE-SEM images of graphene oxide-ZnO and graphene oxide-TiO_2 nanoparticles are shown in the figure 35. These images were recorded using Carl-Zesis Ultra 55 model.

5.2.3.3 Powder X-ray diffraction studies

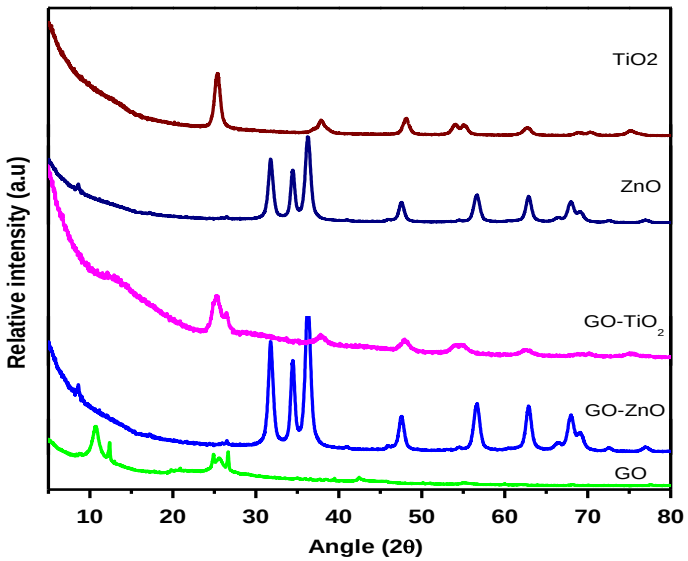

Figure 36. X-ray diffraction patterns of TiO_2 nanoparticles, ZnO nanoparticles, graphene oxide, graphene oxide-TiO_2 and graphene oxide-ZnO nanoparticles.

Figure 36 shows the powder XRD pattern of GO, GO-ZnO, GO-TiO_2 composites and pure metal nanoparticles. For graphene oxide, the diffraction peaks appear at around 2θ=10.78º corresponds to the (001) reflection while the peak at 2θ= 26.45º in graphite shifts negatively to 24-26º (peak center located at 24.42º)

accompanying with the broadening of the peak, demonstrating that GO will partially retain the graphitic crystal structure. The XRD analysis further shows that the main diffraction peaks of GO-ZnO composite are similar to that of pure ZnO and the peak values at values of 2θ = 31.7, 34.5, 36.1, 47.7, 56.5, 62.8 and 68.1º are consistent with the hexagonal phase wurtzite ZnO structure (JPCDS 36-1451) and the diffraction peaks at 8.67and 24.6 can be attributed to graphene. No diffraction peak from Zn or other impurity phases is found in any of the samples confirming that the products are single phased pure ZnO. The XRD pattern of GO-TiO_2 composites shows anatase TiO_2 structure (figure 36). The GO peak at 2θ = 10.78 º becomes broad possibly due to the reduced amount of graphene in the composite. In all the composite materials, the intensity of GO peak decreases greatly indicating the direct stacking of GO sheets is partly prevented by nanoparticles revealing that the stacking of GO sheets became more disordered.

5.2.3.4 Fourier transform infrared spectroscopy (FT-IR) studies

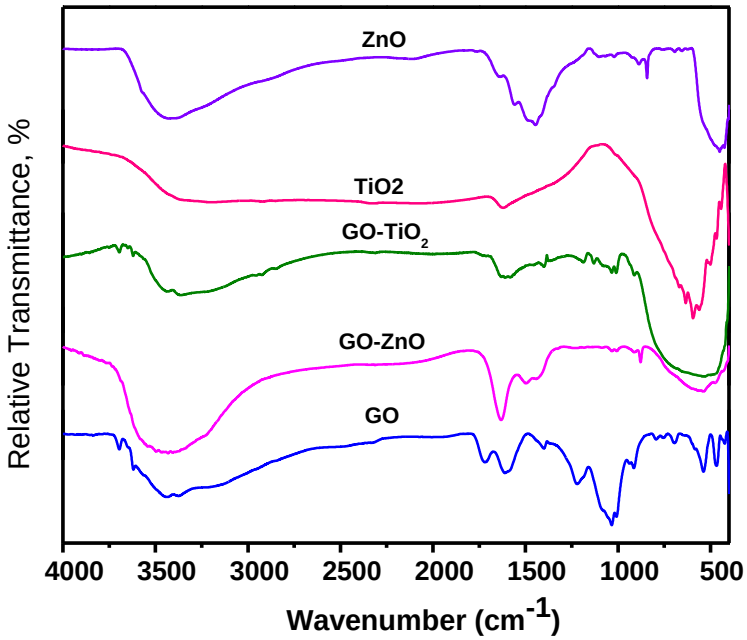

Figure 37. FT-IR spectrum of TiO_2 nanoparticles, ZnO nanoparticles, graphene oxide, graphene oxide-TiO_2 and graphene oxide-ZnO nanoparticles.

The FT-IR spectrum of GO, the band at 3430 cm^{-1} derives from the presence of free or associated hydroxyl groups (n–OH), which is assigned to the –OH groups linked to the basal plane of GO. There are also bands owing to carboxyl C=O

(1630 cm^{-1}) and C–O (1427 cm^{-1}) groups, epoxy C–O (1270 cm^{-1}), and alkoxy C–O (1120 cm^{-1}) groups located at the edges of the GO sheets. The peak at 1735 cm^{-1} is due to the C=O stretching of –COOH group. However, all these bands related with the oxygen-containing functional groups almost vanished in the spectra of GO-ZnO, GO-TiO_2 composites. This indicates oxygen-containing functional groups were almost removed in the process of reduction with hydrazine hydrate and thus the GO is transformed into graphene in the synthesis. The broad absorption peak at 557 cm^{-1} is the characteristic peak of the Zn–O stretching vibration of ZnO, and the peaks at about 1643 cm^{-1} can be attributed to the skeletal vibration of the graphene sheets. The strong absorption around 550 cm^{-1} is attributed to the vibration of Ti–O–Ti bonds in TiO_2. These results demonstrate that the nano particles of ZnO and TiO_2 were grafted onto the graphene plane.

5.2.3.5 Micro- Raman studies

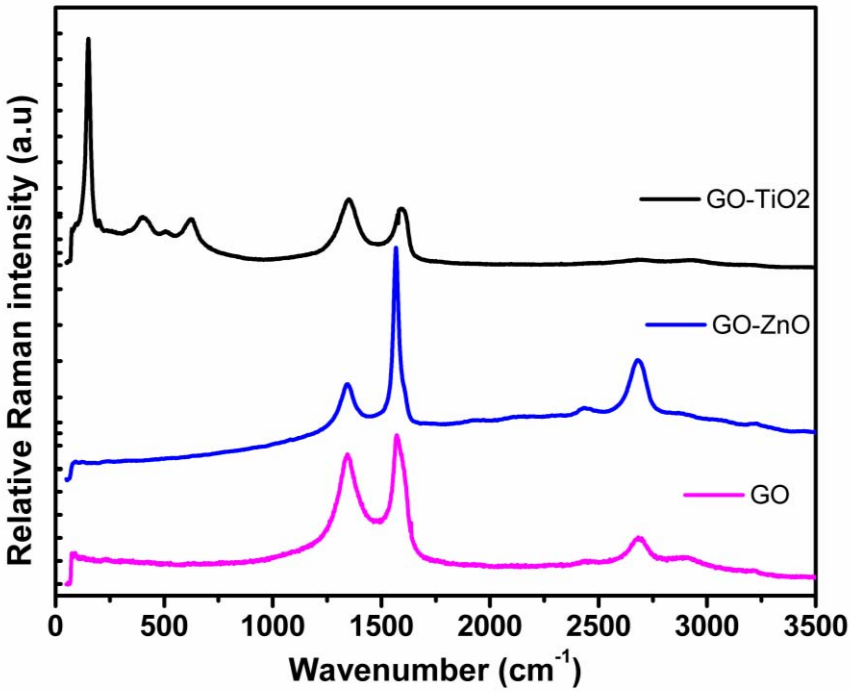

Figure 38. Micro-Raman spectra of graphene oxide, graphene oxide-ZnO and graphene oxide-TiO_2 composites.

The typical bands of graphene oxide can be found at 1598 cm^{-1} and 1350 cm^{-1}, corresponding to the well-documented G and D bands, which are usually

attributed to the E_{2g} phonon of C sp^2 atoms, and the breathing mode of κ-point phonons of A_{1g} symmetry due to local defects and disorders, particularly located at the edges of graphene and graphite platelets. The peak intensity (I_D/I_G) ratio can be assigned to lower defects and disorders of the graphitized structures, smaller fraction of sp^3/sp^2-bonded carbon, and/or larger size of the in-plane graphitic crystallite sp^2 domains. The Raman spectra of GO (figure 38) shows the G band about 1585 cm^{-1} and the D band at 1356 cm^{-1}. The I_D/I_G values are found to be 0.88, 0.73 and 1.08 for GO, GO-ZnO and GO-TiO_2, respectively. It is found that the I_D/I_G ratio decreases for GO-ZnO composites and increases in case of GO-TiO_2 composites. This is due to appearance of further defects in the reduced graphene oxide sheets due to the photocatalytic degradation of GO by TiO_2 nanoparticles. The four peaks observed for GO-TiO_2 at the low frequency region are assigned to the E_{1g} (146 cm^{-1}), B_{1g} (396 cm^{-1}), A_{1g} (517 cm^{-1}) and E_g (636 cm^{-1}) modes of anatase phase. Raman spectroscopy is also used to examine the single, bi and multilayer characteristics of graphene and/or graphene oxide layers. The typical G band peak position of the single-layer graphene oxide appears at 1585 cm^{-1} and the position of the band shifts about 6 cm^{-1} into lower frequencies after stacking further graphene oxide layers (for 2-6 layers G band shifts to 1579 cm^{-1}). In addition, shape and position of the 2D bands are the key parameters indicating formation and the layer numbers of graphene oxide sheets. The 2D peak position of the single-layer graphene oxide sheets are usually observed at 2683 cm^{-1}, while the 2D band of multilayer (2-4 layers) shifts to higher wave numbers by 19 cm^{-1}. Here, the observed 2D bands of the GO sheets were centered at around 2704 cm^{-1} and G-band at 1576 cm^{-1} indicates the formation of multiple layers (6-8 layers) of the GO sheets and the sheets are largely dominated by disorder related features.

5.2.3.6 Linear optical absorption studies

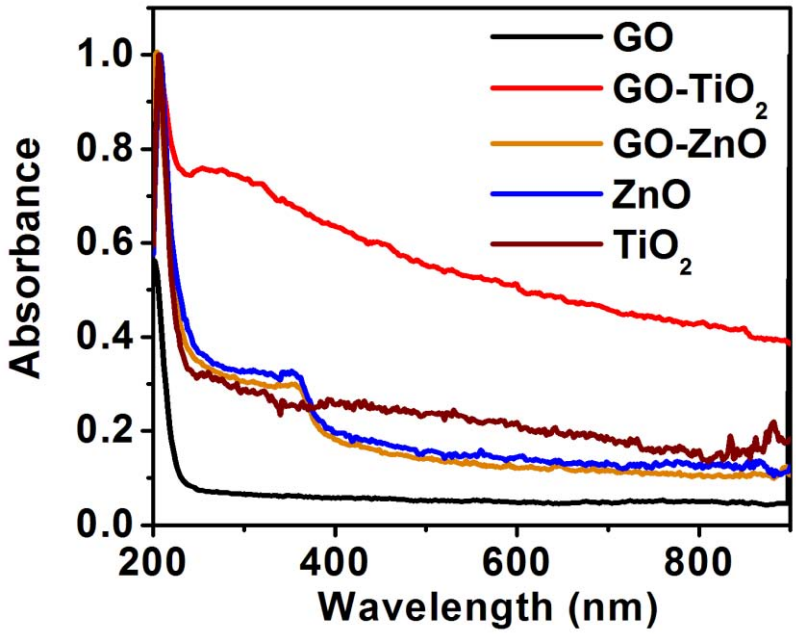

Figure 39. UV-Visible absorption spectra of GO, ZnO nanoparticles, TiO_2 nanoparticles, GO-TiO_2 and GO-ZnO nanoparticles

Figure 39 shows the UV–Vis absorption spectra of synthesized GO, GO-ZnO and GO-TiO_2 nanocomposites, together with pure ZnO and TiO_2 for comparison. For UV–Vis measurements, the samples are dispersed in ethanol by sonication. It can be seen that the graphene oxide (figure 39) shows a strong absorption in the UV region at 206 nm together with a weak shoulder peak at 247 nm. The absorption peak at 247 nm is generally regarded as the excitation of π-plasmon of graphitic structure. The absorption spectrum of GO-ZnO shows a strong absorption peak at 355 nm and a weak peak at 266 nm. The large enhancement of the absorbance in the whole spectral region is observed indicating that GO dispersion is converted into graphene to lead to the restoration of π-conjugated network within the GO-ZnO. GO-TiO_2 absorbs in the entire visible region and the absorption edge of GO-TiO_2 is red-shifted by 10 nm compared with that of pure TiO_2 nanoparticles. This implies that oxygen containing functional groups of GO forms a surface complex with TiO_2 nanoparticles and the rearrangement of the energy levels leads to a charge transfer surface complex on TiO_2.

5.2.3.7 Steady state fluorescence studies

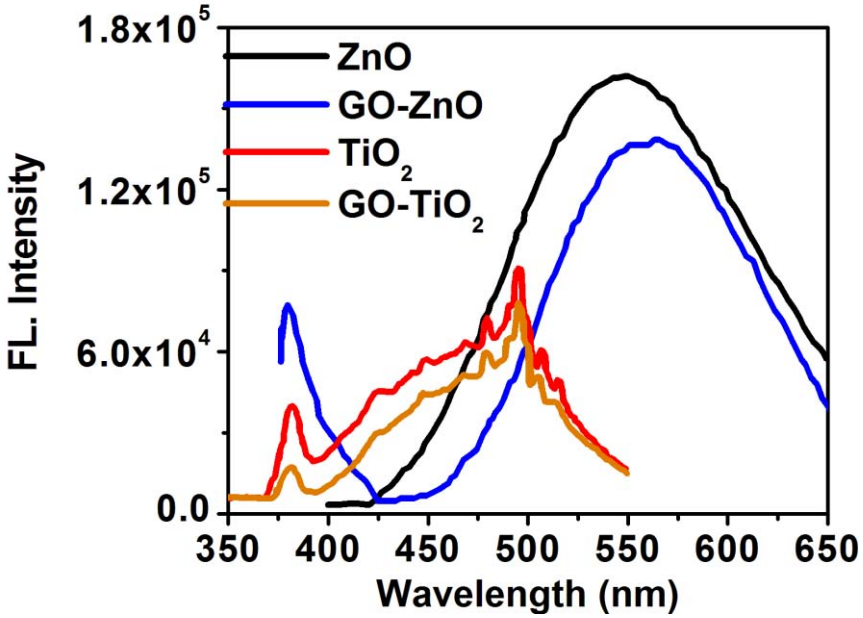

Figure 40. Steady state emission spectra of ZnO, TiO_2, GO-ZnO and GO-TiO_2 composites.

Photoluminescence is employed to study the surface structure and excited states of semiconductor. The electron–hole pair recombination after being irradiated, the semiconductor emits photons, resulting in photoluminescence. Figure 40 shows the photoluminescence spectrum of GO-ZnO composites on excitation at λ_{ex}=320 nm at room temperature. The spectrum exhibits two emission peaks, one located at around 392 nm (UV region) corresponding to the near band gap excitonic emission and the other located at around 520 nm, which attributed to the presence of singly ionized oxygen vacancies. The emission is caused by the radiative recombination of a photogenerated hole with an electron occupying the oxygen vacancy. The emission intensity is found to be lower compared to the emission spectra of pure ZnO nanoparicles. This suggests that an additional pathway for the disappearance of the charge carriers dominates because of the interactions between the excited ZnO particles and the GO sheets. Similar results are also observed for GO-TiO_2 composites. On excitation at λ_{ex}=320 nm, the emission spectra GO-TiO_2 exhibits a broad emission in the range 400-550 nm.

An abrupt emission quenching of TiO_2 is observed in the spectra of GO–TiO_2 composites representing that electrons transferred from excited TiO_2 to graphene.

5.2.3.8 Time-correlated single photon counting (TCSPC) studies

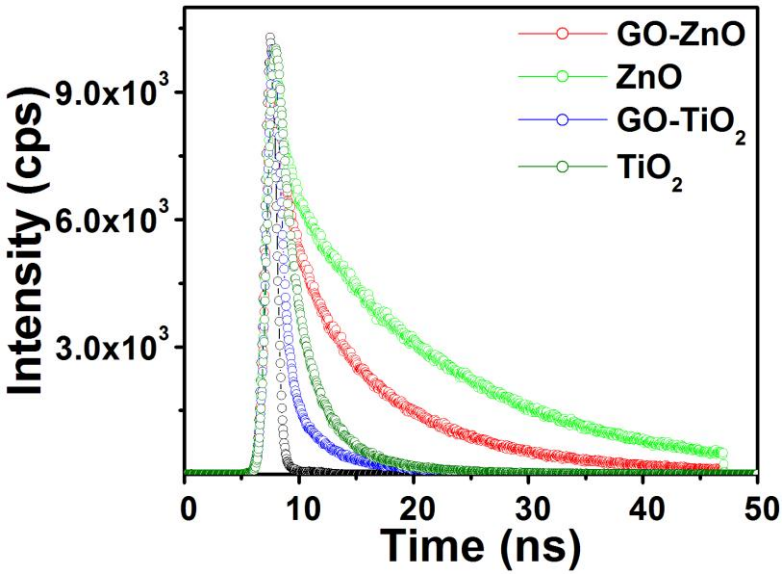

Figure 40. Fluorescence lifetime decay of GO-ZnO, GO-TiO_2 composites along with pure ZnO and TiO_2 nanoparticles. An incident laser pulse wavelength of 295 nm is used for this experiment. Emission is monitored at 550 nm for GO-ZnO and ZnO and 495 nm for the GO-TiO_2 and TiO_2 materials

The interaction between the excited metal nano particles (ZnO and TiO_2) and GO is indeed responsible for emission quenching is further studied by time resolve emission decay. Figure 40 shows the emission decay of GO-ZnO and GO-TiO_2 composites. The fluorescence decay profiles of GO-ZnO and GO-TiO_2 fitted to three exponential decay functions $I(t)= A+B_1\exp(-t/\tau_1)+\exp(-t/\tau_2)+\exp(-t/\tau_3)$. Where I (t) is the fluorescence intensity at time t, A is constant, and B_1, B_2 and B_3 are the pre exponential factors of lifetimes τ_1, τ_2 and τ_3 respectively. The fluorescence lifetime of GO-ZnO exhibits a short lifetime of τ_1= 0.52 ns (12.34 %), τ_2=2.8 ns (45.6 %) and long lifetime τ_3 =28.4 ns (42.06 %). The observed lifetimes are slightly smaller than the pure ZnO nanoparticles. This is consistent with the results observed for the concentration dependent emission decay of ZnO treated with GO. The fluorescence lifetime of GO-TiO_2 exhibits three exponential

decay function with a lifetime of τ_1= 0.03 ns (44.2 %), τ_2= 0.5 ns (15.56 %) and 5.05 (40.24 %) respectively. The average lifetime GO-TiO_2 composite is found to be 4.6 ns.

Compound	τ_1 (ns)	A_1, (%)	τ_2 (ns)	A_2, (%)	τ_3 (ns)	A_3, (%)
ZnO	0.87	10.3	2.76	38.45	32.5	51.25
GO-ZnO	0.23	6.36	1.93	44.67	28.3	48.97
TiO_2	0.09	31.13	0.93	19.89	9.12	48.98
GO- TiO_2	0.03	44.20	0.5	15.56	8.67	40.24

Table.4. Summary of fluorescence lifetime of nano particles and its GO composites

5.2.4 NLO measurements

Nonlinear absorption and optical limiting properties of graphene-semiconductor nanoaparticles are measured using nanosescond laser source, a Nd: YAG laser (INDI-40, Spectra physics) delivers fundamental wavelength 1064 nm and its frequency doubled wavelength 532 nm with 6 ns pulse duration and a repetition rate of 10 Hz. Graphene oxide, semiconductor nanoparticles and their composites are taken as solutions in methanol for the experimental studies. 0.2 mg. mL^{-1} concentration of GO-ZnO/TiO_2, ZnO nanoparticles, TiO_2 nanparticles and 1.5 mg/ml of GO are taken for experimental Z-scan studies. In the composite GO concentration is estimated to be 1.5 mg/ml [10]. Open aperture Z-scan studies are carried out by focusing the input beam on to the sample using a lens of 120 mm focal length forming a 27 μm spot size at the focus in ns regime. The transmitted light is collected with a photodiode. The peak intensities estimated at the focus in Z-scan experiments are 300 MW/cm^2 in ns experiments

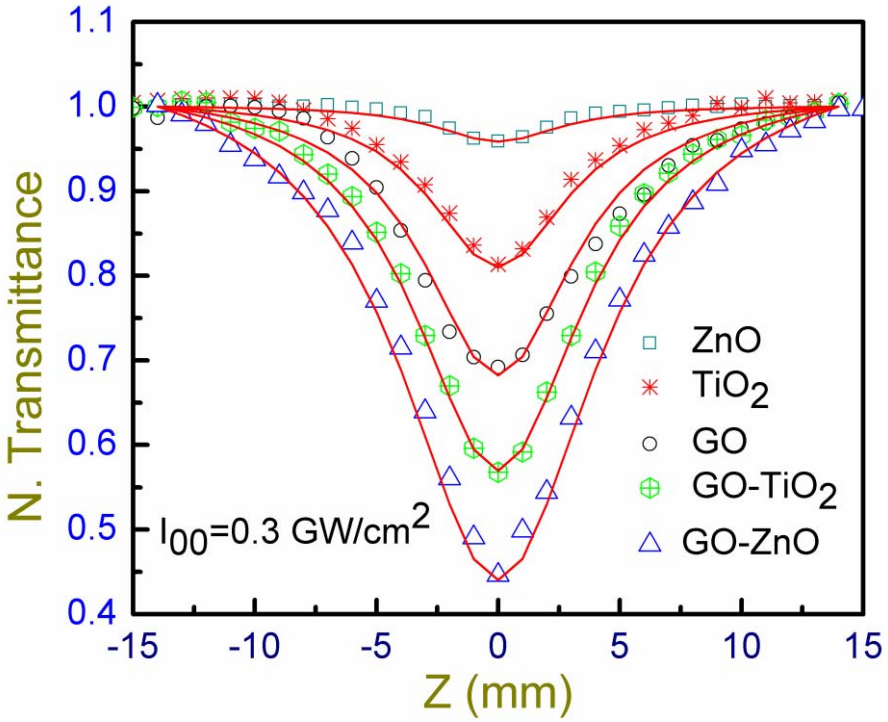

Figure 41. Open aperture Z-scan curves for GO-ZnO/TiO_2, GO, TiO_2 and ZnO nanoparticles.

Figure 41 shows typical open aperture Z-scan curves for composites and pure semiconductor nanoparticles and these curves were fitted with rate equations model which was discussed in the earlier section 5.1.3. Curves for pure nanoparticles and composites show reverse saturable absorption behavior in the nanosecond regime. Composites have shown enhanced nonlinear absorption behavior compared to GO and semiconductor nanoparticles. Nonlinear absorption of composites is predominantly due to two-photon absorption mechanism. GO-ZnO nanoparticles composite has shown high two-photon absorption coefficient over GO, GO-TiO_2 nanoparticles, ZnO nanoparticles and TiO_2 nanoparticles. Excited state parameters of ZnO nanoparticles, TiO_2 nanoparticles, GO, GO-TiO_2 nanoparticles and GO-ZnO nanoparticles are shown in Table 5.

Samples	β (cm/GW)	$(\sigma_1)x10^{-19}$ cm^2	τ_1 (ns)	τ_2 (ps)
ZnO nanoparticles	107	1.04	3.6	4.2
TiO_2 nanoparticles	395	2.24	1.1	3.4
GO	900	5.7	0.009	0.009
GO- ZnO nanoparticles	2280	12.6	2.16	3.5
GO- TiO_2 nanoparticles	1270	8.7	0.53	1.2

Table 5. Excited state parameters β, σ_1, τ_1 and τ_2 of graphene oxide, ZnO nanoparticles, TiO_2 nanoparticles, GO-ZnO nanoparticles and GO-TiO_2 nanoparticles composites in ns regime.

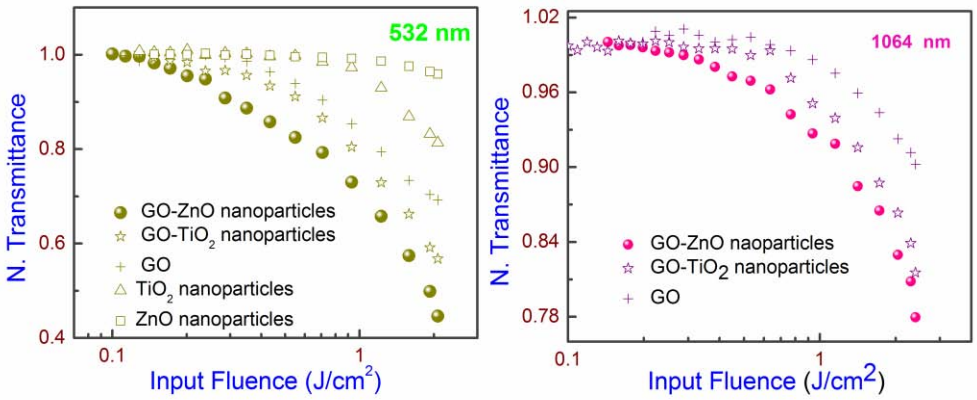

Figure 42. Optical limiting curves for GO-ZnO/TiO_2 nanoparticles at 532 and 1064 nm.

We have observed significant optical limiting behavior in GO-ZnO/TiO_2 composites compared to pure nanopaticles and GO. Recent report on GO shows that it act as a broad band optical limiter [9]. Optical limiting curves at two different wavelengths shown in the figure 42 suggest that these composite materials are suitable for broad band optical limiter. We estimated the limiting thresholds of GO, GO-TiO_2 and GO-ZnO composites to be 0.80, 0.55 and 0.48 J /cm^2 at 532 nm, respectively and 1.65, 1.35 and 1.15 J/cm^2 at 1064 nm, respectively. Composites exhibit enhanced optical limiting behavior which arises from TPA and nonlinear scattering. TPA is a dominant mechanism in both GO and semiconductor nanoparticles, leading to enhanced nonlinear absorption behavior in composites.

5.2.5 Conclusions

We have studied structural, spectroscopic and NLO properties of graphene oxide-semiconductor nanoparticles (ZnO, TiO_2) hybrid composites. Conjugation of semiconductor nanoparticles and graphene oxide is confirmed by optical absorption, FT-IR, TEM and FE-SEM studies. Fluorescence quenching in composites suggests the strong electronic interaction between semiconductor nanoparticles and graphene oxide excited states. This interaction is made through the energy transfer from semiconductor nanoparticles excited states to graphene oxide excited states resulting in reduction of singlet state lifetimes of graphene oxide composites. In comparison with the semiconductor nanoparticles and GO, composites have shown strong nonlinear optical absorption behavior due to higher two-photon absorption coefficient. The composite molecules of graphene oxide and semiconductor nanoparticles have high damage threshold as well as low limiting threshold values leading to better optical limiting applications.

5.3 Graphene oxide-metal (Ag, Au) nanoparticles

5.3.1 Introduction

Metal nanoparticles are well studied for various applications in biology, chemistry and physics. The quantum size effect is involved when the de Broglie wavelength of the valence electrons is of the same order as the size of the particle itself. Then, the particles behave electronically as zero-dimensional quantum dots or quantum boxes relevant to quantum mechanical rules. Freely mobile electrons are trapped in such metal boxes and show a characteristic collective oscillation frequency of the plasma resonance, giving rise to the so-called plasmon resonance band (PRB). It is observed near 530 nm for Au nanoparticles and near 420 nm for Ag nanoparticles in the 5-20 nm diameter range. In recent years, interest is centered on hybrid materials based on metal nanoparticles, and deposition of metal nanoparticles on to material surfaces has been investigated for the following reasons: interparticle properties of Au/Ag metal nanoparticles have potential applications in catalysis, sensing, as well as electronic and optoelectronic devices. Incorporation of metal nanoparticles can improve the physical and mechanical properties of materials. The decoration of various materials with with Au nanoparticles including CNTs and graphene [58, 59] has been demonstrated. The existing approaches for this decoration include covalent, noncovalent and direct deposition of nanoparticles. In this sub chapter, we have prepared graphene oxide-Au/Ag nanocomposites by in situ reduction of gold salt/$AgNO_3$ on graphene oxide using laser assisted photocatalytic reduction. This work was done in aqueous solution at ambient conditions. The main advantage of this method to prepare metal nanoparticles-GO hybrids is to avoid the use of toxic chemical reducing agents thus providing a green approach for the synthesis and processing of metal-graphene oxide nanocomposites. There are few reports on photochemical and photothermal reduction to prepare metal-GO nanocomposites [60, 61]. Here we describe our findings regarding laser photoreduction of GO and the metal ions and the formation of GO-metal nanocomposites. First, we demonstrate that GO can be reduced by the 532 nm nanosecond laser irradiation in reducing environment as water-PVA mixture.

Second, we demonstrate that gold and silver ions can be reduced by laser irradiation on GO sheets.

5.3.2 Experimental details and preliminary results

In the experiments, GO was prepared according to the modified Hummers and offeman method described in section 5.1. For the reduction of GO alone, the GO solution was irradiated with a pulsed 532 nm wavelength Nd:YAG laser (unfocused, hν = 2.32 eV, pulse width τ = 6 ns, repetition rate =10 Hz, Model: Spectra physics-INDI-40) under continuous stirring. For the Au-GO nanocomposite preparation, hydrogen tetrachloroauarate (III) trihydrate ($HAuCl_4$. $3H_2O$) chloride solution in PVA solution, with centrifuged GO solution was added.

5.3.3 Laser assisted photo-reduction of GO

As shown in the figure 43, following 532 nm laser irradiation for few minutes, the yellow golden colour of the GO solution completely changes into black thus partial reduction of GO and the restoration of the sp^2 carbon sites in the laser treated graphene oxide (LTG). The irradiation time required for the reduction of GO varies from a few to several minutes depending on the solvent, laser power and solution volume. The laser irradiation process leads to the formation of multiple defect sites on the surface of partially reduced GO which provide an excellent environment for anchoring the metal nanoparticles, thus impending the particle migration and increasing the catalyst support interaction.

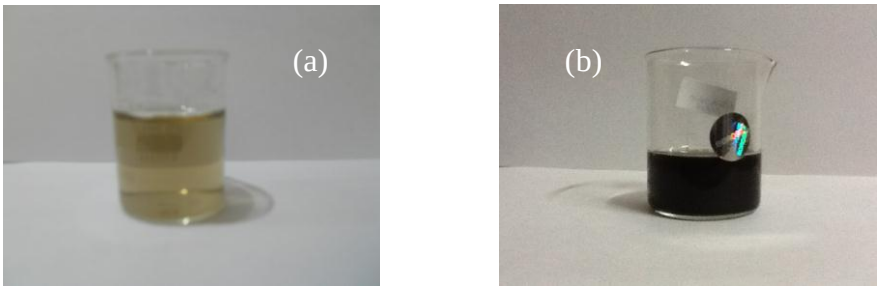

Figure 43. (a) Centrifuged graphene oxide (b) after laser irradiation of graphene oxide for few minutes

5.3.4 Photo-reduction of silver and gold ions on GO in PVA-water mixed solution

Partially oxidized GO has domains of sp^2 and sp^3 carbon hybridization exist as the partial oxidation of graphite sheets takes place. Although fully oxidized GO is an insulator; partially oxidized GO has semiconductor properties with a bandgap that is determined by the extent of oxygenation of graphite sheets which determines the size of the sp^2 π-conjugated domains. The sp^2 domains act as semiconductors with bandgaps that increase with increasing the O/C ratio from 2.5 to 4.0 eV.

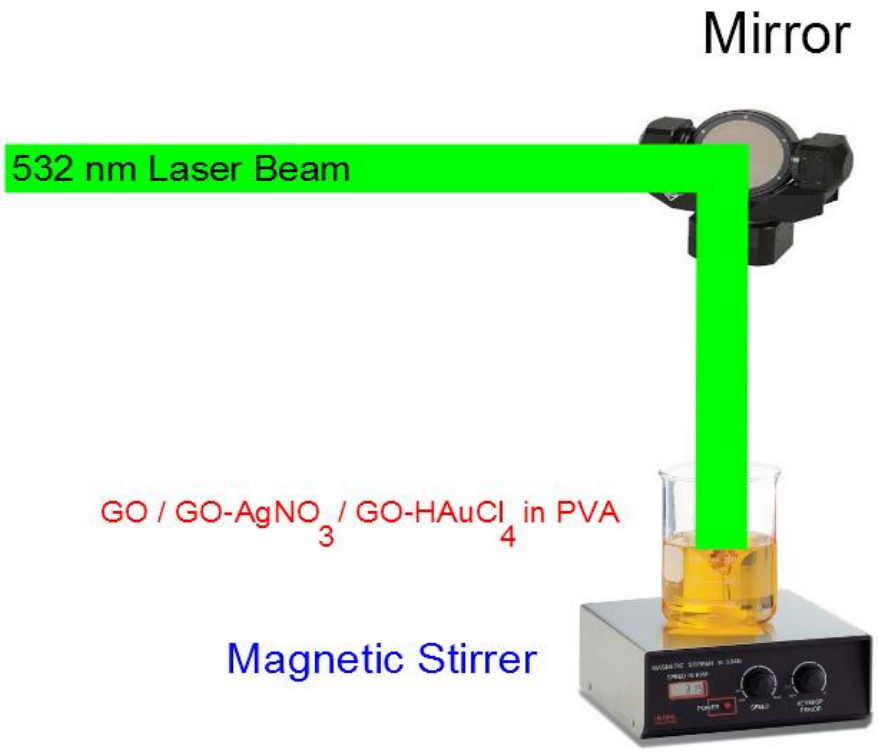

Figure. 44. Laser irradiation method for the preparation of partially reduced graphene oxide (RGO), RGO-Ag nanocomposite and RGO-Au nanocomposite.

The photoexcitation of the sp^2 domains in partially oxidized GO with light energy exceeding their bandgaps results in the generation of an electron-hole pair (e^--h^+) within the semiconductor domain. In this work absorption of two 532 nm photons generates an electron-hole pair within the semiconductor GO. The photogenerated electrons in GO can lead to the reduction of the metal ions simultaneously with the partial reduction of GO and thus the formation of metal

nanoparticles supported on the partially reduced GO. The photogenerated holes can react with GO in the presence of water with evolution of CO and CO_2 gases thus creating structural defects within the partially reduced GO nanosheets. The reduction of silver ions, gold ions, and formation of nanoparticles are clearly evident by the observation of colour of Au and Ag nanoparticles as shown in figure 45. It is also evident from the surface resonance (SPR) band of these nanoparticles as shown in the figures 46 and 47.

Figure 45. Laser treated solutions of Au nanoparticles, GO-Au nanocomposite, Ag nanoparticles and GO-Ag nanocomposite in PVA.

5.3.5 Optical absorption studies

Optical absorption spectra of Au nanoparticles, RGO-Au nanocomposite and pure precursor $HAuCl_4$ are shown in the figure 46. Absorption maximum of RGO-Au nanocomposite was intense and sharp than pure Au nanoparticles at 526 nm. The absorbance value was also quiet high in the nanocomposite. This is due to GO, which also acts as a reducing agent other than PVA for the preparation of gold nanoparticles. These nanoparticles were attached to GO sheets by physical adsorption/chemical modification. This attachment was very strong; it would not break even after centrifuging at 6000 rpm for 30 mins. GO-Au nanocomposite absorption spectrum was recorded with centrifuged solution.

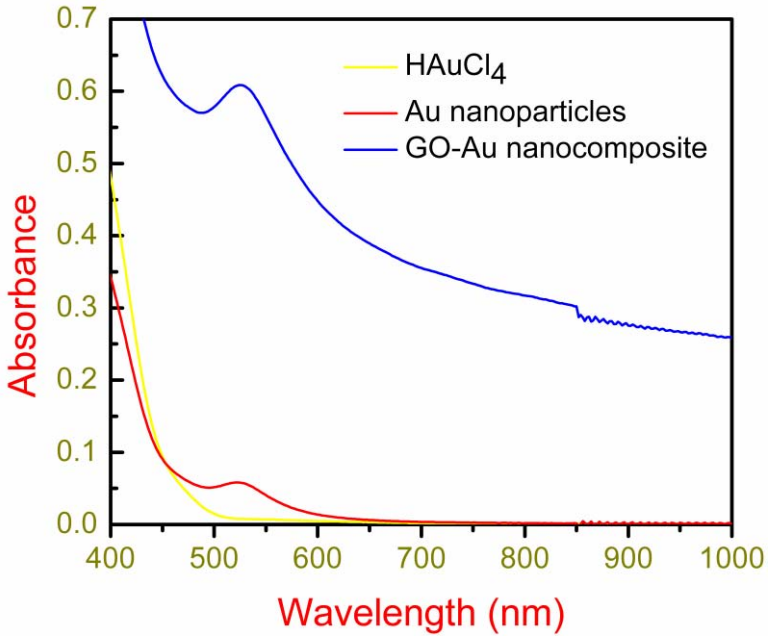

Figure 46. Optical absorption spectra of Au nanoparticles, RGO-Au nanocomposite under laser irradiation and $HAuCl_4.3H_2O$

Figure 47 shows the optical absorption spectra of silver nanoparticles, RGO and RGO-Silver nanoparticles composite. GO has absoprtion maximum at 268 nm [13] where as partially RGO has an absorption peak at 276 nm can be seen in the figure 47. Nanocomposite absorbance was high compared to partially RGO and silver nanoparticles. It has broad absorption from UV to NIR region.

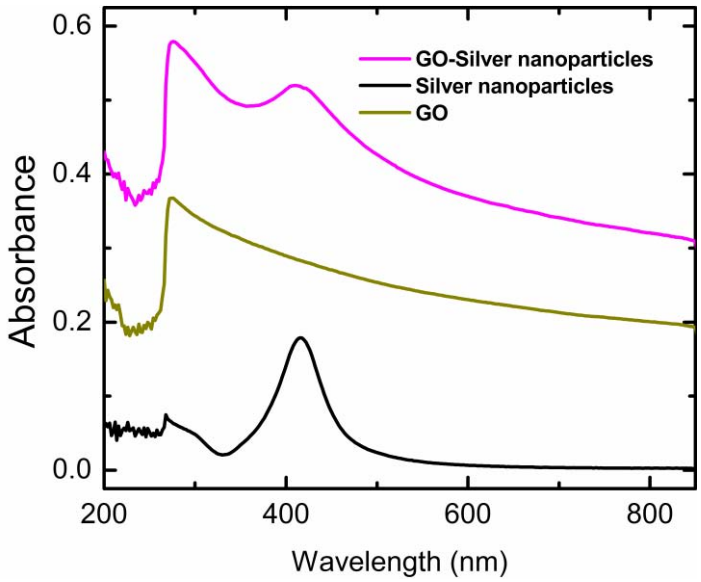

Figure 47. Optical absorption spectra of GO and its composition with silver nanoparticles

5.3.6 Field emission scanning electron microscopy studies

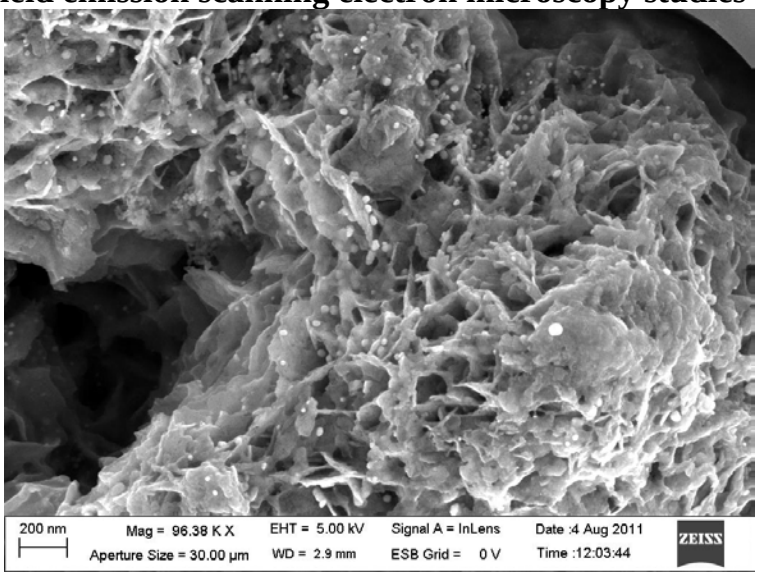

Figure 48. FE-SEM image for attachment of gold naoparticles to partially reduced graphene oxide.

Figures 48 and 49 show the SEM images of gold and silver nanoparticles on graphene oxide sheets by photo irradaiation of graphene oxide and $HAuCl_4.3H_2O$ and graphene oxide and silver salt, respectively.

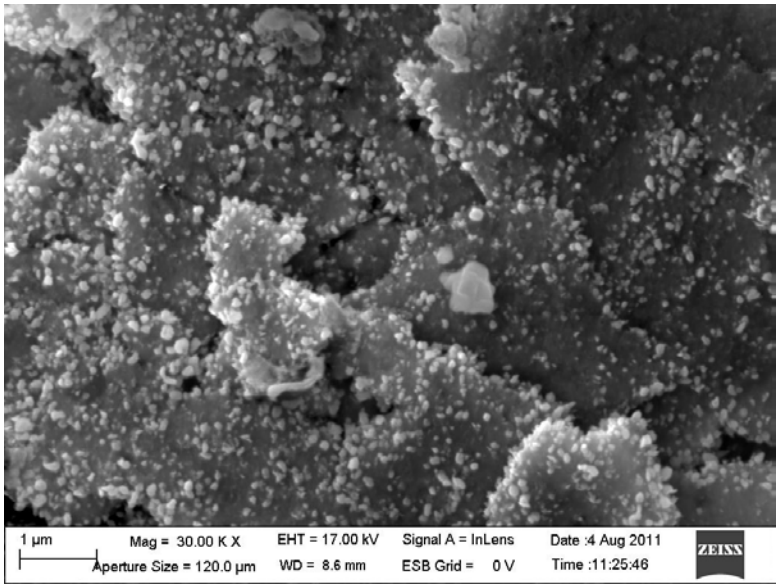

Figure 49. FE-SEM image for attachment of silver naoparticles to graphene oxide

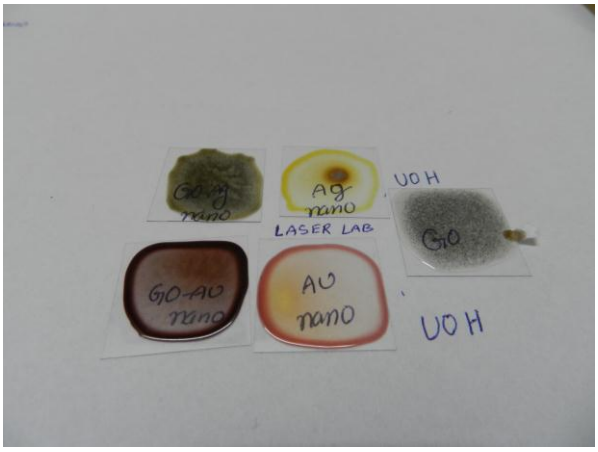

Figure 50. Films prepared from the solutions of nanoparticles and nanocomposties are formed by laser irradaition method.

Figure 50 show the thin films of pure nanoparticles, partially RGO and nanocomposites, which were prepared by using laser irradaited solutions .

5.3.7 Nonlinear optical measurements

Optical limiting studies were carried out by using Z-scan technique. We have observed significant optical limiting behavior in GO-Ag/Au nanoparticles composites compared with pure nanopaticles and GO. Recent report on GO shown that it act as a broad band optical limiter [9]. From the figure 51, we estimated the limiting thresholds of GO, GO-Ag nanoparticles and GO-Au nanoparticles composites to be 0.80, 0.6 and 0.48 J /cm^2 at 532 nm, respectively.

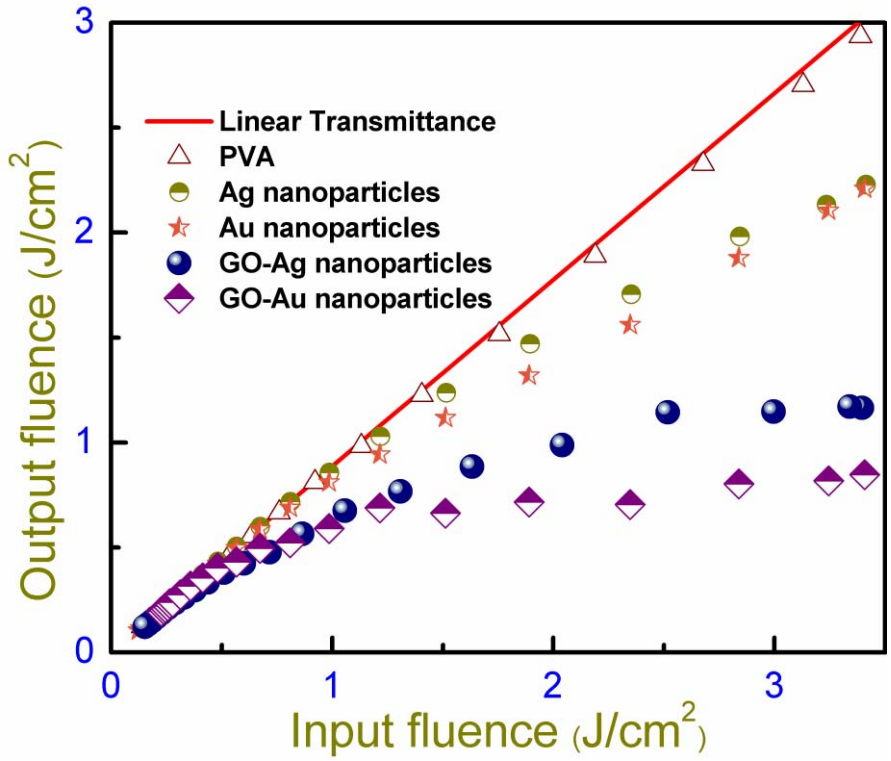

Figure 51. Optical limiting behaviour of GO-metal composites.

Both composites exhibit enhanced optical limiting behavior which arises from TPA and nonlinear scattering. TPA is a dominant mechanism in both GO and semiconductor nanoparticles, leads to enhance nonlinear absorption behavior in composites that result in enhancing the optical limiting behavior.

5.4 References

1. K. S. Novoselov, A. K. Geim, S. V. Morozov, D. Jiang, Y. Zhang, S. V. Dubonos, I. V. Grigorieva and A. A. Firsov. Science, **306**, 666 (2004).

2. F. Bonaccorso, Z. Sun, T. Hasan and A. C. Ferrari, Nature Photon., **4**, 611, (2010).

3. T. Mueller, F. Xia and P. Avouris, Nature Photon., **4**, 297, (2010).

4. F. Schwierz, Nature Nanotech., **5**, 487, (2010).

5. A. K. Geim and K. S. Novoselov, Nature Mater., **6**, 183, (2007).

6. C. N. R. Rao, A. K. Sood, K. S. subrahmanyam and A. Govindraj, Angew. Chem. Int. Ed., **48**, 7752, (2009).

7. J. Yang, C. Tian, L. Wang and H. Fu, J. Mater. Chem., **21**, 3384, (2011).

8. W. Xu, L. Zhang, J. Li, Y. Lu, H. Li, Y. Ma, W. Wang and S. Yu, J. Mater. Chem., **21**, 4593, (2011).

9. Y. Liu, J. Zhou, X. Zhang, Z. Liu, X. Wan, J. Tian, T. Wang and Y. Chen, Carbon, **47**, 3113, (2009).

10. M. Bala Murali Krishna, V. Praveen Kumar, N. Venkatramaiah, R. Venkatesan, and D. Narayana Rao, Appl. Phys. Lett., **98**, 081106, (2011).

11. X. Zhang, X. Zhao, Z. Liu, S. Shi, W. Zhou, J. Tian, Y. Xu and Y. Chen, J. Opt, **13**, 075202, (2011).

12. N. Venkatram, P. Lakshminarayana, M. K. Kumar, B. M. Goh, K. P. Loh, Q. Xu and Wei Ji, Nanotechnology, **21**, 415203 (2010).

13. X. Zhang, X. Zhao, Z. Liu, Y. Liu, Y. Chen and J. Tian, Opt. Exp., **17**, 23959 (2009).

14. Z. Liu, Y. Xu, X. Zhang, X. Zhang, Y. Chen and J. Tian, J. Phys. Chem. B, **113**, 9681 (2009).

15. Y. Xu, Z. Liu, X. Zhang, Y. Wang, J. Tian, Y. Huang, Y. Ma, X. Zhang and Y. Chen, Adv. Mater., **21**, 1275 (2009).

16. M. O. Senge, M. Fazekas, E. G. A. Notaras, W. J. Blau, M. Zawadzka, O. B. Locos, and E. M. N. Mhuircheartaigh, Adv. Mater., **19**, 2737, (2007).

17. P. Prem Kiran, D. R. Reddy, A. K. Dharmadhikari, B. G. Maiya, G. R. Kumar and D. N. Rao, Chem. Phys. Lett., **418**, 442 (2006).

18. D. Narayana Rao, Opt. Mater., **21**, 45, (2002).

19. M. Calvete, G. Y. Yang and M. Hanack, Synthetic Metals, **141,** 231, (2004).

20. S. Keinan, M. J. Therien, D. N. Beratan and W. Yang, J. Phys. Chem. A, 2008, 12203, (**112**).

21. P. C. Ray and J. Leszczynski, Chem. Phys. Lett., **419**, 578 (2006).

22. E. G. A. Notaras, M. Fazekas, J. J. Doyle, W. J. Blau and M. O. Senge, Chem. Comm., 2166 (2007).

23. T. E. O. Screen, K. B. Lawton, G. S. Wilson, N. Dolney, R. Ispasoiu, T. Goodson III, S. J. Martin, D. C. Bradley and H. L. Anderson, J. Mater. Chem., **11**, 312 (2001).

24. A.D.Adler, F.R.Longo, J.D.Finarelli, J.Goldmacher, J.Assour and L. Korsakoff, J.Org.Chem., **32**, 476 (1967).

25. N. Venkatramaiah and R.Venkatesan, Solid. State. Sci., **13**, 616 (2011).

26. H. A. Becerril, J. Mao, Z. F. Liu, R. M. Stoltenberg, Z. N. Bao and Y. S. Chen, ACS Nano, **2**, 463 (2008).

27. Z. F. Liu, Q. Liu, X. Y. Zhang, Y. Huang, Y. F. Ma, S. G. Yin and Y. S. Chen, Adv. Mater., **20**, 3924 (2008).

28. W. S. Hummers and R. E. Offeman, J. Am. Chem. Soc., **80**, 1339 (1958).

29. A. Das, B. Chakraborty and A. K. Sood, Bull. Mater. Sci., **31**, 579 (2008).

30. Y. Liu, J. Zhou, X. Zhang, Z. Liu, X. Wan, J. Tian, T. Wang and Y. Chen, Carbon, **47**, 3113 (2009).

31. Z. Liu, Y. Wang, X. Zhang, Y. Xu, Y. chen and J. Tian, Appl. Phys. Lett., **94**, 021902 (2009).

32. Sunil Kumar, M. Anija, N. Kamaraju, K. S. Vasu, K. S. Subrahmanyam, A. K. Sood and C. N. R. Rao, Appl. Phys. Lett., **95**, 191911 (2009).

33. Jingzhi Shang, Zhiqiang Luo, Chunxiao Cong, Jianyi Lin, Ting Yu, and Gagik G. Gurzadyan, Appl. Phys. Lett., **97**, 163103 (2010).

34. P. Prem Kiran, D. R. Reddy, B. G. Maiya, A. K. Dharmadhikari, G. R. Kumar and D. N. Rao, Opt. Commun., **252**, 150 (2005).

35. P. Prem Kiran, Optical limiting and nonlinear optical properties of photo responsive materials: Tetratolyporphyrins, pure and iron doped $Bi_{12}SiO_{20}$ crystals and codoped Ag-Cu metal nanoclusters, Ph. D Thesis, University of Hyderabad, 2004.

36. S. Stankovich, D. A. Dikin, G. H. B Dommett, K. M. Kohlhaas, E. J. Zimney and E. A. Stach, et al. Nature, **442**, 282 (2006).

37. F. Schedin, A. K. Geim, S. V. Morozov, E. W. Hill, P. Blake, M. I. Katsnelson, et al., Nat. Mater., **6**, 652 (2007).

38. J. T. Robinson, F. K. Perkins, E. S. Snow, Z. Q. Wei, P. E. Sheehan., Nano Lett., **8**, 3137 (2008).

39. R. Arsat, M. Breedon, M. Shafiei, P. G. Spizziri, S. Gilje, R. B. Kaner, et al., Chem. Phys. Lett., **467**, 344 (2009).

40. X. Wang, L. J. Zhi, N. Tsao, Z. Tomovic, J. L. Li, K. Mullen, Angew. Chem. Int. Ed., **47**, 2990 (2008).

41. C. Gomez-Navarro, R. T. Weitz, A. M. Bittner, M. Scolari, A. Mews, M. Burghard, et al., Nano Lett., **7,** 3499 (2007).

42. S. Gilje, S. Han, M. Wang, K. L. Wang, R. B. Kaner., Nano Lett., **7**, 3394 (2007).

43. X. Liang, Z. Fu, S. Y. Chou., Nano Lett., **7**, 3840 (2007).

44. C. Stampfer, E. Schurtenberger, F. Molitor, J. Guttinger, T. Ihn, K. Ensslin., Nano Lett., **8,** 2378 (2008).

45. W. Bao, H. Zhang, J. Bruck, C. N. Lau, M. Bockrath, B. Standley., Nano Lett., **8**, 3345 (2008).

46. N. A. Kotov, Nature, **442**, 254 (2006).

47. S. Watcharotone, D. A. Dikin, S. Stankovich, R. Piner, I. Jung, G. H. B. Dommett, et al., Nano Lett., **7**(7), 1888 (2007).

48. D. Wang, D. Choi, J. Li , Z. Yang, Z. Nie, R. Kou, et al., ACS Nano, **3**, 907 (2009).

49. A. P. Yu, P. Ramesh, M. E. Itkis, E. Bekyarova, R. C. Haddon., J. Phys. Chem. C., **111**, 7565 (2007).

50. X. Zhang, Y. Huang, Y. Wang, Y. Ma, Z. Liu, Y. Chen., Carbon, **47**, 313 (2008).

51. E. Rangel, G. Ruiz-Chavarria, L. F. Magana., Carbon, **47**, 531 (2009).

52. C. Xu, X. Wang, J. Zhu., J. Phys. Chem. C., **112**, 19841 (2008).

53. G. Eda, G. Fanchini, M. Chhowalla., Nat. Nanotechnol., **3**, 270 (2008).

54. G. Williams, P. V. Kamat.,.Langmuir, **25**, 13869 (2009).

55. X. Sun, Z. Liu, K. Welsher, J. Robinson, A. Goodwin, S. Zaric, et al., Nano Res., **1**, 203, (2008).

56. V. L. Colvin, M. C. Schlamp, and A. P. Alivisatos, Nature (London), **370**, 354 (1994).

57. D. L. Klein, R. Roth, A. K. L. Lim, A. P. Alivisatos, and P. L. McEuen, Nature (London), **389**, 699 (1997).

58. H. Ismaili, D. Geng, A. Xueliang Sun, T. Trisevgeni Kantzas, and M. S. Workentin, Langmuir, **27**, 13261 (2011).

59. S. Li , X. Yu , G. Zhang , Y. Ma , J. Yao , B. Keita , N. Louis and H. Zhao, J. Mat. Chem., **21**, 2282 (2011).

60. G. Moon, Y. Park, W. Kim, W. Choi, Carbon, **49**, 3454 (2011).

61. X. Zhao , C. M. Hayner , M. C. Kung and H. H. Kung, Chem. Commun., **48**, 9909 (2012).

Chapter - VI

INFLUENCE OF SOLVENT CONTRIBUTION ON NONLINEARITIES OF MATERIALS IN THE ULTRAFAST PULSED REGIME

Abstract

Third order optical nonlinearities of various solvents like DMF, ethanol, chloroform, CCl_4, acetone, toluene, THF and CS_2 in picosecond (ps) and femtosecond (fs) time scales were studied using Z-scan technique. All the solvents show reverse saturable absorption behavior, originating from significant two-photon absorption (TPA) and three-photon absorption (3PA) processes in both ps and fs time scale regimes, respectively. Positive nonlinear refractive index was observed in both pulse regimes. We have investigated the effect of solvents on the observed nonlinearities of near infra red absorbing squaraine and croconate dye samples. Interestingly, we have observed a change in the sign of nonlinearity of phe cro, ptbu cro, phe squ and ptbu squ when the solvent contribution was removed under ps regime. Further we also observed a change in magnitude of the nonlinearity for all the compounds under both pulse regimes. This shows clear evidence that the solvents play a key role in the measurement of optical nonlinearities and that the true nonlinearities of the solute in fs/ps time domain can only be obtained when the measurements account for the solvent. Therefore, TPA and 3PA coefficients, β and α_3, values of solvents make significant contribution in the ps and fs regimes. Nonlinear optical susceptibility ($\chi^{(3)}$) and molecular second order hyperpolarizability (γ) of croconate and squaraine dyes were measured in the ps domain using degenerate four wave mixing technique.

6.1 Introduction

Third order optical nonlinearities of several materials were measured during the past two decades for various photonic and optoelectronic applications [1-16]. Z-scan is the one of the simplest techniques for the measurement of the third order nonlinear optical susceptibility, and also helps in understanding the nonlinear -absorption (NLA) and -refraction (NLR) phenomena of a material. The NLA and NLR have been investigated in inorganic semiconductros, organic compounds, fullerenes, inorganic metal clusters, and graphene-porphyrin composites and so on [17-40]. The NLA can be classified under two major phenomena; a) saturable absorption (SA), in which the nonlinear absorption coefficient value to be negative in general. b) Reverse saturable absorption (RSA), in which the nonlinear absorption coefficient value to be positive. RSA can occur when the excited state absorption cross section is larger than ground state absorption cross section or with large nonlinear scattering or by two photon absorption (TPA) and multi-photon absorption, while the SA behavior is seen when the excited state gets saturated with higher intensities of the pump laser. From the NLR one can evaluate the sign and magnitude of the nonlinearity of the material. In comparison with nanosecond and picosecond pulses, the femtosecond pulse is of same order as that of the lifetimes of higher excited states, which plays an important role in the NLA phenomena. Pure nonlinearities of the material should be calculated by eliminating the solvent contribution. This is very important for materials with weak third order nonlinearity. For such systems one should eliminate the solvent contribution to know the exact nonlinearity of the material in ultrafast regime. In this work we have presented fs and ps optical nonlinearities of several solvents such as DMF, ethanol, CCl_4, chloroform, acetone, toluene, THF and CS_2. CS_2 is one of the ideal reference materials for nonlinear optics, because it shows a large nonlinearity and widely studied material [41-43]. Few reports are available on solvent effect on optical limiting, nonlinear absorption, two-photon absorption and fluorescence [44-49]. They have shown difference in nonlinear optical behavior when material is taken in different solvents. In this

chapter we have studied the solvent contribution on nonlinearities of croconate and squaraine dye molecules in DMF. The NLR of the croconates and squaraines is changed from positive to negative when the solvent contribution is removed. We are also presenting $\chi^{(3)}$ and γ of croconate and squaraine dyes in the ps domain. These studies were done using Z-scan and degenerate four wave mixing (DFWM) techniques.

6.2 Experimental details

The third order nonlinear optical studies were carried out by the Z-scan method [50]. Ultra-short laser pulses used in the present study were obtained from a conventional chirped pulse amplification system comprising of an oscillator (Maitai, Spectra-Physics Inc.) that delivers a ~80 fs, 82 MHz pulse train with pulse energy of 1 nJ at 800 nm and a regenerative amplifier (Spitfire, Spectra Physics Inc.), pumped by a 150 ns, 1 kHz, Q-switched Nd: YLF laser. After regenerative amplification, we obtained amplified pulses of pulse width ~100 fs determined by second order intensity autocorrelation with output energy of up to 1 mJ, at 1 kHz repetition rate. The ps laser source was a frequency doubled Nd:YAG laser (EKSPLA PL 2143A) delivers 532 nm, 30 ps, 10 Hz laser pulses. Croconate and squaraine dyes are taken as solutions in DMF for the experimental studies. Sample is taken in a 1mm cuvette for Z-scan studies. Open and closed aperture Z-scan studies were carried out by focusing the input beam on the sample using a lens of 120 mm focal length forming a 27 μm, 40 μm spot sizes at focus in ps and fs regimes, respectively. The transmitted light was collected with a fast photodiode. The peak intensity used in the Z-scan experiments was 25 GW/cm^2 in ps and 550 GW/cm^2 in fs time scales. Measurement of nonlinear susceptibility and second order hyperpolarizability are carried out through the DFWM technique in the boxcar geometry [51, 52] using a frequency doubled, Q-switched Nd: YAG laser, delivering 30 ps laser pulses at 532 nm and a repetition rate of 10 Hz. The samples under consideration are taken in the form of solutions filled in a 1mm glass cuvette. Care is taken to reduce the contribution of the cuvette towards the overall DFWM signal by choosing suitable focusing

conditions. Choice of low input powers allowed us to neglect the contributions of higher order nonlinearities.

6.3 Results and discussion

Chemical structures of squaraine and croconate dye molecules are shown in figure 1 (a) and (b).

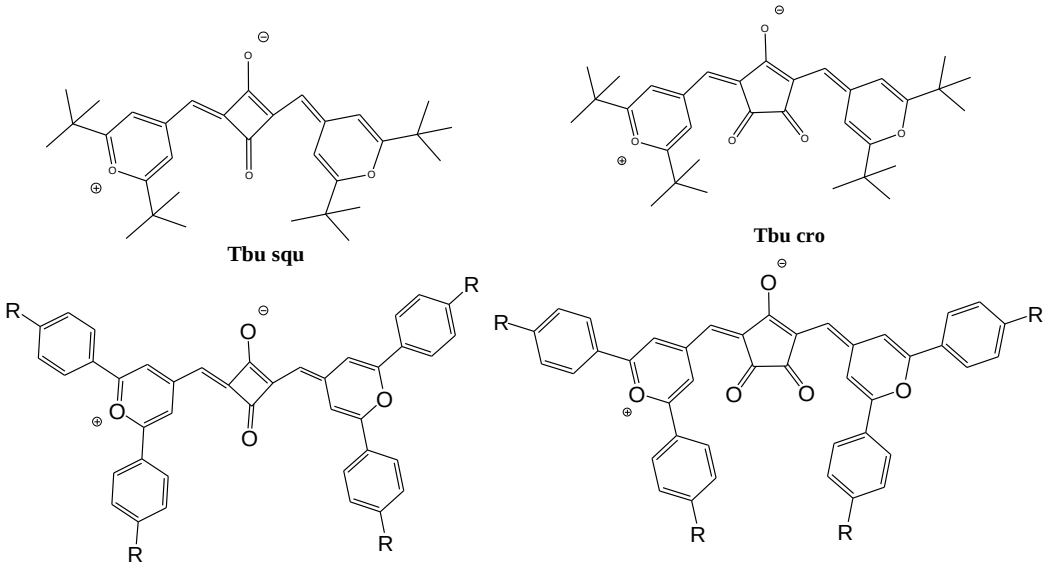

Figure 1. Chemical structures of (a) squaraine dye molecules and (b) croconate dye molecules

These dyes have an absorption maximum in NIR region as seen in figure 2. For UV-VIS absorption recordings 1×10^{-6} M concentration of dye molecules are taken in DMF. One can find the wavelength maximum for Tbu squ, Phe squ, Pme squ and Ptbu squ are at 718, 819, 823 and 826 nm, respectively, as shown in figure 2 (a), and also for Tbu cro, Phe cro, Pme cro and Ptbu cro are at 847, 958, 961 and 963 nm, respectively, from figure 2 (b). These dye molecules have large optical transmission window from UV to visible and also in far IR.

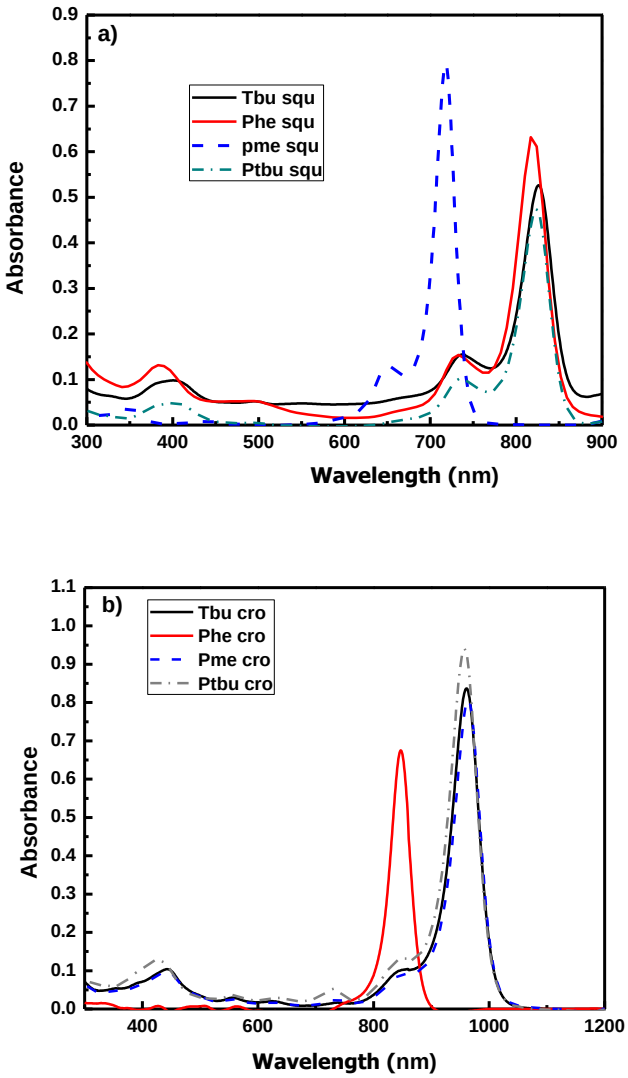

Figure 2. UV-Vis absorption spectra of a) squaraine and b) croconate dyes in DMF at 1×10^{-6} M concentration.

Picosecond optical nonlinearities of solvents were measured at 532 nm using Z-scan technique. Figure 3 shows open and closed aperture Z-scan curves for solvents, revels the nonlinear absorption and nonlinear refraction behavior. In this regime all the solvents were showing RSA kind of nonlinear absorption behavior due to two-photon absorption process and also show the valley-peak configuration in closed aperture curves due to the positive nonlinearity of solvents. Theoretical fittings of these curves will give the nonlinear absorption

and nonlinear refraction coefficients such as two-photon absorption coefficient (β) and nonlinear refractive index (n_2). In order to estimate, whether two photon absorption or three photon absorption is dominating, the experimental data is fitted using formalism developed by Sheik Bhase et al. [50], with transmittance given as

$$T_{OA(nPA)} = 1 - \frac{\alpha_n I_0^{n-1} L_{eff}^{(n)}}{n^{3/2}(1+z^2/z_0^2)^{n-1}} \quad (1)$$

$$T_{OA(2PA)} = 1 - \frac{\alpha_2 I_0 L_{eff}}{2^{3/2}(1+z^2/z_0^2)} \quad (2)$$

$$T_{OA(3PA)} = 1 - \frac{\alpha_3 I_0^2 L_{eff}^{/}}{3^{3/2}(1+z^2/z_0^2)^2} \quad (3)$$

where I_0 is the peak intensity, z is the sample position, $z_0 = \pi\omega_0^2/\lambda$ is Rayleigh range; ω_0 is the beam waist at the focal point (z = 0), λ is the laser wavelength; effective path lengths in the sample of length $L_{eff}^{(n)}$ for TPA and Three photon absorption (3PA) is given as $L_{eff} = [1- \exp(-\alpha_0 L)]/\alpha_0$, and $= [1-\exp(-2\alpha_0 L)]/2\alpha_0$, respectively. α_2 (β) and α_3 represent nonlinear absorption coefficients for TPA and 3PA, respectively. Z-scan traces were fitted, using the equations (1) and (2). The red line represents TPA and the blue line 3PA process.

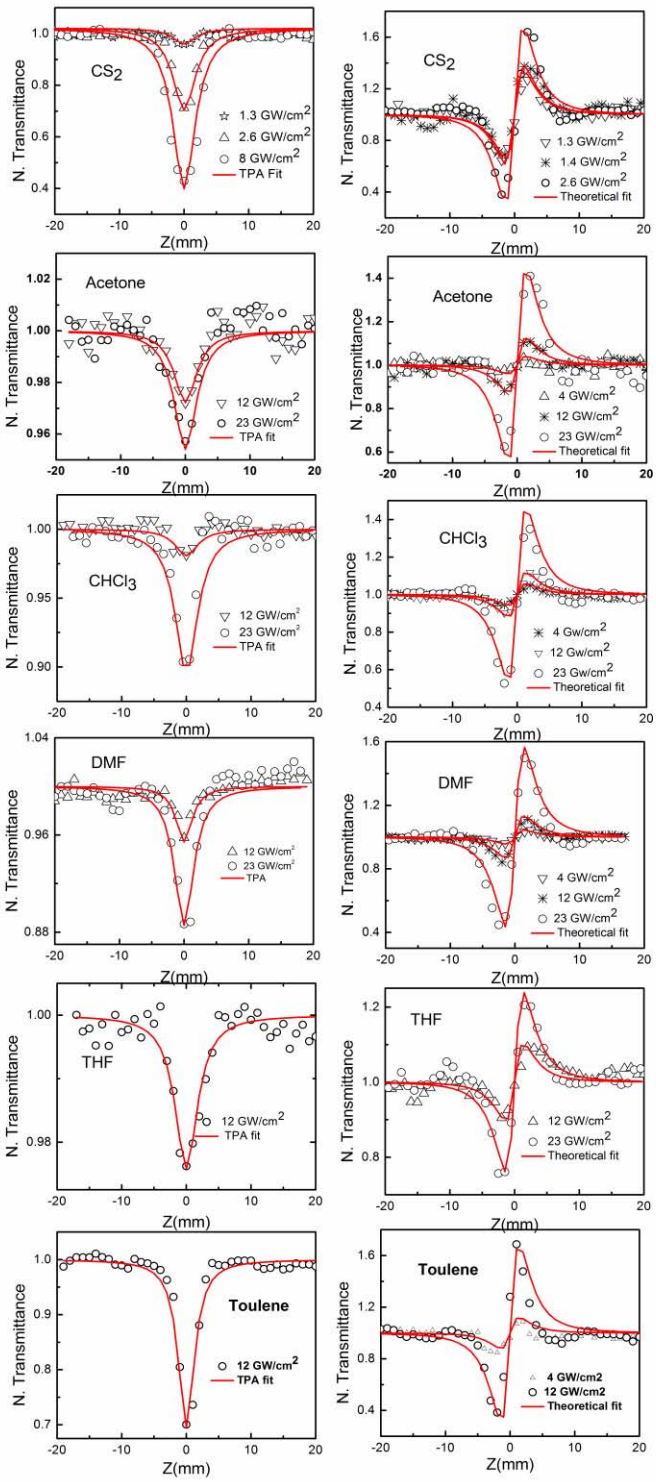

Figure 3. Open and closed aperture Z-scan curves for CS_2 and several solvents with 532 nm, 30 ps and 10 Hz repetition rate laser pulse excitation. Symbols represent experimental data and solid line represent theoretical fit

The nonlinear refraction coefficient (n_2) is obtained by fitting the nonlinear transmission expression of the closed aperture Z scan [50] data.

$$T_{CA} = \frac{4\Delta\Phi_0(z/z_0)}{[1+(z/z_0)^2][9+(z/z_0)^2]} \quad (4)$$

where $\Delta\varphi_0$ is the phase change of laser beam due to the nonlinear refraction. $\Delta\varphi_0$ value is estimated from a theoretical fit to the experimental data. Third order nonlinear refractive index n_2 is calculated from

$$n_2(cm^2W^{-1}) = \frac{|\Delta\Phi_0|\lambda}{2\pi I_{00} L_{eff}} \quad (5)$$

Nonlinear refractive index of the solvents is in the order of 10^{-15} cm^2/W and β is in the order of 10^{-10} cm/W. We estimated Im $\chi^{(3)}$ from β and Re $\chi^{(3)}$ from n_2. $\chi^{(3)}$ will then be the $\sqrt{\left(\mathrm{Im}\,\chi^{(3)}\right)^2 + \left(\mathrm{Re}\,\chi^{(3)}\right)^2}$, and is in the order of 10^{-13} esu. All these parameters for the individual solvents are tabulated in Table 1.

Solvent	**n_2 (cm^2/W) $\times10^{-15}$**	**B (cm/W) $\times10^{-10}$**	**Im$\chi^{(3)}$esu $\times10^{-14}$**	**Re$\chi^{(3)}$esu $\times10^{-13}$**	**$\chi^{(3)}$esu $\times10^{-13}$**
Acetone	4.37	0.60	1.19	2.04	2.05
Chloroform	5.19	1.25	2.81	2.75	2.76
DMF	4.70	1.22	2.68	2.43	2.45
THF	4.01	0.57	1.21	2.01	2.01
Toluene	4.27	3.2	7.70	2.42	2.54
CS_2	113	20	57.10	76.00	76.21

Table 1. Third order nonlinear optical parameters of solvents in picosecond regime with 532 nm, 10 Hz and 30 ps laser pulses

CS_2 has large optical nonlinearities in this regime due to large nonlinear absorption and refraction. The values of β and n_2 are found to be 1.13×10^{-13} cm^2/W and 2 cm/GW. Due to these large nonlinear optical coefficients CS_2 acts as an ideal reference material. Transmittance Vs the input fluence curves for various solvents in ps regime is shown in the figure 4. Solvents have large transmittance (L.T) over 95 % with 532 nm wavelength. CS_2 alone has shown

deviation from the linear transmittance compared to other solvents at input fluence of 0.1 J/cm^2. This could be due to strong multi-photon absorption in CS_2.

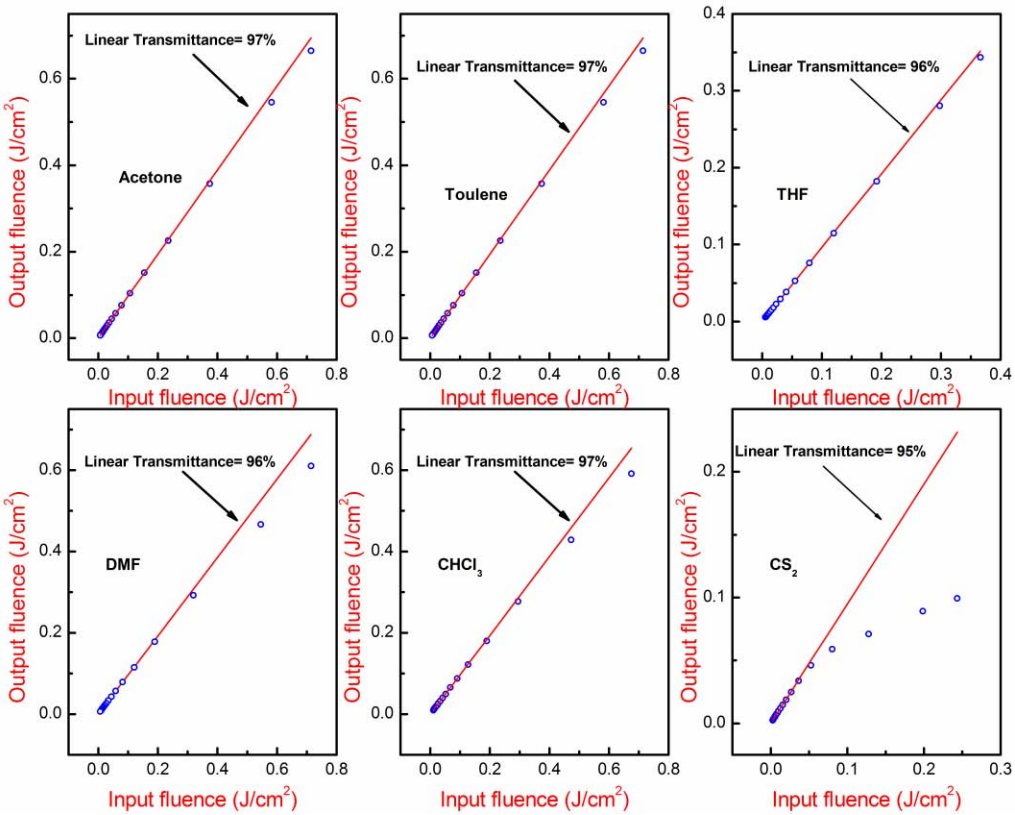

Figure 4. Transmittance curves for various solvents with 532 nm, 30 ps pulse duration of 10 Hz laser pulses.

Figure 5 shows open and closed aperture Z-scan curves of solvents recorded with 800 nm wavelength, 1 kHz repetition rate and 110 fs pulse duration of laser excitation. In this regime all the solvents have shown RSA kind of nonlinear optical absorption behavior due to 3PA. From the open aperture Z-scan curves of solvents shown in figure 5, one can see that three-photon absorption fit (solid blue line) matches well, while the two-photon absorption fitting (dashed red line) does not fit properly. Closed aperture Z-scan curves of solvents in figure 5 show valley-peak configuration indicating positive nonlinearity. We have studied intensity dependent observations for some of the samples such as CS_2, THF and DMF in closed aperture configuration and CS_2, THF, DMF, Toluene, Acetone, Chloroform and Ethanol in open aperture configuration. Nonlinear absorption

and nonlinear refraction coefficients remain unchanged with intensity dependent nonlinear transmission curves. Nonlinear refractive index of solvents was in the order of 10^{-16} cm^2/W and three-photon absorption coefficient (α_3) was in the order of 10^{-23} cm^3/W^2. Estimated value of Re $\chi^{(3)}$ is in the order of 10^{-14} esu. All these parameters of individual solvents are tabulated in Table 2. CS_2 has highest nonlinearities compared to the other solvents with α_3 and n_2 as $1.77x10^{-15}$ cm^2/W and $7.5x10^{-22}$ cm^3/W^2, respectively.

Solvent	**$n_2(cm^2/W)$ $\times10^{-16}$**	**$\alpha_3(cm^3/W^2)\times10^{-23}$**	**Re$\chi^{(3)}$esu$\times10^{-14}$**
Acetone	9.34	7.8	4.37
Chloroform	9.37	5.2	4.96
DMF	10.36	9.7	5.37
THF	12.88	15.0	6.46
Toluene	14.00	20.5	7.95
Ethanol	10.90	21.0	5.11
Ccl_4	11.68	18.2	6.31
CS_2	17.75	74.7	12.00

Table 2. Third order nonlinear optical parameters of solvents in femtosecond regime with 800 nm, 1 kHz and 110 fs laser pulses.

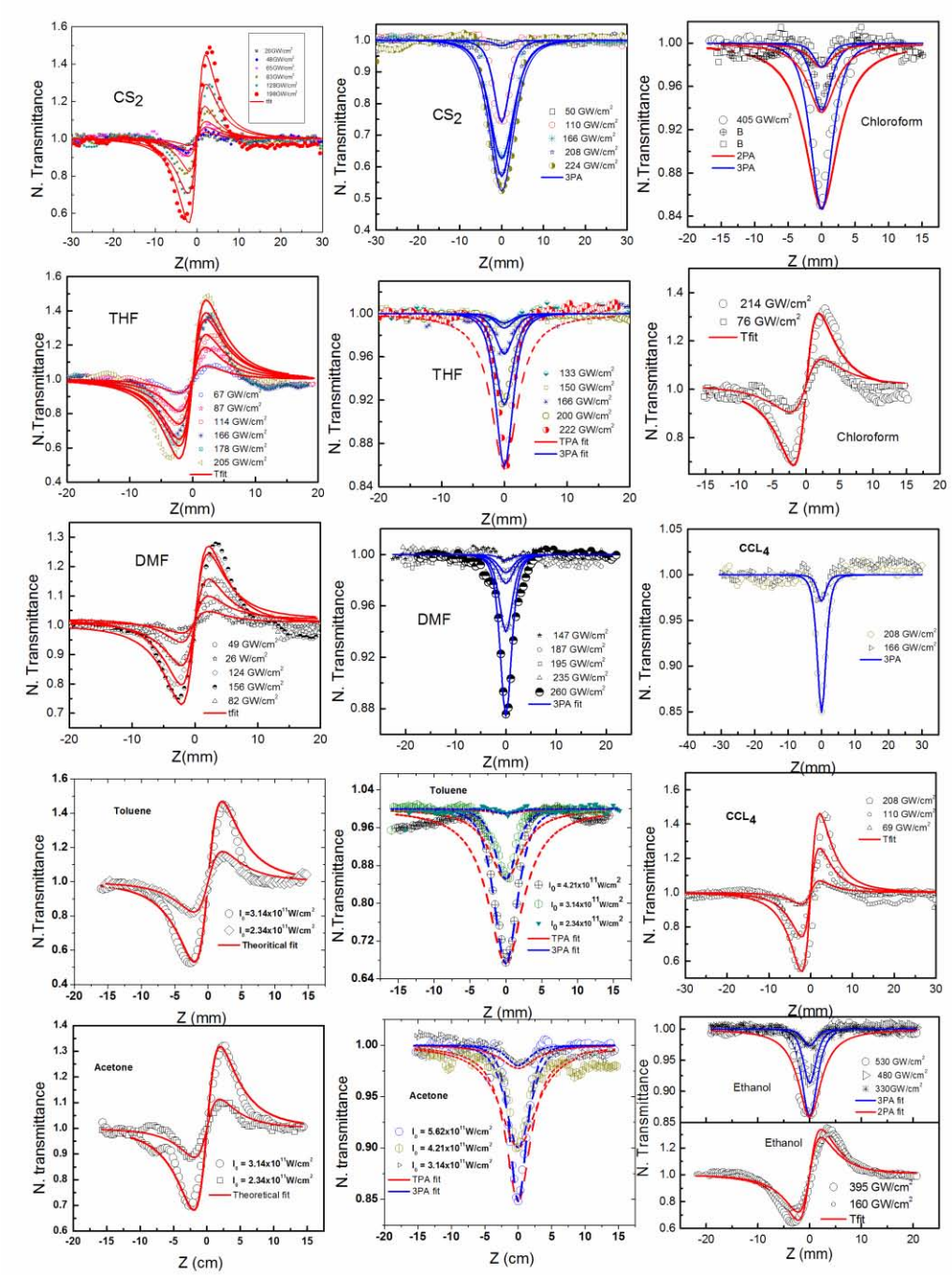

Figure 5. Closed and open aperture Z-scan curves for CS_2 and several solvents with 800 nm, 110 fs and 1kHz repetition rate laser pulse excitation.

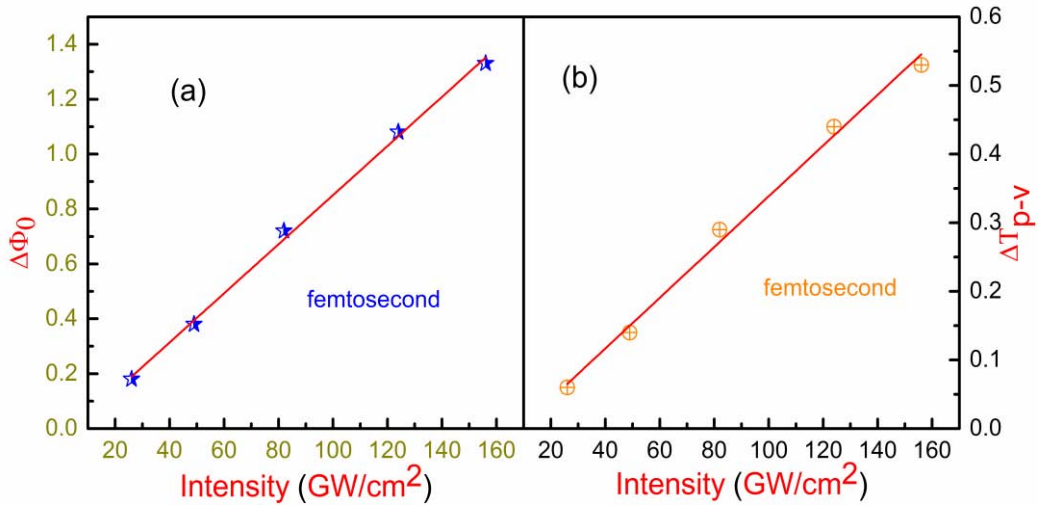

Figure 6 (a) Phase shift $\Delta\Phi_0$ versus incident laser intensity and (b) difference between normalized peak and valley transmittance ΔT_{p-v} versus incident laser intensity for DMF with 800 nm, 110 fs and 1 kHz repetition rate laser pulse excitation. Symbols represent experimental data and solid line represents theoretical fit.

Figure 6 (a) represents the dependence of the $\Delta\Phi_0$ with incident laser intensity for DMF. As can be seen, no saturation of the nonlinear refraction is present since $\Delta\Phi_0$ increases linearly with input intensity for our experimental conditions. A plot of ΔT_{p-v} versus incident laser irradiance which is measured from various Z-scan curves on the same DMF sample is shown in Figure 6 (b). The linear behavior of this plot represents that sample nonlinearities are from pure cubic nonlinearity [50]. Output vs input fluence curves for all the solvents in the femtosecond regime has shown in the figure 7. Every solvent shows a tendency of deviation from the linear transmittance due to 3PA. Compared to all other solvents, CS_2 shows optical limiting behavior with a limiting threshold 22 mJ/cm^2 in fs regime.

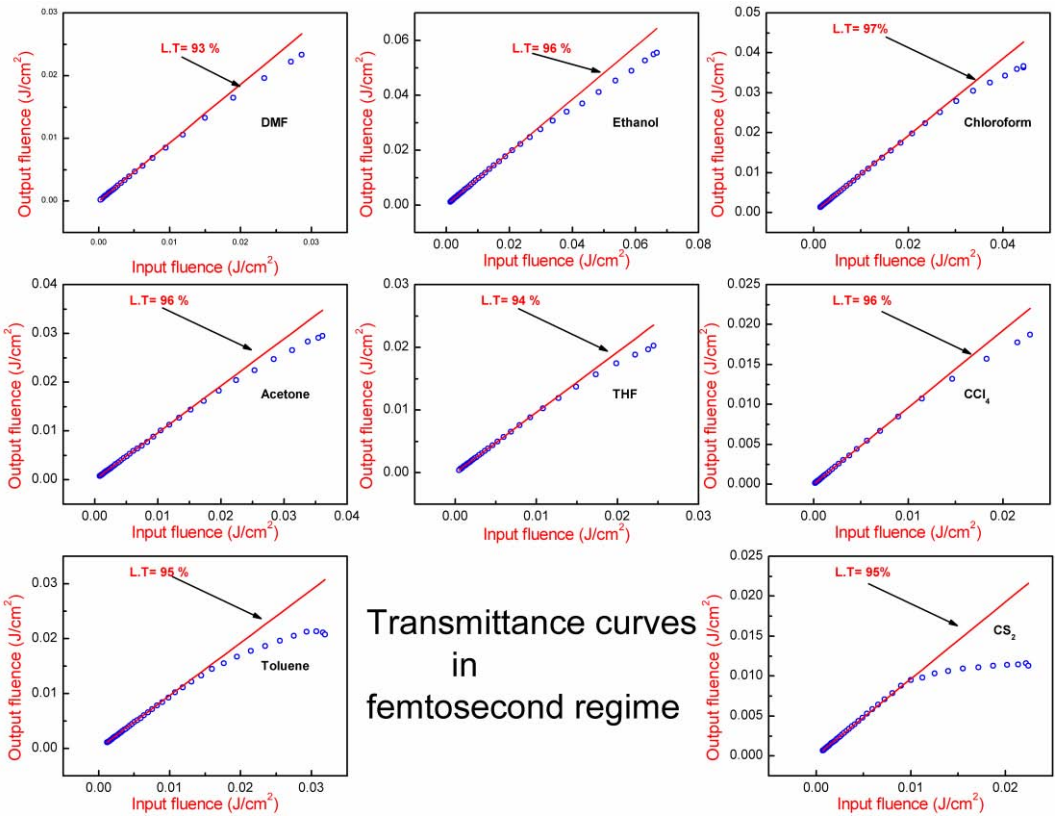

Figure 7. Transmittance curves for DMF, Ethanol, Chloroform, Acetone, THF, CCl4, CS2 and Toluene with 800 nm, 110 fs pulse duration and 1 kHz repetition rate laser pulses.

Closed aperture Z-scan curves of squaraines and croconates with 532 nm, 30 ps laser excitation are shown in figure 8. We estimated the n_2 values of these samples through a theoretical fit using equations 4 and 5. As the solvents show comparable nonlinearities, solvent contribution needs to be subtracted from the sample data. A systematic study was undertaken to take out the solvent contribution on the measured nonlinearities. First, we measured the nonlinear refractive index of the sample along with the solvent contribution. Then we measured pure solvent nonlinear refractive index. Solvent contribution is now subtracted from the sample solution to obtain solute contribution to the nonlinear refractive index. DMF was the solvent and it has n_2 value of 4.7×10^{-15} cm^2/W.

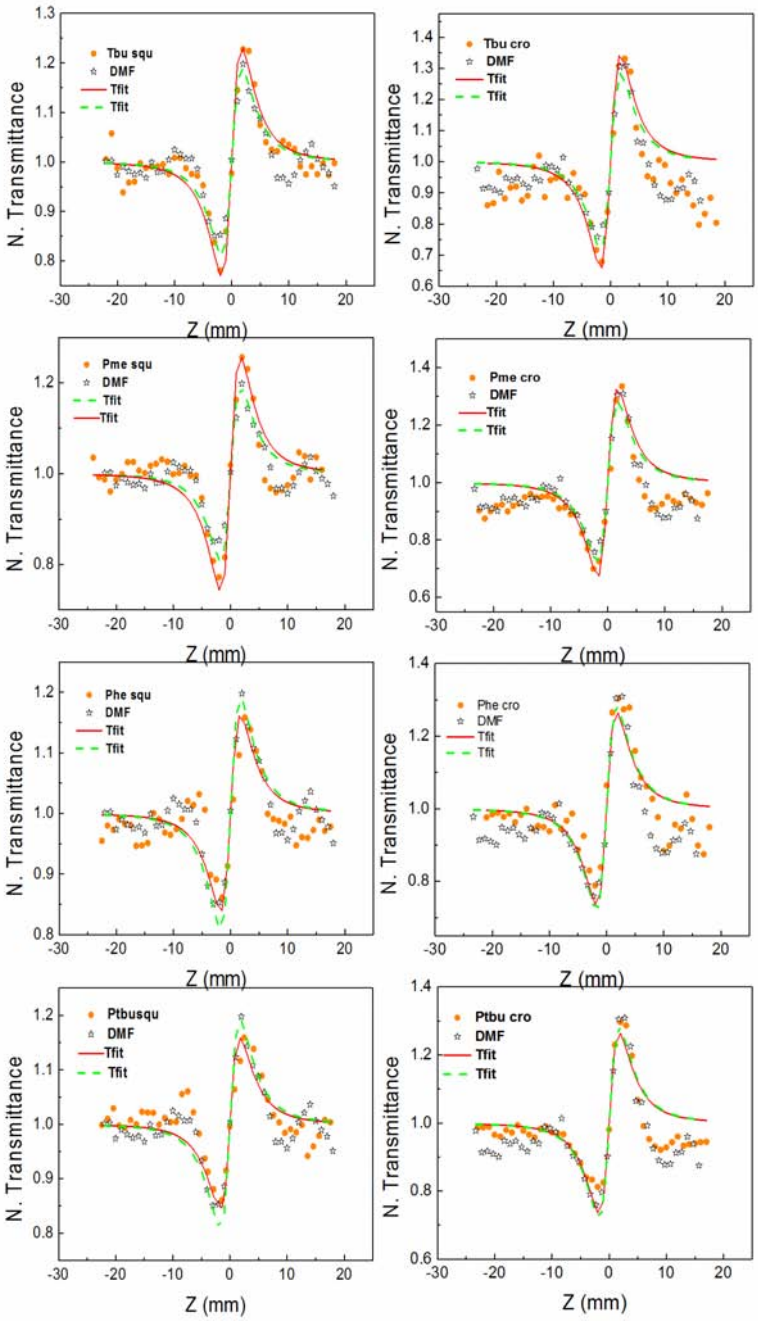

Figure 8. Closed aperture Z-scan curves for squaraines and croconates with 532 nm, 30 ps and 10 Hz repetition rate laser pulse excitation with intensity 25 GW/cm^2.

After removal of solvent nonlinearity from the solution of the samples, we observe a reduction in the magnitude of nonlinearity, and in few of the samples we also see a change in sign of the nonlinearity. Phe squ, Ptbu squ, Phe cro and

Ptbu cro show a change in sign of the nonlinearity from positive to negative and the magnitude from 4.51, 4.52, 4.53 and 4.57×10^{-15} cm^2/W to -1.90, -1.80, -1.70 and -1.30×10^{-16} cm^2/W, respectively. Other samples Pme squ, Tbu squ, Pme cro and Tbu cro has shown change in magnitude only and the sign remains same after removal of solvent contribution. n_2 and Re $\chi^{(3)}$ values of these dye molecules without the contribution of the solvent is tabulated in the Table 3. In the figure 8, the symbols represent experimental data; the solid line represents theoretical fit for sample and dashed line represent theoretical fit for DMF.

Sample	**β (cm/W) $\times10^{-10}$ After removal of solvent contribution**	**$n_2(cm^2/W)\times10^{-15}$ With solvent contribution**	**$n_2(cm^2/W)\times10^{-16}$ After removal of solvent contribution**	**Re $\chi^{(3)}$esu $\times10^{-14}$**
Pme cro	14.5	5.01	3.10	1.61
Phe Cro	24.9	4.53	-1.70	-0.88
Tbu cro	3.42	5.02	3.20	1.66
Ptbu cro	24.6	4.57	-1.30	-0.67
Pme squ	12	5.04	3.40	1.76
Phe squ	3.73	4.51	-1.90	-0.98
Tbu squ	3.74	5.04	3.40	1.76
Ptbu squ	3.74	4.52	-1.80	-0.93

Table 3. Third order nonlinear optical coefficients of croconate and squaraine dyes in picosecond regime with 532 nm, 10 Hz repetition rate and 30 ps laser pulses

Closed aperture Z-scan curves of squaraines and croconates with 800 nm, 110 fs laser excitations are shown in figure 9. We found that n_2 values of these compounds are in the order of $10^{-15}cm^2/W$ before removing the solvent contribution. Removal of the solvent contribution leads to reduction in the nonlinear refractive index, which is in the order of 10^{-16} cm^2/W.

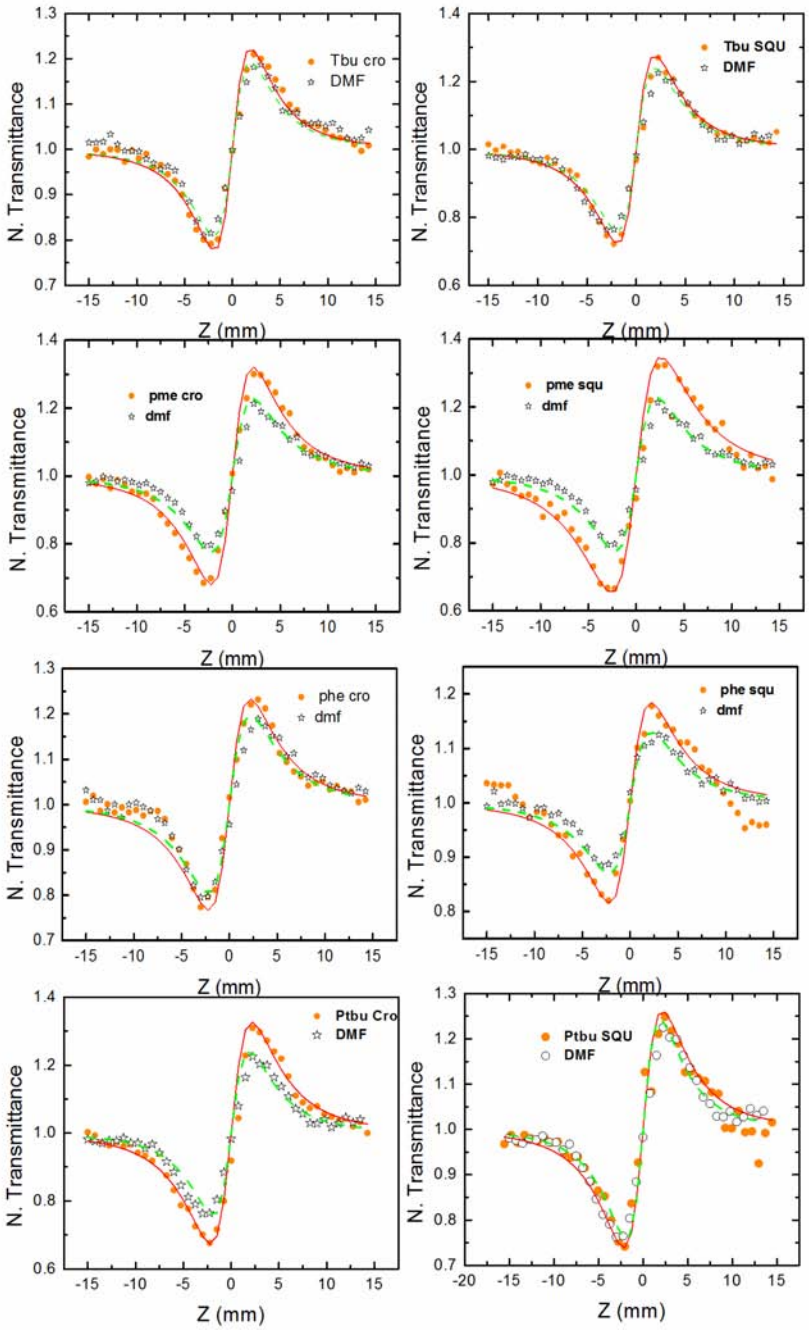

Figure 9. Closed aperture Z-scan curves for squarainates and croconates with 800 nm, 110 fs and 1 kHz repetition rate laser pulse excitation with intensity 120 GW/cm^2.

In the femtosecond regime samples do not show any change in sign of the nonlinearity but magnitude shows a reduction after removal of solvent contribution. Measurements for all the dyes were recorded at the input peak

intensity of 120 GW/cm^2 in the Z-scan studies. Measured n_2 and Re $\chi^{(3)}$ values are presented in Table 4.

Sample	**n_2(cm^2/W) ×10^{-15} With solvent contribution**	**n_2(cm^2/W) ×10^{-16} After removal of solvent contribution**	**Re $\chi^{(3)}$esu×10^{-14}**
Pme cro	1.77	7.33	3.80
Phe Cro	1.35	3.16	1.63
Tbu cro	1.39	3.54	1.83
Ptbu cro	1.78	7.47	3.87
Pme squ	2.37	13.35	6.91
Phe squ	1.39	3.56	1.84
Tbu squ	1.48	4.40	2.28
Ptbu squ	1.80	7.68	3.98

Table 4. Third order nonlinear optical coefficients of croconate and squaraine dyes in femtosecond regime with 800 nm, 1 kHz repetition rate and 110 fs laser pulses

Nonlinear absorption behavior of croconates and squaraines were measured with 532 nm, 10 Hz and 30 ps laser pulses. All the dye molecules show RSA kind of behavior due to two photon absorption process. Nonlinear absorption of solvent was removed from the solution data and pure nonlinear absorption behavior of the molecules is shown in the figure 10. Removal of solvent contribution in graphene-porphyrin composites is done as mentioned in earlier work [40]. After removal of solvent contribution in graphene-porphyrin composites, nonlinear absorption shows a switch over behavior from RSA to SA. Phe cro and Ptbu cro have shown large nonlinear absorption compared to other dye molecules. Two photon absorption coefficient, β, values are presented in the Table 3.

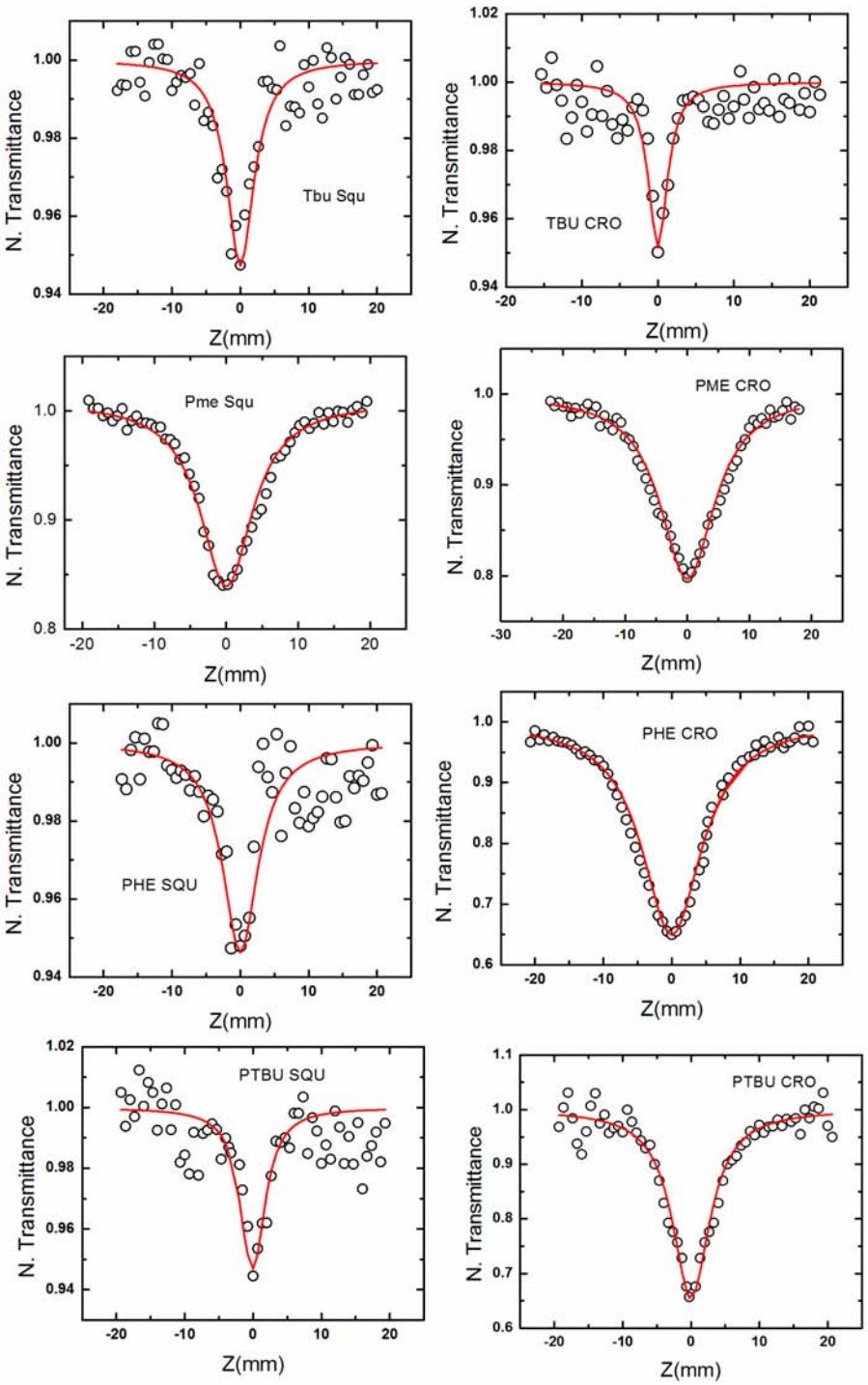

Figure 10. Open aperture Z-scan curves for squarainates and croconates with 532 nm, 30 ps and 10 Hz repetition rate laser pulse excitation with intensity 32 GW/cm^2.

The third order nonlinear optical susceptibility $\chi^{(3)}$ is also measured by comparing the DFWM signal for the sample with that of DMF as reference ($\chi^{(3)}$ = 4.70X10^{-15}esu) for picosecond pulses. Reference $\chi^{(3)}$ value is taken from the Z-scan study of DMF. The following relationship is used to determine the sample $\chi^{(3)}$.

$$\chi^{(3)}{}_{sample} = \left(\frac{n_{sample}}{n_{ref}}\right)^2 \left(\frac{I_{sample}}{I_{ref}}\right)^{1/2} \left(\frac{L_{ref}}{L_{sample}}\right) \alpha L_{sample} \left(\frac{e^{\frac{\alpha L_{sample}}{2}}}{1-e^{-\alpha L_{sample}}}\right) \chi^{(3)}_{ref}$$

where I is the DFWM signal intensity, α is the linear absorption coefficient, L is the sample path length, and n is the refractive index. As the sample concentration is very low, the refractive index of DMF (n = 1.4305) has been taken as the refractive index of solution. $\chi^{(3)}$ for croconate and squaraine dyes are estimated in DMF at a concentration of 1×10^{-4} M. The value of $\chi^{(3)}$ at this concentration range from $7.68\text{x}10^{-14}$ to $5.52 \text{ x } 10^{-13}$ esu (listed in Table 5). $\chi^{(3)}$ has three independent components namely $\chi^{(3)}_{1111}, \chi^{(3)}_{1212}$ and $\chi^{(3)}_{1122}$ in an isotropic medium. In the case of non-resonant electronic NLO, $\chi^{(3)}_{1111} = 3\chi^{(3)}_{1212} = 3\chi^{(3)}_{1122}$ when the three input beams are all vertically polarized. To determine $\chi^{(3)}_{1212}$, the probe beam is made to incident at orthogonal polarization and the phase conjugated signal too is detected at the orthogonal polarization with respect to the two pump beams. A ratio of $\chi^{(3)}_{1111}$to $\chi^{(3)}_{1212}$ ~3 is obtained for all the dye samples investigated in this study and indicates that no significant contribution arises from the coherent coupling effects. DFWM signal for squaraine and croconate dyes are shown in figure 11 as a function of the input intensity. A slope of ~3 obtained for all the samples indicates that origin of DFWM does not have contribution from any two-photon absorption in which case the slope of the curve would have been higher than 3.

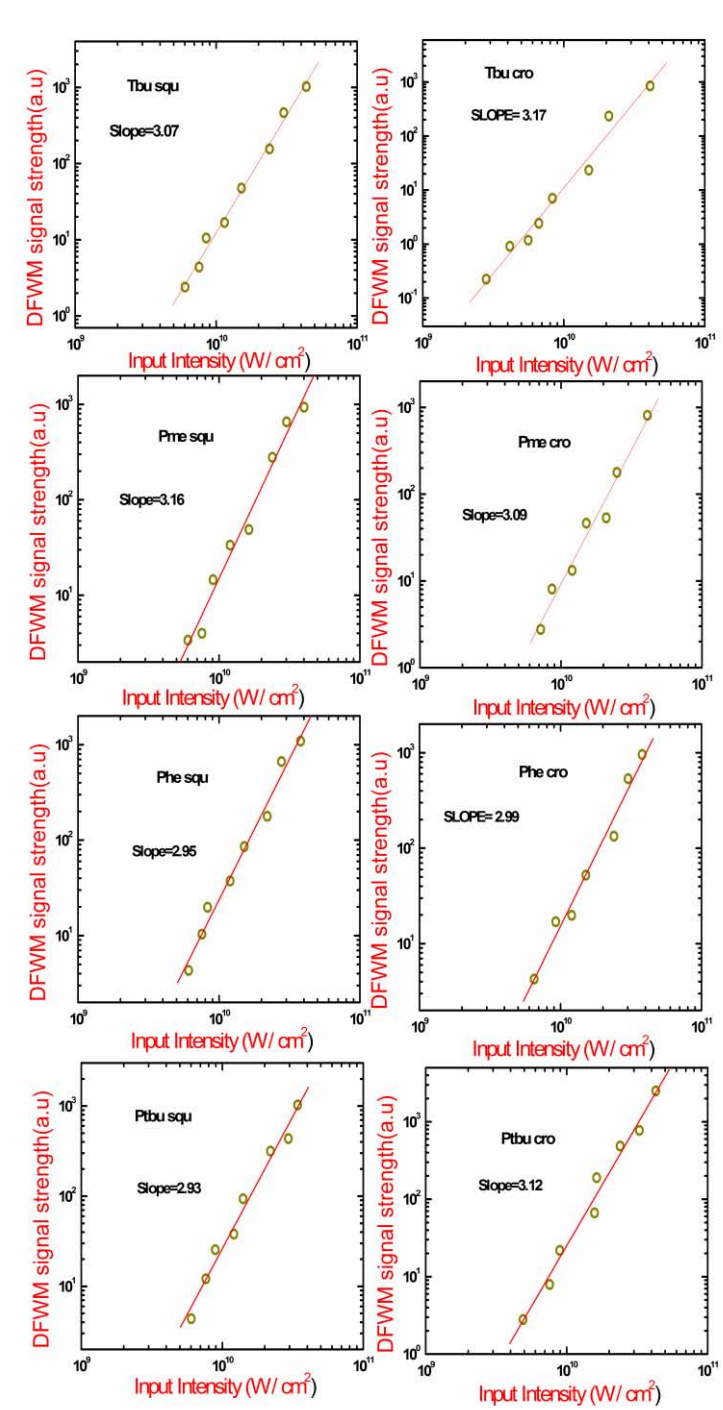

Figure 11. Plots showing the cubic dependence of DFWM signal as a function of input intensity for squarainate and croconate dye molecules

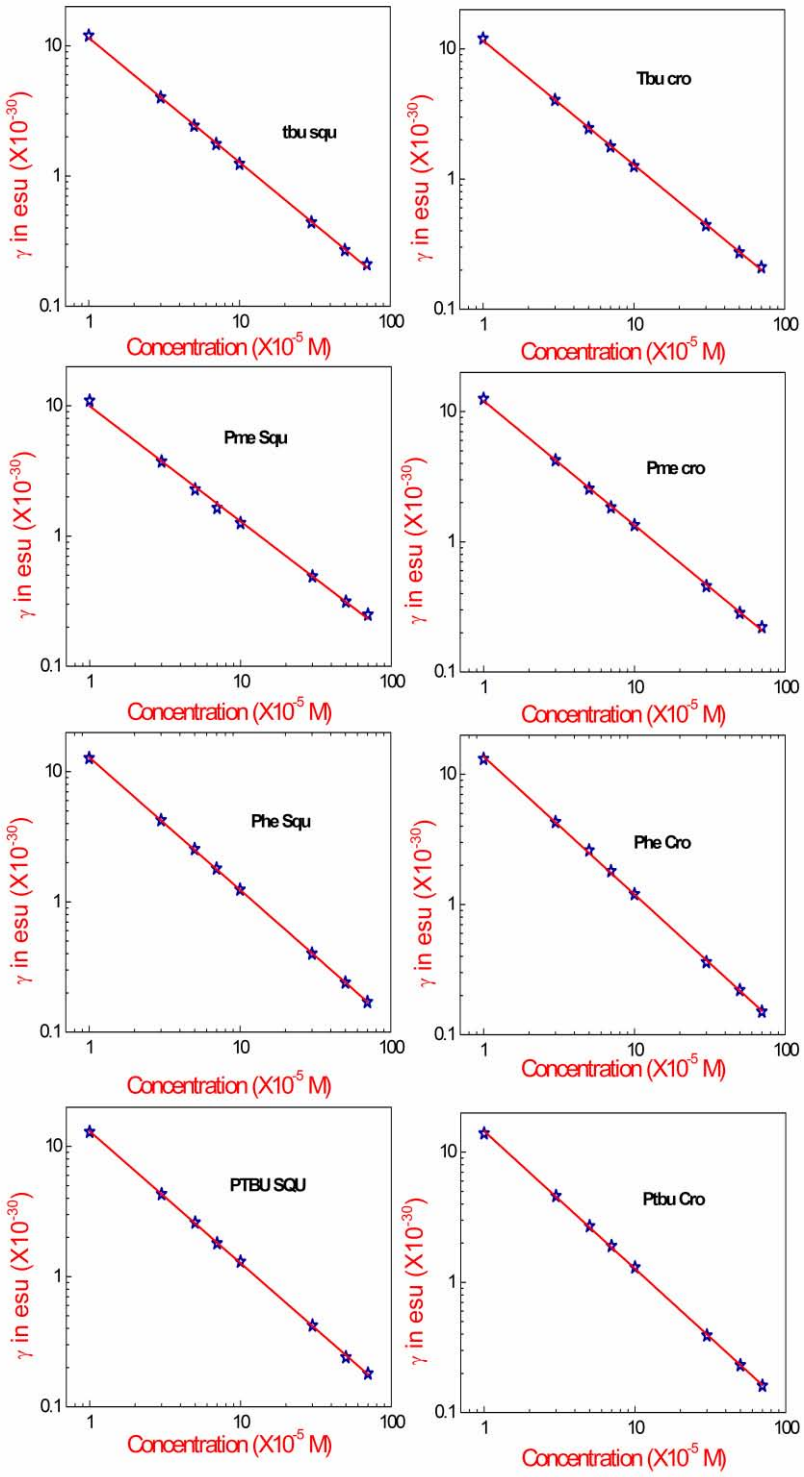

Figure 12. Plots of concentration dependence on γ for squarainate and croconate dye molecules

The second order hyperpolarizability (γ) is obtained for the molecule through the following equation.

$$\chi^{(3)}_{sample} = T^4\left[N_{solvent}\gamma_{solvent} + N_{sample}\gamma_{sample}\right]$$

Here the term T is a local field factor, $T = \left(\frac{n^2+2}{3}\right)$

Where n is the refractive index, N is the number density of the solvent and the sample and γ is the second order hyperpolarizability of the respective molecules. The Number density N is related to the Avogadro number and concentration of solution (C_s) as

$$N = N_0 C_s / 1000$$

The experimentally determined γ values for compounds studied are in range of 0.4-2.8X10^{-30} esu in picosecond regime. We repeated the experiment thrice to check the reproducibility of the results. We have observed ±0.1X10^{-30} variation in the γ values. The observed variations for different samples are much larger than this experimental error. The concentration dependence on γ is shown in the figure 12. The results are summarized in the Table 5. The third order nonlinear optical susceptibility ($\chi^{(3)}$) of the croconate and squaraine dyes are in the range of 0.8-5.5x10^{-13} esu and second order hyperpolarizability (γ) of these compounds are in the range of 0.4-2.8X10^{-30} esu.

Sample	**Nonlinear optical susceptibility ($\chi^{(3)}$) in esu**	**Second order hyper-polarizability (γ) in esu**
Pme cro	3.18×10^{-13}	1.61×10^{-30}
Phe Cro	5.52×10^{-13}	2.80×10^{-30}
Tbu cro	7.68×10^{-14}	3.89×10^{-31}
Ptbu cro	5.36×10^{-13}	2.72×10^{-30}
Pme squ	2.61×10^{-13}	1.32×10^{-30}
Phe squ	8.21×10^{-14}	4.16×10^{-31}
Tbu squ	8.32×10^{-14}	4.22×10^{-31}
Ptbu squ	8.24×10^{-14}	4.18×10^{-31}

Table 5. Nonlinear optical susceptibility and second order hyperpolarizability of croconate and squaraine dyes in picosecond regime with 532 nm, 10 Hz repetition rate and 30 ps laser pulses.

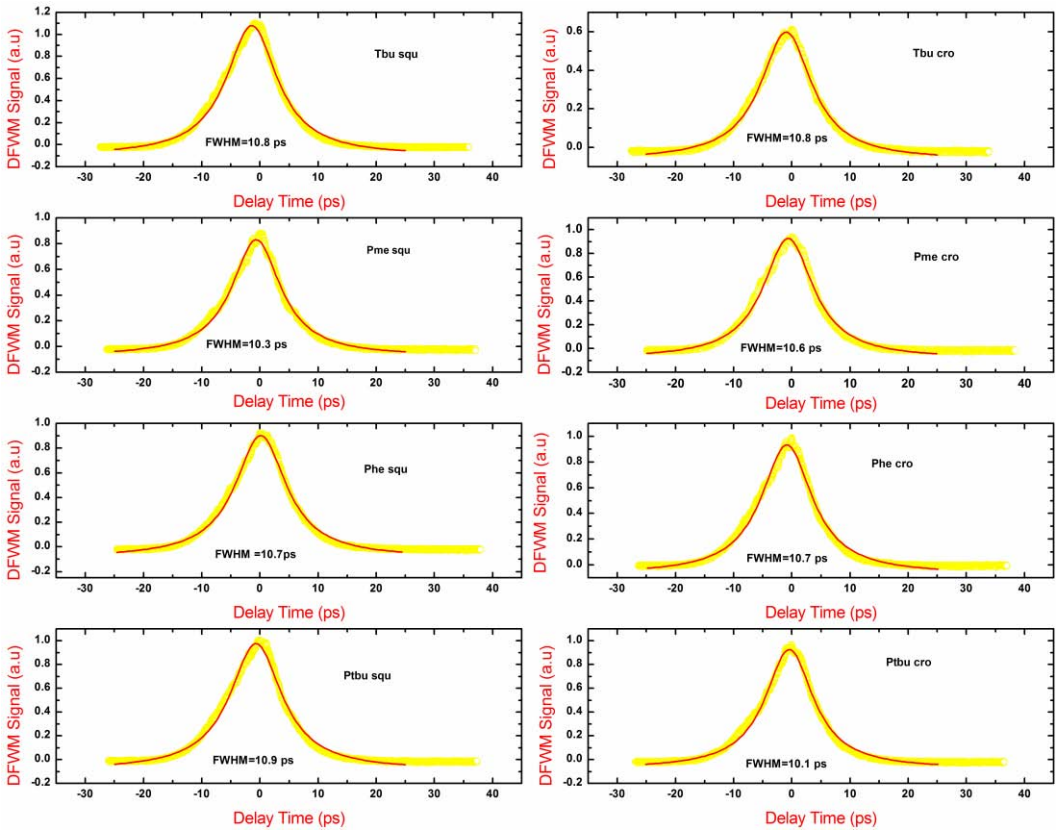

Figure 13. Temporal profile of DFWM signal for squarainate and croconate dye samples

The temporal behavior of squarainate and croconate dye samples is shown in the figure 13. The nonlinear responses are fast and are of the order of 11 ps or faster. The data of third order nonlinear optical susceptibility ($\chi^{(3)}$) and second order hyperpolarizability (γ) are impressive due to larger values when compared with the earlier reported values[53]. Third order NLO susceptibility and second order hyperpolarizability can play a very useful role in all optical signal processing.

6.4 Conclusions

- ✓ Influence of solvent contribution to third order optical nonlinearity of croconate and squarainate dye molecules was studied in the picosecond and femtosecond regime.
- ✓ Phe cro, ptbu cro, phe squ and ptbu squ dye molecules show change in the sign of the nonlinearity from positive to negative after removing the solvent contribution and other dyes do not show any sign change but only show a change in magnitude of nonlinearity.
- ✓ All the dye molecules show strong two photon absorption in the picosecond regime.
- ✓ Large off-resonant $\chi^{(3)}$ and γ values are found for dye molecules to be in the order of 10^{-14} to 10^{-13} esu and 10^{-31} to 10^{-30} esu, respectively.

6.5 References

1. Hales, J. M., Zheng, S., Barlow, S., Marder, S. R., Perry, J. W. J. Am. Chem. Soc., **128**, 11362 (2006).

2. Zhang, C., Song, Y., Wang, X. Coordination Chemistry Reviews, **251**, 111 (2007).

3. Hales, J. M. et al. Science, **327**, 1485 (2010).

4. Ando, M., Kadono, K., Haruta, M., Sakaguchi, T., Miya, M. Nature, **374**, 625 (1995).

5. Xie, R.-H. & Jiang, J. Chem. Phys. Lett., **280**, 66 (1997).

6. Ogawa, K., Zhang, T., Yoshihara, K., Kobuke, Y., J. Am. Chem. Soc. **124**, 22 (2001).

7. Palffy-muhoray, P. et al. Molecular Crystals and Liquid Crystals, **207**, 291 (1991).

8. S.M. O'Flaherty, S.V. Hold, M.J. Cook, T. Torres, Y. Chen, M. Hanack, W.J. Blau., Advanced Materials, 15, 19 (2003).

9. Wang, Y. Cheng, L. T., J. Phys. Chem., **96**, 1530 (1992).

10. Zakery, A. Elliott, S., Journal of Non-Crystalline Solids, **330**, 1 (2003).

11. H. S. Nalwa, Advanced Materials, **5**, 341 (1993).

12. Calvete, M., Yang, G. Y., Hanack, M., Synthetic Metals **141**, 231 (2004).

13. Bredas, J. L., Adant, C., Tackx, P., Persoons, A., Pierce, B. M., Chem. Rev. **94**, 243 (1994).

14. Dinu, M., Quochi, F., Garcia, H., Applied Physics Letters, **82**, 2954 (2003).

15. Banyai, L., Hu, Y. Z., Lindberg, M., Koch, S. W., Phys. Rev. B, **38**, 8142 (1988).

16. Xie, R. H., Rao, Q., Chemical Physics Letters, **313**, 211 (1999).

17. Chen, Z. R., Hou, H. W., Xin, X. Q., Yu, K. B., Shi, S., J. Phys. Chem. **99**, 8717 (1995).

18. Miller, D. A. B., Seaton, C. T., Prise, M. E., Smith, S. D., Phys. Rev. Lett. **47**, 197 (1981).

19. Sathyavathi, R., M. Bala Murali Krishna, Rao, S. V., Saritha, R., Rao, D. N. Advanced Science Letters, **3**, 138 (2010).

20. Sathyavathi, R., M. Bala Murali Krishna, Rao, D. N., Journal of Nanoscience and Nanotechnology, **11**, 2031 (2011).

21. Wei, T. H. et al., Applied Physics B: Photophysics and Laser Chemistry, **54**, 46 (1992).

22. Chattopadhyay, M., Kumbhakar, P., Sarkar, R., Mitra, A. K., Applied Physics Letters, **95**, 163115 (2009).

23. Krauss, T. D., Wise, F. W., Applied Physics Letters, **65**, 1739 (1994).

24. Taheri, B. et al. Applied Physics Letters, **68**, 1317 (1996).

25. Ganeev, R. A., Ryasnyansky, A. I., Tugushev, R. I., Usmanov, T. Journal of Optics A: Pure and Applied Optics, **5**, 409 (2003).

26. Varnavski, O., Leanov, A., Liu, L., Takacs, J., Goodson, T., J. Phys. Chem. B, **104**, 179 (1999).

27. Chakraborty, P., Journal of Materials Science, **33**, 2235 (1998).

28. Peticolas, W. L., Annual Review of Physical Chemistry, **18**, 233 (1967).

29. Shi, S., Ji, W., Lang, J. P., Xin, X. Q., J. Phys. Chem., **98**, 3570 (1994).

30. Kyoung, M., Lee, M., Optics Communications, **171**, 145 (1999).

31. Bhawalkar, J. D., He, G. S., Prasad, P. N., Reports on Progress in Physics, **59**, 1041 (1996).

32. Ganeev, R., Ryasnyansky, A., Kodirov, M., Usmanov, T., Optics Communications, **185**, 473 (2000).

33. M. Bala Murali Krishna, Kumar, V. P., Venkatramaiah, N., Venkatesan, R., Rao, D. N., Applied Physics Letters, **98**, 081106 (2011).

34. Ganeev, R. A., Ryasnyansky, A. I., Kamalov, S. R., Kodirov, M. K., Usmanov, T., Journal of Physics D: Applied Physics, **34**, 1602 (2001).

35. Perry, J. W. et al., Science, **273**, 1533 (1996).

36. Liu, Z.-B. et al., J. Phys. Chem. B, **113**, 9681 (2009).

37. Chemla, D., Miller, D., Smith, P., Gossard, A., Wiegmann, W., IEEE Journal of Quantum Electronics, **20**, 265 (1984).

38. Wei, T.-H., Huang, T.-H., Wu, T.-T., Tsai, P.-C., Lin, M.-S., Chemical Physics Letters, **318**, 53 (2000).

39. Shi, S., Ji, W., Tang, S. H., Lang, J. P., Xin, X. Q., J. Am. Chem. Soc., **116**, 3615 (1994).

40. M. Bala Murali Krishna, Venkatramaiah, N., Venkatesan, R., Rao, D. N., J. Mater. Chem., **22**, 3059–3068

41. Zhai, T., Lawson, C. M., Gale, D. C., Gray, G. M., Optical Materials, **4**, 455 (1995).

42. Ganeev, R. A. et al., Applied Physics B: Lasers and Optics, **78**, 433 (2004).

43. Falconieri, M., Salvetti, G., Applied Physics B: Lasers and Optics, **69**, 133 (1999).

44. Liu, Y.-L., Liu, H.-L., Liu, Z.-B., Zang, W.-P., Tian, J.-G., Optik - International Journal for Light and Electron Optics, **123**, 1015 (2012).

45. Nooraldeen, A. Y., M., P., K. P., P., International Journal of Nonlinear Science, **7**, 290 (2009)

46. Wang, J., Blau, W. J., J. Phys. Chem. C, **112**, 2298 (2008).

47. Sun, W. et al., Society of Photo-Optical Instrumentation Engineers (SPIE) Conference Series, **4106**, 280 (2000).

48. Nag, A., Goswami, D., Journal of Photochemistry and Photobiology A: Chemistry, **206**, 188 (2009).

49. Gao, Y. et al., Applied Physics B, **88**, 89 (2007).

50. Sheik-Bahae, M., Said, A. A., Wei, T.-H., Hagan, D. J., Van Stryland, E. W., IEEE Journal of Quantum Electronics, **26**, 760 (1990).

51. Prabhakar, C. et al., J. Phys. Chem. C, **112**, 13272 (2008).

52. Prabhakar, C., Bhanuprakash, K., Rao, V. J., Balamuralikrishna, M., Rao, D. N., J. Phys. Chem. C, **114**, 6077 (2010).

53. Srivastava, P. C. et al., Inorganica Chimica Acta, **388,** 175 (2012).

Chapter - VII

SUMMARY AND FUTURE PERSPECTIVE

This thesis makes an attempt to identify new materials for optical limiting based on two-photon absorption, multi-photon absorption, excited state absorption and nonlinear scattering. We have studied three different classes of materials: Organic molecules, bio-synthesized silver nanoparticles and graphene based hybrid composites.

In organic molecules, two classes of compounds are studied. First class of compound is phthalocyanine, where we have studied zinc octa carboxy phthalocyanine (ZnOCPc). –COOH is attached at eight peripheral positions of phthalocyanine leading to chemical variation and the electronic structure. This resulted in improved solubility as well as enhanced, nonlinear optical coefficients. ZnOCPc is soluble in most of the common solvents like water, DMF and ethanol. Large nonlinear optical absorption is observed in ns and ps regimes for ZnOCPc, which is mainly due to strong two-photon absorption, its cross-sections are 1.07×10^5 and 1.04×10^3 GM, respectively. ZnOcPc shows high non-resonant second order hyperpolarizability values in ns, ps and fs as 7.9×10^{-28}, 6.3×10^{-30} and 0.67×10^{-31} esu, respectively. Second class of compound is porphyrin, where we have studied various metal and metal free porphyrins. Significant change in the optical absorption is observed with different metal substitution at the core of the porphyrin molecules. Even at low concentration, these porphyrin molecules have shown good nonlinear optical absorption behavior.

Silver nanoparticles are synthesized by bio-reduction method using coriander and moringa oleifera leaf extracts. These leaf extracts act as a reducing as well as stabilizing agents. This method of preparation is very fast, echo friendly, cost effective and also there is no need to use high pressure, energy, temperature and toxic chemicals. Nonlinear optical absorption in these nanoparticles is due to two-photon and excited state absorption. Silver nanoparticles reduced from moringa oleifera and coriander leaf extracts have shown nonlinear optical absorption coefficients as 272 cm/GW and 72.5 cm/GW,

respectively. Third order optical nonlinear susceptibility is estimated as $1.38x10^{-11}$ esu for coriander leaf extract reduced Ag nanoparticles.

In graphene based hybrid materials, we have studied graphene oxide (GO)-(Cu, Zn, Sn, VO, H_2) porphyrin composites, GO-semiconductor (ZnO, TiO_2) nanoparticles and GO-metal (Ag, Au) nanopartilces for optical limiting application. GO-porphyrin composites are covalently conjugated and confirmed by various spectroscopic techniques like optical absorption, FT-IR, steady state and time resolved fluorescence. We have observed fluorescence quenching behavior in GO-porphyrin composites suggesting that there is an electron interaction between GO and porphyrin molecules. GO is well known electron acceptor, therefore, the energy transfer phenomena can occur from porphyrin molecule to GO. About 27 % quenching is observed for GO-H_2 porphyrin with highest quenching constant of $3.57x10^{9}$ S^{-1} over all other GO-porphyrin composites. We have observed significant decrease in the life time for GO-porphyrin composites compared to pure porphyrin molecules indicating that the charge separation or electron transfer phenomena takes place between GO and porphyrins. Excellent nonlinear absorption behavior was observed in GO-porphyrin composites due to strong two-photon absorption, excited state absorption and nonlinear scattering. We have succeeded in getting three different mechanisms in one material to achieve good optical limiting behavior. Nonlinear optical coefficients are enhanced in GO-porphyrin composites when compared to pure porphyrins and GO. We have achieved the *highest* two-photon absorption coefficient of 4920 cm/GW for GO-H_2 porphyrin composite (this is the highest value till date in the literature) as well as the highest excited state absorption and figure of merit. We estimated the limiting thresholds of copper porphyrin, Zinc porphyrin, VO porphyrin, Sn porphyrin, H_2MHTP, graphene oxide, graphene oxide-VO porphyrin, graphene oxide-Sn porphyrin and graphene oxide-H_2MHTP, graphene oxide-zinc porphyrin, graphene oxide- copper porphyrin as 1.7, 1.3, 0.8, 0.9, 1.1, 0.8, 0.32, 0.45 and 0.25, 0.2, 0.1 J/cm^2, respectively. GO-porphyrin composites also have high damage threshold, therefore these composites can act as effective optical limiter.

GO-semiconductor nanoparticles are characterized for optical limiting at two different wavelengths such as 532 nm and 1064 nm. The limiting thresholds of GO, GO-TiO_2 and GO-ZnO composites are 0.80, 0.55 and 0.48 J /cm^2 at 532 nm, respectively and 1.65, 1.35 and 1.15 J/cm^2 at 1064 nm, respectively. High damage threshold of these materials leads them to become effective optical limiters. We have prepared graphene oxide-Au/Ag nanocomposites by *in-situ* reduction of gold salt/$AgNO_3$ on graphene oxide using laser assisted photo-catalytic reduction. This work was done in aqueous solution at ambient conditions. The main advantage of this method to prepare metal nanoparticles-GO hybrids is to avoid the use of toxic chemical reducing agents, thus providing a green approach for the synthesis and processing of metal-graphene oxide nanocomposites.

We have also investigated the effect of solvents on the observed nonlinearities of near infra-red absorbing squaraine and croconate dye samples. Interestingly, we observed a change in the sign of the nonlinearity of phe cro, ptbu cro, phe squ and ptbu squ when solvent contribution was subtracted under ps regime. Further we also observed a change in magnitude of the nonlinearity for all the compounds under both pulse regimes. This is clarity indicates that the solvents play a key role in the measurement of optical nonlinearities and that the true nonlinearities of the solute in fs/ps time domain can only be obtained when the measurements account for the solvent. Therefore, 2PA and 3PA coefficients, β and α_3 values of solvents make significant contribution in the ps and fs regimes.

Out of all three classes of the materials, graphene based hybrid materials have shown excellent nonlinear optical absorption result in high nonlinear optical coefficients. These materials have shown high damage threshold, high dynamic range and low limiting threshold values, therefore these materials achieve the criteria of effective optical limiter.

The scope of our study can thus be further extended by attaching different compounds like liquid crystals, organometallics and donor-acceptor-donor systems to graphene oxide in order to get good optical limiting materials with low limiting threshold values. For practical applications, optical limiting devices are highly desirable and operate efficiently at broadband wavelengths. Carbon nanotubes, as the benchmark optical limiter have been shown to exhibit excellent broadband optical limiting responses. As a new member of the carbon family, graphene oxide is increasingly being studied as a potential optical limiter. Our study demonstrated that graphene oxide-porphyrin composites have shown enhanced optical limiting properties at 532 nm. However, it is of practical importance to study the nonlinear optical response of graphene hybrid materials at different wavelengths to study broadband optical limiting.